



**HAL**  
open science

# Platinum complexes and their luminescent assemblies

Alessandro Aliprandi

► **To cite this version:**

Alessandro Aliprandi. Platinum complexes and their luminescent assemblies. Other. Université de Strasbourg, 2015. English. NNT : 2015STRAF041 . tel-01291440

**HAL Id: tel-01291440**

**<https://theses.hal.science/tel-01291440>**

Submitted on 21 Mar 2016

**HAL** is a multi-disciplinary open access archive for the deposit and dissemination of scientific research documents, whether they are published or not. The documents may come from teaching and research institutions in France or abroad, or from public or private research centers.

L'archive ouverte pluridisciplinaire **HAL**, est destinée au dépôt et à la diffusion de documents scientifiques de niveau recherche, publiés ou non, émanant des établissements d'enseignement et de recherche français ou étrangers, des laboratoires publics ou privés.

**ÉCOLE DOCTORALE DES SCIENCES CHIMIQUES**  
Institut de science et d'ingénierie supramoléculaires

**THÈSE** présentée par :  
**Alessandro ALIPRANDI**

soutenue le : **30 Octobre 2015**

pour obtenir le grade de : **Docteur de l'université de Strasbourg**

Discipline/ Spécialité : Chimie

**PLATINUM COMPLEXES AND THEIR  
LUMINESCENT ASSEMBLIES**

**THÈSE dirigée par :**

**[Mme DE COLA Luisa]**

Professeur, Université de Strasbourg

**RAPPORTEURS :**

**[M. CAMPAGNA Sebastiano]**

Professeur, University of Messina

**[Mme HISSLER Muriel]**

Professeur, University of Rennes 1

---

**AUTRES MEMBRES DU JURY :**

**[M. HOSSEINI Mir Wais]**

Professeur, Université de Strasbourg



# TABLE OF CONTENTS

Résumé.....	xi
Chapter 1: Introduction .....	<b>1</b>
1.1 Interaction between light and matter .....	2
1.2 Transition metal complexes.....	8
1.2.1 Crystal Field Theory and Ligand field Theory.....	9
1.2.2 Photophysical properties of platinum(II) complexes .....	12
1.3 Self-assembly .....	16
1.3.1 Supramolecular polymerization.....	17
1.3.2 Self-assembly and chirality .....	21
1.3.3 Self-assembly of platinum(II) complexes.....	23
1.4 Mechanochromic properties of platinum(II) complexes.....	31
1.5 Bioimaging.....	37
1.5.1 Organic fluorophores.....	40
1.5.2 Quantum dots .....	42
1.5.3 Lanthanide complexes .....	44
1.5.4 Transition metal complexes.....	46
1.5.5 Platinum(II) complexes .....	48
1.6 Scope of the thesis .....	52
1.7 References.....	53

Chapter 2: Experimental techniques .....	<b>61</b>
2.1 Absorption spectroscopy .....	62
2.2 Fluorescence spectroscopy .....	63
2.3 Luminescence quantum yields.....	65
2.4 Lifetime measurements .....	67
2.5 Scanning electron microscope (SEM) .....	69
2.6 Fluorescence microscopy.....	71
2.7 References.....	73
Chapter 3: Self-assembly of a neutral platinum(II) complex into highly emitting microcrystalline fibers through metallophilic interactions .....	<b>75</b>
3.1 Introduction .....	76
3.2 Result and discussion .....	77
3.2.1 Synthesis and characterization .....	77
3.2.1.1 Synthesis of the tridentate ligands .....	77
3.2.1.2 Synthesis of the platinum complexes .....	80
3.2.2 Photophysical properties .....	82
3.2.3 Morphological characterization of the self-assembled fibers.....	85
3.2.4 Fluorescence anisotropy .....	87
3.3 Conclusion .....	89
3.4 Experimental section .....	90
3.4.1 Synthesis and characterization .....	90
3.4.1.1 Pyridine-2,6-bis(carboxamidine) dihydrochloride .....	90

3.4.1.2	2,6-bis(3-(trifluoromethyl)-1H-1,2,4-triazol-5-yl)pyridine (pyC <sub>5</sub> -CF <sub>3</sub> -tzH <sub>2</sub> ) .....	91
3.4.1.3	Pyridine-2,6-bis(carboximidhydrazide) (1) .....	91
3.4.1.4	Py-CF <sub>3</sub> -tzH <sub>2</sub> (Optimized version) .....	91
3.4.1.5	Synthesis of 2,6-bis(3-methyl-1H-1,2,4-triazol-5-yl)pyridine (pyC <sub>5</sub> -CH <sub>3</sub> -tzH <sub>2</sub> ).....	92
3.4.1.6	Platinum [2,6-bis[5-(trifluoromethyl)-1,2,4-triazol-3-yl-κN <sup>2</sup> ]pyridinato(2-)-κN](4-pentylpyridine-κN) (Pt-CF <sub>3</sub> tz-pyC <sub>5</sub> ).....	93
3.4.2	Fluorescence microscopy.....	93
3.4.3	Small-angle/Wide-angle X-ray Scattering (SAXS/WAXS) .....	93
3.4.4	Scanning electron microscopy (SEM) .....	94
3.4.5	Transmission electron microscopy (TEM).....	94
3.5	References.....	95
Chapter 4: Chiral amplification by self-assembly of neutral platinum(II) complexes ..		<b>97</b>
4.1	Introduction .....	98
4.2	Result and discussion .....	99
4.2.1	Synthesis and characterization .....	99
4.2.2	Photophysical properties	100
4.2.3	Morphological characterization of the self-assembled fibers.....	104
4.3	Conclusion .....	105
4.4	Experimental section .....	106
4.4.1	Synthesis and characterization .....	106
4.4.1.1	S(+)-hydroxy-N-(4-pyridinylmethyl)-benzeneacetamide (3a)...	106
4.4.1.2	R(-)-hydroxy-N-(4-pyridinylmethyl)-benzeneacetamide (3b)....	107

4.4.1.3	Platinum [2,6-bis[5-(trifluoromethyl)-1,2,4-triazol-3-yl- $\kappa N^2$ ]pyridinato(2-)- $\kappa N$ ][S(+)-hydroxy-N-(4-pyridinylmethyl)-benzeneacetamide- $\kappa N$ ] (4a) .....	107
4.4.1.4	Platinum [2,6-bis[5-(trifluoromethyl)-1,2,4-triazol-3-yl- $\kappa N^2$ ]pyridinato(2-)- $\kappa N$ ][R(-)-hydroxy-N-(4-pyridinylmethyl)-benzeneacetamide- $\kappa N$ ] (4b) .....	108
4.4.2	SEM analysis .....	108
4.4.3	Emission microscopy .....	108
4.4.4	Photophysical measurements .....	108
4.5	References.....	109
Chapter 5: Controlling and imaging biomimetic self-assembly process .....		<b>111</b>
5.1	Introduction .....	112
5.2	Result and discussion .....	114
5.2.1	Synthesis and characterization .....	114
5.2.2	Photophysical properties .....	117
5.2.3	Depolymerization curves .....	120
5.2.4	Thermodynamic studies.....	122
5.2.5	Kinetic studies .....	124
5.2.6	Real-time imaging of the self-assembly process .....	126
5.2.7	Seeded living supramolecular polymerization .....	130
5.2.8	Photoconversion .....	131
5.2.9	Effect of the molecular design on the self-assembly process .....	132
5.2.9.1	Photophysical properties .....	133
5.2.9.2	Depolymerization curves .....	134
5.2.9.3	Real-time imaging of the self-assembly process .....	137



5.4.7 Living supramolecular polymerization.....	147
5.4.8 Photoconversion experiments.....	148
5.5 References.....	148
Chapter 6: Bioimaging by self-assembling Pt(II) complexes.....	<b>151</b>
6.1 Introduction .....	152
6.2 Results and discussion .....	152
6.2.1 Synthesis of the platinum complexes .....	154
6.2.2 Photophysical properties .....	155
6.2.3 Bioimaging.....	157
6.2.4 Role of the ancillary ligand .....	166
6.2.4.1 Bioimaging.....	167
6.3 Conclusion .....	169
6.4 Experimental Section .....	170
6.4.1 Synthesis and characterization .....	170
6.4.1.1 Platinum [2,6-bis[5-(trifluoromethyl)-1,2,4-triazol-3-yl- $\kappa\text{N}^2$ ]pyridinato(2-)- $\kappa\text{N}$ ](4-pyridinol- $\kappa\text{N}$ ) ( $\text{CF}_3$ -Pt-4OHpy) .....	170
6.4.1.2 Platinum [2,6-bis[3-(4-methylphenyl)-1,2,4-triazol-5-yl- $\kappa\text{N}^2$ ]pyridinato(2-)- $\kappa\text{N}$ ] (4-pyridinol- $\kappa\text{N}$ ) (Tol-Pt-4OHpy).....	171
6.4.1.3 Platinum [2,6-bis[5-(trifluoromethyl)-1,2,4-triazol-3-yl- $\kappa\text{N}^2$ ]pyridinato(2-)- $\kappa\text{N}$ ][4,5-Bis(hydroxymethyl)-2-methylpyridin-3-ol- $\kappa\text{N}$ ] ( $\text{CF}_3$ -Pt-vitB <sub>6</sub> ).....	171
6.4.1.4 Platinum [2,6-bis[5-(trifluoromethyl)-1,2,4-triazol-3-yl- $\kappa\text{N}^2$ ]pyridinato(2-)- $\kappa\text{N}$ ](diethanolamine- $\kappa\text{N}$ ) ( $\text{CF}_3$ -Pt-DEA) .....	172
6.4.2 Cell culture media .....	172
6.4.3 Platinum complexes incubation with PBS .....	172

6.4.4	Incubation with cell culture media .....	173
6.4.5	Organelle staining .....	173
6.4.6	Photobleaching experiments .....	173
6.4.7	Kinetic of internalization of the complex in cell culture media.....	173
6.4.8	Kinetic of cellular expulsion of the complex after cell culture media addition .....	174
6.4.9	Fluorescence confocal microscopy .....	174
6.5	References.....	175
Chapter 7: $\beta$ -lactam bioconjugates bearing luminescent platinum(II) tags: synthesis and photophysical characterization .....		<b>177</b>
7.1	Introduction .....	178
7.2	Results and discussion .....	180
7.2.1	Synthesis and characterization .....	180
7.2.2	Photophysical Characterization .....	184
7.3	Conclusions .....	189
7.4	Experimental Section .....	189
7.4.1	Synthesis and characterization .....	189
7.4.1.1	(3R,4R)-3-((R)-1-[(tert-Butyldimethylsilyl)oxy]ethyl)-4-(pyridin-4- yloxy)azetidin-2-one (1) .....	190
7.4.1.2	{2,6-Bis[3-(trifluoromethyl)-1,2,4-triazol-5- yl]pyridine}PtII[pyridin-4-ol] (CF <sub>3</sub> -Pt-4OHpy) .....	190
7.4.1.3	(3R,4R)-3-((R)-1-(t-butyldimethylsilyl)oxy)ethyl)-4-(3-(pyridin-4- yl) propoxy)azetidin-2-one (2) .....	191

7.4.1.4	Platinum [2,6-bis[5-(trifluoromethyl)-1,2,4-triazol-3-yl- $\kappa\text{N}^2$ ]pyridinato(2-)- $\kappa\text{N}$ ] [(3R,4R)-3-((R)-1-((t-butyl)dimethylsilyl)oxy)ethyl)-4-(3-(pyridin-4-yl)propoxy)azetidin-2-one- $\kappa\text{N}$ ] .....	191
7.4.1.5	1-(pyridin-4-yl)-2,5,8,11-tetraoxatridecan-13-ol (4).....	192
7.4.1.6	Platinum [2,6-bis[5-(trifluoromethyl)-1,2,4-triazol-3-yl- $\kappa\text{N}^2$ ]pyridinato(2-)- $\kappa\text{N}$ ] [1-(pyridin-4-yl)-2,5,8,11-tetraoxatridecan-13-ol- $\kappa\text{N}$ ].....	193
7.4.1.7	(3R,4R)-3-((R)-1-((t-butyl)dimethylsilyl)oxy)ethyl)-4-((1-(pyridin-4-yl)-2,5,8,11-tetraoxatridecan-13-yl)oxy)azetidin-2-one (6).....	193
7.4.1.8	Platinum [2,6-bis[5-(trifluoromethyl)-1,2,4-triazol-3-yl- $\kappa\text{N}^2$ ]pyridinato(2-)- $\kappa\text{N}$ ] [(3R,4R)-3-((R)-1-((t-butyl)dimethylsilyl)oxy)ethyl)-4-((1-(pyridin-4-yl)-2,5,8,11-tetraoxatridecan-13-yl)oxy)azetidin-2-one- $\kappa\text{N}$ ] (7) .....	194
7.5	References.....	195
 Chapter 8: Mechanochromism: from bulk material to the nanoscale .....		<b>197</b>
8.1	Introduction .....	198
8.2	Result and discussion .....	199
8.2.1	Mechanochromic properties of the bulk materials.....	199
8.2.2	Mechanochromism at the nanoscale .....	203
8.2.3	Nanolithography .....	206
8.2.4	Photochromism.....	207
8.3	Conclusion .....	209
8.4	Experimental section .....	209
8.4.1	Pressure dependent emission .....	210
8.4.2	Wide-field imaging.....	210
8.4.3	Confocal Imaging .....	210

8.4.4 Sample preparation .....	210
8.4.5 AFM studies and nanolithography.....	210
8.5 References.....	212
Summary .....	<b>213</b>
Acknowledgements.....	<b>227</b>
Curriculum vitae.....	<b>229</b>



# Résumé

Il est dit que l'être humain se fie à la vision pour approximativement 80% de l'information qu'il reçoit du monde externe. Donc, comme le dit le proverbe « voir, c'est croire », porter un intérêt à ce que l'on voit devrait être très utile, y compris dans le monde de la science.<sup>1</sup> Malheureusement plusieurs systèmes, incluant les systèmes vivants, ne fournissent pas assez d'informations visuelles détectables à l'oeil nu pour nous permettre de comprendre des événements spécifiques tels que la formation/cassure de liaisons covalentes/non-covalentes ainsi que certains procédés biologiques tels que la signalisation cellulaire et l'expression des protéines.

C'est la raison pour laquelle les outils nous permettant de voir des procédés à l'intérieur de systèmes possédant des complexités diverses sont essentielles non seulement pour la recherche basique, mais également pour révéler la formation de structures particulières ayant différentes propriétés ou fonctions, pour diagnostiquer, traiter ou identifier des anomalies.

L'utilisation de la fluorescence est une méthodologie idéale, comparée à la radioactivité, l'électromagnétisme et l'électrochimie.

La sensibilité élevée (puisque la concentration nécessaire pour détecter l'émission dans la plupart des cas est de l'ordre du nano- ou micro molaire), l'accès facile à la technique et la résolution spatiale et temporelle sans perturber les systèmes sont quelques-unes des caractéristiques intéressantes de la fluorescence. D'autre part, certains inconvénients comme la courte durée de vie de l'état excité et un petit

déplacement de Stokes entre l'excitation et l'émission ont poussé les scientifiques à se tourner vers la phosphorescence.

Parmi les complexes métalliques qui affichent un état triplet à propriétés luminescentes, les complexes organométalliques de platine(II) ont attiré notre attention en raison de leur géométrie carrée plan qui favorise la formation d'agrégats qui, dans certains cas, sont stabilisés à travers les interactions des orbitales  $5d_{z^2}$  qui peuvent fournir une liaison métal-métal.<sup>2-9</sup> Si les interactions électroniques entre le Pt (II) sont fortes (généralement lorsque la distance Pt...Pt est inférieure à 3,5 Å), de nouveaux états excités sont générés, cela peut conduire à un changement vers l'énergie inférieure de l'émission et à d'intéressants rendements quantiques d'émission.

Les transitions résultant sont appelés soit transfert de charges métal-métal-ligand (MMLCT) ou transfert de charges excimérique ligand à ligand. La transition MMLCT implique le transfert de charges entre une orbitale antiliante Pt...Pt pleine et une orbitale  $\pi^*$  vacante (Figure 1). La différence énergétique entre l'HOMO et la LUMO de cet état excité montre une forte dépendance de la distance métal-métal: il diminue en effet avec la distance Pt...Pt.<sup>10,11</sup>

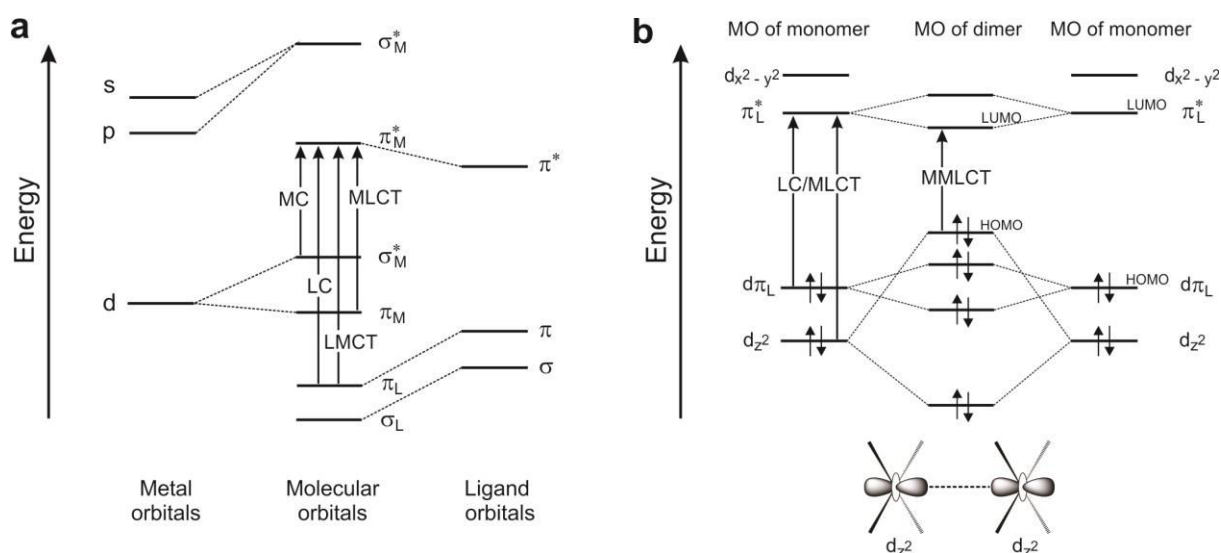


Figure 1. (a) Schéma simplifié d'OM pour un complexe de métal de transition générique et transitions relatives et spectroscopiques d'excitation. (b) Schéma simplifié d'OM de deux complexes plan carré de platine (II) interagissant, montrant le chevauchement d'orbitales  $d_{z^2}$  intermoléculaires à l'état fondamental et son influence sur l'énergie des niveaux de l'OM.

Notre groupe a reporté une classe de complexes de Pt(II) neutres très émissifs portant un ligand tridentate dianionique de type N<sup>N</sup>N et une pyridine comme ligand auxiliaire. Un contrôle rationnel de la conception de ces molécules permet le contrôle de la tendance d'empilement, qui peut être complètement évitée en faveur de la pureté de la couleur;<sup>12</sup> ce qui est important pour la technologie OLED. Elle peut être également fortement favorisée pour former une structure auto-assemblée.<sup>6-8</sup>

Après l'agrégation, de tels matériaux affichent non seulement un effet bathochrome pour les spectres d'absorption et d'émission dû à la formation d'un nouvel état excité de caractère <sup>3</sup>MMLCT, mais également une émission induite par l'agrégation (AIE) / une émission induite par l'agrégation améliorée (AIEE) avec un rendement quantique de photoluminescence (PLQY) allant jusqu'à 87%<sup>6</sup> et ce même sous air, ce qui suggère que le chromophore est protégé contre le dioxygène ou contre l'extinction due à l'environnement.

**L'objectif** de cette thèse est de concevoir, de synthétiser et d'étudier de nouveaux complexes de platine et ainsi de comprendre comment la structure chimique peut dicter la formation d'agrégats luminescents. Un intérêt particulier est consacré à la compréhension et à la maîtrise des procédés d'assemblage, avec pour dernier défi de passer de la solution à un environnement plus concurrentiel tel que les systèmes vivants afin de concevoir une nouvelle génération de sondes dans la bio-imagerie. Certaines applications possibles sont également examinées dans les matériaux méchanochromiques.

### **Complexes de platine et leurs assemblages en solution**

Ces travaux de thèse portent sur l'étude de complexes de Pt(II) possédant un ligand tridentate portant différents dérivés de pyridine pour compléter la sphère de coordination. Le premier composé à étudier est **Pt-CF<sub>3</sub>tz-pyC<sub>5</sub>** (figure 2). La coordination d'un groupement alkyle auxiliaire pyridine à des 2,6-bis (3-(trifluorométhyl)-1H-1,2,4-triazol-5-yl) pyridine a permis d'améliorer la solubilité et ainsi la processabilité. L'approche synthétique implique une réaction « one-pot »

dans des conditions douces en présence d'une base adéquate et d'un précurseur inorganique de platine(II).<sup>6,13</sup>

En solution ( $c = 5 \times 10^{-5} \text{M}$ ) dans le chloroforme à température ambiante, le spectre d'absorption présente des bandes intenses dans la région de l'UV, principalement attribuables à des transferts de charge intraligand (<sup>1</sup>IL) et interligand (<sup>1</sup>ILCT) (Figure 2b).

Cependant, la lente évaporation du solvant conduit à la formation de fibres lumineuses jaunes émissives microcristallines qui peuvent être alignées (Figure 2a). L'émission provenant de transitions MMLCT à une bande non structurée,  $\lambda_{em,max} = 559 \text{ nm}$ , et le rendement quantique de photoluminescence (PLQY) est de 0,74 (Figure 2b).

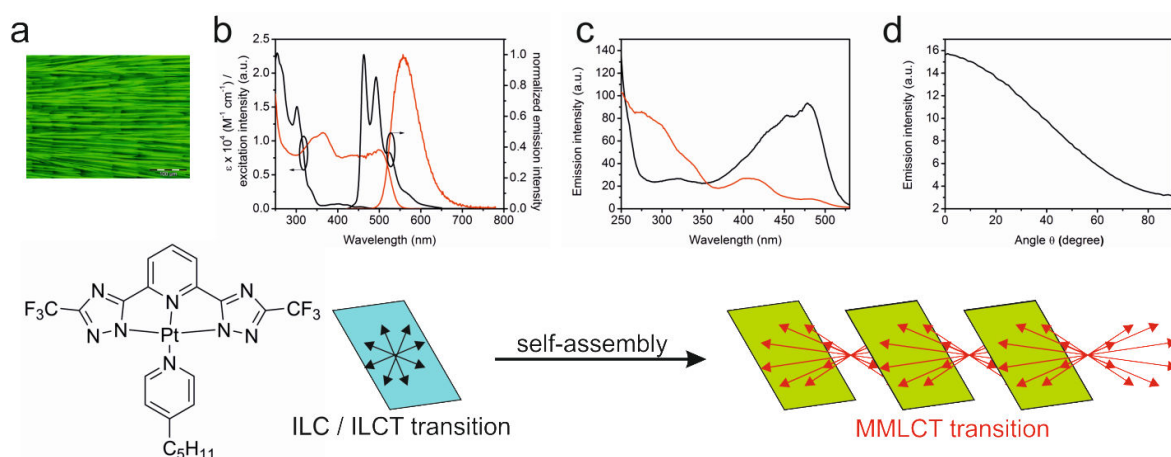


Figure 2. (a) Image en microscopie de fluorescence des fibres alignées obtenus à partir d'acétone, sous irradiation à  $\lambda = 400\text{-}440 \text{ nm}$ . Echelle =  $100 \mu\text{m}$ . (b) spectres d'absorption et spectres d'émission ( $\lambda_{exc} = 300 \text{ nm}$ ) obtenues dans le chloroforme ( $5 \times 10^{-5} \text{ M}$ ) à température ambiante (trace noire); et pour les fibres obtenues à partir d'une solution de  $4 \text{ mg/mL}$  dans l'acétone à  $\lambda_{em} = 630 \text{ nm}$  et lors de l'excitation à  $\lambda_{exc} = 300 \text{ nm}$  (trace rouge). (c) Spectres d'excitation ( $\lambda_{em} = 555 \text{ nm}$ ) en utilisant une lumière polarisée linéairement pour exciter des fibres parallèles à la direction de croissance (traces noires) et à  $90^\circ$  (trace rouge). (d) Polarisation d'émission ( $\lambda_{exc} = 300 \text{ nm}$ ,  $\lambda_{em} = 555 \text{ nm}$ ).

Des mesures d'anisotropie de fluorescence ont montré une polarisation linéaire élevée à la fois dans l'excitation (Figure 2c) et l'émission (Figure 2d). Nous avons trouvé que l'émission est polarisée parallèlement à la direction de croissance de la fibre (Figure 2d) et il a été remarqué qu'elle est indépendante de la longueur d'onde d'excitation. Quant à sa polarisation, elle indique une relaxation rapide au plus faible

état excité ( $^3\text{MMLCT}$ ) qui possède un moment de transition dipolaire orienté le long des fibres.

Plus intéressant encore, les spectres d'excitation obtenus en utilisant l'excitation polarisée linéairement montre clairement qu'un tel moment dipolaire émissif correspond à la bande de basse énergie qui est absente lorsque le complexe est dissous dans un solvant pur (Figure 2b). Nous avons constaté que le moment dipolaire d'une telle transition est orthogonal au moment dipolaire de transition des bandes dans la région UV.

Afin de corrélérer la structure chimique du complexe avec le comportement d'autoassemblage, nous avons décidé d'étudier des composés possédant le même ligand tridentate mais un substituant pyridine différent. Nous avons examiné l'effet de l'introduction d'un seul centre chiral dans la conception moléculaire puisque ces structures auto-assemblées luminescentes sont susceptibles de présenter des propriétés chiro-optiques très intéressantes<sup>14-16</sup> et d'éventuelles applications en interrupteurs chiro-optiques<sup>17</sup> et appareils électroluminescents tels que les diodes électroluminescentes organiques 3D (OLED 3D).<sup>18</sup>

Nous avons synthétisé deux complexes énantiomères de Pt(II) en utilisant un motif chiral comme ligand ancillaire. Comme attendu, les deux complexes énantiomères en solution diluée ( $c = 5 \times 10^{-5}$  M) présentent les mêmes propriétés photophysiques caractérisées par une forte absorption dans la région de l'UV et une très faible (PLQY < 1 %) émission de structure bleue qui ressemble bien au complexe discuté ci-dessus (Figure 3a).

En déposant des gouttes de solution à  $1,03 \text{ mg.mL}^{-1}$  dans le THF des énantiomères soit S soit R sur des substrats en verre, nous avons observé la formation de fibres claires émissives (Figure 3d). Dans ce cas aussi, la formation d'une faible bande d'absorption et la formation d'une large émission déplacée par effet bathochrome est due à l'établissement d'interactions métallophiles Pt...Pt à l'état fondamental qui donne une hausse à la bande MMLCT (Figure 3a).

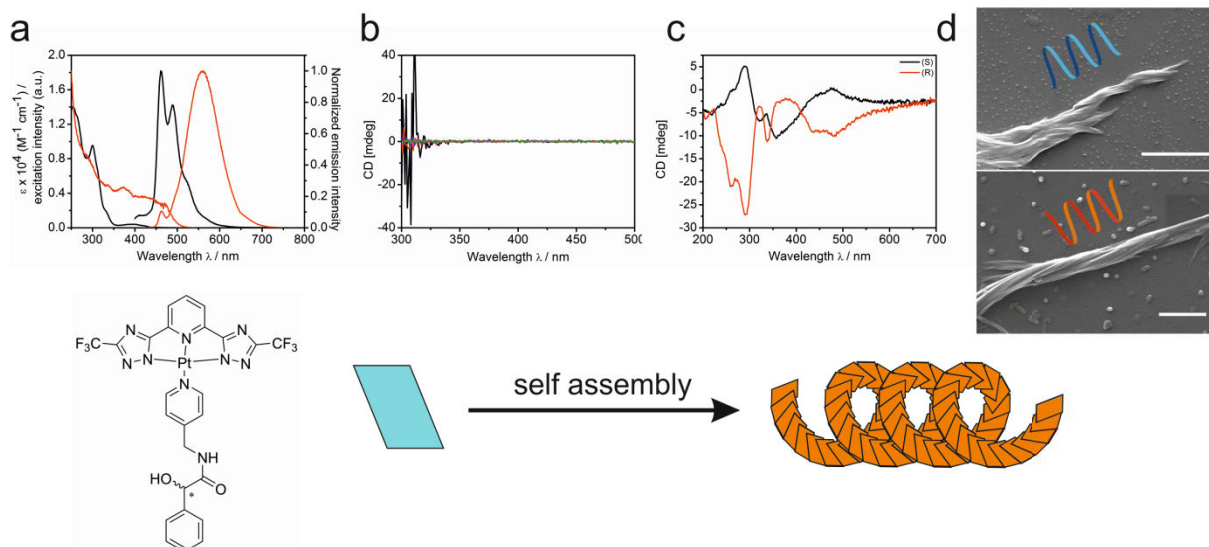


Figure 3. (a) Spectres d'absorption et spectres d'émission ( $\lambda_{exc} = 300$  nm) obtenus dans le THF ( $5 \times 10^{-5}$  M) à température ambiante (trait noir) et pour les fibres obtenus à partir d'une solution dans l'acétone à  $1,03$  mg.mL<sup>-1</sup> à  $\lambda_{em} = 630$  nm et sous excitation à  $\lambda_{exc} = 300$  nm (trait rouge). (b) Signal de DC du complexe de platine (gamme de concentration  $10^{-6}$ - $10^{-4}$  M). (c) Signal de DC des fibres auto-assemblées après avoir déposé des gouttes d'une solution de THF contenant l'énantiomère S (trait noir) et l'énantiomère R (trait rouge) sur du verre. (d) Photos au MEB des fibres chirales des énantiomères R (en haut) et S (en bas) montrant les différentes hélicités.

Lorsque les complexes sont dissous à l'état moléculaire, il n'est pas possible de détecter un signal de dichroïsme circulaire (CD) (gamme de concentration  $10^{-6}$ - $10^{-4}$  M) même si la pyridine auxiliaire seule donne un signal clair de CD. Au contraire, les fibres auto-assemblées présentent un signal de CD avec deux paramètres distincts pour les deux fibres chirales (Figure 3c).

De l'analyse par microscopie électronique, en l'occurrence, la MEB, a été effectuée sur les structures auto-organisées et les échantillons ont donné des fibres interconnectées avec une hélicité apparente suite à l'organisation supramoléculaire chirale des complexes dans les assemblages et un bon ratio d'aspect. En particulier, les énantiomères R et S s'agrègent dans un arrangement « clockwise » et « counterclockwise » respectivement, résultant en des agrégats autoassemblés avec des configurations hélicoïdales de type main droite (P) et main gauche (M) respectivement (Figure 3d). Par ailleurs, dans les deux cas, les nanostructures

fibreuses semblent être les résultats d'un auto-assemblage de nanostructures plus fines telles que des nanofibrilles.

La formation de telles structures supramoléculaires chirales est en effet responsable de l'amplification du signal de CD qui n'a pas lieu lorsque les complexes sont dissous à l'état moléculaire à cause de l'écrasante absorption du complexe par rapport à la force du signal de CD donné par l'unique centre chiral.

Afin d'étudier l'effet de différentes chaînes et d'améliorer la solubilité du matériau dans des solvants plus polaires tels que l'eau, en donnant un caractère amphiphile à la molécule, en la maintenant toujours non chargée, nous avons préparé des dérivés de polyéthylène glycol.

Dans le chapitre 5 sont décrites la synthèse, la caractérisation et le comportement photophysique du complexe **Pt-CF3tz-pyPEG** (Figure 4a) dans lequel la pyridine ancillaire a été fonctionnalisée avec un triéthylène glycol hydrophile à travers un motif capable d'engendrer des liaisons hydrogène directionnelles telles que N–H.

Lorsque le complexe est dissous à l'état moléculaire dans le 1,4-dioxane «airequilibrated» ( $c = 0.1\text{--}200 \times 10^{-5}$  M), seulement une faible émission bleue est détectée avec un rendement quantique de photoluminescence (PLQY) d'environ 1 %. Sous l'injection éclair d'une solution de dioxane de **Pt-CF3tz-pyPEG** ( $c = 2 \times 10^{-3}$  M) dans l'eau, agissant comme le non-solvant, nous sommes parvenus à cinétiquement piéger ce composé dans un état métastable (assemblage **A**).

Un tel assemblage, constitué de nanoparticules molles, présente une forte phosphorescence orange (PLQY = 84 %), malgré la condition «air-equilibrated», et, par conséquent, la présence de dioxygène qui devrait inhiber l'état excité triplet à longue vie. La raison du manque d'inhibition peut être attribuée à la formation de nanostructures compactes dans lesquelles l'établissement d'interactions métallophiles<sup>4,6,10,19-21</sup> empêche une diffusion efficace de l'inhibiteur dans la structure.

Nous avons constaté qu'en jouant avec le ratio solvant/non solvant et en utilisant une sphère intégrante pour étudier les changements dans les propriétés photophysiques, nous sommes parvenus à caractériser et contrôler un paysage



entre nucléation-élongation caractérisé par une étape de nucléation défavorable et suivant un processus d'élongation favorable.

Avec la composition en solvant 95:5 d'eau:dioxane, le processus très lent de nucléation-élongation de **B** et de **C** est piégé, rendant possible l'étude du contrôle de l'expansion coopérative de **C** en utilisant l'ensemencement vivante de la polymérisation supramoléculaire.<sup>22</sup>

Dans ce but, en partant de l'assemblage pure **A** à 95% dans l'eau ( $c = 5 \times 10^{-5} \text{M}$ ,  $D_h = 114.4 \text{ nm}$ ,  $\text{IPD} = 0.188$ ) nous obtenons sélectivement les semences **C** avec une plutôt bonne distributivité en taille ( $D_h = 265.3 \text{ nm}$ ,  $\text{IPD} = 0.150$ ) après sonication. L'addition de différents aliquotes d'une telle suspension de seeds **C** à un excès du métastable **A** pure (95%  $\text{H}_2\text{O}$ ) amène à un changement dans le spectre d'émission électronique en respectant le temps de réaction avec une cinétique d'ordre 1 concordant à un ordre typique (seeds **C**) de l'expansion de la polymérisation en chaîne.<sup>23</sup>

Les analyses au microscope confocale montres la formation de bâtonnets émettant dans le bleu de longueur uniforme qui augmente en diminuant la quantité en **C** (Figure 5 à gauche). Le contrôle de la taille de l'assemblage **C** a aussi été faite, cependant, un succès total pour obtenir l'assemblage **B** par «off-pathway» comme une isoforme pure semble toujours être écarté.

Cela est dû à la nature transitoire intrinsèque de **B** aussi bien qu'à la formation concomitante de **C**. Maintenant, nous découvrons qu'il est possible de produire une rapide interconversion  $\text{C} \rightarrow \text{B}$  dans 95:5%  $\text{H}_2\text{O}$ :dioxane avec une bonne résolution spatiale, en gardant les caractéristiques structurales intactes, en irradiant ce premier avec un laser plus puissant que celui utilisé pour l'imagerie (Figure 5 à droite).

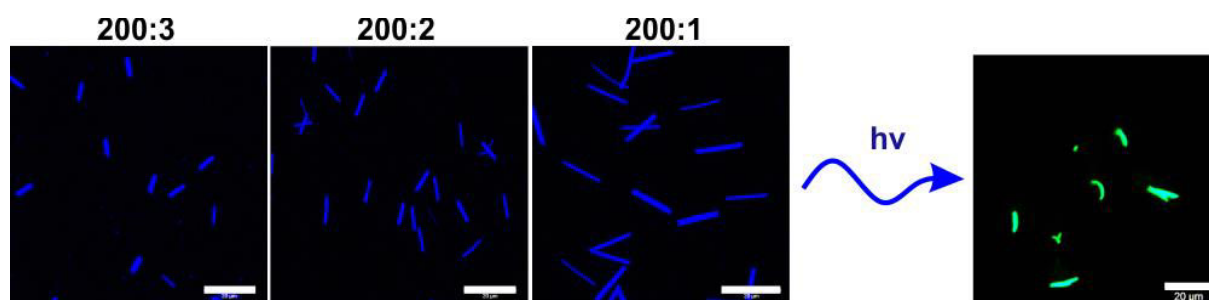


Figure 5. Images au microscope confocales fibres obtenues à partir de polymérisations sous différentes conditions and photoconversions  $[\text{A}]/[\text{C}]$ .

Ces résultats indiquent clairement comment une conception rationnelle d'une molécule peut amener à une nouvelle classe de sonde luminescente dans laquelle un environnement spécifique peut déclencher un processus d'auto assemblage.

### **L'auto-assemblage comme outil pour la bio-imagerie**

Les interactions métallophiles qui mènent à la formation de bandes MMLCT peuvent être utilisées à notre avantage afin d'induire un déplacement bathochrome de l'émission et de l'excitation tout en augmentant le rendement quantique de photoluminescence (PLQY). De telles recherches pourraient mener au développement de nouvelles sondes optiques pour l'imagerie *in vitro* possédant une forte luminescence ainsi que des temps de vie de luminescence très long.<sup>24</sup>

Néanmoins, plusieurs conditions sont requises pour qu'un luminophore soit utilisable en bio-imagerie. En effet, la stabilité et la solubilité dans des tampons aqueux et des milieux de cultures, la faible toxicité dans l'organisme et l'assimilation rapide par les cellules sont indispensables. Il est également préférable d'éviter l'ajout d'agents chimiques et d'induire une localisation préférentielle dans certains organites.<sup>25,26</sup>

Il est facile de comprendre que certaines propriétés entre en conflit avec d'autres. Par exemple, l'internalisation rapide du luminophore dans les cellules requière un caractère lipophile afin de passer la barrière phospholipidique des cellules, ce qui rentre en contradiction avec la solubilité aqueuse voulue. Beaucoup de ces caractéristiques telles que la localisation ou les propriétés photophysiques dans des conditions physiologiques ne peuvent être prédites *a priori*.

De fait, la plupart des molécules luminescentes ont été découvertes de manière fortuite ou en criblant une série de composés.<sup>27-29</sup> Afin d'étudier l'auto-assemblage dans un environnement aussi complexe qu'une cellule vivante, deux nouveaux complexes ont été imaginés, synthétisés et étudiés dans un milieu cellulaire. Nous avons découvert que les complexes **Tol-Pt-4OHpy** et **CF3-Pt-4OHpy** (Figure 6) sont internalisées dans les cellules cancéreuses cervicales, HeLa, sous certaines conditions. Notons que le composé fluoré s'accumule principalement dans le noyau des cellules

menant à des assemblages très émissifs. Le composé tolylé s'accumule quant à lui dans le cytoplasme.

Le spectre d'émission pris aux endroits les plus émissifs correspondent à ceux des systèmes auto-assemblés mesurés indépendamment dans une solution DMSO-eau. Les agrégats possèdent de très faibles bandes d'absorption <sup>1</sup>MMLCT qui s'étendent jusque dans le visible, ce qui les rend intéressant pour la bio-imagerie. Nous pouvons en effet les exciter à de basses énergies, jusqu'à 550 nm, alors que l'espèce monomérique ne possède pas de bandes d'absorption dans cette région.

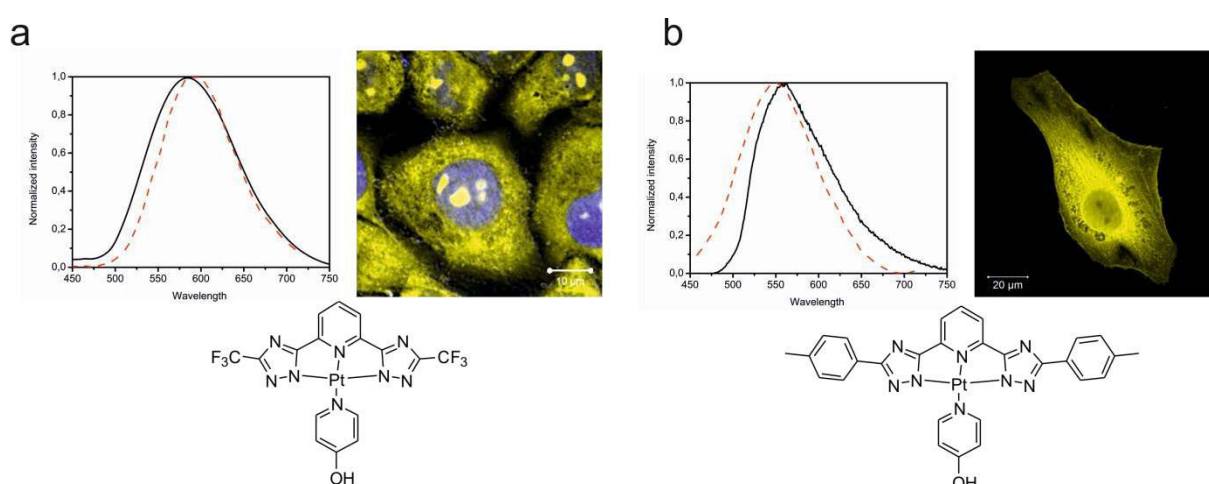


Figure 6. Microscopie confocale montrant les distributions de **CF<sub>3</sub>-Pt-4OHpy** (a), DAPI en bleu et **Tol-Pt-4OHpy** (b) dans des cellules HeLa; spectres d'émission mesurés dans une solution de DMSO:H<sub>2</sub>O (en noir) et dans les cellules HeLa (en pointillés rouges).  $\lambda_{exc} = 330$  nm dans les solvants, et 405 nm in cellulo.

Nous avons démontré que le phénomène d'agrégation ne conduit pas seulement à la protection du complexe de platine mais permet également d'éviter les phénomènes de photo-blanchiment. Il est important de noter que l'internalisation et l'assimilation de ces complexes dans les cellules HeLa ne se fait que lorsque l'on utilise du tampon PBS (solution saline tamponnée au phosphate). Cependant, les cellules endommagées ou mortes internalise les luminophores quel que soit le milieu cellulaire.

Les images de cellules vivantes HeLa incubées avec **CF<sub>3</sub>-Pt-4OHpy** et excitées à 405 nm ne révèlent aucune assimilation lors des 30 premières minutes, mais commence rapidement lorsque l'on expose ces cellules plus longtemps à la lumière UV.<sup>30</sup>

Comme vous pouvez le voir dans la Figure 7, seule la zone irradiée par la lumière UV présente une assimilation du complexe alors que les cellules environnantes ne l'internalisent pas étant donné qu'elles n'ont pas été endommagées.

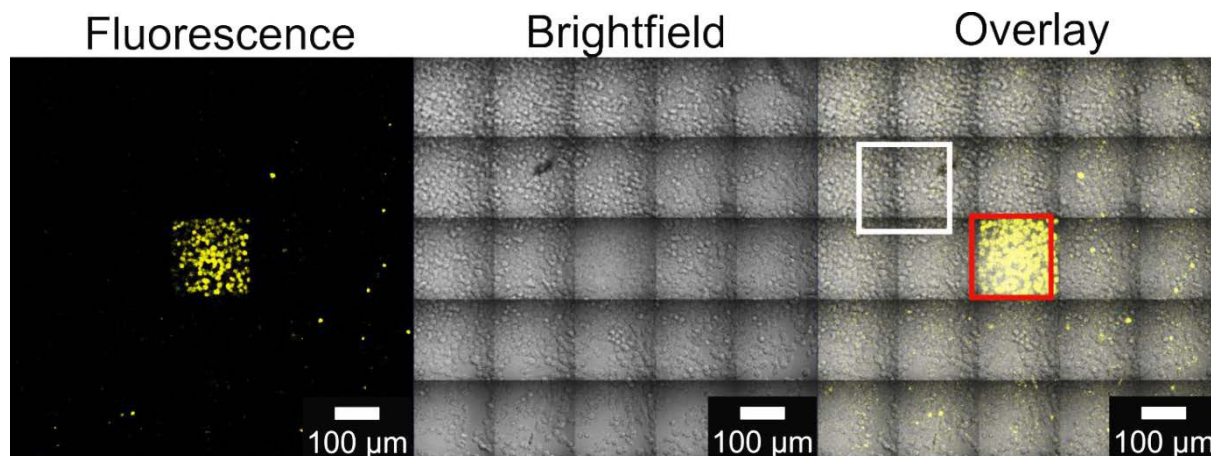


Figure 7. Internalisation induite par la lumière de **CF<sub>3</sub>-Pt-4OHpy** dans un milieu de culture après 60 minutes d'irradiation montrant les régions non excitées et celle exposé à une irradiation à 405 nm.

Nous n'avons pour l'heure pas de preuve que le complexe est internalisé en tant qu'espèce monomérique et que les agrégats se forment *in cellulo* ou qu'il est internalisé en tant que petits agrégats. La formation de tels agrégats peut être considérée comme une nouvelle classe de sondes dynamiques car leurs émissions peuvent être modulées et leur long temps de vie peut être facilement détecté. En outre, nous pouvons modifier la structure des ligands entourant le métal afin de localiser le complexe dans une zone spécifique de la cellule. Le complexe étudié ici peut par exemple permettre de localiser les cellules mortes.

### **Auto-assemblage à l'état solide**

Comme décrit précédemment, les propriétés de photoluminescence de cette classe de composé dépendent fortement non seulement de l'éclatement du champ de ligands, mais aussi des distances intermoléculaires entre complexes. Il a déjà été démontré que la séparation Pt...Pt peut être modulée à l'état solide, sous exposition de petites molécules organiques (VOCs),<sup>31</sup> et de stimuli mécanique,<sup>32,33</sup> ce qui

conduit à un changement réversible de couleur par vapochromisme<sup>34,35</sup> ou méchanochromisme.

De telles propriétés ont attiré un intérêt grandissant pour la création de nouveaux matériaux et le changement de couleur par agrégation peut être utilisable pour des diodes blanche organiques électroluminescentes (WOLED)<sup>36,37</sup> ou encore pour le développement de «nez électriques» qui peuvent détecter de petites molécules organiques volatiles.

Dans le chapitre 7, nous avons étudié les propriétés du complexe **Pt-CF<sub>3</sub>tz-pyPEG** à l'état solide. Le complexe présente une émission dans le bleu (Figure 8b) avec des maximums à  $\lambda_{em} = 465$  et  $495$  nm et un PLQY de 20%. Après broyage, le complexe devient émissif dans le jaune avec un PLQY de 51% et un spectre d'émission contenant une bande large à  $\lambda_{max} = 598$  nm (Figure 8b). Après ajout de quelques gouttes d'acétone, le complexe redevient émissif dans le bleu après séchage (Figure 8e).

La réversibilité de ce système et la résistance à la fatigue du matériau sont une confirmation que ces changements sont dus à une différence d'empilement des complexes. Le complexe **Pt-Toltz-pyPEG** (Figure 8d) présente également une réponse méchanochrome similaire. Avant broyage, le complexe présente une émission dans le vert ( $\lambda_{max} = 542$  nm) avec un PLQY de 46% alors qu'après broyage, l'émission subit un déplacement bathochrome ( $\lambda_{max} = 582$  nm) et le PLQY passe à 35% (Figure 8d). Quelques gouttes d'acétone permettent de retrouver l'émission initiale après séchage (Figure 8g).

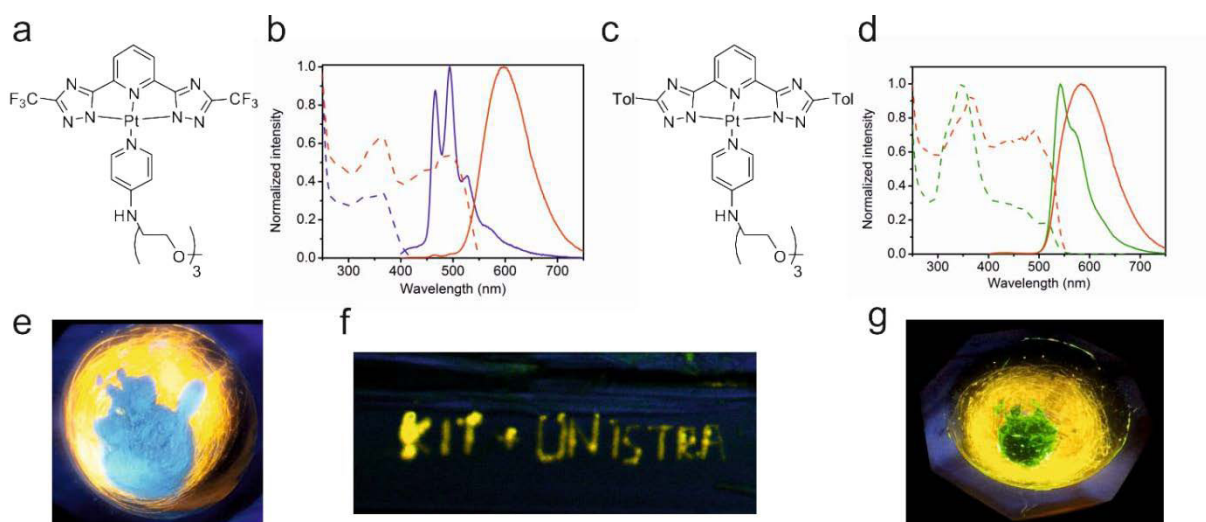


Figure 8. (a) et (c) Structures chimiques de **Pt-CF<sub>3</sub>tz-pyPEG** et **Pt-Toltz-pyPEG** et leur spectre d'émission (lignes pleines) et d'excitation (lignes pointillées) avant (ligne bleue et vertes) et après broyage (ligne rouge). (e) et (g) photographies du solide après broyage montrant la réversibilité du processus par addition d'acétone. (f) Image confocale d'une fibre seule obtenue à partir de **Pt-CF<sub>3</sub>tz-pyPEG** après broyage AFM.

De tels comportements ont été observés et étudiés sur des matériaux volumineux et comme le complexe **Pt-CF<sub>3</sub>tz-pyPEG** peut s'auto-assembler en de micro rubans, nous avons étudié ce phénomène à l'échelle microscopique.

Nous avons étudié en particulier le mechanochromisme à l'échelle nanoscopique en induisant diverse sources de stimuli mécaniques, tout en étudiant le matériau par microscopie électronique.

Nous avons découvert qu'il est possible d'utiliser la lithographie AFM (Figure 8f) afin d'enregistrer des données à l'échelle submicrométrique. De plus, ces informations peuvent être effacées après une exposition de quelques minutes à la lumière UV.

En conclusion, nous avons démontré comment des complexes de Pt(II) peuvent s'auto-assembler de manière contrôlée et que le matériau résultant peut avoir des propriétés de photoluminescence améliorées, ce qui pourrait être utile dans le domaine de la bio-imagerie ou encore le développement de nouveaux matériaux.

## Références

- [1] T. Terai; T. Nagano, *Pflugers Arch - Eur J Physiol*, **2013**, 465, 347-359.
- [2] Y. Sun; K. Ye; H. Zhang; J. Zhang; L. Zhao; B. Li; G. Yang; B. Yang; Y. Wang; S.-W. Lai; C.-M. Che, *Angew. Chem. Int. Ed. Engl.*, **2006**, 118, 5738-5741.

- [3] M. Y. Yuen; V. A. Roy; W. Lu; S. C. Kui; G. S. Tong; M. H. So; S. S. Chui; M. Muccini; J. Q. Ning; S. J. Xu; C. M. Che, *Angew. Chem. Int. Ed. Engl.*, **2008**, *47*, 9895-9899.
- [4] M. Krikorian; S. Liu; T. M. Swager, *J. Am. Chem. Soc.*, **2014**, *136*, 2952-2955.
- [5] F. Camerel; R. Ziessel; B. Donnio; C. Bourgoigne; D. Guillon; M. Schmutz; C. Iacovita; J.-P. Bucher, *Angew. Chem. Int. Ed. Engl.*, **2007**, *46*, 2659-2662.
- [6] C. A. Strassert; C. H. Chien; M. D. Galvez Lopez; D. Kourkoulos; D. Hertel; K. Meerholz; L. De Cola, *Angew. Chem. Int. Ed. Engl.*, **2011**, *50*, 946-950.
- [7] N. K. Allampally; C. A. Strassert; L. De Cola, *Dalton Trans.*, **2012**, *41*, 13132-13137.
- [8] N. K. Allampally; M. Bredol; C. A. Strassert; L. De Cola, *Chem. Eur. J.*, **2014**, *20*, 16863-16868.
- [9] C. Po; Z. Ke; A. Y. Tam; H. F. Chow; V. W. Yam, *Chem. Eur. J.*, **2013**, *19*, 15735-15744.
- [10] B. Ma; J. Li; P. I. Djurovich; M. Yousufuddin; R. Bau; M. E. Thompson, *J. Am. Chem. Soc.*, **2005**, *127*, 28-29.
- [11] K. M.-C. Wong; V. W.-W. Yam, *Acc. Chem. Res.*, **2011**, *44*, 424-434.
- [12] C. Cebrian; M. Mauro; D. Kourkoulos; P. Mercandelli; D. Hertel; K. Meerholz; C. A. Strassert; L. De Cola, *Adv. Mater.*, **2013**, *25*, 437-442.
- [13] M. Mydlak; M. Mauro; F. Polo; M. Felicetti; J. Leonhardt; G. Diener; L. De Cola; C. A. Strassert, *Chem. Mater.*, **2011**, *23*, 3659-3667.
- [14] Y. Wang; J. Xu; Y. Wang; H. Chen, *Chem. Soc. Rev.*, **2013**, *42*, 2930-2962.
- [15] F. Garcia; L. Sanchez, *J. Am. Chem. Soc.*, **2012**, *134*, 734-742.
- [16] F. Aparicio; F. Vicente; L. Sanchez, *Chem. Commun.*, **2010**, *46*, 8356-8358.
- [17] P. Guo; L. Zhang; M. Liu, *Adv. Mater.*, **2006**, *18*, 177-180.
- [18] M. Grell; D. D. C. Bradley, *Adv. Mater.*, **1999**, *11*, 895-905.
- [19] M. Mauro; A. Aliprandi; C. Cebrian; D. Wang; C. Kübel; L. De Cola, *Chem. Commun.*, **2014**, *50*, 7269-7272.
- [20] V. W.-W. Yam; K. M.-C. Wong; N. Zhu, *J. Am. Chem. Soc.*, **2002**, *124*, 6506-6507.
- [21] C. Po; A. Y. Tam; K. M. Wong; V. W. Yam, *J. Am. Chem. Soc.*, **2011**, *133*, 12136-12143.
- [22] S. Ogi; K. Sugiyasu; S. Manna; S. Samitsu; M. Takeuchi, *Nat. Chem.*, **2014**, *6*, 188-195.
- [23] *Principles of Polymerization*, ed. John Wiley & Sons, Inc., **2004**
- [24] R. Weissleder; V. Ntziachristos, *Nat Med*, **2003**, *9*, 123-128.
- [25] V. Fernandez-Moreira; F. L. Thorp-Greenwood; M. P. Coogan, *Chem. Commun.*, **2010**, *46*, 186-202.
- [26] F. L. Thorp-Greenwood; R. G. Balasingham; M. P. Coogan, *J. Organomet. Chem.*, **2012**, *714*, 12-21.
- [27] E. Kim; M. Koh; J. Ryu; S. B. Park, *J. Am. Chem. Soc.*, **2008**, *130*, 12206-12207.
- [28] A. Samanta; M. Vendrell; R. Das; Y.-T. Chang, *Chem. Commun.*, **2010**, *46*, 7406-7408.
- [29] Y. Kawazoe; H. Shimogawa; A. Sato; M. Uesugi, *Angew. Chem. Int. Ed. Engl.*, **2011**, *50*, 5478-5481.
- [30] K. V. Bogdanov; A. B. Chukhlovina; A. Y. Zaritsky; O. I. Frolova; B. V. Afanasiev, *British journal of haematology*, **1997**, *98*, 869-872.
- [31] M. Kato; A. Omura; A. Toshikawa; S. Kishi; Y. Sugimoto, *Angew. Chem. Int. Ed. Engl.*, **2002**, *41*, 3183-3185.
- [32] A. L. Balch, *Angew. Chem. Int. Ed. Engl.*, **2009**, *48*, 2641-2644.
- [33] T. Abe; T. Itakura; N. Ikeda; K. Shinozaki, *Dalton Trans.*, **2009**, 711-715.
- [34] A. Han; P. Du; Z. Sun; H. Wu; H. Jia; R. Zhang; Z. Liang; R. Cao; R. Eisenberg, *Inorg. Chem.*, **2014**, *53*, 3338-3344.
- [35] J. Ni; Y. G. Wang; H. H. Wang; L. Xu; Y. Q. Zhao; Y. Z. Pan; J. J. Zhang, *Dalton Trans.*, **2014**, *43*, 352-360.

- [36] L.-M. Huang; G.-M. Tu; Y. Chi; W.-Y. Hung; Y.-C. Song; M.-R. Tseng; P.-T. Chou; G.-H. Lee; K.-T. Wong; S.-H. Cheng; W.-S. Tsai, *J. Mater. Chem. C*, **2013**, *1*, 7582-7592.
- [37] B. Ma; P. I. Djurovich; S. Garon; B. Alleyne; M. E. Thompson, *Adv. Funct. Mater.*, **2006**, *16*, 2438-2446.

# Chapter 1

## Introduction

**Abstract:** This chapter introduces the basic concepts regarding the interactions between light and matter in terms of electronic states and transitions, providing also some fundamentals of fluorescence polarization and anisotropy measurements. We will focus on the photophysical properties of  $d^6$  and  $d^8$  transition metal complexes, in particular Pt(II) complexes. Moreover, the self-assembly of Pt(II) complexes into supramolecular architectures and the application of such materials will be briefly introduced.

## 1.1 Interaction between light and matter

Light consists of electromagnetic waves, which are synchronized oscillations of electric and magnetic fields. The oscillations of the two fields are perpendicular to each other, and perpendicular to the direction the wave. They are characterized by either the frequency or wavelength of their oscillations, which determines their energies ( $E=h\nu$ ). The resulting electromagnetic spectrum and the corresponding interactions with matter are depicted in Figure 1.1.

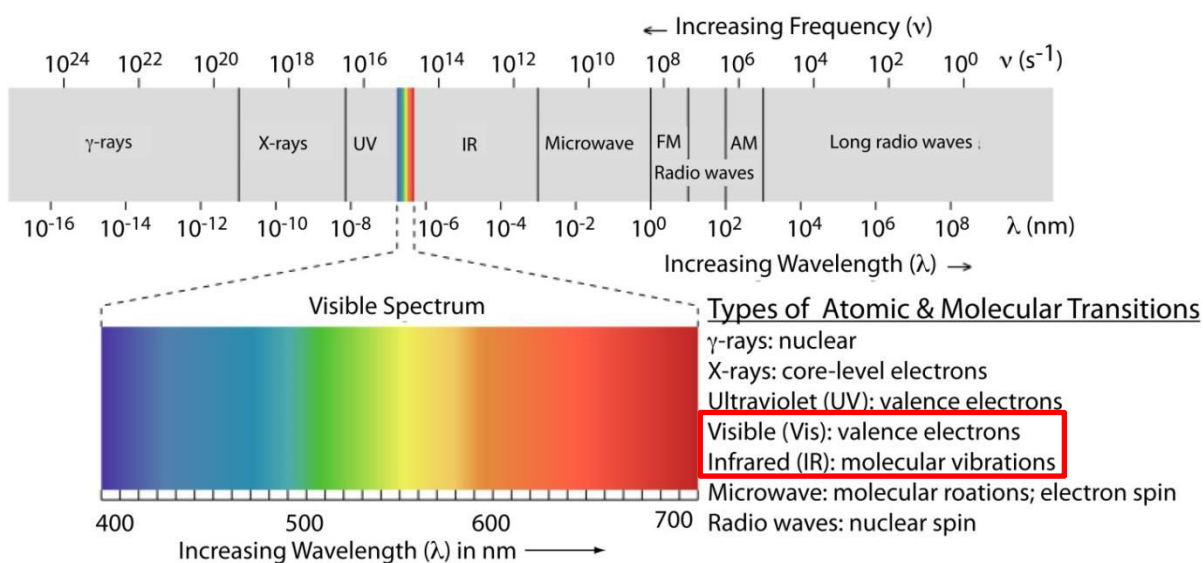


Figure 1.1. The electromagnetic spectrum showing the boundaries between different regions and the type of atomic or molecular transition responsible for the change in energy. The UV-vis region is where photochemistry takes place.<sup>1</sup> The colored inset shows the visible spectrum.

The interaction of light with matter as a natural phenomenon and/or as an artificial process permeates most branches of science, from biology to materials science.<sup>2,3</sup> For instance, our life depends on photosynthesis, a photochemical process taking place in nature. Vision process is due to a photochemical process occurring in our eyes. In addition, many of the most common functions exploited in our technological environment, from signal processing, storage, display to the use of pigments, sensors and sensitizers are based on the interaction of light with matter. Solar energy, the most important resource on which humanity can rely, is artificially converted into useful energy forms by photophysical and photochemical processes.<sup>1</sup>

As regards the interaction of light with molecular systems, on which this entire work is based, can be simply defined as an interaction between one molecule and one photon. It can be written in the general form  $A + h\nu \rightarrow A^*$  where  $A$  denotes the ground state molecule,  $h\nu$  the absorbed photon, and  $A^*$  the molecule in an electronically excited state. As the equation implies, the excited molecule  $A$  is the molecule  $A$  with an extra energy  $h\nu$ . It is important to notice that, because of the availability of such an extra amount of energy, an excited molecule has to be considered as new chemical species. It has indeed its own chemical and physical properties, often quite different from the properties of the ground state molecule. The various transitions involving electronic states of similar or different spin multiplicities, as well as vibrational manifold associated with electronic states, are conveniently represented in the so-called Jablonski diagram (Figure 1.2).

Upon light absorption, a molecule can be quickly ( $10^{-15}$  s) promoted from ground state (usually singlet,  $S_0$ ) to an excited electronic state. Due to spin selection rules, the excited state has the same spin multiplicity as the initial state. The electron cloud can quickly rearrange upon external perturbation, whereas the heavier nuclei can be considered stationary (Born–Oppenheimer approximation) and the electronic transition vertical (Frank-Condon principle).

Absorption of a photon leads to the population of a matching vibronic state which is followed by a fast (typically with  $10^{-14}$  -  $10^{-11}$  s) vibrational relaxation to the lowest vibrational state followed by internal conversion (IC) to the lowest singlet state ( $S_1$ ). Due to the time scale, the most relevant photophysical and photochemical processes occur from lowest excited singlet state (Kasha's rule).

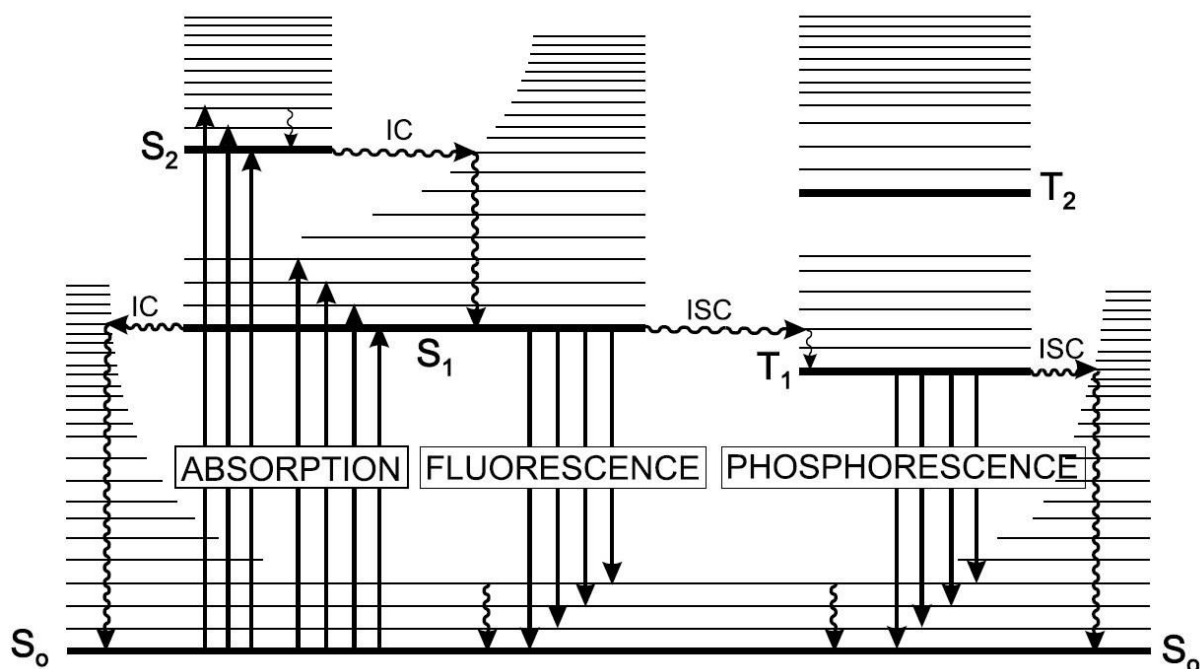


Figure 1.2. Perrin–Jablonski diagram. The vibrational manifold associated with electronic states is also depicted. Straight lines indicate radiative processes, whereas wavy lines denote non-radiative transitions.<sup>4</sup>

Depending on the molecular rigidity radiative and non-radiative deactivation can take place. However, the IC decreases exponentially with the increase of the energy gap between states (energy gap law). The radiative deactivation between lowest excited state and ground state is called fluorescence if it occurs with conservation of electronic spin ( $10^{-7} - 10^{-9}$  s). Generally the emitted light possesses lower energy compared to the absorbed light (Stokes shift) due to the loss of heat and reorganization energy. Intersystem crossing (ISC) between singlet and triplet state can also occur. Due to its spin-forbidden nature it is generally negligible (conservation of electronic spin) and characterized by long lifetimes ( $10^{-6} - 1$  s). Nonetheless, spin orbit coupling (SOC) can overcome the selection rule as the flip of the electronic spin is coupled to a change of orbital angular momentum (El-Sayed's rules). Heavy atoms favor ISC, for instance, by collision (external heavy atom effect). The effect is much more pronounced if they are part of the molecule and involved in the electronic transitions.

In particular, transition metals such as Cu, Ru, Os, Re, Ir, Pt and Au can induce SOC very efficiently, as the SOC constant scales with the fourth power of atomic number.

Singlet and triplet states can be mixed leading to excited states with partial singlet and triplet character. Thus, the otherwise strictly forbidden radiative transition from the lowest triplet state can be partially allowed. Provided that the rigidity of molecule hinders the non-radiative deactivation of the lowest triplet state, a phosphor is obtained (phosphorescence). The deactivation of the excited states follows first order kinetics and the lifetime of the excited states ( $S_1$  or  $T_1$ ) can be represented with the equations shown below.

$$\tau_F(S_1) = \frac{1}{k_F + k_{ISC} + k'_{IC}} \quad \text{eq (1)}$$

$$\tau_P(T_1) = \frac{1}{k_P + k'_{ISC}} \quad \text{eq (2)}$$

The ratio between the emitted and the absorbed photons is defined photoluminescent quantum yield ( $\Phi$ ). This parameter is particularly useful to understand both the nature of the excited state of a molecule and, as it will be further discussed, to probe the self-assembly processes. In fact, it is directly related to the radiative and non-radiative rate constants, as shown below, and to the inter system crossing efficiency ( $\eta_{isc}$ ).

$$\Phi_F = \frac{k_F}{k_F + k_{ISC} + k'_{IC}} = k_F \tau_F \quad \text{eq. (3)}$$

$$\eta_{ISC} = \frac{k_{ISC}}{k_F + k_{ISC} + k'_{IC}} = k_{ISC} \tau_F \quad \text{eq. (4)}$$

$$\Phi_P = \frac{k_P}{k_P + k'_{ISC}} k_{ISC} \quad \text{eq. (5)}$$

The value of  $\Phi$  and  $\eta_{isc}$  can vary from 0 to 1. Known the excited state life time and the quantum yield, the radiative and non-radiative decay constants can be calculated.

$$k_r = \frac{\Phi}{\tau} \quad (\text{For fluorescence } k_r = k_F \text{ and for phosphorescence } k_r = k_P) \quad \text{eq. (6)}$$

$$k_{nr} = \frac{1-\Phi}{\tau}; k_{nr} = k_{IC} + k'_{IC} + k_{ISC} \quad (\text{fluorescence}); k_{nr} = k'_{IC} + k'_{ISC} \quad (\text{phosphorescence}) \quad \text{eq.(7)}$$

As already discussed, light is an electromagnetic wave consisting of an electric field  $\mathbf{E}$  and a magnetic field  $\mathbf{B}$  perpendicular both to each other and to the direction of propagation, and oscillating in phase. For natural light, these fields have no

preferential orientation, but for linearly polarized light, the electric field oscillates along a given direction; the intermediate case corresponds to partially polarized light (Figure 1.3)<sup>4</sup>.

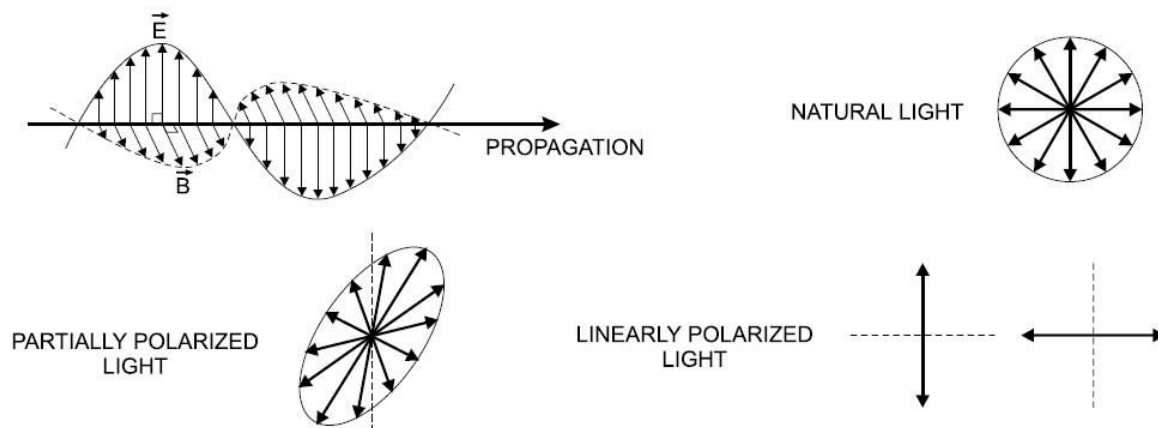


Figure 1.3. Natural light and polarized light.<sup>4</sup>

Most chromophores absorb and emit light along a preferred direction depending on the electronic state. If the incident light is linearly polarized, the probability of excitation of a chromophore is proportional to  $\cos^2\theta_A$ ,  $\theta_A$  being the angle between the electric vector  $\mathbf{E}$  of the incident light and the absorption transition moment  $\mathbf{M}_A$ . This probability is the maximum when  $\mathbf{E}$  is parallel to  $\mathbf{M}_A$  of the molecule while it is zero when the  $\mathbf{E}$  is perpendicular, as shown in Figure 1.4. Thus, when a population of fluorophores is illuminated by a linearly polarized incident light, those  $\mathbf{M}_A$  oriented in a direction close to that of the  $\mathbf{E}$  of the incident beam are preferentially excited. This phenomenon is called photoselection and since the distribution of excited fluorophores is anisotropic, the emitted fluorescence is also anisotropic. Any change in direction of  $\mathbf{M}_A$  during the lifetime of the excited state will cause this anisotropy to decrease. This can be caused for example by non-parallel absorption and emission transition moments, torsional vibrations, Brownian motion or transfer of the excitation energy to another molecule with different orientation. It follows that fluorescence polarization measurements can provide useful information on molecular mobility, size, shape and flexibility, fluidity of a medium, and order parameters (e.g. in a lipid bilayer). In addition, in the case of rigid system characterized by a high level

of order (i.e. crystals), it can provide useful information on the spatial orientation of the transition dipole moments which can be also correlated to the molecular packing.

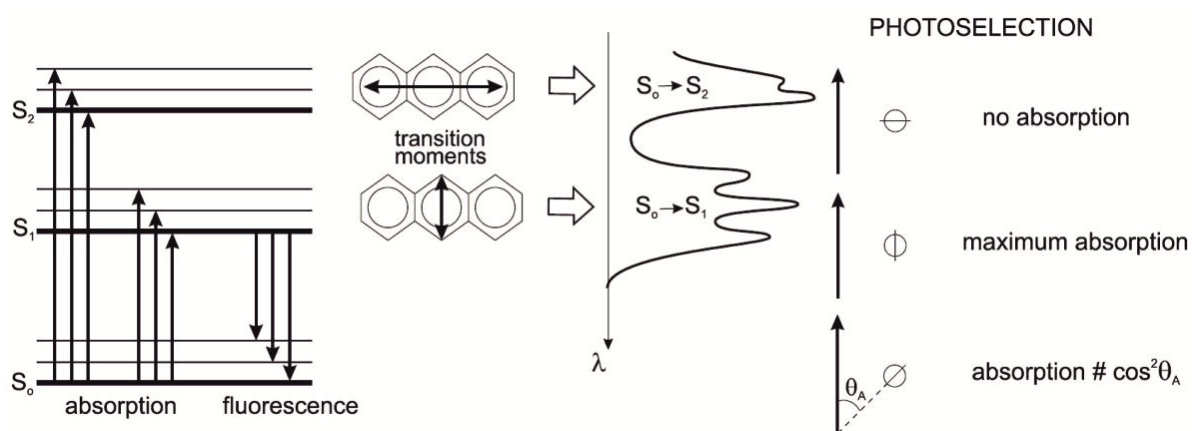


Figure 1.4. Transition moments (e.g. anthracene) and photoselection.

Fluorescence can be considered as the result of three independent sources of light polarized along three perpendicular axis  $x$ ,  $y$  and  $z$  with  $I_x$ ,  $I_y$  and  $I_z$  the respective intensities. The total will be the sum of these three components ( $I = I_x + I_y + I_z$ ) each of which depend on the polarization of the incident light and on the depolarization processes, as shown in Figure 1.5.

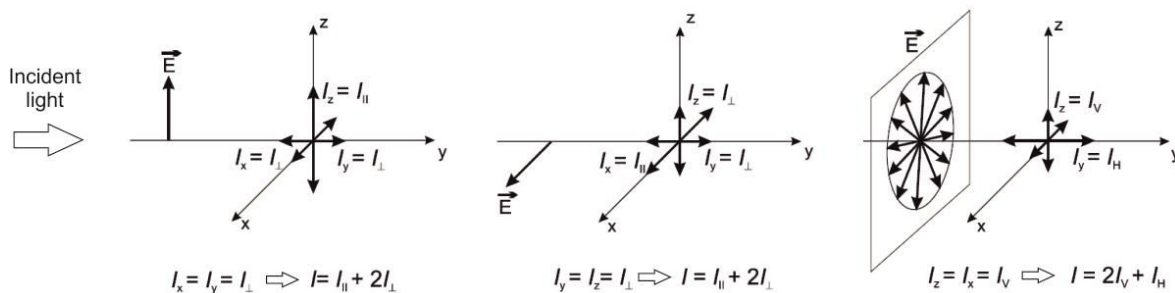


Figure 1.5. Relations between the fluorescence intensity components resulting from symmetry principle. The fluorescent sample is placed at the origin of the system of coordinates.

When the incident light is vertically polarized, the vertical axis  $z$  is an axis of symmetry for the emission of fluorescence and  $I_x = I_y$ . The components of the fluorescence intensity that are parallel and perpendicular to the electric vector of the incident beam are usually denoted as  $I_{\parallel}$  and  $I_{\perp}$ , respectively. For vertically polarized incident light,  $I_z = I_{\parallel}$  and  $I_x = I_y = I_{\perp}$ . In most cases, fluorescence is observed in a

horizontal plane at  $90^\circ$  to the propagation direction of the incident beam, i.e. in direction  $x$  (Figure 1.5). The fluorescence intensity components  $I_{\parallel}$  and  $I_{\perp}$  are measured by a photomultiplier in front of which a polarizer is rotated. The total fluorescence intensity is  $I = I_x + I_y + I_z = I_{\parallel} + 2I_{\perp}$ . The polarization state of fluorescence is characterized either by the polarization ratio  $p$  defined as  $p = \frac{I_{\parallel} - I_{\perp}}{I_{\parallel} + I_{\perp}}$  or the emission anisotropy  $r$  defined as  $r = \frac{I_{\parallel} - I_{\perp}}{I_{\parallel} + 2I_{\perp}}$ . In the expression of the polarization ratio, the denominator represents the fluorescence intensity in the direction of observation, whereas in the formula giving the emission anisotropy, the denominator represents the total fluorescence intensity. The relationship between  $r$  and  $p$  is  $r = \frac{2p}{3-p}$ . When the incident light is horizontally polarized, the fluorescence intensity  $I_y = I_z$ . This configuration is of practical interest in checking the possible residual polarization, due to imperfect optical tuning. When a monochromator is used, the observed polarization is due to the dependence of its transmission efficiency on the polarization of light. The corrected emission anisotropy is then obtained measuring the polarization with a horizontally polarized incident beam.

In the case in which unpolarized light is used to excite the sample, since the light can be decomposed into two perpendicular components, the effects on the excitation of a population of fluorophores are additive. Therefore, the emission anisotropy is the half of that occurring upon excitation by vertically polarized light.

## 1.2 Transition metal complexes

In the last few decades, photoactive transition metal complexes (TMCs) have received a great deal of attention because of their rich and peculiar physico-chemical and redox properties. Particular interest has been devoted to second and third row transition metals with  $d^6$ ,  $d^8$  and  $d^{10}$  electronic configuration, such as Ir(III), Ru(II),

Os(II), Re(I), Pt(II), Pd(II), Ag(I) and Au(I),<sup>5</sup> as well as to the first row ones, e.g. Cu(I)<sup>6-9</sup> and Zn(II).

The presence of heavy metal atoms in TMCs introduces much more complicated, yet fascinating and unique, photochemical and photophysical attributes, when compared to a general fluorescent organic molecule. Amongst all, the judicious choice of metal ions and ligands leads to luminescent compounds, which show great photo- and electro-chemical stability, high photoluminescence quantum yield (PLQY), tunable emission color across the visible electromagnetic spectrum, from ultra-violet (UV) to near infra-red (NIR),<sup>10,11</sup> as well as long-lived emissive excited states. Indeed, as a consequence of the strong spin-orbit coupling (SOC) exerted by the heavy atom, intersystem crossing (ISC) processes lead to the population of energetically low-lying triplet excited states allowing the harvesting of both singlet and triplet excitons in electroluminescent devices, and leading to an efficient radiative decay to the singlet ground state. The photoluminescent quantum yield (PLQY) can, in some cases, approach 100%.<sup>12</sup>

Nowadays, growing interest in such photoactive TMCs is currently driven by their potential and real-market applications in optoelectronics,<sup>13,14</sup> photo-catalysis,<sup>15-17</sup> electrochemiluminescence (ECL),<sup>18,19</sup> metallogelators,<sup>20</sup> molecular devices,<sup>21</sup> non-linear optical (NLO) materials,<sup>22</sup> spin-cross over (SCO),<sup>23</sup> components for electron and energy transfer systems,<sup>1</sup> bio-sensing,<sup>24</sup> and bio-imaging.<sup>25</sup> In very recent years, they emerged indeed as promising candidates as active species in photonic devices which are attractive and powerful alternatives to conventional lighting, such as energy-saving organic light-emitting diodes (OLEDs) and light-emitting electrochemical cells (LEECs),<sup>26-32</sup> as well as solar light harvesting materials for photovoltaic technology, such as in dye-sensitized solar cells (DSSCs).<sup>33-35</sup>

### 1.2.1 Crystal Field Theory and Ligand Field Theory<sup>36</sup>

In order to rationalize and correlate the optical spectra, thermodynamic stability, and magnetic properties of complexes, the physicists Hans Bethe and John Hasbrouck van Vleck<sup>37</sup> developed the so-called Crystal-Field Theory (CFT).

According to CFT, a ligand lone pair is modelled as a point negative charge (or as the partial negative charge of an electric dipole) that repels electrons in the d orbitals of the central metal ion. The theory concentrates on the resulting splitting of the d orbitals depending on the electronic configuration as shown in Figure 1.6. The separation of the two sets of orbitals is called the ligand-field splitting parameter  $\Delta_0$  (where the subscript O signifies an octahedral crystal field). Generally, metal ions with  $d^6$  electronic configuration, such as Fe(II) ( $3d^6$ ), Ru(II) ( $4d^6$ ), Os(II) ( $5d^6$ ) and Ir(III) ( $5d^6$ ), adopt octahedral geometries. Instead, metal ions with  $d^8$  electronic configuration, such as Pt(II), Pd(II), Au(III), Ir(I) and Rh(I) tend to adopt square planar geometries.

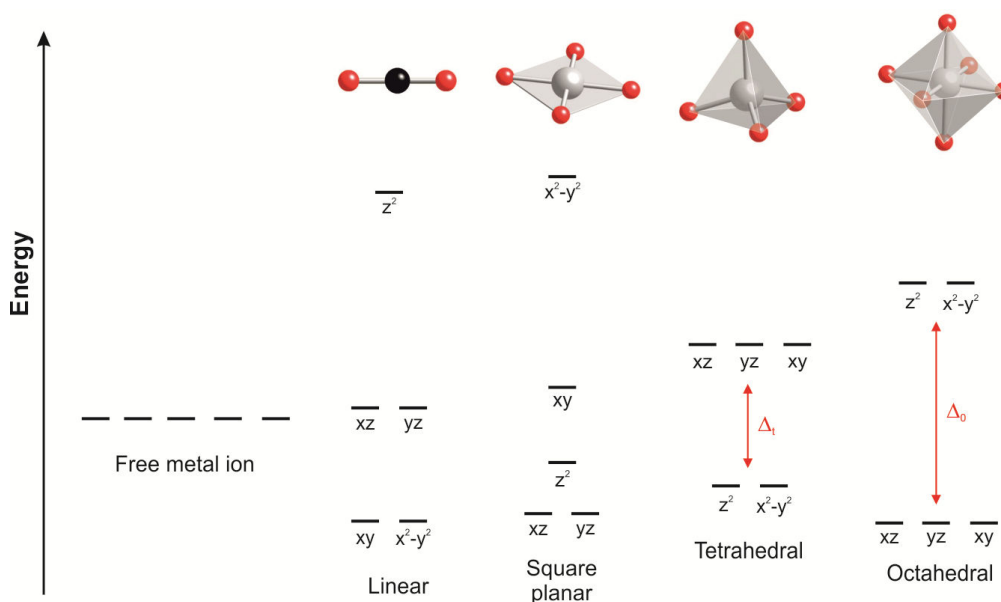


Figure 1.6. Splitting of five degenerate d-orbitals of a transition metal ion in the presence of a crystal field.

Square planar geometries can be correlated with octahedral field by removing ligands on the z-axis. Consequently, the d-orbitals with z-component ( $d_{xz}$ ,  $d_{yz}$  and  $d_{z^2}$ ) are stabilized, whereas the d-orbitals in the xy-plane are destabilized compared to octahedral field. Depending on the strength of the ligand, the orbital can be higher or lower in energy than the  $d_{xy}$  orbital. Similarly the other geometry can be correlated to the octahedral field upon weighting the different interaction along the x, y and z axes.

However, the CFT provides only a simple conceptual model: it treats ligands as point charges or dipoles and does not take into account the overlap of ligand and metal atom orbitals. A more complete approach is given by the Ligand-Field Theory (LFT),<sup>38</sup> which is an application of Molecular Orbital Theory. In fact, the LFT describes the molecular orbitals of a d-metal complex similarly to polyatomic molecules. It means that the metal and ligand valence orbitals are used to form symmetry-adapted linear combinations and to estimate the relative energies of the molecular orbitals by using empirical energy and overlap considerations.

In the light of this, in order to better understand the photochemical processes that involve both  $d^6$  and  $d^8$  it is important to briefly describe what happens upon excitation of the system. As shown in Figure 1.7, if a metal is coordinated by  $\pi$ -conjugated ligands, the set of s, p and d orbitals of the metal are mixed with symmetry-adapted orbitals from the ligands. Upon optical excitation, electronic transitions between the different orbitals can occur and such processes can be described as electron density redistributions between part of the molecules, where filled and virtual orbitals with a certain nature are located.

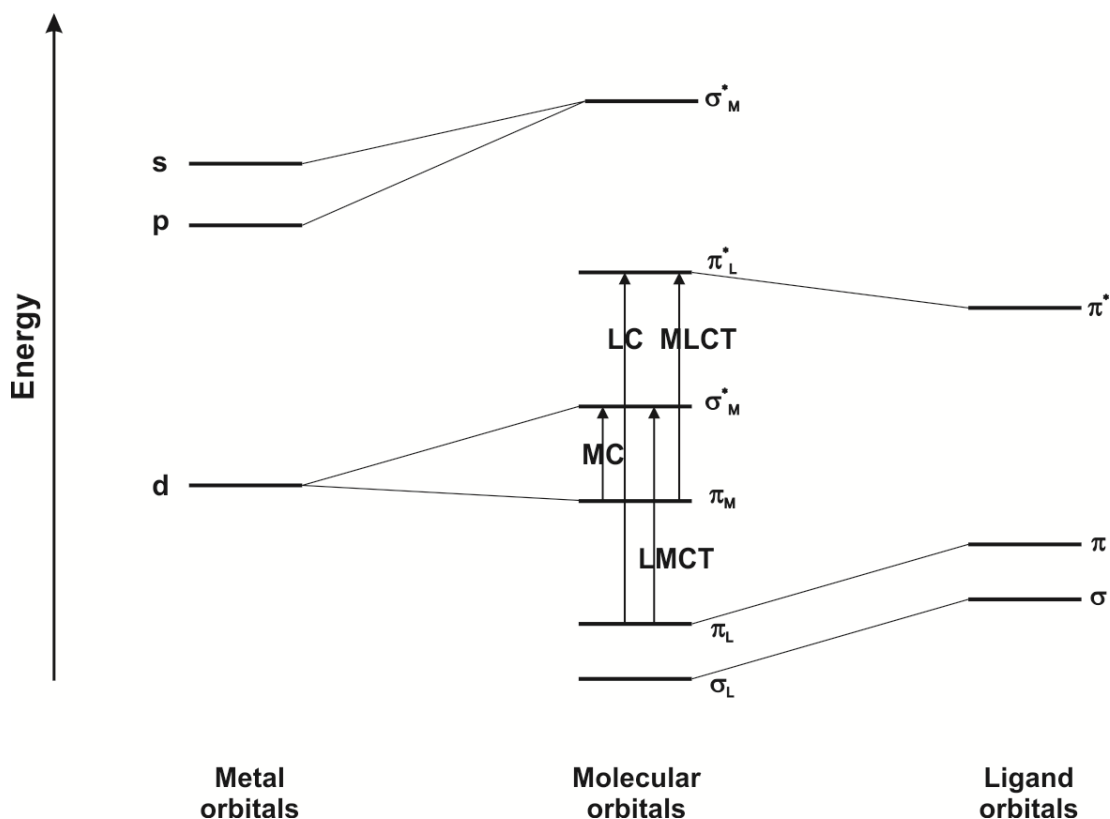


Figure 1.7. Simplified MO diagram for a generic transition metal complex and relative spectroscopic excitation transitions.

Photoexcitation of transition metal complexes with electromagnetic radiation occurring in the ultraviolet-visible (UV-VIS) region leads to the formation of excited states described, on the basis of their electronic transition configuration that can be classified as

- i) metal centred (MC) involving mainly d-orbitals, occupied non-bonding  $\pi_M$  and anti-bonding unoccupied  $\sigma_M^*$  orbitals. Deactivation to the ground state occurs through non-radiative pathway, as the equilibrium geometry of the excited state strongly differs from the ground state due to the placement of electron density in the anti-bonding orbitals.
- ii) ligand centered (LC) involving mainly occupied bonding orbital  $\pi_L$  and unoccupied anti-bonding  $\pi_L^*$  orbital located on the ligands. These states are also known as intra-ligand states, and can have also charge transfer character such as interligand or ligand-to-ligand charge transfer (ILCT or LLCT).
- iii) Metal to ligand charge transfer (MLCT) involving mainly occupied metal centered bonding orbitals  $\pi_M$  and unoccupied ligand centered anti-bonding

orbitals  $\pi_L^*$ . Also LMCT (ligand to metal charge transfer) can occur from occupied ligand centered bonding orbitals  $\pi_L^*$  and unoccupied metal centered anti-bonding orbitals  $\pi_M^*$ .

The relative energies of these states depend on many factors. For instance, if the size of the metal increases, the interaction of d-orbitals with the ligand orbitals is more effective, so the MC states are pushed to higher energy levels. In a similar way, oxidation state of the metal center, type, strength and substitution of ligands (electron donating or withdrawing groups) alter the character and energy of the state. According to perturbation theory, the character of two states can be mixed in nature, leading to new states (mixing of states by configuration interaction or spin orbit coupling).

### **1.2.2 Photophysical properties of platinum(II) complexes**

Most of the work herein reported is based on Pt(II) complexes so an overview on the photophysical properties of such systems is therefore given in this paragraph. As mentioned above, Pt(II) usually forms square planar complexes irrespectively of the strength of the ligands and the typical splitting of the degenerate d-orbitals in the presence of a square planar ligand field is shown in Figure 1.8. Furthermore, the square-planar geometry leads to a high stacking tendency, through establishment of ground-state intermolecular non-covalent weak metal...metal and/or ligand–ligand interactions through the  $\pi$ -electron cloud of the aromatic rings.<sup>39-48</sup> The diagram of the molecular orbital closer to the frontier region for two axially interacting platinum complexes is also shown in Figure 1.8.

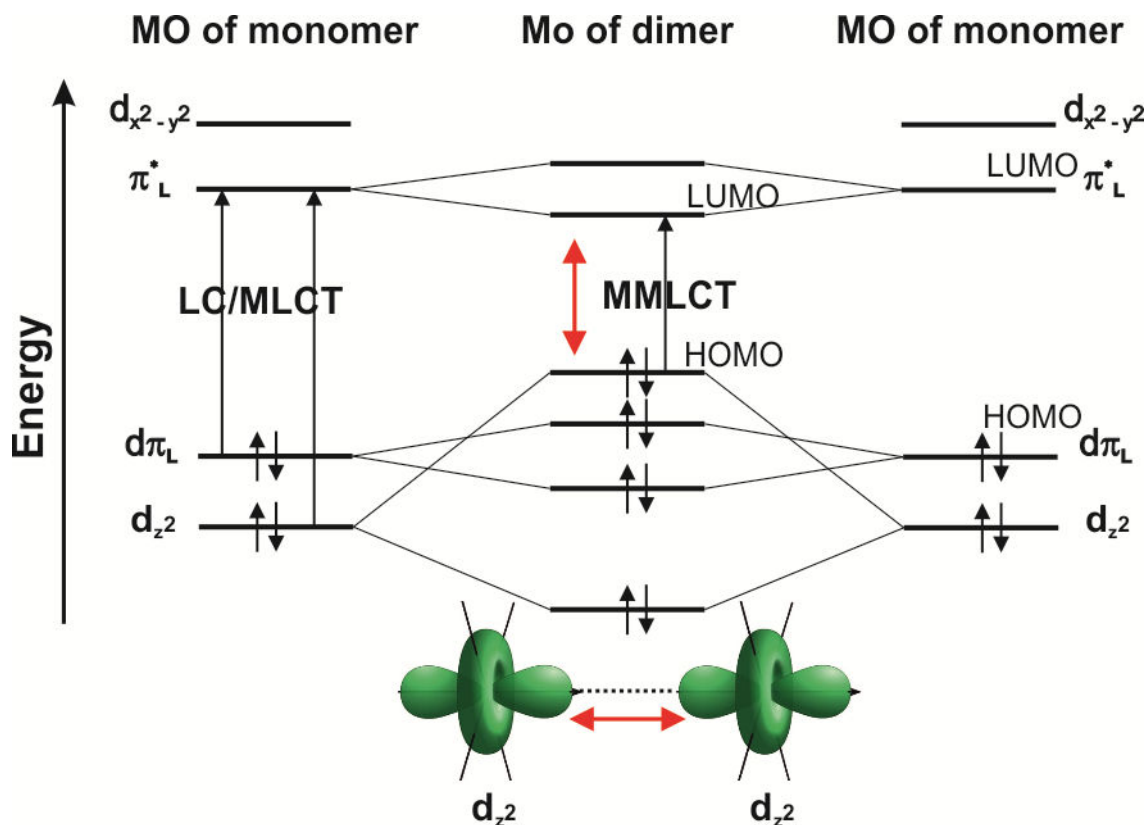
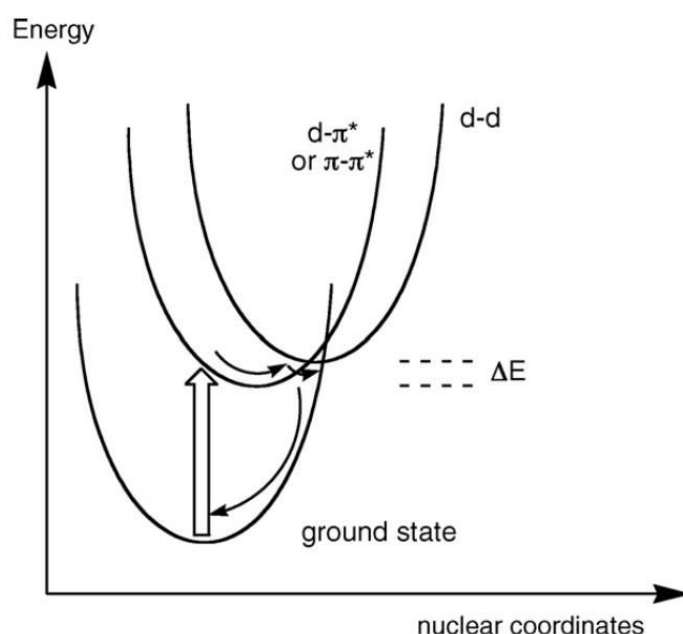


Figure 1.8. Simplified MO diagram of two interacting square-planar Pt(II) complexes, showing the intermolecular  $d_{z^2}$  orbital overlap in the ground-state and its influence on the energy of the MO levels. Red arrows show the correlation between the distance of the Pt(II) ions and the HOMO-LUMO gap.

Typical luminescent platinum compounds bearing strong field cyclometalating ligands as well as good  $\pi$ -accepting moieties possess highest occupied and lowest unoccupied molecular orbitals, namely HOMO and LUMO, with  $d\pi$  and  $\pi^*$  character, respectively. Generally, for the monomeric form of the complex, the HOMO is mainly constituted by bonding orbitals of the ligands  $\pi_L$ . The LUMO is also mainly centered on the ligands with main contributions from the anti-bonding orbitals  $\pi_L^*$ . The relative energy levels of MLCT and LC states depend on the energy of the orbitals,  $\pi_L$  and  $d_{z^2}$ , involved in the electronic configuration of the excited state.

On the basis of the LFT, for a metal center set in a square planar arrangement of the coordinating ligands, relaxation of degeneracy of the d orbitals leads to a filled  $d_{z^2}$  orbital normal to the plane of the molecule, which does not (or only weakly) interact with the ligands coordination sphere, and energetically lies below the HOMO level. The  $d_{z^2}$  occupied orbital is thus prone to interact with surrounding species, as for instance solvent molecules or neighboring platinum complexes. In the latter case, the

formation of such ground-state metallophilic interaction, through the free axial position, destabilizes the filled  $d_{z^2}$  orbitals, leading to a switch of the character of the HOMO level from  $d\pi$  to  $\sigma^*$  (i.e.,  $d_{z^2}\cdots d_{z^2}$ ). Owing to the Pt $\cdots$ Pt interaction, new excited-states are formed such as metal-metal-to-ligand charge transfer, namely MMLCT<sup>5</sup> ( $d\sigma^*-\pi^*$ ), and ligand-to-metal-metal charge-transfer (LMMCT). Interestingly, these charge transfer (CT) states typically show absorption and luminescence that are sizably bathochromically shifted compared to the parental non-interacting platinum complexes. Moreover, it is important to note that the energy of such CT transitions strongly depends on the metal–metal distance, since the electronic interaction starts to occur at a distance typically below 3.5 Å (red arrow of Figure 1.8).



*Figure 1.9. The potential energy surface of the  $d-d$  excited state in Pt(II) complexes is displaced relative to the ground state, owing to the strongly antibonding character of the  $d_{x^2-y^2}$  orbital that is populated. Although other states (e.g.  $d-\pi^*$  or  $\pi-\pi^*$ ) may lie at lower energies, the  $d-d$  state can provide a thermally activated pathway of non-radiative decay. Thick arrow represents absorption of light; thin ones indicate vibrational relaxation and non-radiative decay.<sup>49</sup>*

The strong preference of Pt(II) complexes to be square planar, owing to ligand field stabilization, results in the unoccupied  $d_{x^2-y^2}$  orbital being strongly antibonding. Population of this orbital will be accompanied by elongation of Pt–L bonds and severe distortion, promoting non-radiative decay from the MC ( $d-d$ ) excited states to the

ground state at the isoenergetic crossing point of the potential energy surfaces. Even if excited states of different character, such as MLCT ( $d-\pi^*$ ) or LC ( $\pi-\pi^*$ ) states, lie at lower energies than the  $d-d$  states, the latter can still exert a deleterious influence if they are thermally accessible, i.e. if  $\Delta E$  is comparable to  $kT$  (Figure 1.9).<sup>49,50</sup>

Even if two closed-shell metal cations (such as Pt(II)) would normally be expected to repel each other, evidence of the presence of attractive interactions between closed shell metal ions have been increasingly studied in the last few years and are generally designated as metallophilic<sup>51</sup>. The best evidences has been found in the solid state where structural data obtained by X-ray diffraction provide precise information about the distance between the metals involved. Metallophilic interactions involving  $d^{10}$  ions,<sup>52-55</sup>  $d^8$  ions,<sup>56-59</sup> or the combination of both in heterometallic systems<sup>60-63</sup> have been reported in the last decade. Numerous theoretical studies on metallophilic interactions continue to be carried out at various levels of sophistication which take into account relativistic and correlation effects to describe these van der Waals-type interactions.<sup>64,65</sup>

The strength of such metal–metal interactions has been compared to that of hydrogen bonding (ca. 29–46 kcal mol<sup>-1</sup>)<sup>53</sup> which is sufficient to be employed in the preparation of novel structures in the supramolecular chemistry world.

### 1.3 Self-assembly

Supramolecular chemistry, an expression introduced by Jean-Marie Lehn and often defined as “chemistry beyond the molecule”, is the chemistry of complex, organized assemblies formed by the association of single molecules through the interplay of noncovalent interactions.<sup>66</sup> While a covalent bond normally has a homolytic bond dissociation energy that ranges between 100 and 400 kJ mol<sup>-1</sup>, noncovalent interactions are generally weak and vary from less than 5 kJ mol<sup>-1</sup> for van der Waals forces, through approximately 50 kJ mol<sup>-1</sup> for hydrogen bonds, to 250 kJ mol<sup>-1</sup> for Coulomb interactions (see Table 1).<sup>67</sup>

Deep understanding of such interactions is of paramount importance, as they affect the properties of the final aggregate.<sup>68,69</sup> The chemical self-assembly of relative small

and simple molecules into macroscopic, hierarchically organized, complex structures is known as supramolecular polymerization.<sup>67,70,71</sup>

type of interaction or bonding	strength (kJ mol <sup>-1</sup> )
covalent bond	100-400
Coulomb	250
hydrogen bond	10-65
ion-dipole	50-200
dipole-dipole	5-50
cation- $\pi$	5-80
$\pi$ - $\pi$	0-50
van der Waals forces	<5
hydrophobic effects	difficult to assess
metal-ligand	0-400

Table 1. Strength of several noncovalent forces.<sup>67</sup>

### 1.3.1 Supramolecular polymerization

Supramolecular polymerizations can be classified in different ways: *i*) on the basis of the physical nature of the noncovalent forces (physical origin classification) *ii*) according to the type of monomer (structural monomer classification) or *iii*) in terms of the Gibbs free energy evolution of the self-assembling system (thermodynamic classification).

The thermodynamic approach is directly correlated to the mechanism according to which the polymer grows from the monomeric components, upon variation of concentration or temperature. The two main mechanisms of growth, which are briefly described here below, are the isodesmic and the cooperative polymerization.

The isodesmic polymerization is characterized by the fact that at all steps of the process the association constant  $K$  of the linking supramolecular units is identical and its value determines the degree of polymerization. In other terms, the reactivity of

the monomers and the growing polymer is the same. The supramolecular polymerization process is not affected by any neighboring-group effects (Figure 1.10).

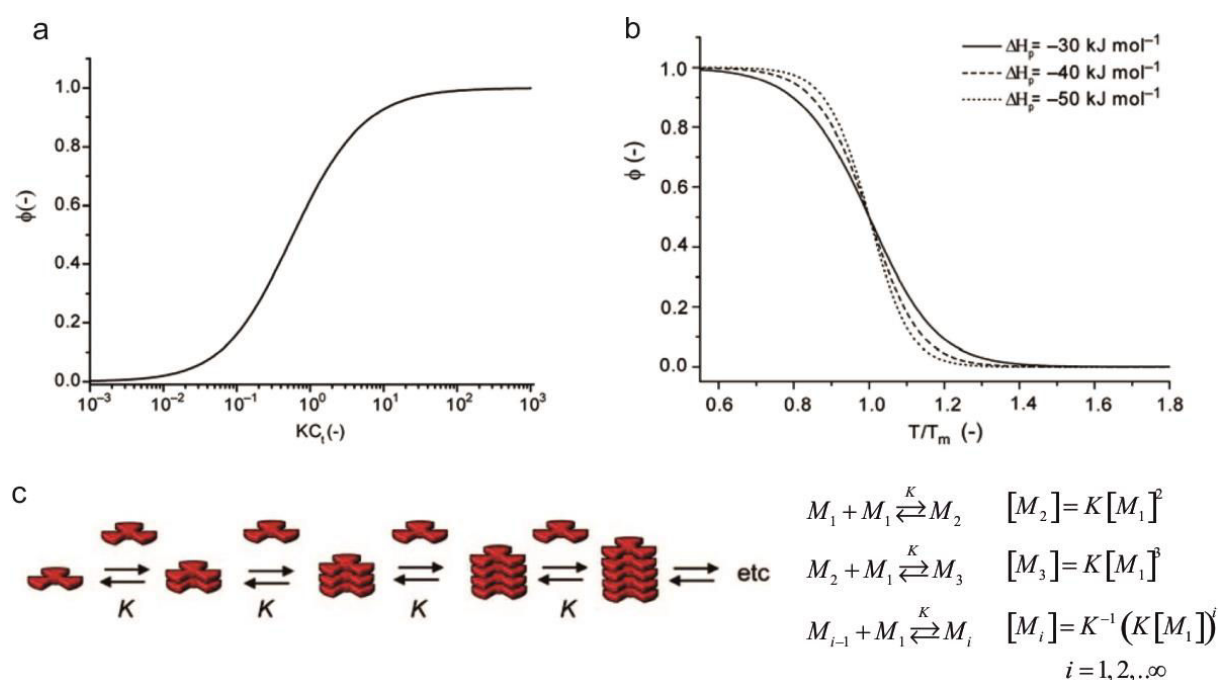


Figure 1.10. Concentration (a) and temperature (b) dependent properties of a isodesmic supramolecular polymer in ideal solution where  $\phi$ , the fraction of polymerized material, is plotted as a function of the dimensionless concentration  $KC_t$  (a) or the dimensionless temperature  $T/T_m$  (b). The latter is given for various values of  $\Delta H_p$  (-30, -40, and -50  $\text{kJ mol}^{-1}$ , respectively). (c) Schematic representation of isodesmic supramolecular polymerizations.<sup>71</sup>

Indeed, the successive addition of monomers to the growing chain leads to a constant decrease in the free energy, meaning that the affinity of a subunit for a polymer end is independent of the length of the polymer. In addition, due to the equivalence of each step during the polymerization, isodesmic supramolecular polymerization is characterized by the absence of a critical concentration (Figure 1.10a) or critical temperature (Figure 1.10b).<sup>72-78</sup>

As regards the effect of the concentration, a high degree of polymerization can be obtained only for high values of the dimensionless concentration  $KC_t$ , it means that high concentration  $C_t$  or high value of the equilibrium constant  $K$  are therefore required (Figure 1.10a). Instead, upon variation of the temperature the system evolves in such a way that the degree of polymerization (DPN) gradually increases when the temperature is lowered. To better understand this point, Figure 1.10b

shows the fraction of polymerized material ( $\phi$ ) as a function of the dimensionless temperature  $T/T_m$ , where  $T_m$  is defined as the temperature at which the fraction of monomer equals 0.5. The behavior is described for a supramolecular polymer that polymerizes upon cooling, taking into account three realistic values of  $\Delta H_p$  (temperature independent polymerization enthalpy).

As it can be observed, the shape of the curve is clearly sigmoidal, whereas the steepness of the transition depends on the value of the polymerization enthalpy  $\Delta H_p$  and is not related to any degree of cooperativity.

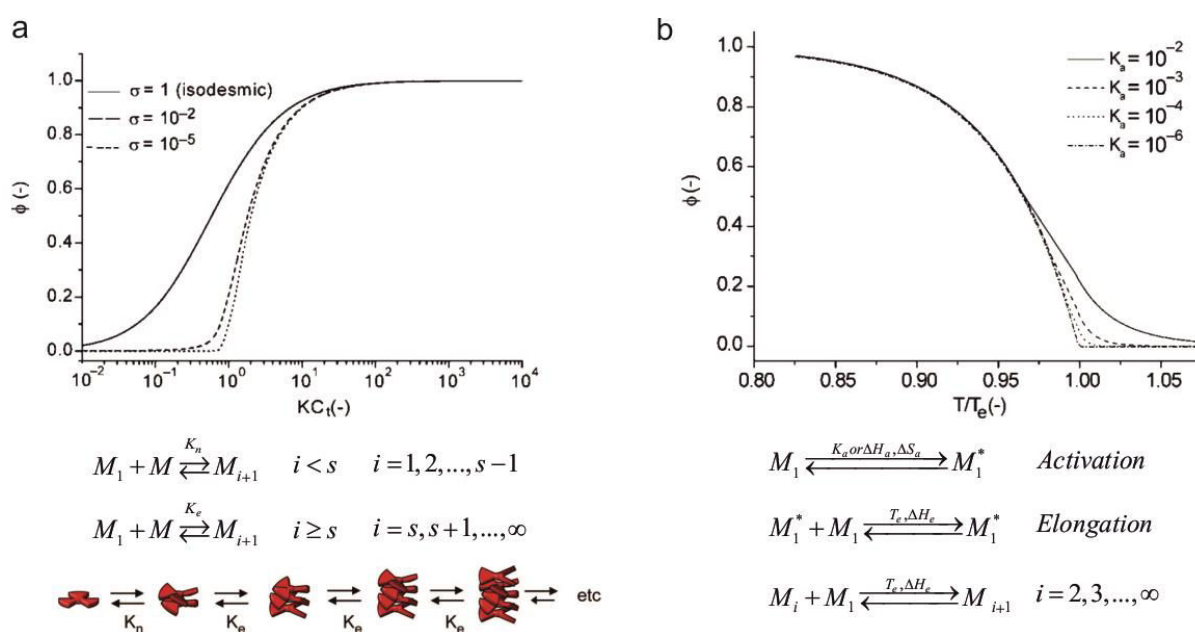


Figure 1.11. Concentration (a) and temperature (b) dependent properties of a cooperative supramolecular polymer where  $\phi$ , the fraction of polymerized material, is plotted as a function of the dimensionless concentration  $KC_t$  (a) for several values of  $\sigma$  (defined as  $K_e/K_n$ ) or the dimensionless temperature  $T/T_e$  (b) for four values of  $K_a$ , with  $\Delta H_e = 60 \text{ kJ mol}^{-1}$ .<sup>73</sup>

As regards the cooperative mechanism (Figure 1.11), the growth of the supramolecular polymer occurs in at least two distinct stages. The first step consists of linear isodesmic polymerization process (nucleation phase) with an association constant  $K_n$  for the addition of each monomer. During such a process the Gibbs free energy of the system increases until a nucleus of a certain degree of polymerization is formed. Then the polymerization becomes energetically favorable and the addition of a monomer occurs with an association constant  $K_e$  that is higher than  $K_n$ . (elongation phase).

In this nucleated supramolecular polymerization, the nucleus is the least stable and hence least prevalent species in the reaction and acts as a bottleneck against the formation of new supramolecular polymers. This mechanism can be distinguished from the isodesmic by the presence of a time-dependent lag in the formation of the supramolecular polymer. Such a lag can be abolished by the addition of a preformed nucleus (seeding) and by reaching a critical concentration and a critical temperature, which for this kind of process do exist.

To illustrate the concentration-dependent properties of cooperative supramolecular polymerizations in ideal solutions Zhao and Moore<sup>78</sup> have modified the isodesmic model assuming that the dimerization step has a different equilibrium constant from that of the elongation constant, defining the degree of cooperativity ( $\sigma$ ) as the ratio of  $K_n/K_e$ , which is smaller than unity for a cooperative process and larger than a unity for an anticooperative process.

Figure 1.11a displays the mole fraction of self-assembled material ( $\phi$ ) as a function of the dimensionless concentration  $KC_t$  for three different values of  $\sigma$  (with  $C_t$  defined as the total concentration of monomer and  $\phi$  defined as  $(C_t - M)/C_t$ ). Increasing the cooperativity (i.e., smaller values of  $\sigma$ ) has a clear influence on the growth profile of the polymeric species. Whereas for the isodesmic growth ( $\sigma = 1$ ) a gradual increase in polymeric species is observed with increasing concentration, for the cooperative systems, below a critical  $KC_t$  of 1, hardly any polymeric species are formed.

Only when the concentration is raised above the critical concentration the chain growth occurs and all monomers are converted into high molecular weight polymers over a relatively small concentration range. Furthermore, in sharp contrast to isodesmic supramolecular polymerizations, higher DP values can be obtained not only by increasing  $K$  but also by decreasing  $\sigma$ . The temperature-dependent properties of cooperative supramolecular polymers can be described as thermally activated equilibrium polymerizations.<sup>79</sup> Such a polymerization is described by the reaction shown in Figure 1.11b, where the activated species  $M1^*$  react only with non-activated monomers  $M1$  to form dimers, but  $M1^*$  does not participate in the successive chain elongation steps.

The monomeric activation step is described by a dimensionless activation constant  $K_a$ , whereas subsequent elongation of the polymers is described by a temperature-independent elongation enthalpy ( $\Delta H_e$ ) and a critical concentration-dependent elongation temperature ( $T_e$ ). For supramolecular polymers that polymerize upon cooling, the elongation enthalpy is negative ( $\Delta H_e < 0$ ). Above the critical elongation temperature, most of the molecules in the system are in an inactive state (nucleation regime), which means that the activation step between inactive and active monomer lies almost completely to the left.

At the critical elongation temperature activation occurs, meaning that the equilibrium describing the elongation steps is shifted to the right. As a result, below the critical elongation temperature, the small fraction of activated monomer can readily elongate to form supramolecular polymers with a high  $DP$ . The fraction of polymerized material increases abruptly (Figure 1.11b) and the transition becomes sharper as  $K_a$  becomes smaller. Hardly any polymeric species are present at temperatures above the critical  $T_e$ . Hence, the dimensionless activation constant  $K_a$  in this model has a role identical to that of the cooperativity parameter  $\sigma$  described before. In contrast to isodesmic supramolecular polymerizations, the shape of the curves that describe the fraction of aggregated material as a function of temperature is clearly nonsigmoidal.

Very recently, examples of cooperative supramolecular polymerization driven by metallophilic interaction has been reported by Fernández group<sup>80-82</sup> which have demonstrated how Pd(II)  $\cdots$  Pd(II) metallophilic interactions can efficiently induce the cooperative supramolecular polymerization of a oligophenyleneethynylene (OPE)<sup>83</sup>-based Pd(II) pyridyl complex. Cooperative supramolecular polymerization induced by Pt(II)  $\cdots$  Pt(II) metallophilic interactions has been proved only in 2014 by Meijer<sup>84</sup> group who have demonstrated how platinum(II) acetylide complexes can form one-dimensional chiral helical supramolecular polymers by the cooperative growth mechanism.

### 1.3.2 Self-assembly and chirality

It's important to underline how supramolecular polymerization is indeed intimately related with chirality. The term chirality is used to describe the structural property of an object that lacks in symmetry elements. Chiral phenomena are ubiquitous in nature from the macroscopic to the molecular level.<sup>85-87</sup> For example, right-handed shells are popular, whereas the left handed are rare and expensive; and most vine plants also tend to grow along the right-handed direction. The origin of such consistent chirality is mysterious and probably closely related to the beginning of life.<sup>88</sup> At a macroscopic level chiral components are necessary to couple rotational motions to axial thrust, and vice versa (e.g. screws, bolts, gears, fans, and propellers are all chiral).

By taking a helical shape the packing can be maximized while minimizing the formation of sharp kinks, as well as to reversibly store energy in the form of elastic deformation since the induced strain can be evenly distributed along the entire wire without the formation of sharp kinks. From a biochemical point of view, such macroscopic phenomena originate from the chirality of natural small biomolecules (e.g. L-amino acids, D-sugars, L-phospholipids, etc.), which usually show high preference toward specific enantiomers.

Even if the two enantiomers of a chiral molecule have identical chemical properties and differ only in the ability to rotate the plane of polarization of light,<sup>89</sup> the chiral recognition has been proven to be a fundamental process in life activities and of primary importance in pharmacology.<sup>90</sup> DNA helices and amyloid or cellulose fibrils are examples of natural helical structures with specific functions. The helical morphology of such biomolecules expresses the chirality of their components and demonstrates the direct relationship between the molecular and the supramolecular chirality.<sup>91-93</sup>

The first chiral helical supramolecular polymer was prepared by Lehn and co-workers via molecular-recognition-directed self-assembly from complementary chiral components.<sup>94,95</sup> The synthesis of chiral structures between the molecular level and the macroscopic world (nano and micro scale) is still a great challenge due to the fact

that they are too big to be made by well-established molecular synthesis, and too small to be made individually by top-down methods.<sup>96-105</sup> From a synthetic point view the breaking of symmetry by imparting chirality in nanostructures can help in designing multiple functionalities with more controllable assembly methods which has been already shown with Janus (two-sided) particles<sup>106-111</sup>

The physical and photophysical properties of chiral nanostructures could be of interest, for example, an electric current flowing through a helical wire can induce a magnetic field,<sup>112</sup> chiral plasmonic nanostructures have been shown to rotate the plane of the polarization of light like molecules<sup>113-116</sup> and can, in principle, provide new platforms for asymmetric catalysis. Self-assembly is indeed the most efficient way in the bottom-up approach in nanotechnology for the fabrication of complex 'supermolecules' and structures.<sup>117,118</sup> In this approach the chirality at the molecular level, displayed when the atoms of a molecule are arranged in one unique manner in space, is transferred to the supramolecular level which involves the nonsymmetric arrangement of molecules in a noncovalent assembly and consequently to the macroscopic dimension.<sup>91,67</sup>

### 1.3.3 Self-assembly of platinum(II) complexes

The self-assembly of phosphorescent platinum(II) complexes containing  $\pi$ -conjugated ligands through Pt...Pt and/or ligand–ligand interactions has been employed in the last decades as an efficient *bottom-up* approach towards the preparation of both chiral and achiral supramolecular materials up to the micrometer scale.<sup>119-123</sup> Furthermore, the anisotropic growth of ordered supramolecular structures often observed in such systems suggests that molecular propagation is faster along the axis of the Pt...Pt interaction than in the lateral directions<sup>124,125</sup>. Nevertheless, the cooperative growth mechanism, which has been demonstrated recently for Pt(II) complexes<sup>84,126</sup>, can be considered as a milestone to find reasonable explanation for the formation of highly organized aggregates with well-defined size, shapes and properties.

Due to the weak and non-covalent nature of the Pt...Pt interaction, the so-formed self-assembled architectures are generally very much affected by changes in the microenvironment such as temperature, solvent compositions and counterions. Furthermore, when stimuli-responsive groups are incorporated into these building blocks, the assembling and disassembling behavior can be controlled by application of external stimuli like pH, temperature, redox, and light, amongst all<sup>127,128</sup>. As already discussed, distinctive spectroscopic properties, such as both lower-energy absorption and/or emission bands, have often been observed and considered as a fingerprint of the establishment of Pt...Pt interactions. Change of such properties can be hence used to probe dynamic transformation of the supramolecular assemblies.<sup>42,125,129</sup>

As a result, a rich variety of supramolecular functional architectures has been reported which range from pseudo-0D structures such as micelles, to 1D arrays, to 2D layers and up to 3D networks. As consequence of their square-planar molecular geometry, the most commonly observed self-assembly form is certainly fibrils (1D) that often tend to bundle into entangled 3D networks leading, in some cases, to the formation of supramolecular gels.<sup>121,130,131</sup> In this respect, terpyridine  $\sigma$ -alkynyl Pt(II) complexes have received considerable attention in recent years due to their photoluminescence properties.<sup>132</sup>

An example of how color changes can be used to probe the self-assembly process has been reported by Chan *et al.*<sup>133</sup> Interestingly, such compounds are not only sensitive to the changes in the microenvironment, upon variations of solvent compositions, counterions, and pH, but positively charged alkynylplatinum(II) terpyridyl complexes can interact with several (bio-)polymers carrying multiple negatively charged functional groups<sup>134</sup> or biologically relevant biomolecules, such as citrate, thus allowing the monitoring of enzymatic activities<sup>135</sup>. Also oligonucleotides<sup>119</sup> were found to interact with such class of Pt(II) complexes, resulting into a stabilization of the helical conformation through Pt...Pt and  $\pi$ ... $\pi$  interactions as revealed by significant enhancement of circular dichroism (CD) signal.

Among all the reported alkynylplatinum(II) complexes, those bearing an amphiphilic anionic bzipmy moiety as terdentate ligand, where bzipmy is 2,6-bis(N-

alkylbenzimidazol-2'-yl)pyridine (**1**), have shown very interesting properties in terms of morphological transformation associated with spectroscopical changes both in terms of photoluminescence and electronic absorption.<sup>136</sup>

At high water content, pseudo-0D micellar structures have been observed, characterized by a broad featureless emission band ( $\lambda_{em} = 675\text{--}683\text{ nm}$ ), attributed to a  $^3\text{MMLCT}$  band due to ground-state Pt $\cdots$ Pt interactions. Interestingly, upon the addition of acetone to the aqueous solution of compound **1**, the color of the solution changed from red to yellow to blue moving from 100% water to 1:1 and finally 9:1 acetone:water, respectively, as shown in Figure 1.12. Such spectroscopic changes were attributed to variation of the low-lying  $^1\text{MMLCT}$  absorption bands.

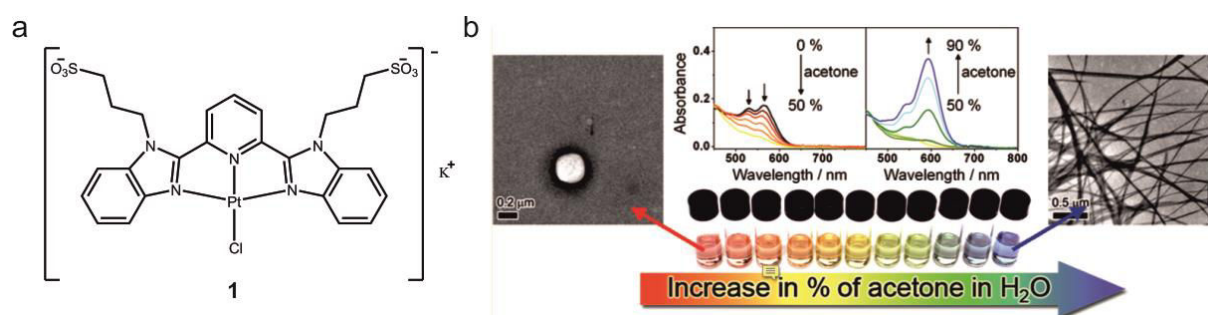


Figure 1.12. (a) Structure of complex **1** and (b) the correlation of the morphology with the spectroscopic properties obtained by varying the solvent composition for solution of complex **1**.<sup>136</sup>

In particular, the authors attributed the drop of the absorption bands at 532 and 564 nm for the red solution upon increasing the acetone content (pure water  $\rightarrow$  1:1 acetone:water) as indication of a partial disaggregation process with disruption of Pt $\cdots$ Pt and  $\pi$ - $\pi$  interactions. At acetone concentration above 50%, formation of a new  $^1\text{MMLCT}$  absorption bands at even lower energy was observed attributable to a second aggregated form with stronger Pt $\cdots$ Pt and  $\pi$ - $\pi$  interactions. Interestingly, the formation of such second aggregates is affected by the ancillary ligand, where presence of a bulky trimethylsilyl group completely inhibited aggregation processes. As demonstrated by scanning electron micrography (SEM) and transmission electron micrography (TEM) images, the change of the spectroscopic properties for **1** was accompanied by a neat variation of the morphological features of the aggregates in

aqueous solutions from vesicular, at high water content, to long nanofibers at higher acetone content. It is likely that, in water, the charged sulfonate groups would point toward solvent molecules; while, the hydrophobic Pt(bzimpy) moieties would be forced to pack together through Pt···Pt and  $\pi$ - $\pi$  stacking interactions in order to avoid unfavorable contact with water, forming the bilayered structures of the vesicles.

Upon addition of acetone, expected to well solvate Pt(bzimpy) moieties, the complex molecules would be more well dispersed, resulting in the drop of the  $^1\text{MMLCT}$  absorption band. Finally, as the acetone content was further increased, the sulfonate groups are no longer well solvated by the organic solvent; thus, the sulfonate ionic heads would start to aggregate and pull the complexes into close proximity, leading to their aggregation into nanofibers or nanorods.

In a more systematic study, the same group<sup>137</sup> reported on how the alkynyl functionalization, in particular, the alkyl chain lengths affects the self-assembly process in terms of both morphologic and spectroscopic properties.

The different morphology was rationalized in terms of the packing parameter (P), which correlates molecular structure with shape of amphiphiles and help to define molecular geometrical criteria needed to pack molecules in a defined shape. The incorporation of neutral triethylene glycol units into platinum(II) bzimpy scaffold (**2**), led to an unusual thermo-responsive behavior as demonstrated by temperature-dependent UV-visible absorption studies and heating–cooling cycles (Figure 1.13).<sup>138</sup>

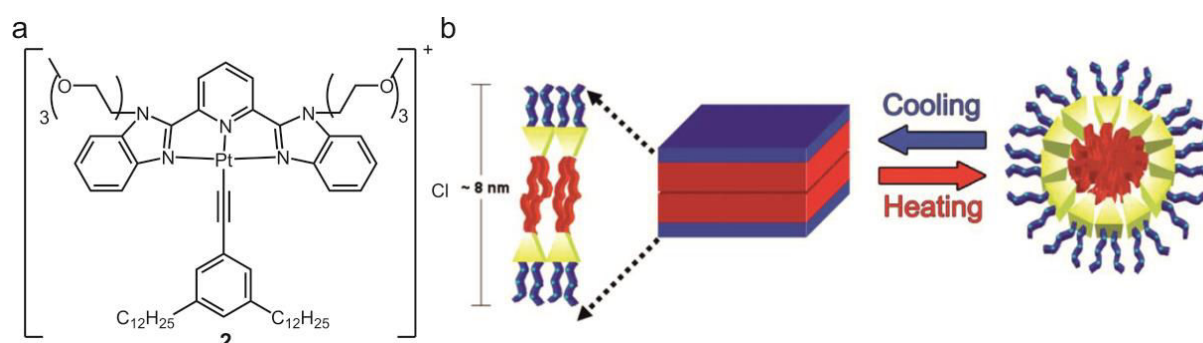


Figure 1.13 (a) Structure of complex **2** and (b) Schematic diagram showing the temperature dependent formation of the bilayered sheet and micelle of compound **2**.<sup>138</sup>

The observed enhancement of the  $^1\text{MMLCT}$  absorption and  $^3\text{MMLCT}$  emission band at higher temperature is contradictory to the commonly observed findings, *i.e.* that Pt...Pt interactions would usually be disrupted at elevated temperatures due to the molecular dissolution of the complex. Such finding along with electron microscopy analysis pointed towards formation of distinct assemblies at lower and higher temperature, namely micellar vs. bilayered structure, respectively.

Interestingly also polyhedral oligomeric silsesquioxanes (POSS) moieties can be incorporated onto such class of Pt(II) complexes resulting into organosilane hybrids that still exhibit self-association behavior.<sup>139</sup> Importantly, various distinguishable nanostructures, associated with spectroscopic changes due the establishment of Pt...Pt and  $\pi$ - $\pi$  interactions, can be formed in various solvent media ranging from nanorings to rods, opening up a new strategy for the development of new functional supramolecular materials with defined shape.

Another interesting approach to build up soft nanomaterials with phosphorescent organoplatinum(II) complexes consists of combining metallophilic interactions with ionic self-assembly. A nice example has been recently reported by Chen *et al.*<sup>140</sup> in which a cationic Pt(II) derivative (**3**) is rendered soluble in non-polar solvents by counterion metathesis with a highly lipophilic anion.

Although such compounds are also soluble in polar solvents, the spectroscopic features observed in non-polar solvents are distinct from those in the formers and the bathochromic shifted absorption/emission spectra have been used to discern monomeric to oligomeric species. Interestingly, honeycomb mesostructures can be obtained by drop-casting a dilute (0.5 wt.%)  $\text{CH}_2\text{Cl}_2$  solution onto a  $\text{SiO}_2$  wafer. SEM micrographs of the so-prepared film showed honeycomb patterns assembled presumably through extended metallophilic interactions and ionic self-assembly and covering an area of tens of  $\text{mm}^2$ , where each edge of the hexagons is about 1  $\mu\text{m}$  long and 200 nm wide (Figure 1.14).

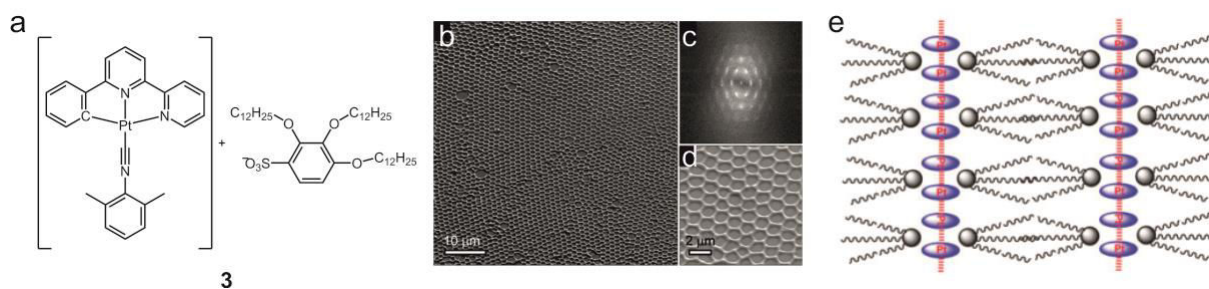


Figure 1.14 (a) Molecular structure of the Pt(II) complex **3**; (b) SEM micrograph and its corresponding fast Fourier transform image (c) of the honeycomb mesostructured onto the surface of a silicon wafer; (d) amplified SEM micrograph; (e) proposed molecular packing.<sup>140</sup>

Incorporation of chiral moieties onto the molecular structures can lead to the formation of chiral supramolecular architectures such as helicoidal fibers<sup>141,142</sup> and metallogels.<sup>143</sup> In this respect, a recent example of the formation of chiral supramolecular structures has been reported by Yi and coworkers<sup>144</sup> who have synthesized a series of amphiphilic bipyridyl alkyneplatinum(II) complexes bearing cholesteric groups and ethylene glycol chains.

Interestingly a solvent-dependent chiral switching of self-assembled structure has been observed, where the longer ethylene glycol chains forms regular left-handed helical structures in aqueous EtOH solution at H<sub>2</sub>O content <5% v/v. As H<sub>2</sub>O ratio increased, the chirality changed from left- to right-handed helix as supported by circular dichroic (CD) spectroscopy, with concomitant alteration of the packing mode from monolayer to a hexagonal motifs. At water content greater than 50% v/v, the structure finally transforms into bilayer vesicles with loss of CD signal. The observed morphological changes were ascribed as due to a delicate balance between hydrophobic and hydrophilic interactions.

Another example of supramolecular self-assembly of chiral structures has been reported by Yam and coworkers<sup>145</sup> who have shown how achiral alkyneplatinum(II) complexes can interact with carboxylic  $\beta$ -1,3-glucan motifs leading to chiral helicoidal structures. Interestingly, the handedness of this two-component helical assembly is affected by different parameters such as temperature, aging, components ratios and mode of preparation and was tentatively rationalized in terms of kinetic vs. thermodynamic control.

Moreover, when chiral moieties are incorporated onto luminescent Pt(II) complexes, the self-assembly process can lead to chiral supramolecular architectures that nicely display circularly polarized luminescence. An interesting example has been very recently reported by Zhang *et al.*<sup>146</sup> who have synthesized chiral cyclometalated Pt(II) complexes by incorporating an enantiopure pinene group onto the chromophoric terdentate ligand. Solvent-induced aggregation of such compound led to the formation of one-dimensional helical structures through Pt···Pt,  $\pi$ - $\pi$ , and hydrophobic-hydrophobic interactions with enhanced and distinct chiroptical properties, which can be reversibly switched *on* and *off* upon temperature change. A series of cationic Pt(II) complexes bearing monoanionic ancillary ligands (either Cl<sup>-</sup> or CN<sup>-</sup>) has been reported by De Cola and co-workers and are displayed in Figure 1.15.<sup>147</sup> They found out that in such derivatives variation of the substitution pattern on either tridentate 1,2,3-triazole moieties and ancillary ligand affects the intermolecular interactions between neighbor complexes and, therefore, the degree of electronic overlap between the platinum centers.

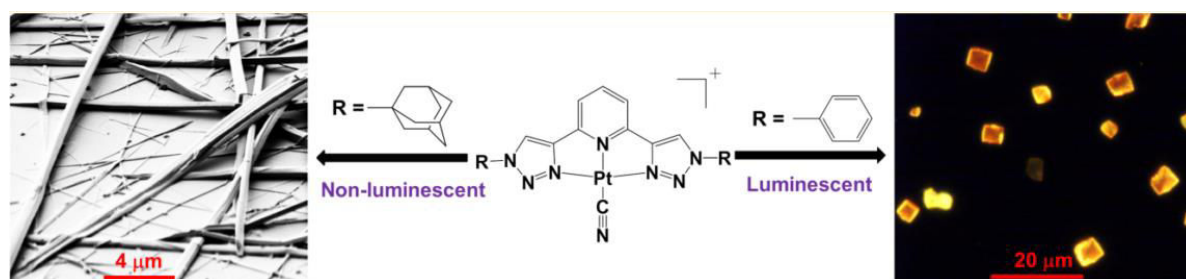


Figure 1.15. Schematic representation of the effects of the different functionalization of the triazole moieties on the luminescent and morphological properties of the resulting self-assembled structures.<sup>147</sup>

Interestingly, all the compounds possessing Cl<sup>-</sup> as the ancillary ligand were not photoluminescent at room temperature and did not display any self-assembly property; while, the presence of more  $\pi$ -accepting ancillary ligand, such as CN<sup>-</sup>, induces assembly upon establishment of Pt(II)···Pt(II) interactions and led to emissive Pt aggregates when bulky adamantyl groups were replaced with more planar phenyl moieties.

The replacement of 1,2,3-triazolyl moieties with 1,2,3,4-tetrazolyl rings leads to dianionic terdentate ligand that combined with a neutral ancillary moiety, such as substituted pyridines, results in neutral Pt(II) complexes with high stacking tendency toward formation of 1D fibrils. Such fibers often bundle into entangled 3D networks leading to the formation of highly emissive supramolecular gels as reported by Strassert *et al.*<sup>148</sup> In their recent communication, the authors have shown that while molecularly dissolved Pt(II) complex displayed no luminescence at room temperature; using the compound as low molecular weight gelating agent, a metallo gel that can reach PLQY up to 90% can be prepared. They also demonstrated that gelation, morphological as well as photoluminescence properties of the resulting 3D network could be tuned by further functionalization of the ancillary pyridine. As an example, introduction of tetraethylene glycol chain<sup>149</sup> (**4**) led to a reversible formation of highly luminescent gels in both CH<sub>2</sub>Cl<sub>2</sub> and DMF with solvent-dependent photophysical properties and morphology (Figure 1.16).

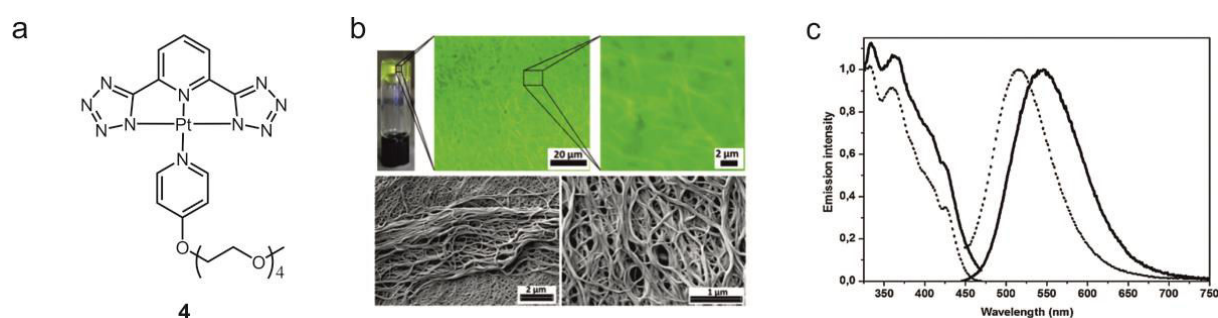


Figure 1.16. (a) Molecular structure of the Pt(II) complex **4**; (b) Fluorescence microscope images (top) and SEM images (bottom) of CH<sub>2</sub>Cl<sub>2</sub> gel. (c) Excitation (left) and emission (right) spectra of the CH<sub>2</sub>Cl<sub>2</sub> gel (solid line) and DMF gel (dotted line).<sup>149</sup>

The corresponding self-assembled fibers can be prepared by either pouring a CH<sub>2</sub>Cl<sub>2</sub> solution of the complex into cyclohexane or drop-casting the CH<sub>2</sub>Cl<sub>2</sub> solution directly onto a glass slide leading to bundled filaments. Furthermore, if the critical gelating concentration was reached, supramolecular metallo gel formation took place and the so-formed gel collapsed into sol by shaking or sonication. In a different manner, the gel can be reversibly obtained upon thermal treatment when DMF is employed. Both gels were photoluminescent under UV light excitation, whereas the corresponding

sols are not emissive in the same condition. The luminescence of the gel states was attributed as arising from an excited state with  $^3\text{MMLCT}$  character and displayed intense broad emission maximum centered at  $\lambda_{\text{em}} = 550$  and  $515$  nm for  $\text{CH}_2\text{Cl}_2$  and DMF as solvent, respectively. SEM and fluorescence microscopy images of xerogel and gel, respectively, showed that the latter is constituted by a dense entanglement of fibers leading to a 3D network. The different PLQY values of 7.5 and 60% recorded for the gel prepared from  $\text{CH}_2\text{Cl}_2$  and DMF respectively was attributed to the different solvation of the polar PEG tail and the apolar chromophoric part in the two solvents. Indeed, the Pt(II) centers are expected to interact more strongly with the apolar  $\text{CH}_2\text{Cl}_2$ , whereas the polar chains entangle in order to reduce their exposure to the solvent, thus bundling on the same side. On the other hand, in DMF, the Pt...Pt interactions are less pronounced due to the solvation of the polar PEG chains, thus preventing a closer approach of the metal centers. Consequently, the PEG chains could adopt an alternating configuration that favors a longer-range order and therefore increase emission quantum yield. The addition of a second tetraethylene glycol chain to the ancillary pyridine increased further the amphiphilic character of the molecule allowing the preparation of phosphorescent hydrogels through host-guest interactions between cyclodextrins and the tetraethylene glycol tails of the Pt(II) complex.<sup>150</sup>

In summary, several classes of square planar Pt(II) complexes yield highly luminescent supramolecular self-assembled structures. The proper design of the chelating ligands in terms of both bulkiness and electronic properties allows the formation of architectures with different morphologies, shapes and interesting functions as well as the modulation of the photophysical features. As hereafter discussed, these investigations paved the way for their use as active materials in different fields of applications.

#### **1.4 Mechanochromic properties of platinum(II) complexes**

Interest on stimuli-responsive materials has been largely increasing in the last decade, in the ongoing effort of developing artificial systems that can dynamically

interact with their environment. The specific input and output of a responsive system, *i.e.* the stimulus and the material property subject to change, determine the field of application of the responsive material.

Pt(II) complexes have been found to change either (or both) absorption and emission colors as a result of a variety of stimuli, including vapors of volatile organic compounds (VOCs) as recently reviewed by Wenger<sup>151</sup> and Kato,<sup>152</sup> as well as mechanical stresses such as grinding, scraping, or compression.<sup>153</sup> Both absorption and emission colors are excellent signal candidates for sensing applications, since the sensitivity of human eye and of common charge-coupled device (CCD) sensors allows for implementation of fast tests performed by individual, non-trained persons, or by low-cost automated sensors such as smartphone or industrial cameras.

Nonetheless, luminescence overcomes absorption by several orders of magnitude in terms of sensitivity, and it is thus compulsorily the signal of choice when miniaturization is required.

The particular interest on Pt(II) complexes as mechanochromic materials arises from the peculiar tunability of their luminescence spectrum as a function of metal···metal distance. In particular, spectral variations can be schematized as two-steps transitions, occurring when shortening the distance between two adjacent Pt complexes. First, a very sharp transition takes place when Pt···Pt distance becomes shorter than approximately 3.5 Å: metal–metal interaction triggers energy levels splitting and formation of a new <sup>3</sup>MMLCT band. This MO diagram change results in a correspondingly sharp variation in emission spectra, where a structured band corresponding to <sup>3</sup>MLCT transition disappears and a broader, unstructured band corresponding appears (see Figure 1.8). The latter is typically bathochromically-shifted by a degree of 70–200 nm and can be ascribed to an excited state with <sup>3</sup>MMLCT character. This constitutes a truly efficient switch with both *ON-OFF* and *OFF-ON* signals to be monitored, which, combined together, yield a strong ratiometric signal in the visible range, *i.e.* a color change detectable by human eye or by CCD camera without the need for lengthy calibration procedures. Furthermore, a smoother transition can occur when the Pt···Pt distance is tuned below 3.5 Å: in this

case, a continuous bathochromic shift of the emission band can be observed, which provide *i*) deeper insight on the aggregation state; *ii*) allow to differentiate aggregates with different Pt...Pt distances; *iii*) allows design of multiple states (multiplexing) optoelectronic devices.

In a recent contribution,<sup>154</sup> Ni and coworkers were able to prepare a diimine-platinum(II) complex with 4-bromo-2,2'-bipyridine (**5**) that exhibits mechanoresponsive luminescence, with the typical spectral transition from a structured band to unstructured broad emission, and corresponding shift in peak emission wavelength of 165 nm upon grinding. X-ray diffraction studies (XRD) revealed that such spectral variation corresponds to a crystalline-to-amorphous state transition. Interestingly, an analogous crystalline-to-amorphous transition was observed upon heating the Pt complex, apart from the fact that the broad emission band was in this case shifted by only about 100 nm. This result suggests that the final amorphous aggregation state, and in particular the metal-to-metal distance, can strongly depend on the way energy is delivered to the Pt complex crystals. Mechanical grinding is hence able to bring metals closer while exposure to solvent vapors, such as DCM, can restore the original crystalline state (Figure 1.17).

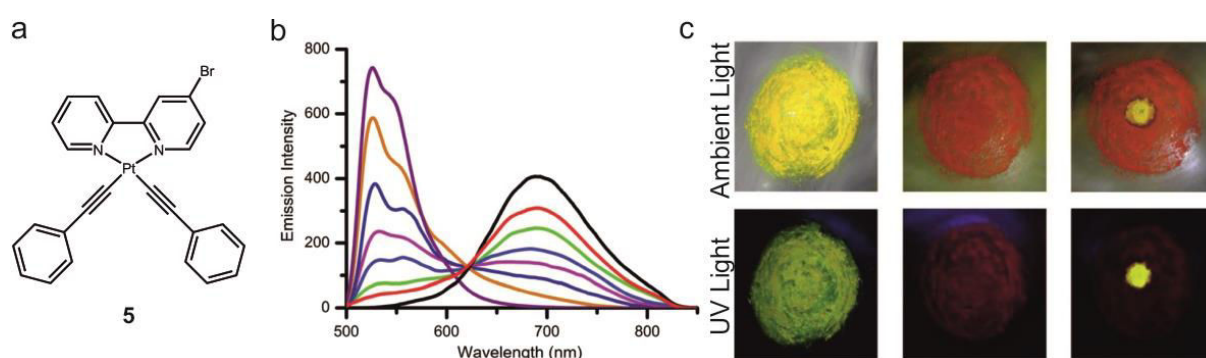


Figure 1.17. (a) Chemical structure of the complex **5**. (b) the solid-state emission spectral changes of the complex in response to dichloromethane vapor, showing a gradual emission attenuation of the broad unstructured band centered at ca. 690 nm and a progressive emission growing vibronic-structured bands at ca. 525 and 549 nm. (c) Photographic images of the complex in response to mechanical grinding under ambient light and UV light irradiation (365 nm), showing the color changes from yellow-green to red upon grinding and in the reverse process from red to yellow-green on addition of  $\text{CH}_2\text{Cl}_2$ .<sup>155</sup>

The same researchers found out that the final emission wavelength of the broad band corresponding to the ground aggregates can be tuned with the bulkiness of ligand substitutions. They ascribe the much smaller bathochromic shift of a *tert*-butyl-substituted derivative, 89 nm vs. 155 nm, the latter observed in absence of *tert*-butyl pendant – to the longer Pt...Pt distance induced by the hindrance of this bulky lateral group. The effect of spatially encumbered ligands was also explored by Tsai and coworkers. Similarly, they concluded that bulky substituents favor the formation of monomer-like emitting crystals, which can then show mechanoresponsive properties if the substituents allow the crystalline structure to have enough sliding freedom.<sup>156</sup>

A recent paper reports the synthesis of a series of imidoamidinato platinum(II) complexes featuring bright luminescence in solid state and mechanochromic behavior.<sup>157</sup>

Even though the ground state of Pt complexes has always been found to be an amorphous aggregate state, Eisenberg and coworkers were able to record X-ray structures of a red-emitting polymorph of a terpyridyl Pt complex, analogous to the red-emitting ground aggregate. Their findings allowed them to conclude that mechanical stresses induce slipping of layers in the crystalline structure, resulting in a less dense aggregation state featuring Pt...Pt distances shorter than 3.5 Å.<sup>158</sup>

Remarkably, not all reports on mechanoresponsive Pt(II) complex agree on the fact that red-shifted emission arise from the formation of aggregates where strong metallophilic interactions take place as consequence of the establishment of short Pt...Pt distances. Early studies reported that the red-shifted emission of Pt(5dpb)Cl, where 5dpbH is 1,3-di(5-methyl-2-pyridyl)benzene, was the result of an interaction only taking place at the excited state, *i.e.* an excimer emission, as observed by time resolved spectroscopy.<sup>159</sup>

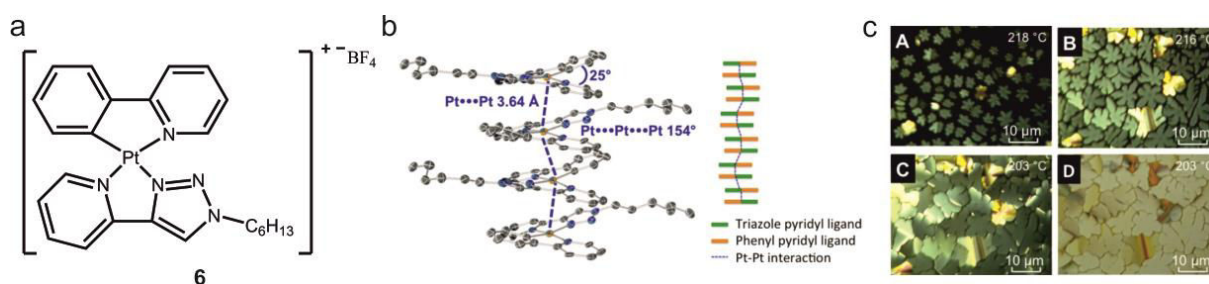


Figure 1.18. (a) Chemical structure of the complex (**6**). (b) Crystal structure packing and representation of stacking orientation by the green and orange colors representing a set of ligands on the molecule and dotted lines representing Pt...Pt interactions. (c) Polarized optical microscopy images of the Colh phase. (A–C) 90° polarized and (D) non polarized generated by cooling from the isotropic phase (2 °C/min) between glass substrates.

Very recently, Swager<sup>+</sup> and coworkers prepared a cationic cyclometalated Pt(II) complex (**6**) which form columnar liquid crystal phases owing to the Pt...Pt interactions, acting as the dominant attractive force.<sup>160</sup> Interestingly, the complex (Figure 1.18a) did not display emission properties in the liquid crystalline state in which the observed Pt...Pt distance ( $d = 3.65 \text{ \AA}$ ) is at the threshold to trigger formation of <sup>3</sup>MMLCT band.

Whereas the solid state crystals showed a broad intense (PLQY up to 86%) luminescence band and exhibited mechanochromism as demonstrated by the bathochromic shift upon grinding. This was not the first report of Pt complexes forming liquid phase crystals responsive to tribological stimulation.<sup>161</sup> Furthermore, the complex showed strong dependence on environmental factors such as nature of polymer matrix in which it is embedded and doping level. Indeed, a bathochromic shift in the emission maximum was observed upon varying the polymer matrix, suggesting the possibility of tuning of the Pt...Pt distance in aggregated phases.

Embedment in polymer matrix is a key step for application of Pt complexes as responsive materials, in particular as sensors for pressure or mechanical stresses, or as memories. Methacrylate polymers have been identified as good candidates to obtain mechanically stable, responsive films. In addition, the possibility of changing the glass transition of the polymer matrix ( $T_g$ ) with the length of the methacrylate chain allowed to investigate the role of  $T_g$  in the response of the luminescent Pt complexes embedded in polymers.<sup>162</sup>

It was found that mechanical as well as vapochromic response was detectable and stable for high  $T_g$  polymers (polymethyl methacrylate,  $T_g = 90$  °C), while the same response was only temporary when  $T_g$  approached room temperature (polybutyl methacrylate,  $T_g = 30$  °C). Furthermore, as soon as each polymer mixture was heated above its  $T_g$ , the luminescence could be reset to the initial – non ground – state, while attempts to stress the films above  $T_g$  gave no observable response, due to the tendency of the polymer to flow, and thus to absorb the mechanical energy conveyed for structural rearrangement of the Pt(II) complex crystals.

PMMA was also employed by Chen<sup>163</sup> and coworkers to obtain a device acting as a logic gate with mechanical and vapor based stimuli. By using platinum complexes, bearing 4-trifluoromethylacetylide ligands (**7**) (Figure 1.19a), they were able to fabricate a proof-of-principle device that can be considered as an example of multi-state logic gate (Figure 1.19c). The device relies on the ability of Pt complexes to undergo not only the transition from absence to presence of metallophilic interactions, but also other transitions among structures showing different Pt...Pt distances. In their system, such different and well-defined Pt...Pt distances were induced by the inclusion of different volatile organic molecules in the crystal structure, while the ground powder exhibited the most red-shifted luminescence corresponding to an amorphous aggregate.

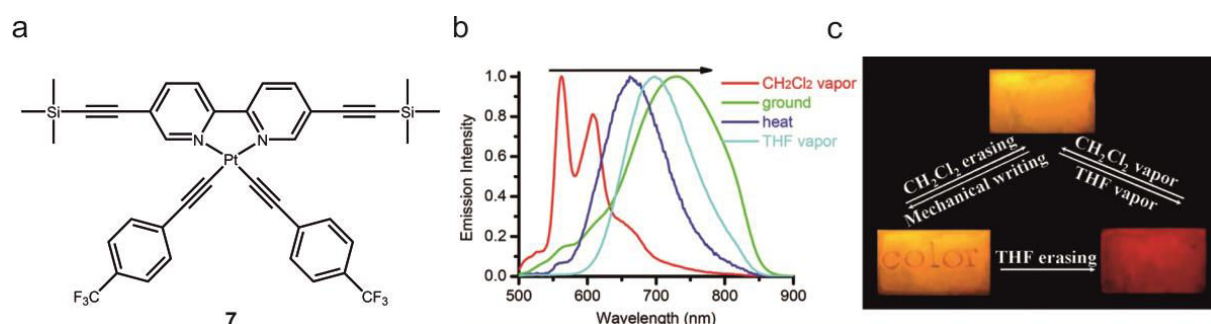


Figure 1.19. (a) Chemical structure of the Pt(II) complex. (b) Solid state emission spectra upon different stimuli ( $\text{CH}_2\text{Cl}_2$  vapor, grinding, heat and THF vapor and (c) the PMMA based device doped with the complex acting as a logic gate with mechanical and vapor based stimuli.<sup>163</sup>

A similar phenomenon was observed by Kanbara and coworkers. The compound bears an amide moiety, which was responsible for setting different H-bond networks

with DMF and MeOH, resulting in different Pt...Pt distances (emission maxima at 512 and 574 nm, respectively). Such metal distances could be further shortened upon grinding as demonstrated by the red-shifted of the emission peak of the ground aggregate down to 635 nm.<sup>164</sup>

An interesting development in terms of mechanoresponsive materials with optical reading was achieved by You and coworkers. They designed chiral Pt complex, which resulted responsive to mechanical stimuli. For such complex, not only the luminescence spectrum changes upon grinding, but even more interestingly the CD signal is completely depleted, which gives the opportunity to couple optical activity and luminescence color as the read-on signals.<sup>165</sup>

Overall, the reversible and dynamic establishment of metallophilic interactions upon application of mechanical stimuli in platinum complexes as condensed phases represents a valuable and interesting manner to prepare luminescent stimuli-responsive materials with optical read-outs.

## **1.5 Bioimaging**

Compounds able to dynamically change the emission colors upon external stimuli or modification of the microenvironment (e.g. pH, polarity of the environment, oxygen content, formation of redox species etc..) are particular important in biology as well as in the whole world of science.<sup>166</sup> In fact, it is said that humans rely on vision for approximately 80% of all the information they receive from the external world as the proverb "seeing is believing" suggests. Unfortunately, living systems generally do not supply enough visual information detectable with the naked eye to allow us to understand specific biological events, such as cell signaling and protein expression. Therefore, tools that allow us to see inside biological systems from cells to whole body are essential not only for basic research, but also for revealing internal structures hidden by the skin and bones, as well as to diagnose, treat or to identify abnormalities. However to the sensitivity required to visualize biological compounds at physiological concentrations, which in most cases range from nano- to micromolars, a spatial and temporal resolution to analyze dynamic cell signaling processes

is also necessary. Since invasive technique should be avoided for medical application, fluorescence imaging is an ideal methodology, compared with other technologies based on radioactivity, bioluminescence, electromagnetism, and electrochemistry. This is the reason why fluorescence live imaging is probably becoming more and more diffused in cell biology.

Several efforts has been made to overcome some limitations of traditional wide-field fluorescence microscopes from the invention of the confocal microscopy<sup>167</sup> to the more recent super-resolution microscopy<sup>168,169</sup> which enables the capture of images with a higher resolution than the diffraction limit as well as by the development of a new method (termed CLARITY) able to transform intact tissue into a nanoporous hydrogel-hybridized form that is fully assembled but optically transparent<sup>170</sup>.

Although internal or endogenous fluorescent molecules in cells<sup>171-173</sup> including tryptophan, NAD(P)H, and flavins can be imaged, in the most cases, an external chemically or genetically synthesized fluorophore is used. Before the middle of the 1990s, when Shimomura<sup>174</sup> discovered the green fluorescent protein which is now widely used as a marker for gene expression<sup>175,176</sup> and to label proteins in general, organic fluorescent molecules were the only choices. Even if organic fluorescent compounds are still important and widely used for both labeling and sensing due to the fact they are relatively inexpensive and versatile, nowadays many different probes using fluorescent proteins, quantum dots (QDs), lanthanide ions and transition metal complexes (TMCs) have been developed and successfully employed. In order to be suitable for *in vivo* application compounds that emits with high quantum yield in the NIR wavelength range are required due to the fact that hemoglobin (the principal absorber of visible light) and water and lipids (the principal absorbers of infrared light) have their lowest absorption coefficient in the NIR region from around 650 nm to 900 nm (Figure 1.20, inset) often called “biological window”.<sup>177</sup>

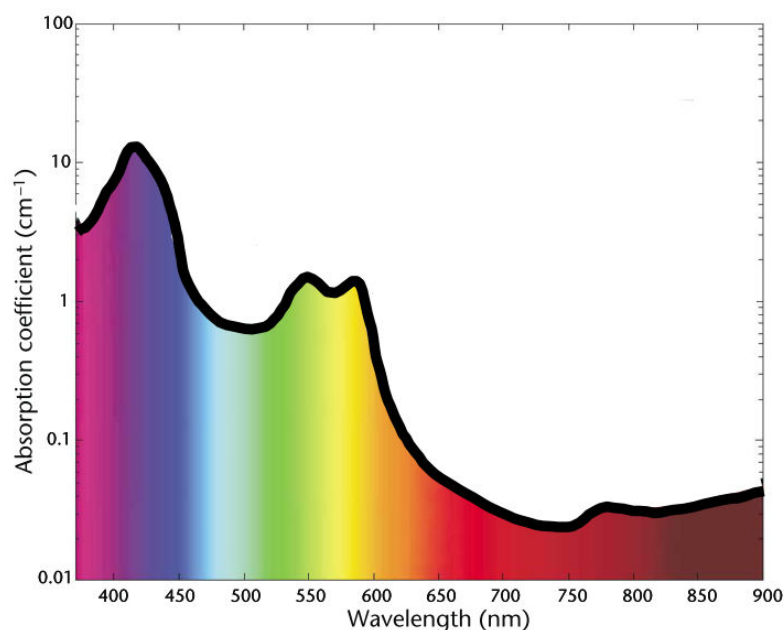


Figure 1.20. Interaction of light with tissue.<sup>177</sup>

Imaging in the NIR region has also the advantage of minimizing the intrinsic fluorescence of tissue,<sup>178</sup> which can further improve target/background ratios. At the same time the possibility to use NIR light to excite the molecule through a multiphoton process<sup>179,180</sup> allow the imaging of small animals. Several attributes are indeed required for a generic lumophore to be used as a label for biological application such as stability and solubility in aqueous buffers and growth media, low toxicity in the organism, fast uptake kinetic into the cells, preferably without the addition of chemical agents, a preferential localization for example in a certain organelle and finally they should be able to operate in the “biological window”. However some of these properties are in conflict with each other like the water solubility and the fast internalization which generally requires, instead, a lipophilic character in order to cross the phospholipidic membrane of the cells. Many of these features such as localization as well as the photophysical properties under physiological conditions, cannot be predicted a priori so most of the novel luminescent molecules were discovered serendipitously or by screening library of compounds<sup>181-183</sup>.

While several lumophores especially small organic fluorescent molecules and TMCs display an intrinsic localization, a specific targeting can be achieved by bioconjugation

or using genetically encoded fluorescent fusion tags<sup>184</sup>. The covalently labeled antibodies with fluorescein isocyanate in 1942 by Coons, was the beginning of immunofluorescence, which is still widely used today<sup>185</sup>. In the last decade, the use of labelled antibodies<sup>186,187</sup> and peptides<sup>188,189</sup> allow to visualize mouse tumors in vivo. Another important class of luminescent compounds is made up by molecules whose own optical properties are altered in response to the target chemical species or specific environments and is defined as luminescent probes (Figure 1.21).

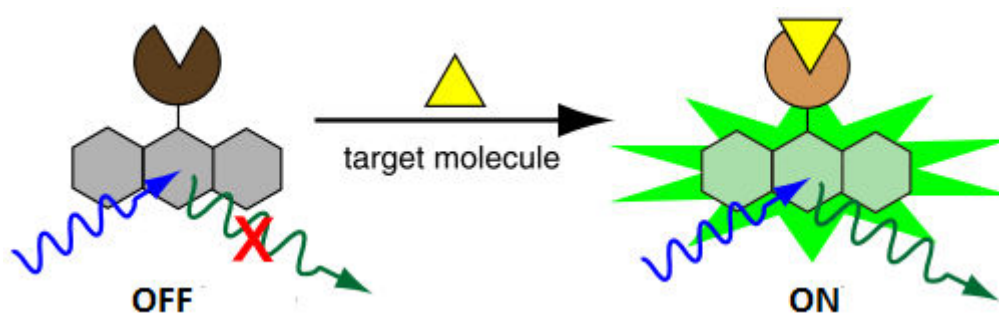


Figure 1.21. Concept of luminescent probes.<sup>166</sup>

By a rational design of the label the fluorescence signal of a molecule can be drastically modulated and the emission can be activated by specific interaction for example with metal ions in order to visualize metal accumulation, trafficking, and function or toxicity in living systems<sup>190</sup>, reactive oxygen species<sup>191</sup>, membrane potential changes<sup>192</sup>, enzyme activity<sup>193</sup> and pH<sup>194</sup>. To trigger specific signal, photoinduced processes has been successfully applied such as photoinduced electron transfer (PeT)<sup>195-197</sup> and Föster resonance energy transfer (FRET)<sup>198,199</sup>. Intramolecular reaction such as spirocyclization<sup>200</sup> and bioconversion can also be used, for example Uesugi<sup>183</sup> reported a fluorescent probe that, upon bioconversion, specifically stains mitochondrial surfaces.

### 1.5.1 Organic fluorophores

From the discover of the first fluorescent organic molecule by Sir John Herschel in 1845<sup>201</sup>, many other organic compounds have been found or created with strong fluorescence across all the visible spectra and beyond. As representative platforms

fluorescein and rhodamine derivatives (Figure 1.22a and b) must be mentioned, which are currently largely employed as fluorescent labels together with BODIPY dyes (Figure 1.22c) and cyanine dyes (Figure 1.22d).

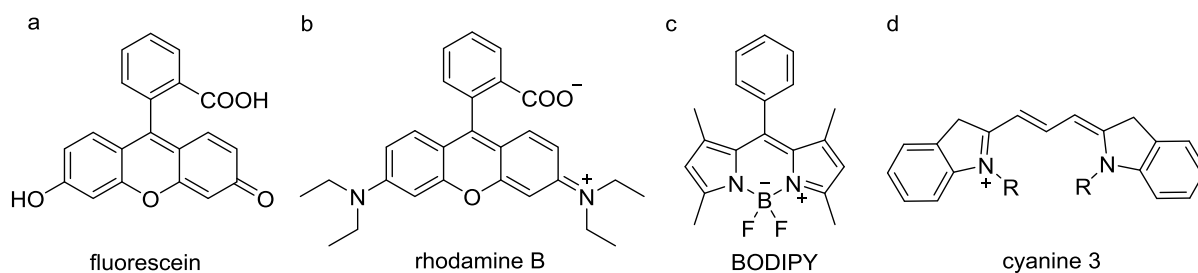


Figure 1.22. Chemical structures of representative organic fluorescent molecules. (a) fluorescein, (b) rhodamine B, (c) BODIPY, (d) cyanine 3.

Due to their long history, organic fluorescent dyes are indeed the most studied and the most used in cellular biology. Their use in cellular staining and to study cellular viability is now a standard protocol in every laboratory, and a full library of dyes able to selectively stain cellular target organelle, such as mitochondria, lysosomes, endoplasmic reticulum, or Golgi apparatus, is commercially available. Some examples of this type of compounds used to stain the cellular nucleus include 4',6-diamidino-2-phenylindole (DAPI)<sup>202</sup> and Hoechst<sup>203</sup>, that become emissive when bound to DNA (Figure 1.23).

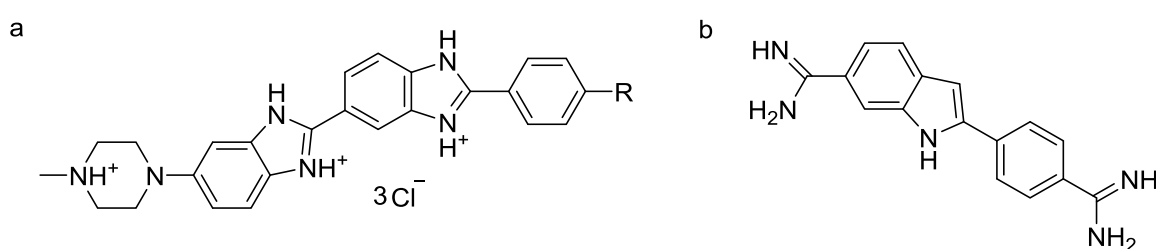


Figure 1.23. Chemical structure of representative commercial fluorescent dyes for nucleus staining. a) Hoechst b) DAPI

Fluorescent molecules that undergo reversible or irreversible photoswitching or photoactivation have become of particular interest for super-resolution imaging<sup>204</sup>, including stochastic optical reconstruction microscopy (STORM)<sup>205</sup> and photoactivated localization microscopy (PALM)<sup>206</sup>.

A classical application of organic fluorophores is probably as probe for metal ions since they are required for the proper function of all cells within every living organism and interesting reviews has indeed been published on this topic<sup>166,190</sup>. For sure the main advantage of this class of molecules is their easy functionalization: dyes with reactive groups such as Isothiocyanate or succinimidyl esters, which are reactive towards amino groups to form a thioureido or amide linkage respectively, are also commercial available and their application to tag molecules range from biology to material chemistry.

Generally this fluorescent tags display strong and tunable absorption with molar extinction coefficient ( $\epsilon$ ) up to  $10^5$  in magnitude as well as high photo luminescent quantum yield (PLQY) up to 100% across the all visible region. However they suffer from small Stokes shifts, short luminescence lifetimes and high susceptibility to photobleaching.

### 1.5.2 Quantum dots

A quantum dot (QD) is a nanocrystal made of semiconductor materials that, due to its size, exhibit quantum mechanical properties. It was first discovered by Brus in 1983<sup>207</sup>. The photophysical and electronic properties of QDs are determined by the physical confinement of excitons, which occurs when the dimensions of the nanocrystal approaches that of the exciton. The bandgap of the QD widens with decreasing size, giving rise to unique, size-dependent optical and spectroscopic properties.

Respects to organic fluorophores, QDs have broader absorption spectra, which can be actually seen as both a positive or negative feature depending on the application. For instance different colored QDs can be simultaneously excited using a single wavelength, but, for other application, a selective excitation of a single label may be required and a narrow excitation band is indeed preferred (Figure 1.24)<sup>208</sup>.

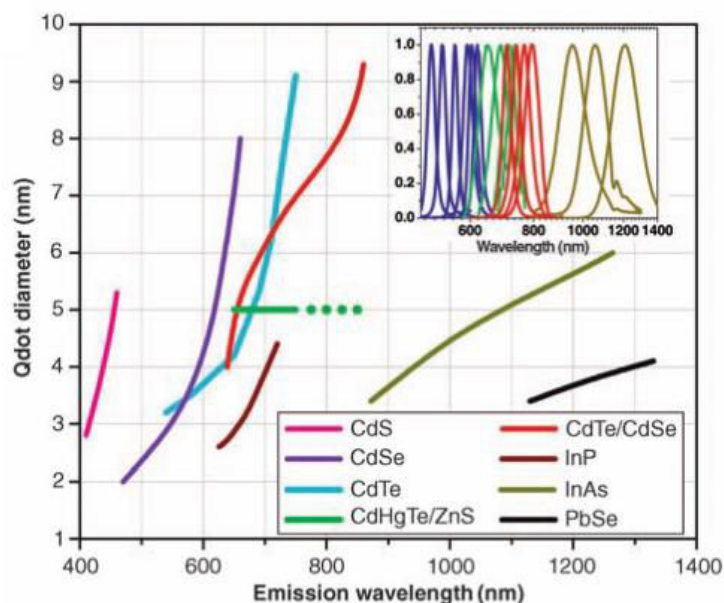


Figure 1.24. Emission maxima and sizes of QD of different composition.<sup>209</sup>

However QDs have narrow emission spectra, which can be controlled in a relatively simple manner by variation of core size and composition, and through variation of surface coatings allowing a relatively easy separation of the different signals making them well suited to multiplexed imaging. For example Gao and coworkers showed the possibility to combine multiple colors and intensities to encode genes, proteins and small-molecule libraries<sup>210-212</sup>.

Another important feature of QD is their good photostability, which is fundamental to monitor the long-term interactions of labelled biological molecules in cells; QDs can actually undergo repeated cycles of excitation and fluorescence for hours with a high level of brightness and photobleaching threshold. Dihydrolipoic acid (DHLA)-capped cadmium selenide-zinc sulfide (CdSe-ZnS) QDs showed no loss in intensity after 14 h, and were nearly 100 times as stable as, and also 20 times as bright as, rhodamine<sup>213</sup>.

QDs also have a longer fluorescent lifetime respect to organic fluorophores up to 100 ns and allow some application in time-gated imaging since endogenous fluorescent molecules as well as commercial organic dyes own excited state lifetimes of few nanoseconds.

Even if QDs display many advantages including the possibility to image small animals<sup>209</sup> there are also several drawbacks. While size and shape can be controlled within using precise growth techniques, the surface defects in the crystal structure and the poor surface passivation reduce the overall quantum yield<sup>214</sup>. The cores are highly reactive due to their large surface area:volume ratio, resulting in a very unstable structure which is particularly prone to (photo)chemical degradation which include desorption of highly toxic free Cd ions. The extent of cytotoxicity has been found to be dependent upon a number of factors including size, capping materials, color, dose of QDs, surface chemistry, coating bioactivity and processing parameters<sup>215</sup>. In addition QDs are mostly synthesized in nonpolar organic solvents. If they are to be solubilized in aqueous buffers, their hydrophobic surface must be covered with amphiphilic ones. In conclusion a coating of the QD core is necessary in order to render them soluble and biocompatible. Keeping into account the possibility of the breakdown of the shell and the requirement for such refinements, the production of suitable quantum dots for particular applications can be very complex and expensive.

### 1.5.3 Lanthanide complexes

As an alternative to classical organic fluorescent labels, lanthanide complexes emerged in the last decade<sup>216</sup> due to their peculiar luminescent properties. Europium was the first lanthanide to be studied in solution by Freed *et al*<sup>217</sup> in the 1939. They discover that the relative intensity of the line-like emission spectra (almost atomic spectral characteristics) is affected by the solvents in which they are studied making this class of compounds potential probes for sensing local environmental changes. This characteristic, combined with the extremely long luminescence lifetimes (up to ms) and, in some cases, with the photoluminescence in the NIR region<sup>218</sup>, makes this class of compounds extremely attractive in bioimaging.

Trivalent lanthanides ions such as Sm, Tb, Eu and Yb can coordinate up to eight or nine ligands which generally are combinations of Lewis bases, such as amines and carboxylic groups, due to the hard characteristics of these metals. Since free

lanthanide ions are toxic, very stable complexes are paramount to be viable in imaging applications and cage-like ligands are preferred to improve their stability such as DOTA<sup>219</sup> or EDTA.

Lanthanide complexes can be distinguished by their characteristic wavelengths of emission which are wholly due to the metal centered f-f transitions. Due to the fact that f-f transitions are symmetry forbidden (Laporte rule) the direct excitation of the metal center is inefficient (very small molar absorption coefficients) and an antenna (commonly an organic chromophore) is required to pump energy in the lanthanide acceptor states. For this reason the resulting complexes show large Stokes shifts upon ligand excitation up to several hundred of nanometers with gaps of zero absorption. In addition they display very small sensitivity to photobleaching in view of their ability to efficiently harvest energy from triplet states. Perhaps the most interesting applications rise from their long excited state lifetimes which enable their use as probes in time resolved techniques such as time-resolved fluoro-immunoassays (TR-FIA), DNA hybridization assays<sup>220</sup> and time-resolved luminescence microscopy (TRLM)<sup>221</sup>.

About the biological applications of lanthanide complexes several interesting reviews has been published on this topic<sup>222-224</sup>. An interesting example of the use of lanthanide coordination complexes as emissive optical probes is given by Montgomery *et al.*<sup>225</sup> by systematically studying more than 60 emissive complexes, examining the time dependence of cellular uptake and compartmentalization, cellular toxicity, protein affinity, and quenching sensitivity they were able to identify certain structure-activity relationships (Figure 1.25).

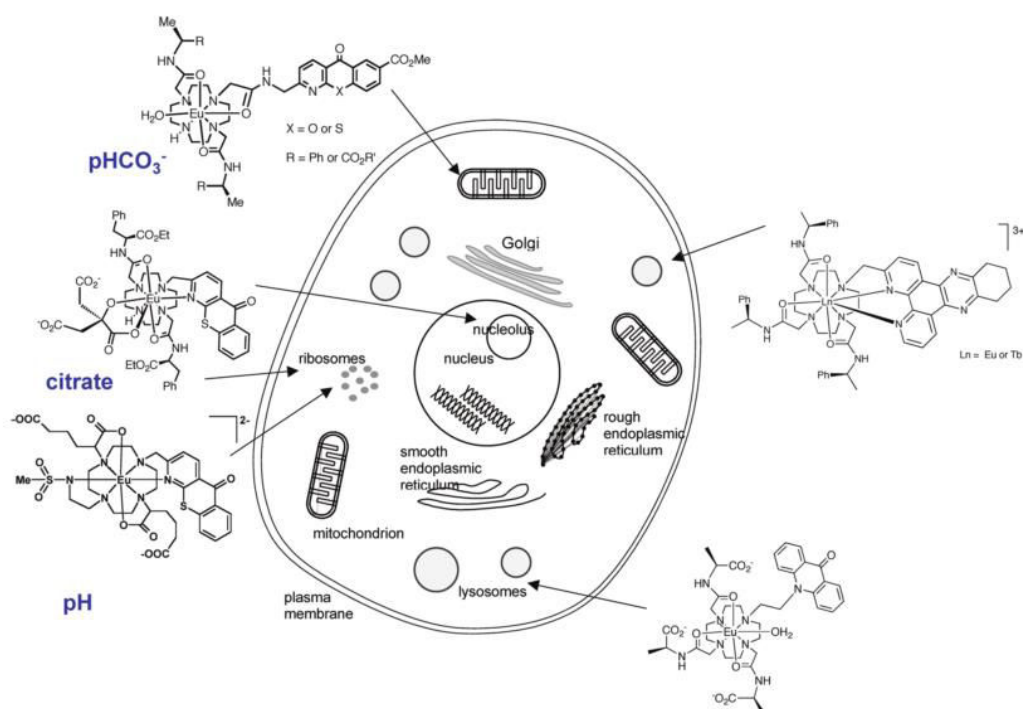


Figure 1.25. Schematic illustration of the dominant intracellular localization profiles of the emissive Eu and Tb macrocyclic complexes.<sup>225</sup>

They reported several Eu and Tb macrocyclic complexes able to report on the concentration of key biochemical variables such as local pH, metal concentration (Ca and Zn) as well as the concentration of certain anionic metabolites, such as citrate, lactate, bicarbonate, or urate (Figure 1.25).

#### 1.5.4 Transition metal complexes

Heavy-metal complexes including Re(I)-, Ru(II)-, Os(II)-, Ir(III)- and Rh(III) that possess  $d^6$  electron configuration, Pt(II) complexes with  $d^8$  electronic structures, Au(I) and Cu(I) complexes with  $d^{10}$  have attracted much attention because of their rich and peculiar physico-chemical and redox properties. The main property induced by the presence of the heavy atom is the strong spin-orbit coupling which allows an efficient intersystem crossing from singlet state to the triplet manifold. Thus, the spin selection rule can be removed to a large extent, resulting in highly intense phosphorescent emission with useful radiative decay times.

The judicious choice of metal ions and ligands leads to luminescent compounds, which show great photo- and electro-chemical stability, high photoluminescence

quantum yield (PLQY), tunable emission color across the visible electromagnetic spectrum, from ultra-violet (UV) to near infrared (NIR)<sup>10,11</sup>.

Several interesting reviews have been reported<sup>25,226-228</sup> trying to rationalize the relationship among the structure, the cellular uptake kinetics and the compartmentalization. Many TMCs show indeed an intrinsic specific localization as can be observed in Figure 1.26. However, as for the organic fluorophores, there are not general rules able to predict localization depending on the chemical structure.

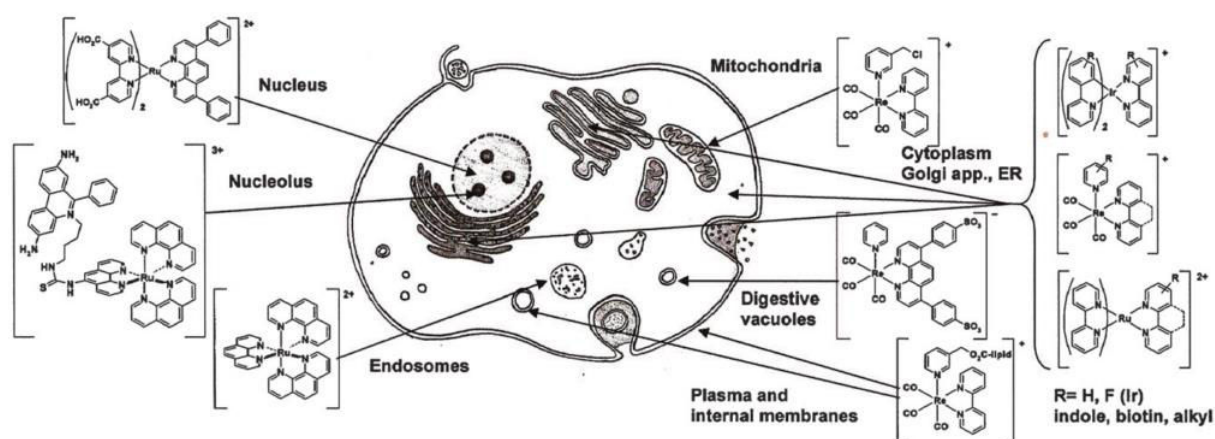


Figure 1.26. Localization of some  $d^6$  TMCs in cells.<sup>25</sup>

For example triphenylphosphonium ion is known to bind to mitochondria<sup>229</sup>, however Chi-Kin Koo *et al.*<sup>230</sup> reported a triphenylphosphonium-functionalised cyclometalated Platinum(II) complex that, instead, is selective for the nucleus while a Zhengqing Guo *et al.*<sup>231</sup> reported oligo(ethylene glycol)-functionalized cyclometalated platinum(II) complexes bearing a triphenylphosphine as ancillary ligand that is, indeed, mitochondria-specific.

Octahedral  $d^6$  transition metal complexes such as Ru(II), Ir(III) and Re(I), probably the most studied so far, display high kinetic inertness due their low rates of ligand exchange. The most common structure of luminescent Ru(II) species entails three neutral N<sup>N</sup> ligands, mainly derivatives of 2,2'-Bipyridine (bpy) and Phenanthroline (phen), coordinated to the metal center. The most applied family of luminescent Ir(III) complexes are bis-cyclometallated of general formulation  $[(C^N)_2Ir(L^A)]$  where the

C<sup>N</sup> belongs to the phenylpyridine (ppy) family and the L<sup>L</sup> chelating ligand can be a neutral N<sup>N</sup> ligand such as a bpy or an anionic C<sup>N</sup> ligand giving monocationic and neutral complexes respectively. Re complexes instead are based around fac-tricarbonyl Re(I) with a N<sup>N</sup> ligand and typical formulas are [ReX(bipy)(CO)<sub>3</sub>] (X = halogen) for neutral complexes or [Re(bipy)(CO)<sub>3</sub>(L)]<sup>+</sup> for cationic compounds where L is generally a pyridine derivative.

The charge of heavy-metal complexes significantly affects their cellular uptake. Generally when complexes own positive charges they can easily interact with the negative surface of the membrane and enter living cells.

This class of molecules displays several advantages respect to the classes discussed previously: ligands can be rationally designed and synthesized to modulate photophysical properties and easily functionalized like the small organic fluorescent dyes. The coordination to a transition metal ion leads to an increase of the lifetimes due to the population of triplet states that allow time resolved techniques, followed by an increase of the Stokes shift and a bathochromic shift of both excitation and emission spectra generally due to the formation of new <sup>3</sup>MLCT transition at lower energy. However this bands have smaller molar absorption coefficient compared to the spin allowed  $\pi$ - $\pi^*$  transition of the isolated ligand, but still easier to excite if compared with lanthanides. Even if PLQY are very high and close to the unit in some cases, the excited state lifetimes are subject to shortening by triplet quenchers (e.g. <sup>3</sup>O<sub>2</sub>). On the hand this property can be exploited to map <sup>3</sup>O<sub>2</sub> concentration, on the other reactive toxic species can be formed such as <sup>1</sup>O<sub>2</sub>.

### 1.5.5 Platinum(II) complexes

Even though Pt(II) complexes have been extensively studied for cancer therapy<sup>232</sup> due to their high toxicity, much less work has been done for their application as bio-imaging probes compared to the compounds discussed previously. Organometallic complexes of Pt(II) possess attractive properties and several groups has reported luminescent Pt(II) complexes able to enter living cells and, in some cases, to selectively stain specific compartments<sup>233</sup>.

An important contribution to the bioimaging field comes from Williams group<sup>234,235</sup> who show how highly emissive and photostable Pt(II) complexes can be used in bioimaging using a combination of confocal one-photon excitation or nonlinear two photon excitation (TPE) with time-resolved emission imaging microscopy (TREM) on a hitherto uncharted microsecond time scale.

TPE is emerging as a powerful tool for noninvasive imaging of live cells and tissues. It excites chromophores in the range of 600-1000 nm (biological window) by using simultaneous absorption of two photons which enables a deeper analysis of the sample up to hundreds of micrometers due to the higher transparency of the tissue in this optical region. The high photon flux also provides a better spatial resolution but demands exceptional photostability of the chromophores used.

The long lifetime up to  $\mu\text{s}$  allows an easy separation of the signal coming from the phosphorescent complex from fluorescent signals such as from a solution of fluorescein in 1M concentration. The general formula of the Pt(II) complex, the concept of time gating and its ability to eliminate short-lived background fluorescence are depicted in Figure 1.27.

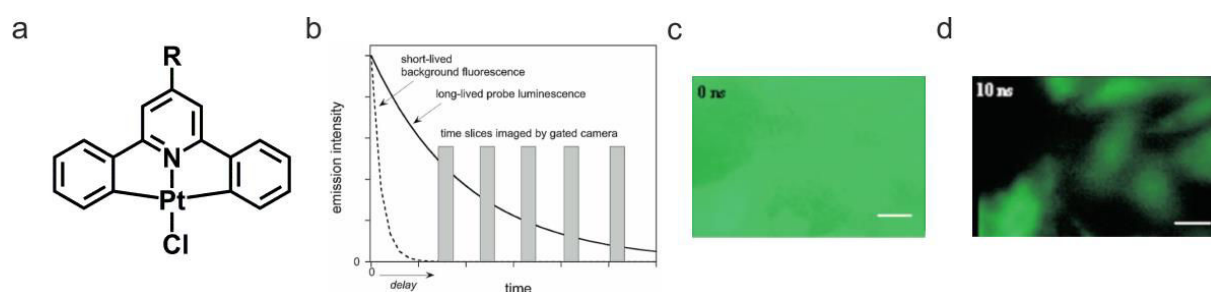


Figure 1.27. a) general structure of the Pt(II) complexes investigated by Williams and coworkers<sup>234,235</sup>; b) diagrammatic illustration of the concept of time gated imaging<sup>234</sup>. Time-gated cellular imaging of live CHO cells preincubated with a Pt(II) complex and imaged in the presence of a solution of fluorescein. The images were taken at 0 ns (c) and at 10 ns (d) delays after the 355-nm laser pulse. (Scale bar 10  $\mu\text{m}$ ).<sup>234,236</sup>

In addition, they show how lifetime mapping can be used to image live cells and tissue section with a wealth of detail within the cell, in particular, nuclear and cell membranes which are not visible in the intensity image. They have observed that the excited state lifetime increases when moving from the cell membrane, through the cytoplasm and into the nucleolus. As shown in Figure 1.28.

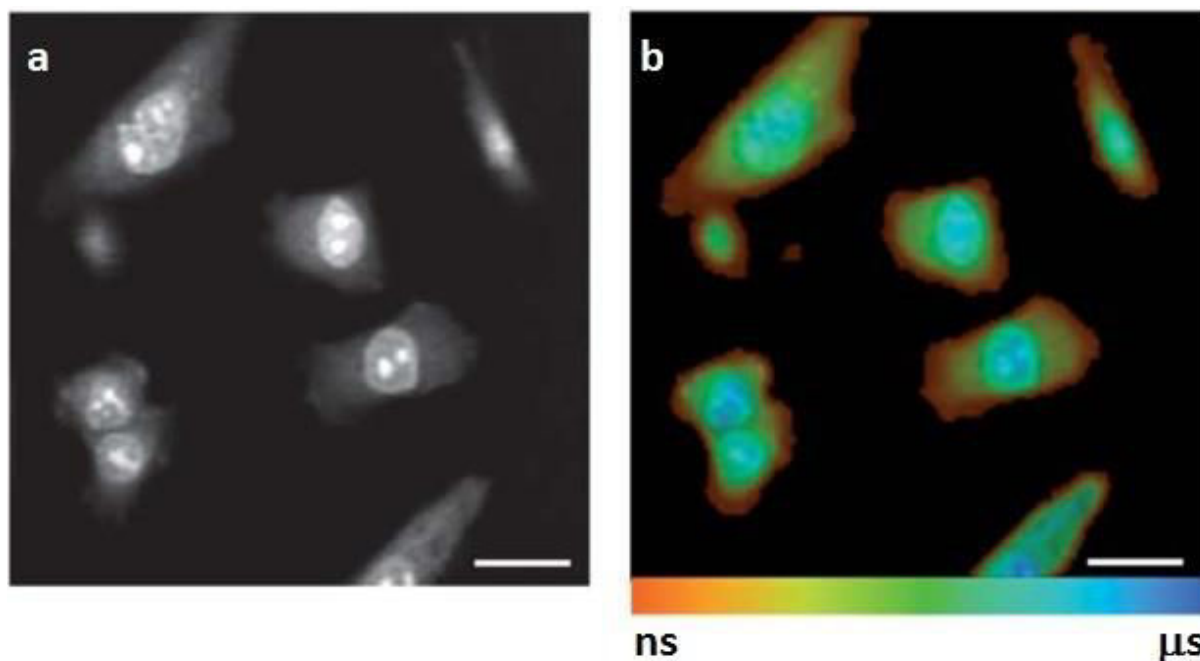


Figure 1.28. Live CHO-K1 cells labelled with a Pt(II) complex. (a) TP-TREM intensity image under 760 nm two-photon excitation, reconstructed by integrating total emission intensity pixel-per-pixel; (b) lifetime distribution map corresponding to image (a).<sup>235</sup>

The emission lifetime varies by more than a factor of 20 depending on the location, in particular they found it to be shorter (around 300 ns) in the membrane, longer in the cytoplasm (around 2 μs) up to 4 μs in the nucleus with, discrete zones of almost 6 μs, value similar to that obtained in fully deoxygenated solution. Such differences were tentatively assigned to a variable degree of protection from quenching by oxygen since this complex, as well as TMCs in general, are strongly quenched by oxygen. Self-quenching via interactions with another Pt(II) molecule and even binding to proteins or intercalating into DNA was also not excluded. Although these probes can comfortably sense oxygen to sub- micromolar level, the formation of  $^1\text{O}_2$  can represent a drawback due to the intrinsic toxicity.

The use of the self-assembly properties of Pt(II) complexes to obtain dynamic labels for cell imaging has been recently reported by Yam and coworkers.<sup>237</sup> The authors reported a water-soluble alkynylplatinum(II) terpyridine complex **8** (Figure 1.29a) that can reversibly form aggregates upon changes in pH which are in the physiological range. Formation of the aggregates upon establishment of Pt...Pt metallophilic interactions result in a “switch on” of the emission in the NIR region (Figure 1.29b).

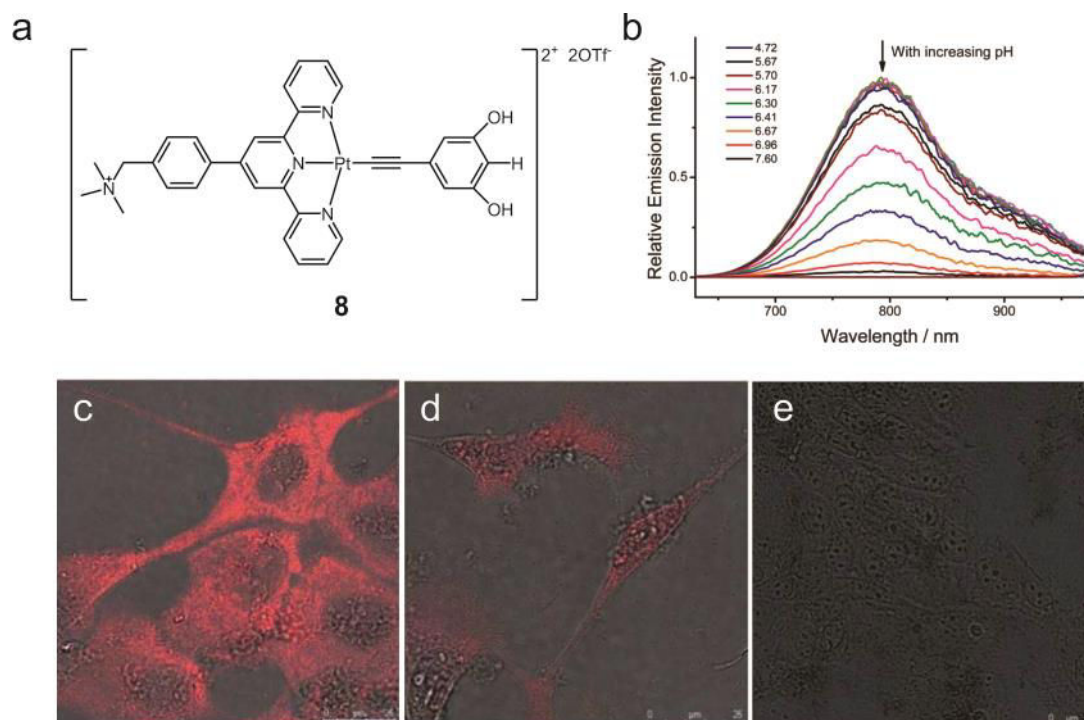


Figure 1.29. (a) Chemical structure of complex **8**. (b) Emission spectra of **8** (200  $\mu\text{M}$ ) in aqueous solution (50  $\mu\text{M}$  NaCl) at various pH values ( $\lambda_{\text{ex}} = 480 \text{ nm}$ ). (c–e) Confocal microscopy images of fixed MDCK cells incubated with 20  $\mu\text{M}$  of complex **8** for 1 hour followed by incubation with buffer solutions at different pH: pH 5.72 (c), pH 6.75 (d) and pH 7.80 (e).  $\lambda_{\text{ex}} = 488 \text{ nm}$ .<sup>237</sup>

The trigger for the changes in the aggregation properties is the acidity of the phenolic proton which at high pH increases the hydrophilicity of the complex and hence its deaggregation in aqueous medium. The emission of the complex is present only when the compound is in the aggregate format pH between 3.5 and 5.6. Above 5.6 in pH the NIR emission shows a significant drop in intensity and becomes completely “turned-off” at or above pH 7.6 (Figure 1.29b).

Confocal microscopy images of fixed MDCK cells incubated with the complex in serum and phenol red free Dulbecco’s modified Eagle’s medium (DMEM) revealed a strong NIR emission band in vesicular distribution (Figure 1.29c). The MDCK cells remained viable after the incubation (MTT assay results ca. 97% viability as compared to untreated MDCK cells) and showed good co-localization, with the green emission of LysoSensor Green DND-189, in acidic organelles such as lysosomes. The

relationship between their chemical structures and cell uptake, localization and toxicity remains elusive.

## 1.6 Scope of the thesis

The work described in this thesis is focused on the synthesis and characterization of luminescent Pt(II) complexes. Particular attention is paid to their self-assembly properties, exploited to create new functional in- and out-of-equilibrium architectures, such as polarized emitting fibers and (chiral) micro/nanostructures. Moreover, the dramatic changes in the photophysical properties, shown by such materials upon self-assembly, are used to probe in real time the evolution of a system with complex pathway dynamics. Finally, some possible applications are reported, in particular these assemblies have been used as new phosphorescent labels for bioimaging and as devices for data storage and security.

After a short description of the instruments and the techniques used in this work (chapter 2), chapter 3 explores the synthesis of the dianionic tridentate ligands and of the resulting Pt(II) complexes. The study of the self-assembly of the latter ones revealed the formation of fibers with polarized emission. Fluorescence anisotropy studies have clearly shown, for the first time, how the new electronic transition dipole moment, originated by the  $d_{z^2}\pi \cdots d_{z^2}\pi$  interactions, is indeed oriented along the fiber growth direction.

In Chapter 4, the syntheses of an ancillary ligand bearing a chiral moiety and the corresponding Pt(II) complexes (both enantiomers) are described. The complexes can assemble in helicoidal structures, which have been investigated in detail, both photophysically and morphologically. Noteworthy, these assemblies represent the first examples of enhancement of the chiro-optical properties driven by metallophilic interactions in the solid state.

Chapter 5 is dedicated to the understanding and control of the self-assembly mechanism underlying the formation of the above mentioned highly organized structures. We describe indeed how interlocked dynamic pathways comprising more than two assemblies can be characterized and kinetically controlled. This has allowed

us to visualize in real-time the events involved and to fine tune the size of the assemblies.

In addition, the self-assembled architectures show bright emission and enhanced stability. Since the emission can be easily modulated and the long-lived emissions easily detected, such materials can be applied as labels in biomedicine, as reported in Chapters 6 and 7.

Finally, Chapter 8 focuses on the solid state properties of such materials and, in particular, on the changes in the photophysical properties upon mechanical stimulus. We show that luminescent mechanochromism, a phenomenon generally observed in bulk materials, can be brought on the microscopic level and used to achieve high-density information writing with AFM nanolithography.

## 1.7 References

- [1] P. Ceroni, *The Exploration of Supramolecular Systems and Nanostructures by Photochemical Techniques*, ed. Springer Netherlands, **2011**
- [2] N. J. Turro; V. Ramamurthy; J. C. Scaiano, *Modern Molecular Photochemistry of Organic Molecules*, ed. University Science Books, **2010**
- [3] P. Klán; J. Wirz, *Photochemistry of Organic Compounds: From Concepts to Practice*, ed. Wiley, **2009**
- [4] B. Valeur; M. N. Berberan-Santos, *Molecular Fluorescence: Principles and Applications*, ed. Wiley, **2013**
- [5] V. Balzani; S. Campagna, *Photochemistry and Photophysics of Coordination Compounds I*, Springer Berlin Heidelberg, **2007**
- [6] A. Barbieri; G. Accorsi; N. Armaroli, *Chem. Commun.*, **2008**, 2185-2193.
- [7] D. V. Scaltrito; D. W. Thompson; J. A. O'Callaghan; G. J. Meyer, *Coord. Chem. Rev.*, **2000**, 208, 243-266.
- [8] A. Laviecampot; M. Cantuel; Y. Leydet; G. Jonusauskas; D. Bassani; N. McClenaghan, *Coord. Chem. Rev.*, **2008**, 252, 2572-2584.
- [9] D. R. McMillin; J. R. Kirchhoff; K. V. Goodwin, *Coord. Chem. Rev.*, **1985**, 64, 83-92.
- [10] N. Darmawan; C. H. Yang; M. Mauro; M. Raynal; S. Heun; J. Pan; H. Buchholz; P. Braunstein; L. De Cola, *Inorg. Chem.*, **2013**, 52, 10756-10765.
- [11] M. S. Lowry; S. Bernhard, *Chem. Eur. J.*, **2006**, 12, 7970-7977.
- [12] Y. Kawamura; K. Goushi; J. Brooks; J. J. Brown; H. Sasabe; C. Adachi, *Appl. Phys. Lett.*, **2005**, 86, 071104.
- [13] M. Mauro; E. Q. Procopio; Y. Sun; C.-H. Chien; D. Donghi; M. Panigati; P. Mercandelli; P. Mussini; G. D'Alfonso; L. De Cola, *Adv. Funct. Mater.*, **2009**, 19, 2607-2614.
- [14] P. T. Chou; Y. Chi, *Chem. Eur. J.*, **2007**, 13, 380-395.
- [15] M. S. Lowry; J. I. Goldsmith; J. D. Slinker; R. Rohl; R. A. Pascal; G. G. Malliaras; S. Bernhard, *Chem. Mater.*, **2005**, 17, 5712-5719.
- [16] S. Rau; D. Walther; J. G. Vos, *Dalton Trans.*, **2007**, 915-919.

- [17] R. Reithmeier; C. Bruckmeier; B. Rieger, *Catalysts*, **2012**, *2*, 544.
- [18] M. Staffilani; E. Höss; U. Giesen; E. Schneider; F. Hartl; H.-P. Josel; L. De Cola, *Inorg. Chem.*, **2003**, *42*, 7789-7798.
- [19] M. M. Richter, *Chem. Rev.*, **2004**, *104*, 3003-3036.
- [20] A. Y. Tam; V. W. Yam, *Chem. Soc. Rev.*, **2013**, *42*, 1540-1567.
- [21] *Molecular Devices and Machines: Concepts and Perspectives for the Nanoworld*, ed. Wiley, **2008**
- [22] S. Di Bella, *Chem. Soc. Rev.*, **2001**, *30*, 355-366.
- [23] *Spin-Crossover Materials: Properties and Applications*, ed. Wiley, **2013**
- [24] A. Ruggi; F. W. B. van Leeuwen; A. H. Velders, *Coord. Chem. Rev.*, **2011**, *255*, 2542-2554.
- [25] V. Fernandez-Moreira; F. L. Thorp-Greenwood; M. P. Coogan, *Chem. Commun.*, **2010**, *46*, 186-202.
- [26] *Highly Efficient OLEDs with Phosphorescent Materials*, ed. Wiley, **2008**
- [27] *Comprehensive organometallic chemistry III: Applications I : main group compounds in organic synthesis*, ed. Elsevier, **2007**
- [28] C. Cebrian; M. Mauro; D. Kourkoulos; P. Mercandelli; D. Hertel; K. Meerholz; C. A. Strassert; L. De Cola, *Adv. Mater.*, **2013**, *25*, 437-442.
- [29] M. Mauro; C. H. Yang; C. Y. Shin; M. Panigati; C. H. Chang; G. D'Alfonso; L. De Cola, *Adv. Mater.*, **2012**, *24*, 2054-2058.
- [30] M. Mydlak; M. Mauro; F. Polo; M. Felicetti; J. Leonhardt; G. Diener; L. De Cola; C. A. Strassert, *Chem. Mater.*, **2011**, *23*, 3659-3667.
- [31] R. D. Costa; E. Ortí; H. J. Bolink; F. Monti; G. Accorsi; N. Armaroli, *Angew. Chem. Int. Ed. Engl.*, **2012**, *51*, 8178-8211.
- [32] T. Hu; L. He; L. Duan; Y. Qiu, *J. Mater. Chem.*, **2012**, *22*, 4206-4215.
- [33] B. E. Hardin; H. J. Snaith; M. D. McGehee, *Nat. Photon.*, **2012**, *6*, 162-169.
- [34] A. Orbelli Biroli; F. Tessore; M. Pizzotti; C. Biaggi; R. Ugo; S. Caramori; A. Aliprandi; C. A. Bignozzi; F. De Angelis; G. Giorgi; E. Licandro; E. Longhi, *J. Phys. Chem. C*, **2011**, *115*, 23170-23182.
- [35] M. Mba; M. D'Acunzo; P. Salice; T. Carofiglio; M. Maggini; S. Caramori; A. Campana; A. Aliprandi; R. Argazzi; S. Carli; C. A. Bignozzi, *J. Phys. Chem. C*, **2013**, *117*, 19885-19896.
- [36] *Shriver and Atkins' Inorganic Chemistry*, ed. OUP Oxford, **2010**
- [37] J. H. Van Vleck, *Phys. Rev.*, **1932**, *41*, 208-215.
- [38] J. S. Griffith; L. E. Orgel, *Quarterly Reviews, Chemical Society*, **1957**, *11*, 381-393.
- [39] J. Muniz; C. Wang; P. Pyykkö, *Chem. Eur. J.*, **2011**, *17*, 368-377.
- [40] V. H. Houlding; V. M. Miskowski, *Coord. Chem. Rev.*, **1991**, *111*, 145-152.
- [41] V. M. Miskowski; V. H. Houlding, *Inorg. Chem.*, **1991**, *30*, 4446-4452.
- [42] *Adv. Inorg. Chem.*, ed. Rudi van, E., Grażyna, S., Academic Press, **2011**
- [43] I. M. Sluch; A. J. Miranda; O. Elbjeirami; M. A. Omary; L. M. Slaughter, *Inorg. Chem.*, **2012**, *51*, 10728-10746.
- [44] B. Ma; P. I. Djurovich; M. E. Thompson, *Coord. Chem. Rev.*, **2005**, *249*, 1501-1510.
- [45] D. Kim; J.-L. Brédas, *J. Am. Chem. Soc.*, **2009**, *131*, 11371-11380.
- [46] M. Kato; C. Kosuge; K. Morii; J. S. Ahn; H. Kitagawa; T. Mitani; M. Matsushita; T. Kato; S. Yano; M. Kimura, *Inorg. Chem.*, **1999**, *38*, 1638-1641.
- [47] H. B. Gray; A. W. Maverick, *Science*, **1981**, *214*, 1201-1205.
- [48] G. Arena; G. Calogero; S. Campagna; L. M., Scolaro; V. Ricevuto; R. Romeo, *Inorg. Chem.*, **1998**, *37*, 2763-2769

- [49] J. A. Gareth Williams; S. Develay; D. L. Rochester; L. Murphy, *Coord. Chem. Rev.*, **2008**, *252*, 2596-2611.
- [50] G. S. Tong; C. M. Che, *Chem. Eur. J.*, **2009**, *15*, 7225-7237.
- [51] P. Pyykkö, *Chem. Rev.*, **1997**, *97*, 597-636.
- [52] H. Schmidbaur; A. Schier, *Chem. Soc. Rev.*, **2012**, *41*, 370-412.
- [53] S. Sculfort; P. Braunstein, *Chem. Soc. Rev.*, **2011**, *40*, 2741-2760.
- [54] H. Schmidbaur, *Gold Bull*, **2000**, *33*, 3-10.
- [55] H. Schmidbaur, *Chem. Soc. Rev.*, **1995**, *24*, 391-400.
- [56] M. J. Katz; K. Sakai; D. B. Leznoff, *Chem. Soc. Rev.*, **2008**, *37*, 1884-1895.
- [57] Y. Kajitani; K. Tsuge; Y. Sasaki; M. Kato, *Chem. Eur. J.*, **2012**, *18*, 11196-11200.
- [58] D. L. M. Suess; J. C. Peters, *Chem. Commun.*, **2010**, *46*, 6554-6556.
- [59] T. Murahashi; H. Kurosawa, *Coord. Chem. Rev.*, **2002**, *231*, 207-228.
- [60] M. Kim; T. J. Taylor; F. P. Gabbaï, *J. Am. Chem. Soc.*, **2008**, *130*, 6332-6333.
- [61] E. J. Fernandez; A. Laguna; J. M. Lopez-de-Luzuriaga, *Dalton Trans.*, **2007**, 1969-1981.
- [62] R. Józszai; I. Beszeda; A. C. Bényei; A. Fischer; M. Kovács; M. Maliarik; P. Nagy; A. Shchukarev; I. Tóth, *Inorg. Chem.*, **2005**, *44*, 9643-9651.
- [63] B.-H. Xia; H.-X. Zhang; C.-M. Che; K.-H. Leung; D. L. Phillips; N. Zhu; Z.-Y. Zhou, *J. Am. Chem. Soc.*, **2003**, *125*, 10362-10374.
- [64] F. Scherbaum; A. Grohmann; B. Huber; C. Krüger; H. Schmidbaur, *Angew. Chem. Int. Ed. Engl.*, **1988**, *27*, 1544-1546.
- [65] P. Pyykko; M. Straka, *Phys. Chem. Chem. Phys.*, **2000**, *2*, 2489-2493.
- [66] J.-M. Lehn, *Science*, **2002**, *295*, 2400-2403.
- [67] F. J. M. Hoeben; P. Jonkheijm; E. W. Meijer; A. P. H. J. Schenning, *Chem. Rev.*, **2005**, *105*, 1491-1546.
- [68] *Supramolecular Chemistry: Concepts and Perspectives*, ed. VCH Weinheim, **1995**
- [69] J.-M. Lehn, *Angew. Chem. Int. Ed. Engl.*, **2015**, *54*, 3276-3289.
- [70] L. Brunsveld; B. J. B. Folmer; E. W. Meijer; R. P. Sijbesma, *Chem. Rev.*, **2001**, *101*, 4071-4098.
- [71] T. F. A. De Greef; M. M. J. Smulders; M. Wolfs; A. P. H. J. Schenning; R. P. Sijbesma; E. W. Meijer, *Chem. Rev.*, **2009**, *109*, 5687-5754.
- [72] A. Ciferri, *Macromolecular rapid communications*, **2002**, *23*, 511-529.
- [73] *Supramolecular Polymers, Second Edition*, ed. Taylor & Francis, **2005**
- [74] R. B. Martin, *Chem. Rev.*, **1996**, *96*, 3043-3064.
- [75] P. Mukerjee; A. K. Ghosh, *J. Am. Chem. Soc.*, **1970**, *92*, 6408-6412.
- [76] J. R. Henderson, *Physical Review E*, **1997**, *55*, 5731-5742.
- [77] *Binding constants: the measurement of molecular complex stability*, ed. Wiley, **1987**
- [78] D. Zhao; J. S. Moore, *Org. Biomol. Chem.*, **2003**, *1*, 3471-3491.
- [79] A. V. Tobolsky; A. Eisenberg, *J. Am. Chem. Soc.*, **1959**, *81*, 780-782.
- [80] M. J. Mayoral; C. Rest; V. Stepanenko; J. Schellheimer; R. Q. Albuquerque; G. Fernández, *J. Am. Chem. Soc.*, **2013**, *135*, 2148-2151.
- [81] C. Rest; A. Martin; V. Stepanenko; N. K. Allampally; D. Schmidt; G. Fernandez, *Chem. Commun.*, **2014**, *50*, 13366-13369.
- [82] N. K. Allampally; A. Florian; M. J. Mayoral; C. Rest; V. Stepanenko; G. Fernández, *Chem. Eur. J.*, **2014**, *20*, 10669-10678.
- [83] A. Gopal; M. Hifsudheen; S. Furumi; M. Takeuchi; A. Ajayaghosh, *Angew. Chem. Int. Ed. Engl.*, **2012**, *51*, 10505-10509.
- [84] Y.-J. Tian; E. W. Meijer; F. Wang, *Chem. Commun.*, **2013**, *49*, 9197-9199.
- [85] W. Bonner, *Origins Life Evol Biosphere*, **1991**, *21*, 59-111.
- [86] R. Bentley, *Chem. Soc. Rev.*, **2005**, *34*, 609-624.

- [87] M. Zhang; G. Qing; T. Sun, *Chem. Soc. Rev.*, **2012**, *41*, 1972-1984.
- [88] R. Breslow; M. Levine; Z. L. Cheng, *Origins of life and evolution of the biosphere : the journal of the International Society for the Study of the Origin of Life*, **2010**, *40*, 11-26.
- [89] Y. Wang; J. Xu; Y. Wang; H. Chen, *Chem. Soc. Rev.*, **2013**, *42*, 2930-2962.
- [90] H. Caner; E. Groner; L. Levy; I. Agranat, *Drug Discovery Today*, **2004**, *9*, 105-110.
- [91] M. A. Mateos-Timoneda; M. Crego-Calama; D. N. Reinhoudt, *Chem. Soc. Rev.*, **2004**, *33*, 363-372.
- [92] *Topics in Stereochemistry, Materials-Chirality*, ed. Wiley, **2004**
- [93] F. Aparicio; F. Vicente; L. Sanchez, *Chem. Commun.*, **2010**, *46*, 8356-8358.
- [94] T. Gulik-Krzywicki; C. Fouquey; J. Lehn, *Proc. Natl. Acad. Sci. U.S.A*, **1993**, *90*, 163-167.
- [95] C. Fouquey; J.-M. Lehn; A.-M. Levelut, *Adv. Mater.*, **1990**, *2*, 254-257.
- [96] Y. Xia; G. M. Whitesides, *Angew. Chem. Int. Ed. Engl.*, **1998**, *37*, 550-575.
- [97] S.-M. Yang; S. G. Jang; D.-G. Choi; S. Kim; H. K. Yu, *Small*, **2006**, *2*, 458-475.
- [98] L. J. Guo, *Adv. Mater.*, **2007**, *19*, 495-513.
- [99] M. Cavallini; C. Albonetti; F. Biscarini, *Adv. Mater.*, **2009**, *21*, 1043-1053.
- [100] Z. Luo; S. Zhang, *Chem. Soc. Rev.*, **2012**, *41*, 4736-4754.
- [101] H. Qiu; S. Che, *Chem. Soc. Rev.*, **2011**, *40*, 1259-1268.
- [102] J. Yu; R. Xu, *Acc. Chem. Res.*, **2010**, *43*, 1195-1204.
- [103] Y. Zhang; L. Zheng, *Nanoscale*, **2010**, *2*, 1919-1929.
- [104] C. Gautier; T. Bürgi, *ChemPhysChem*, **2009**, *10*, 483-492.
- [105] M. Yang; N. A. Kotov, *J. Mater. Chem.*, **2011**, *21*, 6775-6792.
- [106] H. Gu; Z. Yang; J. Gao; C. K. Chang; B. Xu, *J. Am. Chem. Soc.*, **2005**, *127*, 34-35.
- [107] C. Xu; J. Xie; D. Ho; C. Wang; N. Kohler; E. G. Walsh; J. R. Morgan; Y. E. Chin; S. Sun, *Angew. Chem. Int. Ed. Engl.*, **2008**, *47*, 173-176.
- [108] J. Gao; H. Gu; B. Xu, *Acc. Chem. Res.*, **2009**, *42*, 1097-1107.
- [109] Q. Chen; S. C. Bae; S. Granick, *Nature*, **2011**, *469*, 381-384.
- [110] Q. Chen; J. K. Whitmer; S. Jiang; S. C. Bae; E. Luijten; S. Granick, *Science*, **2011**, *331*, 199-202.
- [111] Q. Chen; E. Diesel; J. K. Whitmer; S. C. Bae; E. Luijten; S. Granick, *J. Am. Chem. Soc.*, **2011**, *133*, 7725-7727.
- [112] K. Kamata; S. Suzuki; M. Ohtsuka; M. Nakagawa; T. Iyoda; A. Yamada, *Adv. Mater.*, **2011**, *23*, 5509-5513.
- [113] C. Noguez; I. L. Garzon, *Chem. Soc. Rev.*, **2009**, *38*, 757-771.
- [114] A. Guerrero-Martínez; J. L. Alonso-Gómez; B. Auguie; M. M. Cid; L. M. Liz-Marzán, *Nano Today*, **2011**, *6*, 381-400.
- [115] A. Kuzyk; R. Schreiber; Z. Fan; G. Pardatscher; E.-M. Roller; A. Hoge; F. C. Simmel; A. O. Govorov; T. Liedl, *Nature*, **2012**, *483*, 311-314.
- [116] A. J. Mastroianni; S. A. Claridge; A. P. Alivisatos, *J. Am. Chem. Soc.*, **2009**, *131*, 8455-8459.
- [117] S. De Feyter; F. C. De Schryver, *Chem. Soc. Rev.*, **2003**, *32*, 139-150.
- [118] D. Philp; J. F. Stoddart, *Angew. Chem. Int. Ed. Engl.*, **1996**, *35*, 1154-1196.
- [119] C. Yu; K. H. Chan; K. M. Wong; V. W.-W. Yam, *Proc. Natl. Acad. Sci. U.S.A*, **2006**, *103*, 19652-19657.
- [120] J. Moussa; K. M.-C. Wong; L. M. Chamoreau; H. Amouri; V. W.-W. Yam, *Dalton Trans.*, **2007**, 3526-3530.
- [121] T. Cardolaccia; Y. Li; K. S. Schanze, *J. Am. Chem. Soc.*, **2008**, *130*, 2535-2545.
- [122] M. Y. Yuen; V. A. Roy; W. Lu; S. C. Kui; G. S. Tong; M. H. So; S. S. Chui; M. Muccini; J. Q. Ning; S. J. Xu; C. M. Che, *Angew. Chem. Int. Ed. Engl.*, **2008**, *47*, 9895-9899.

- [123] W. Lu; Y. Chen; V. A. Roy; S. S. Chui; C. M. Che, *Angew. Chem. Int. Ed. Engl.*, **2009**, *48*, 7621-7625.
- [124] W. Lu; S. S. Chui; K. M. Ng; C. M. Che, *Angew. Chem. Int. Ed. Engl.*, **2008**, *47*, 4568-4572.
- [125] Y. Guo; L. Xu; H. Liu; Y. Li; C. M. Che; Y. Li, *Adv. Mater.*, **2015**, *27*, 985-1013.
- [126] A. Aliprandi; M. Mauro; L. De Cola, *submitted*.
- [127] A. Y.-Y. Tam; K. M.-C. Wong; V. W.-W. Yam, *J. Am. Chem. Soc.*, **2009**, *131*, 6253-6260.
- [128] V. W. Yam; Y. Hu; K. H. Chan; C. Y. Chung, *Chem. Commun.*, **2009**, 6216-6218.
- [129] K. M.-C. Wong; M. M.-Y. Chan; V. W.-W. Yam, *Adv. Mater.*, **2014**, *26*, 5558-5568.
- [130] F. Camerel; R. Ziessel; B. Donnio; C. Bourgogne; D. Guillon; M. Schmutz; C. Iacovita; J.-P. Bucher, *Angew. Chem. Int. Ed. Engl.*, **2006**, *119*, 2713-2716.
- [131] M. Chen; C. Wei; X. Wu; M. Khan; N. Huang; G. Zhang; L. Li, *Chem. Eur. J.*, **2015**, *21*, 4213-4217.
- [132] K. M.-C. Wong; V. W.-W. Yam, *Acc. Chem. Res.*, **2011**, *44*, 424-434.
- [133] K. H. Chan; J. W. Lam; K. M. Wong; B. Z. Tang; V. W.-W. Yam, *Chem. Eur. J.*, **2009**, *15*, 2328-2334.
- [134] C. Yu; K. H. Chan; K. M. Wong; V. W.-W. Yam, *Chem. Eur. J.*, **2008**, *14*, 4577-4584.
- [135] C. Y. Chung; V. W. Yam, *Chem. Eur. J.*, **2014**, *20*, 13016-13027.
- [136] C. Po; A. Y. Tam; K. M. Wong; V. W. Yam, *J. Am. Chem. Soc.*, **2011**, *133*, 12136-12143.
- [137] C. Po; A. Y.-Y. Tam; V. W.-W. Yam, *Chem. Sci.*, **2014**, *5*, 2688-2695.
- [138] C. Po; V. W.-W. Yam, *Chem. Sci.*, **2014**, *5*, 4868-4872.
- [139] H. L. Au-Yeung; S. Y. Leung; A. Y. Tam; V. W. Yam, *J. Am. Chem. Soc.*, **2014**, *136*, 17910-17913.
- [140] Y. Chen; C. M. Che; W. Lu, *Chem. Commun.*, **2015**, *51*, 5371-5374.
- [141] S. Y.-L. Leung; V. W.-W. Yam, *Chem. Sci.*, **2013**, *4*, 4228-4234.
- [142] S. Y.-L. Leung; W. H. Lam; V. W.-W. Yam, *Proc. Natl. Acad. Sci. U.S.A*, **2013**, *110*, 7986-7991.
- [143] C. Po; Z. Ke; A. Y. Tam; H. F. Chow; V. W. Yam, *Chem. Eur. J.*, **2013**, *19*, 15735-15744.
- [144] Y. Mao; K. Liu; L. Meng; L. Chen; L. Chen; T. Yi, *Soft Matter*, **2014**, *10*, 7615-7622.
- [145] C. Y. Chung; S. Tamaru; S. Shinkai; V. W. Yam, *Chem. Eur. J.*, **2015**, *21*, 5447-5458.
- [146] X. P. Zhang; V. Y. Chang; J. Liu; X. L. Yang; W. Huang; Y. Li; C. H. Li; G. Muller; X. Z. You, *Inorg. Chem.*, **2015**, *54*, 143-152.
- [147] N. K. Allampally; C. G. Daniliuc; C. A. Strassert; L. De Cola, *Inorg. Chem.*, **2015**, *54*, 1588-1596.
- [148] C. A. Strassert; C. H. Chien; M. D. Galvez Lopez; D. Kourkoulos; D. Hertel; K. Meerholz; L. De Cola, *Angew. Chem. Int. Ed. Engl.*, **2011**, *50*, 946-950.
- [149] N. K. Allampally; C. A. Strassert; L. De Cola, *Dalton Trans.*, **2012**, *41*, 13132-13137.
- [150] N. K. Allampally; M. Bredol; C. A. Strassert; L. De Cola, *Chem. Eur. J.*, **2014**, *20*, 16863-16868.
- [151] O. S. Wenger, *Chem. Rev.*, **2013**, *113*, 3686-3733.
- [152] A. Kobayashi; M. Kato, *Eur. J. Inorg. Chem.*, **2014**, 4469-4483.
- [153] Y. Sagara; T. Kato, *Nat. Chem.*, **2009**, *1*, 605-610.
- [154] J. Ni; Y. G. Wang; H. H. Wang; L. Xu; Y. Q. Zhao; Y. Z. Pan; J. J. Zhang, *Dalton Trans.*, **2014**, *43*, 352-360.
- [155] J. Ni; X. Zhang; N. Qiu; Y.-H. Wu; L.-Y. Zhang; J. Zhang; Z.-N. Chen, *Inorg. Chem.*, **2011**, *50*, 9090-9096.
- [156] L.-M. Huang; G.-M. Tu; Y. Chi; W.-Y. Hung; Y.-C. Song; M.-R. Tseng; P.-T. Chou; G.-H. Lee; K.-T. Wong; S.-H. Cheng; W.-S. Tsai, *J. Mater. Chem. C*, **2013**, *1*, 7582-7592.

- [157] T. Tanaka; R. Nouchi; Y. Nakao; Y. Arikawa; K. Umakoshi, *RSC Advances*, **2014**, *4*, 62186-62189.
- [158] A. Han; P. Du; Z. Sun; H. Wu; H. Jia; R. Zhang; Z. Liang; R. Cao; R. Eisenberg, *Inorg. Chem.*, **2014**, *53*, 3338-3344.
- [159] T. Abe; T. Itakura; N. Ikeda; K. Shinozaki, *Dalton Trans.*, **2009**, 711-715.
- [160] M. Krikorian; S. Liu; T. M. Swager, *J. Am. Chem. Soc.*, **2014**, *136*, 2952-2955.
- [161] V. N. Kozhevnikov; B. Donnio; D. W. Bruce, *Angew. Chem. Int. Ed. Engl.*, **2008**, *47*, 6286-6289.
- [162] J. R. Kumpfer; S. D. Taylor; W. B. Connick; S. J. Rowan, *J. Mater. Chem.*, **2012**, *22*, 14196-14204.
- [163] X. Zhang; J.-Y. Wang; J. Ni; L.-Y. Zhang; Z.-N. Chen, *Inorg. Chem.*, **2012**, *51*, 5569-5579.
- [164] S. J. Choi; J. Kuwabara; Y. Nishimura; T. Arai; T. Kanbara, *Chem. Lett.*, **2012**, *41*, 65-67.
- [165] X.-P. Zhang; J.-F. Mei; J.-C. Lai; C.-H. Li; X.-Z. You, *J. Mater. Chem. C*, **2015**, *3*, 2350-2357.
- [166] T. Terai; T. Nagano, *Pflugers Arch - Eur J Physiol*, **2013**, *465*, 347-359.
- [167] M. Minsky, *Scanning*, **1988**, *10*, 128-138.
- [168] S. W. Hell; J. Wichmann, *Opt. Lett.*, **1994**, *19*, 780-782.
- [169] D. Baddeley; C. Batram; Y. Weiland; C. Cremer; U. J. Birk, *Nat. Protocols*, **2007**, *2*, 2640-2646.
- [170] K. Chung; J. Wallace; S. Y. Kim; S. Kalyanasundaram; A. S. Andalman; T. J. Davidson; J. J. Mirzabekov; K. A. Zalocusky; J. Mattis; A. K. Denisin; S. Pak; H. Bernstein; C. Ramakrishnan; L. Grosenick; V. Gradinaru; K. Deisseroth, *Nature*, **2013**, *497*, 332-337.
- [171] L. Brancalion; A. J. Durkin; J. H. Tu; G. Menaker; J. D. Fallon; N. Kollias, *Photochem. Photobiol.*, **2001**, *73*, 178-183.
- [172] C. K. Brookner; M. Follen; I. Boiko; J. Galvan; S. Thomsen; A. Malpica; S. Suzuki; R. Lotan; R. Richards-Kortum, *Photochem. Photobiol.*, **2000**, *71*, 730-736.
- [173] J. Eng; R. M. Lynch; R. S. Balaban, *Biophys. J.*, **1989**, *55*, 621-630.
- [174] O. Shimomura, *J. Microsc.*, **2005**, *217*, 3-15.
- [175] M. Chalfie; Y. Tu; G. Euskirchen; W. W. Ward; D. C. Prasher, *Science*, **1994**, *263*, 802-805.
- [176] R. Y. Tsien, *Annu. Rev. Biochem.*, **1998**, *67*, 509-544.
- [177] R. Weissleder; V. Ntziachristos, *Nat Med*, **2003**, *9*, 123-128.
- [178] M. G. Müller; I. Georgakoudi; Q. Zhang; J. Wu; M. S. Feld, *Appl. Opt.*, **2001**, *40*, 4633-4646.
- [179] E. B. Brown; R. B. Campbell; Y. Tsuzuki; L. Xu; P. Carmeliet; D. Fukumura; R. K. Jain, *Nat Med*, **2001**, *7*, 864-868.
- [180] K. Zagorovsky; W. C. W. Chan, *Nat. Mater.*, **2013**, *12*, 285-287.
- [181] E. Kim; M. Koh; J. Ryu; S. B. Park, *J. Am. Chem. Soc.*, **2008**, *130*, 12206-12207.
- [182] A. Samanta; M. Vendrell; R. Das; Y.-T. Chang; A. Samanta; M. Vendrell; R. Das; Y.-T. Chang, *Chem. Commun.*, **2010**, *46*, 7406-7408.
- [183] Y. Kawazoe; H. Shimogawa; A. Sato; M. Uesugi, *Angew. Chem. Int. Ed. Engl.*, **2011**, *50*, 5478-5481.
- [184] G. Crivat; J. W. Taraska, *Trends Biotechnol.*, **2012**, *30*, 8-16.
- [185] A. H. Coons; H. J. Creech; R. N. Jones; E. Berliner, *J Immunol*, **1942**, *45*, 159-170.
- [186] B. Ballou; L. A. Ernst; A. S. Waggoner, *Curr. Med. Chem.*, **2005**, *12*, 795-805.
- [187] M. Ogawa; C. A. S. Regino; J. Seidel; M. V. Green; W. Xi; M. Williams; N. Kosaka; P. L. Choyke; H. Kobayashi, *Bioconjug. Chem.*, **2009**, *20*, 2177-2184.
- [188] X. Chen; P. S. Conti; R. A. Moats, *Cancer Res*, **2004**, *64*, 8009-8014.

- [189] S. Ke; X. Wen; M. Gurfinkel; C. Charnsangavej; S. Wallace; E. M. Sevick-Muraca; C. Li, *Cancer Res*, **2003**, *63*, 7870-7875.
- [190] D. W. Domaille; E. L. Que; C. J. Chang, *Nat Chem Biol*, **2008**, *4*, 168-175.
- [191] L.-C. Lo; C.-Y. Chu, *Chem. Commun.*, **2003**, 2728-2729.
- [192] J. E. González; R. Y. Tsien, *Chemistry & Biology*, **1997**, *4*, 269-277.
- [193] A. Razgulin; N. Ma; J. Rao, *Chem. Soc. Rev.*, **2011**, *40*, 4186-4216.
- [194] T. Myochin; K. Kiyose; K. Hanaoka; H. Kojima; T. Terai; T. Nagano, *J. Am. Chem. Soc.*, **2011**, *133*, 3401-3409.
- [195] J. F. Callan; A. P. de Silva; D. C. Magri, *Tetrahedron*, **2005**, *61*, 8551-8588.
- [196] T. Ueno; Y. Urano; K.-i. Setsukinai; H. Takakusa; H. Kojima; K. Kikuchi; K. Ohkubo; S. Fukuzumi; T. Nagano, *J. Am. Chem. Soc.*, **2004**, *126*, 14079-14085.
- [197] A. P. de Silva; R. A. D. D. Rupasinghe, *Journal of the Chemical Society, Chemical Communications*, **1985**, 1669-1670.
- [198] A. Miyawaki, *Annu. Rev. Biochem.*, **2011**, *80*, 357-373.
- [199] K. Kikuchi, *Chem. Soc. Rev.*, **2010**, *39*, 2048-2053.
- [200] G. Lukinavičius; K. Umezawa; N. Olivier; A. Honigmann; G. Yang; T. Plass; V. Mueller; L. Reymond; I. R. Corrêa Jr; Z.-G. Luo; C. Schultz; E. A. Lemke; P. Heppenstall; C. Eggeling; S. Manley; K. Johnsson, *Nat Chem*, **2013**, *5*, 132-139.
- [201] J. F. W. Herschel, *Philosophical Transactions of the Royal Society of London*, **1845**, *135*, 143-145.
- [202] J. Kapuscinski, *Biotechnic & histochemistry : official publication of the Biological Stain Commission*, **1995**, *70*, 220-233.
- [203] S. A. Latt; G. Stetten, *The journal of histochemistry and cytochemistry : official journal of the Histochemistry Society*, **1976**, *24*, 24-33.
- [204] M. Heilemann; S. van de Linde; A. Mukherjee; M. Sauer, *Angew. Chem. Int. Ed. Engl.*, **2009**, *48*, 6903-6908.
- [205] M. J. Rust; M. Bates; X. Zhuang, *Nat Meth*, **2006**, *3*, 793-796.
- [206] E. Betzig; G. H. Patterson; R. Sougrat; O. W. Lindwasser; S. Olenych; J. S. Bonifacino; M. W. Davidson; J. Lippincott-Schwartz; H. F. Hess, *Science*, **2006**, *313*, 1642-1645.
- [207] R. Rossetti; S. Nakahara; L. E. Brus, *J. Chem. Phys.*, **1983**, *79*, 1086-1088.
- [208] R. C. Somers; M. G. Bawendi; D. G. Nocera, *Chem. Soc. Rev.*, **2007**, *36*, 579-591.
- [209] X. Michalet; F. F. Pinaud; L. A. Bentolila; J. M. Tsay; S. Doose; J. J. Li; G. Sundaresan; A. M. Wu; S. S. Gambhir; S. Weiss, *Science (New York, N.Y.)*, **2005**, *307*, 538-544.
- [210] M. Han; X. Gao; J. Z. Su; S. Nie, *Nat Biotech*, **2001**, *19*, 631-635.
- [211] X. Gao; S. Nie, *J. Phys. Chem. B*, **2003**, *107*, 11575-11578.
- [212] X. Gao; S. Nie, *Analytical Chemistry*, **2004**, *76*, 2406-2410.
- [213] W. C. Chan; S. Nie, *Science*, **1998**, *281*, 2016-2018.
- [214] M. Nirmal; B. O. Dabbousi; M. G. Bawendi; J. J. Macklin; J. K. Trautman; T. D. Harris; L. E. Brus, *Nature*, **1996**, *383*, 802-804.
- [215] T. Jamieson; R. Bakhshi; D. Petrova; R. Pocock; M. Imani; A. M. Seifalian, *Biomaterials*, **2007**, *28*, 4717-4732.
- [216] K. J. Franz; M. Nitz; B. Imperiali, *Chembiochem*, **2003**, *4*, 265-271.
- [217] S. Freed; S. I. Weissman; F. E. Fortess; H. F. Jacobson, *J. Chem. Phys.*, **1939**, *7*, 824.
- [218] F. Caillé; C. S. Bonnet; F. Buron; S. Villette; L. Helm; S. Petoud; F. Suzenet; É. Tóth, *Inorg. Chem.*, **2012**, *51*, 2522-2532.
- [219] J. F. Desreux, *Inorg. Chem.*, **1980**, *19*, 1319-1324.
- [220] E. Soini, *Trends Analyt. Chem.*, **1990**, *9*, 90-93.
- [221] A. Beeby; S. W. Botchway; I. M. Clarkson; S. Faulkner; A. W. Parker; D. Parker; J. A. G. Williams, *J. Photochem. Photobiol. B*, **2000**, *57*, 83-89.

- [222] S. Faulkner; S. J. A. Pope; B. P. Burton-Pye, *Appl. Spectrosc. Rev.*, **2005**, *40*, 1-31.
- [223] J. C. Bunzli; C. Piguet, *Chem. Soc. Rev.*, **2005**, *34*, 1048-1077.
- [224] M. Elbanowski; B. Mąkowska, *J. Photochem. Photobiol. A*, **1996**, *99*, 85-92.
- [225] C. P. Montgomery; B. S. Murray; E. J. New; R. Pal; D. Parker, *Acc. Chem. Res.*, **2009**, *42*, 925-937.
- [226] K. K.-W. Lo; A. W.-T. Choi; W. H.-T. Law, *Dalton Trans.*, **2012**, *41*, 6021-6047.
- [227] E. Baggaley; J. A. Weinstein; J. A. G. Williams, *Coord. Chem. Rev.*, **2012**, *256*, 1762-1785.
- [228] Q. Zhao; C. Huang; F. Li, *Chem. Soc. Rev.*, **2011**, *40*, 2508-2524.
- [229] M. P. Murphy; R. A. Smith, *Annu. Rev. Pharmacol. Toxicol.*, **2007**, *47*, 629-656.
- [230] C. K. Koo; L. K. So; K. L. Wong; Y. M. Ho; Y. W. Lam; M. H. Lam; K. W. Cheah; C. C. Cheng; W. M. Kwok, *Chem. Eur. J.*, **2010**, *16*, 3942-3950.
- [231] Z. Guo; W. L. Tong; M. C. Chan, *Chem. Commun.*, **2014**, *50*, 1711-1714.
- [232] T. C. Johnstone; J. J. Wilson; S. J. Lippard, *Inorg. Chem.*, **2013**, *52*, 12234-12249.
- [233] M. Mauro; A. Aliprandi; D. Septiadi; N. S. Kehr; L. De Cola, *Chem. Soc. Rev.*, **2014**, *43*, 4144-4166.
- [234] S. W. Botchway; M. Charnley; J. W. Haycock; A. W. Parker; D. L. Rochester; J. A. Weinstein; J. A. G. Williams, *Proc. Natl. Acad. Sci. U.S.A.*, **2008**, *105*, 16071-16076.
- [235] E. Baggaley; S. W. Botchway; J. W. Haycock; H. Morris; I. V. Sazanovich; J. A. G. Williams; J. A. Weinstein, *Chem. Sci.*, **2014**, *5*, 879-886.
- [236] E. Baggaley; I. V. Sazanovich; J. A. G. Williams; J. W. Haycock; S. W. Botchway; J. A. Weinstein, *RSC Adv.*, **2014**, *4*, 35003-35008.
- [237] C. Y.-S. Chung; S. P.-Y. Li; M.-W. Louie; K. K.-W. Lo; V. W.-W. Yam, *Chem. Sci.*, **2013**, *4*, 2453-2462.

# Chapter 2

## Experimental techniques

**Abstract:** This chapter briefly describes the major instrumental methods employed in the thesis for the characterization of the compounds both theoretically and practically. UV-Vis absorption, Steady state and time resolved emission techniques are described as well as quantum yield measurements and cyclic voltammetry. Microscopy techniques such as scanning electron microscopy and fluorescence microscopy are discussed. The conditions for all other commonly used characterizations and experimental techniques (i.e. NMR, mass spectroscopy, sample preparation) are given in the experimental sections of the individual chapters.

## 2.1 Absorption spectroscopy<sup>1</sup>

In order to measure such quantity with no influences exerted by other phenomena (mainly related to short-term changes in source intensity), a double-beam UV-Vis spectrophotometer is used. A schematic diagram of a double-beam UV-Vis spectrophotometer is shown in Figure 2.1. The monochromator selects a particular wavelength from the light source, which is split into two separate beams. These two beams ( $I_0$ ) are guided through the sample containing and through the pure solvent (reference) using optically transparent cells (generally quartz cuvettes). The intensity of two beams is compared to give respective absorbances.

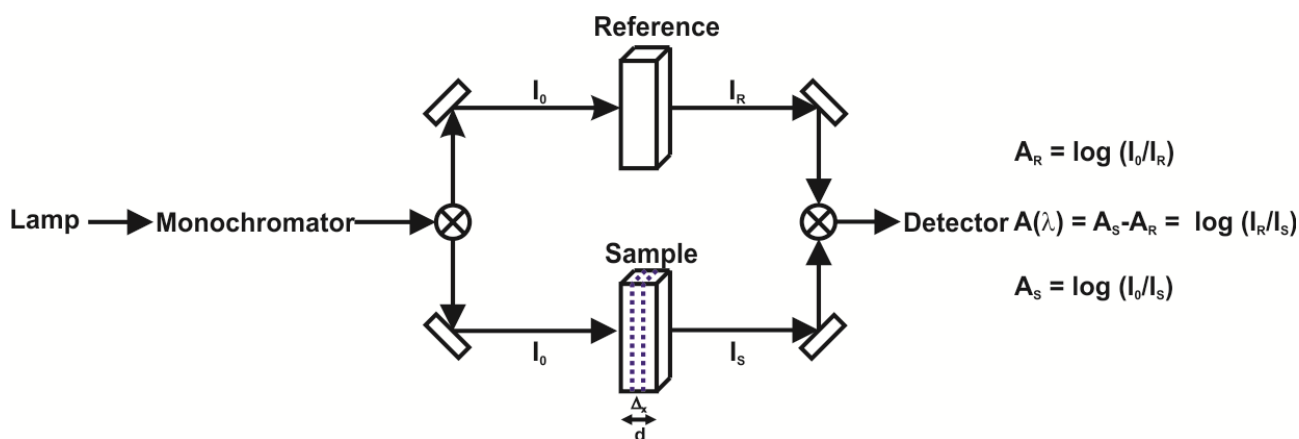


Figure 2.1. Schematic description of a double beam spectrophotometer.

Consider a thin slab of solution of thickness  $dx$  that contains  $n$  light-absorbing molecules/cm<sup>3</sup> (Figure 2.1). If  $\sigma$  is the effective cross-section for absorption in cm<sup>2</sup>, the light intensity  $dI$  absorbed per thickness  $dx$  is proportional to the intensity of the incident light  $I$ ,  $\sigma$  and the number of molecules per cm<sup>3</sup> ( $n$ ):  $\frac{dI}{dx} = I\sigma n$ . Rearrangement and integration, subject to the boundary condition  $I = I_0$  at  $x = 0$ , yields the Beer-Lambert equation, which is generally used in an alternative form:

$\log \frac{I_0}{I} = \epsilon cd$  where  $\epsilon$  is the molar extinction coefficient (in M<sup>-1</sup> cm<sup>-1</sup>) and  $c$  is the concentration in moles/liter. Also the transmittance ( $T$ ) is frequently used and it is defined as the ratio between the intensity of light that passes through a medium (transmitted light,  $I$ ) and the intensity of the incident light ( $I_0$ ). In other words, it is

defined as the negative logarithm of the absorbance. Beer's Law predicts that the optical density is directly proportional to the concentration of the absorbing species. However deviations from Beer's law can result from both instrumental and intrinsic causes. Biological and/or supramolecular systems that contain macromolecules or other large aggregates, can lead to turbid samples that scatter light. The optical density resulting from scatter will be proportional to  $1/\lambda^4$  (Rayleigh scattering), and may thus be easily recognized as a background absorption that increases rapidly with decreasing wavelength.

If the optical density of the sample is high, and the absorbing species fluorescent, the emitted light cannot reach the detector. However this effect can be minimized by keeping the detector distant from the sample, decreasing the efficiency with which the fluorescence emission is collected or with cuvettes having reduced optical path or a different geometry.

Aggregation processes can also take place and the resulting supramolecular systems may possess distinct features from the monomers. Depending upon the wavelength chosen for observation, the deviations from Beer's law may be positive or negative. In our experiments the electronic absorption spectra were recorded on a Shimadzu UV-3600 double-beam UV–VIS–NIR spectrophotometer and baseline corrected. Time- and temperature-dependent absorption spectra were recorded on a JASCO V-650 UV–VIS spectrophotometer equipped with cell holder and temperature control. The quartz cuvettes (from Hellma) have an optical path of 1 cm.

## **2.2 Fluorescence spectroscopy**

An emission spectrum is the wavelength distribution of an emission measured at a single constant excitation wavelength. Conversely, an excitation spectrum is the dependence of emission intensity, measured at a single emission wavelength, upon scanning the excitation wavelength. Such spectra can be presented on either a wavelength scale or a wavenumber scale. Light of a given energy can be described in terms of its wavelength  $\lambda$ , frequency  $\nu$ , or wavenumber. The usual units for wavelength are nanometers, and wavenumbers are given in units of  $\text{cm}^{-1}$ .

Wavelengths and wavenumbers are easily interconverted by taking the reciprocal of each value. For example, 400 nm corresponds to  $(400 \times 10^{-7} \text{ cm})^{-1} = 25,000 \text{ cm}^{-1}$ . On the contrary of absorption spectroscopy in which a double-beam configuration can get rid of many artefacts, there is no ideal spectrofluorometer. The available instruments do not yield true excitation or emission spectra. This is because of the spectral output of the light sources and the wavelength-dependent efficiency of the monochromators and detector tubes are not uniform. The polarization or anisotropy of the emitted light can also affect the measured fluorescence intensities because the efficiency of gratings depends on polarization. Emission spectra recorded on different instruments can be different because of the wavelength-dependent sensitivities of the instruments. In this thesis, steady-state emission spectra were recorded on a HORIBA Jobin-Yvon IBH FL-322 Fluorolog 3 spectrometer equipped with a 450 W xenon arc lamp as a source of exciting light which passes through a monochromator (2.1 nm/mm dispersion; 1200 grooves/mm) and is directed to a reference detector and to the sample.

Emission of the sample, collected at 90° with respect to the incident light, passes through another monochromator (2.1 nm/mm dispersion; 1200 grooves/mm) before reaching the detector. Different detectors were used depending on the considered region of the light spectrum: for the UV-Vis range, a TBX-04 single photon-counting detector was used whereas for the NIR a Hamamatsu R2658P photomultiplier was used. The excitation spectra are corrected for source intensity (lamp and excitation grating) and for detector spectral response and emission grating by standard correction curves. Optical Filters are used, to remove unwanted wavelengths in the excitation beam, or to remove scattered light from the emission channel in particular a 400 nm long pass filter was employed. For anisotropy measurements a PicoQuant FluoTime 300 (PicoQuant GmbH, Germany) equipped with the Multi-Channel Scaling (MCS) electronics NanoHarp 250 and a xenon lamp as a source of exciting light was used. Figure 2.2 shows a schematic diagram of a Fluorolog 3 spectrometer.

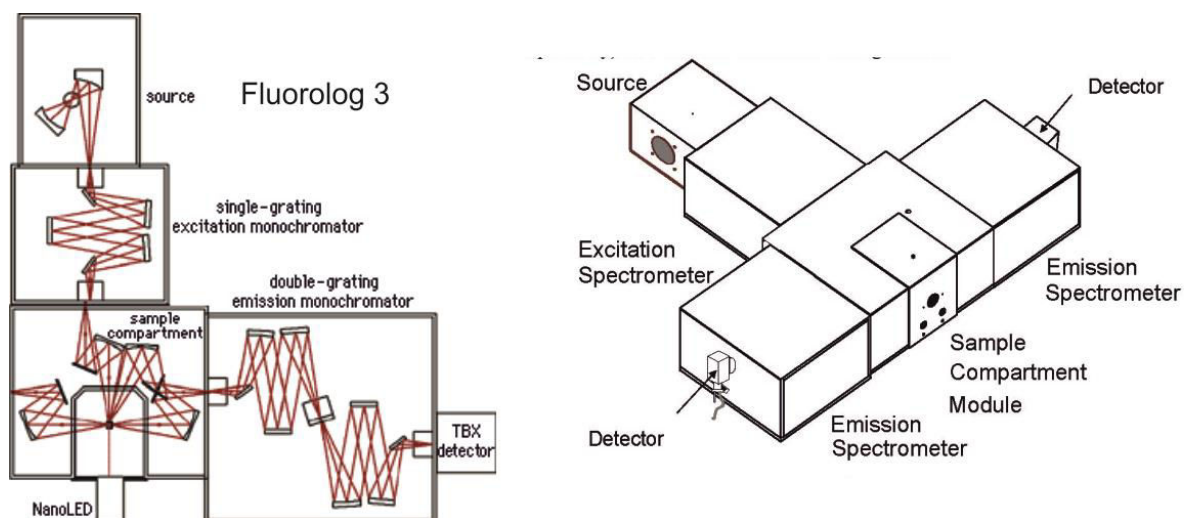


Figure 2.2. Schematic representation of the fluorescence spectrophotometer Fluorolog 3 model FL3-12 from Horiba Scientific (source: [www.horiba.com](http://www.horiba.com)).

### 2.3 Luminescence quantum yields

The photoluminescence quantum yield (PLQY) of a molecule in solution varies depending on the experimental conditions, including the type of solvent, the concentrations of sample and dissolved oxygen in the solution, temperature, and excitation wavelength. When the physical conditions are fully specified, the absolute quantum yield can, in principle, be precisely determined. However, even if these parameters are specified, a number of pitfalls exist. It must be considered explicitly to determine reliable quantum yields. These include polarization effects, refractive index effects, reabsorption/ reemission effects, internal reflection effects, and the spectral sensitivity of the detection system.<sup>2,3</sup> They can be classified into relative (or secondary) methods and absolute (or primary) methods.<sup>4</sup>

The absolute methods require performing various complex corrections to obtain accurate quantum yields. Therefore, in most laboratories relative (secondary) methods are used to determine quantum yields.

In secondary methods, the quantum yield of a sample solution is determined by comparing the integrated fluorescence intensity with a standard solution under identical conditions of incident irradiance. Thus, it is critical to correct for the spectral sensitivity of the instrument, and the measured quantum yield is only as accurate as the certainty of the quantum yield of the fluorescence standard according to the

equation:  $\Phi_S = \Phi_R \frac{I_S}{I_R} \frac{OD_R}{OD_S} \frac{n_S^2}{n_R^2}$  where  $\Phi$  is the photoluminescence quantum yield (PLQY);  $I$  is the integrated emission intensity;  $OD$  is the optical density, and  $n$  is the refractive index. The subscripts  $S$  and  $R$  refer to the sample and reference fluorophore the latter must have a known quantum yield. In this expression it is assumed that the sample and reference are excited at the same wavelength, so that it is not necessary to correct for the different excitation intensities of different wavelengths.<sup>1</sup>

Many different absolute (or primary) methods for determining PLQY have been developed such as the Vavilov method<sup>5</sup> (using magnesium oxide as a standard), the Weber and Teale method<sup>6</sup> (using scattering solution as standard), Calorimetric methods<sup>7-9</sup> and photoacoustic (optoacoustic) methods<sup>10,11</sup> detect the fraction of the energy which is lost by nonradiative processes in a luminescent sample, i.e., the complement of the luminescence energy yield. These photothermal methods generally require making the assumption that the relaxation processes of excited molecules involve no photochemical reactions.

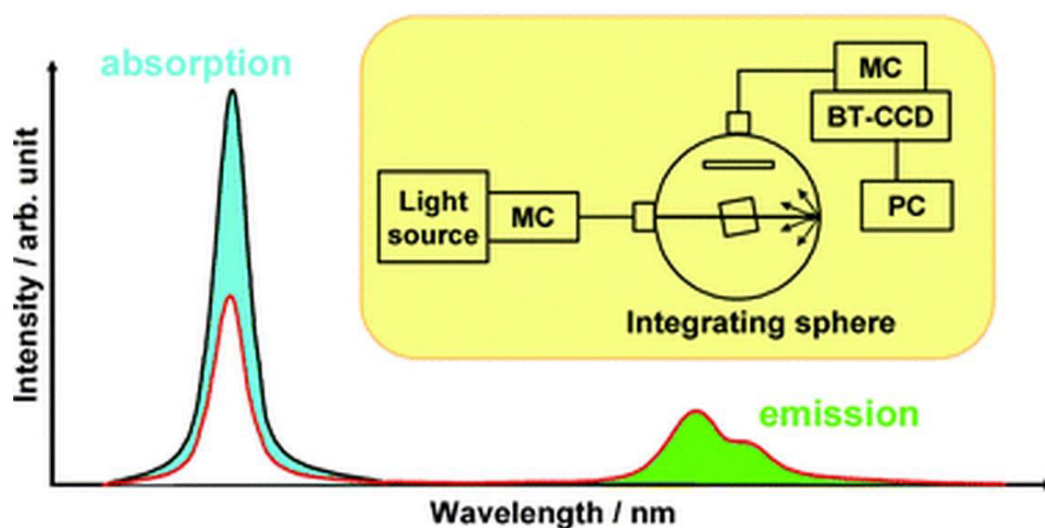


Figure 2.3. Schematic representation of an integrating sphere for measuring absolute luminescence quantum yields. MC stands for monochromator, and BT-CCD is a back thinned CCD. The number of photons absorbed is proportional to the difference of the integrated excitation light profiles, while the number of photons emitted is proportional to the area under its fluorescence spectrum.<sup>4</sup>

Another approach consists in the use of an integrating sphere (Figure 2.3) which collects all the emitted photons with a calibrated photodiode and sets them into relation with the number of absorbed photons. In this way the effects of polarization, scattering and refractive index are eliminated from the measurements.

Light from a xenon lamp is monochromatized at the selected wavelength and guided by an optical fiber into the integrating sphere. The emitted light from the sample is collected by a detector after passing through another optical fiber and a second monochromator. The PLQY ( $\Phi$ ) is then calculated from the number of photons absorbed (difference of the integrated excitation light profiles) and the number of photons emitted (integrated fluorescence spectrum) according to the equation:

$$\Phi = \frac{PN(Em)}{PN(Abs)} = \frac{\int \frac{\lambda}{hc} [I_{em}^{sample}(\lambda) - I_{em}^{reference}(\lambda)] d\lambda}{\int \frac{\lambda}{hc} [I_{exc}^{reference}(\lambda) - I_{exc}^{sample}(\lambda)] d\lambda}$$

where PN(Abs) is the number of

photons absorbed by a sample and PN(Em) is the number of photons emitted from a sample,  $\lambda$  is the wavelength,  $h$  is Planck's constant,  $c$  is the velocity of light,  $I_{exc}^{sample}$  and  $I_{exc}^{reference}$  are the integrated intensities of the excitation light with and without a sample respectively;  $I_{em}^{sample}$  and  $I_{em}^{reference}$  are the photoluminescence intensities with and without a sample, respectively. For this purpose we used Hamamatsu Photonics absolute PL quantum yield measurement system (C9920-02) equipped with a L9799-01 CW Xenon light source (150 W), monochromator, C7473 photonic multichannel analyzer, an integrating sphere and employing U6039-05 PLQY measurement software (Hamamatsu Photonics, Ltd., Shizuoka, Japan).

## 2.4 Lifetime measurements

Time-resolved experiments, such as the excited state lifetime determination, were carried out by time-correlated single-photon counting (TCSPC). The schematic diagram of the setup is shown in Figure 2.4. The experiment starts with the excitation pulse (either a flash lamp or a laser) which excites the samples and sends a signal to the electronics. This signal is passed through a constant function discriminator (CFD), which accurately measures the arrival time of the pulse.

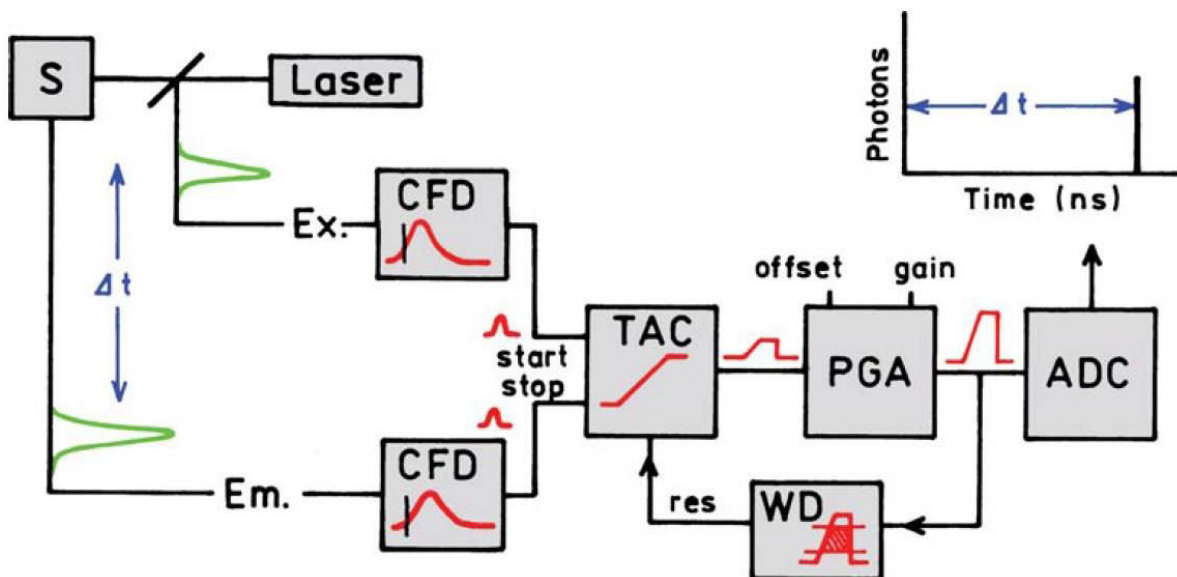


Figure 2.4 Electronic schematic for TCSPC.<sup>1</sup>

The signal (START) is passed to a time-to-amplitude converter (TAC), which starts the charging of the capacitor by generating a voltage ramp. The voltage increases linearly with time on the nanosecond timescale. A second channel detects the pulse from the single detected photon (STOP). The arrival time of the signal is also accurately determined using a CFD, which sends a signal to stop the voltage ramp. TAC now contains a voltage proportional to the time delay and is stored in a histogram in which the x-axis in the histogram is the time difference between START and STOP signal and the y-axis is the number of photons detected for this time difference. As needed the voltage is amplified by a programmable gain amplifier (PGA) and converted to a numerical value by the analog-to-digital converter (ADC). To minimize false readings the signal is restricted to given range of voltages. If the signal is not within this range the event is suppressed by a window discriminator (WD). The voltage is converted to a digital value that is stored as a single event with the measured time delay. By repetitive measurements a statistical time distribution of emitted photons is obtained.

Time-resolved measurements up to  $\sim 10\mu\text{s}$  were performed using the TCSPC option (PicoHarp) of a FluoTime 300 “EasyTau” apparatus (PicoQuant) equipped with subnanosecond LDH sources (375, 405, 440, 510 and 640 nm, with 50–100 ps pulse-width) powered by a PicoQuant PDL 820 variable (0.2–80 MHz) pulsed power supply.

A PMA-C was employed for detection in the UV-visible (200–900 nm). For excited state lifetimes  $>10 \mu\text{s}$ , NanoHarp 250 MCS (Multi Channel scaler Card) histogram accumulating real-time processor was employed.

The multichannel analyzer consists of a multichannel card. The light input is discriminated for its intensity and if the input pulse amplitude falls within the threshold of the lower level discriminator and the upper level discriminator, the control and logic circuit are enabled and the peak amplitude is stored. In general, the signal intensities are collected in different channels for the duration of a dwell time after which an intensity counter moves to the next channel. After the acquisition time is reached, the collected total light intensities in all channels are counted and correlated to the time frame of each channel giving an intensity-time profile.

The decays were analyzed by means of PicoQuant FluoFit Global Fluorescence Decay Analysis Software (PicoQuant GmbH, Germany). The quality of the fit was assessed by minimizing the reduced  $X^2$  function and by visual inspection of the weighted residuals. For multi-exponential decays, the intensity, namely  $I(t)$ , has been assumed to decay as the sum of individual single exponential decays:  $I(t) = \sum_{i=1}^n a_i e^{-\frac{t}{\tau_i}}$  where  $\tau_i$  are the decay times and  $a_i$  are the amplitude of the component at  $t = 0$ . The percentages to the pre-exponential factors,  $a_i$ , are listed upon normalization.

## 2.5 Scanning electron microscope (SEM)

The schematic diagram of a simplified SEM setup is shown in Figure 2.5. The beam of electrons, generated at the top by the electron gun, is accelerated by the anode, which is biased +1 to +50 kV respect to the electron gun, down into the electron column. After being collimated through condenser lens the beam passes through pairs of scanning coils in the electron column, which deflect the beam in the x and y axes so that it scans in a raster fashion over a rectangular area of the sample surface.

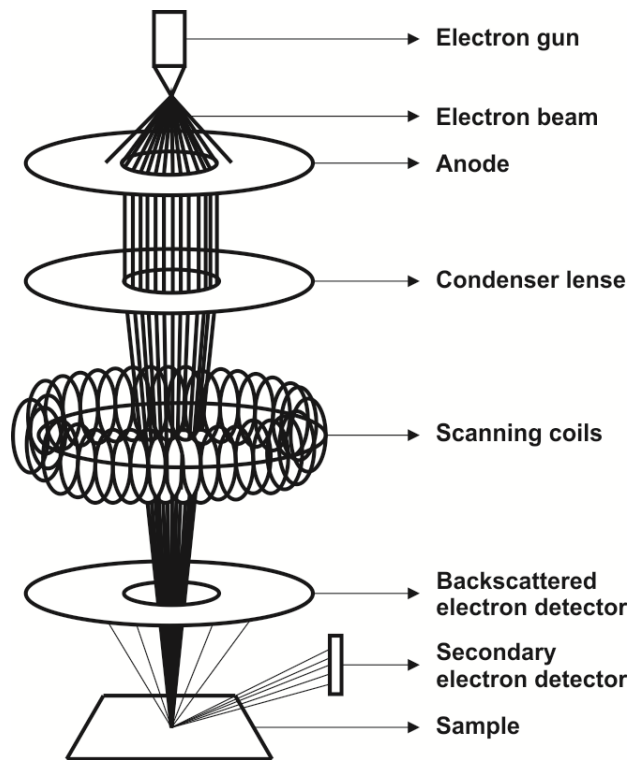


Figure 2.5 Schematic representation of a SEM setup.

Generally the beam is focused in a spot of 1 nm to 5 nm size. The energy exchange between the electron beam and the sample results in the reflection of high-energy electrons by elastic scattering, emission of secondary electrons by inelastic scattering and the emission of electromagnetic radiation, each of which can be detected by specialized detectors.

The most common imaging mode collects low-energy (<50 eV) secondary electrons that are ejected from the k-shell of the specimen atoms by inelastic scattering interactions. The Backscattered electrons, originated by elastic scattering interactions with specimen atoms can also be used for creating the contrast image of the specific regions of the sample.

For conventional imaging in the SEM, specimens must be electrically conductive, at least on the surface, and electrically grounded to prevent the accumulation of electrostatic charge on the surface. Therefore they are usually coated with an ultrathin coating of electrically conducting material, deposited on the sample either by low-vacuum sputter coating or by high-vacuum evaporation.

In this thesis, the samples were covered by a 5 nm thick gold layer, and finally investigated using a FEI Dual Beam 235: FIB-SEM-STEM with an ion beam (FIB, 5 nm) and electron beam (SEM, 1 nm).

## 2.6 Fluorescence microscopy

Figure 2.6 shows a simplified setup of a widefield fluorescence microscope (left) and a laser scanning confocal microscope (right).

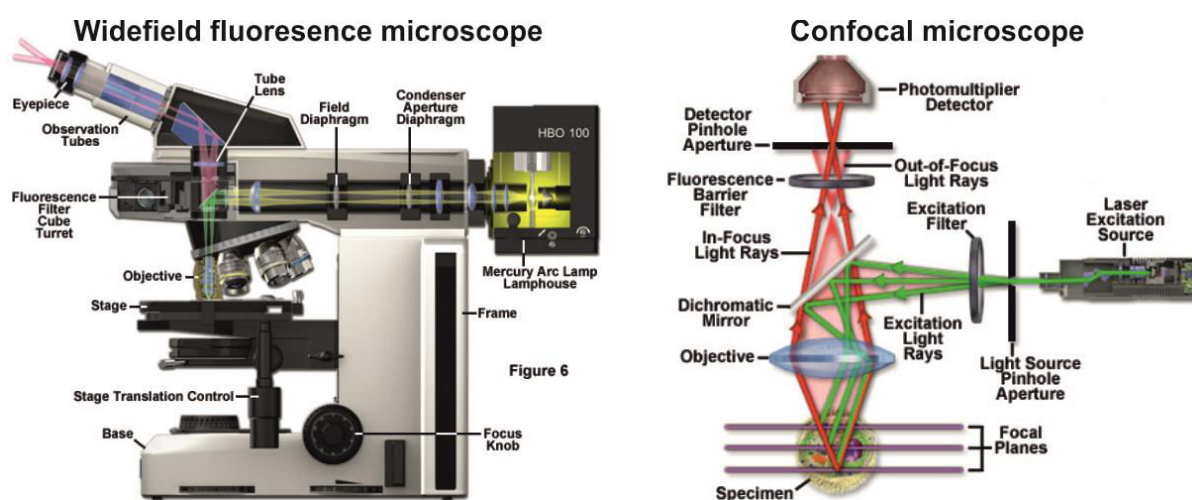


Figure 2.6. Simplified setup of a widefield fluorescence microscope (left) and schematic representation of a Laser Scanning Confocal Microscope (right) adapted from [www.zeiss.com](http://www.zeiss.com).

In the widefield microscopes the light source is usually a xenon arc lamp or mercury-vapor lamp. An excitation filter selects a particular wavelength range, and the excitation beam is deflected at  $90^\circ$  by a dichroic (DIC) mirror, reaching the sample after passing through an emission filter and the objective lens which focuses the light emitted by the sample onto an area array detector system (usually a CCD camera). A shutter system limits the excessive exposure to harmful excitation light. The full aperture of emission light gathered by the microscope objective maximizes the recorded signal and simultaneously minimizes the required exposure times. Thus, specimens can be imaged with very brief illumination periods. The major drawback of widefield imaging is that fluorescence arising from regions far from the focal plane, as well as background signal, often obscures the features of interest. Therefore,

widefield imaging achieves the optimum results when the features of interest are either large (such as an organelle) or highly punctate in nature. Generally DIC microscopy is used in conjunction with widefield fluorescence to monitor the general morphology while simultaneously investigating phenomena of interest with specifically labeled targets. Thus, the DIC image can be captured from a fluorescently labeled specimen using transmitted light followed by imaging in epi-fluorescence mode and combined during analysis.

Nowadays widefield microscopes can capture DIC and fluorescence images simultaneously. Multiple fluorophores can be sequentially imaged to elucidate the spatial and temporal relationships between labeled targets.

Laser scanning confocal microscopes (Figure 2.6 right) offer several advantages over conventional widefield fluorescence microscopes, in particular the possibility to control the depth of field and the elimination of the out-of-focus information. It is also possible to collect series of “optical sections” from thick specimens that can be subsequently used to reconstruct the specimens in three dimensions.

The key to the confocal approach is the usage of spatial filtering to eliminate out-of-focus light or flare in specimens that are thicker than the plane of focus by illuminating the objective through a pinhole. Only if the specimen is in focus, the light can pass through the pinhole and reach a detector (usually a PMT).

As drawback total signal level is lower even if the specific signal-to-noise ratio for the features of interest is increased.

Magnification can be electronically adjusted by altering the scanning laser sampling period which varies the area scanned by the laser without having to change objectives (zoom factor). Increasing the zoom factor reduces the specimen area scanned and simultaneously reduces the scanning rate. However high zoom factor may lead to increase photobleaching.

In this thesis fluorescence microscopy was performed with an Olympus BX51 microscope using a 20x objective and an Olympus U-MWBV. Images and movies were recorded with an Olympus XC-10 color camera. Fluorescence confocal microscopy

was performed with a Zeiss LSM 710 confocal microscope system with a 10-63x magnification objective.

## 2.7 References

- [1] *Principles of Fluorescence Spectroscopy*, ed. Springer, **2007**
- [2] G. A. Crosby; J. N. Demas, *J. Phys. Chem.*, **1971**, *75*, 991-1024.
- [3] D. F. Eaton, *Pure and Applied Chemistry*, **1988**, *60*, 1107.
- [4] K. Suzuki; A. Kobayashi; S. Kaneko; K. Takehira; T. Yoshihara; H. Ishida; Y. Shiina; S. Oishi; S. Tobita, *Phys. Chem. Chem. Phys.*, **2009**, *11*, 9850-9860.
- [5] S. I. Vavilov, *Z. Phys.*, **1924**, *22*, 266.
- [6] D. M. Hercules; H. Frankel, *Science*, **1960**, *131*, 1611-1612.
- [7] B. Gelernt; A. Findeisen; A. Stein; J. A. Poole, *J. Chem. Soc., Faraday Trans. 2*, **1974**, *70*, 939-940.
- [8] M. Mardelli; J. Olmsted Iii, *J. Photochem.*, **1977**, *7*, 277-285.
- [9] J. Olmsted, *J. Phys. Chem.*, **1979**, *83*, 2581-2584.
- [10] S. E. Braslavsky; G. E. Heibel, *Chem. Rev.*, **1992**, *92*, 1381-1410.
- [11] M. J. Adams; J. G. Highfield; G. F. Kirkbright, *Anal. Chem.*, **1977**, *49*, 1850-1852.



# Chapter 3

## Self-assembly of a neutral platinum(II) complex into highly emitting microcrystalline fibers through metallophilic interactions

**Abstract:** This chapter describes the synthesis of tridentate N<sup>N</sup>N ligands and the corresponding Pt(II) complexes with different ancillary ligands. In particular, 3-trifluoromethyl 2,6-bis(1*H*-1,2,4-triazol-5-yl)pyridine has been employed as coordinating ligand to afford neutral platinum complexes. For one of the derivatives, the self-assembly properties have been investigated by using photophysical and morphological techniques. The resulting self-assembled fibers have shown both polarized absorption and emission with highly efficient photoluminescence quantum yield (up to 74%).

### 3.1 Introduction

Supramolecular organometallic nanostructures have attracted a great deal of attention in the last few years because of the possibility to fabricate functional materials with superior properties. In particular, square-planar Pt(II) and Pd(II) complexes with protruding filled  $d_z^2$  orbitals have been known for a long time to show a high tendency towards stacking through weak non-covalent metal...metal and/or  $\pi$ - $\pi$  ligand-ligand interactions<sup>1-3</sup>.

By means of bottom-up approaches, it has been shown that luminescent Pt(II) complexes are able to form either homo-<sup>4</sup> or hetero-metallic<sup>5,6</sup> supramolecular architectures such as liquid crystals<sup>7,8</sup>, nanowires<sup>9</sup>, nanotubes<sup>10</sup>, nanosheets<sup>11</sup>, and metallo-gelators<sup>12,13</sup>, with very appealing (electro)optical,<sup>11,13-15</sup> sensing<sup>14</sup>, and semiconducting properties<sup>15-18</sup>. To date, metal complexes forming long-range ordered soft structures showing polarized light emission and photoluminescence quantum yield (PLQY) exceeding 0.5 are very rare and typically require the aid of orienting scaffolds and special techniques<sup>19</sup>.

Self-assembled functional architectures might have great potential applications in optoelectronic devices such as organic light emitting diodes (OLEDs),<sup>13,15</sup> field effect transistors (FETs),<sup>11,18</sup> and organic light-emitting FETs (OLEFETs)<sup>9</sup>. Noteworthy, linearly polarized materials with uniaxial molecular orientation find great application for improving light extraction in such devices,<sup>15</sup> and as active materials in 3D OLED displays<sup>19</sup>.

In this chapter, the synthesis and chemical characterization of the 3-trifluoromethyl 2,6-bis(1*H*-1,2,4-triazol-5-yl)pyridine tridentate ligand and its methyl-substituted counterpart are described along with the corresponding neutral Pt(II) complexes. In particular, the Pt(II) derivative containing a formally dianionic N-donor tridentate and trifluoromethyl-substituted chromophoric ligand (**pyC<sub>5</sub>-CF<sub>3</sub>-tzH<sub>2</sub>**, see Figure 3.1) and 4-amyl pyridine as ancillary ligand, namely **Pt-CF<sub>3</sub>tz-pyC<sub>5</sub>**, is able to self-assemble into micrometer-long and highly crystalline fibers with solvent-dependent morphological features. As a consequence of high degree of order imparted by weak non-covalent intermolecular (metal...metal and  $\pi$ - $\pi$ ) interactions within the supramolecular

structures, the resulting self-assembled fibers have shown both polarized absorption and emission with highly efficient photoluminescence quantum yield (up to 74%).

## 3.2 Result and discussion

### 3.2.1 Synthesis and characterization

#### 3.2.1.1 Synthesis of the tridentate ligands

The general chemical structure of the 3-substituted tridentate ligands 2,6-bis(1H-1,2,4-triazol-5-yl)pyridine employed in this chapter is shown in Figure 3.1.

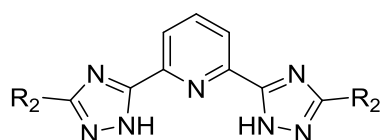
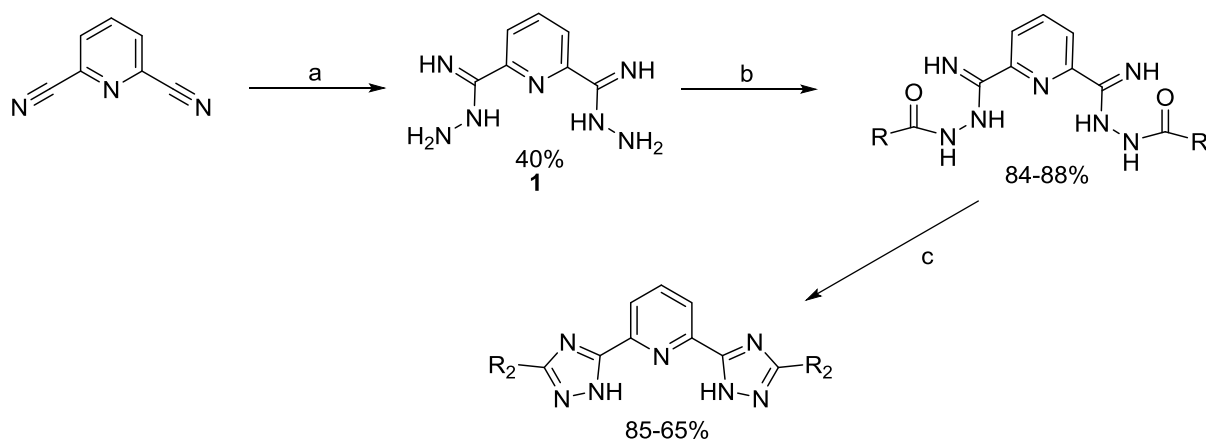


Figure 3.1. General chemical structure of the tridentate ligands studied in this chapter.  $R = CH_3, CF_3$ . When  $R = CF_3$  the ligand is named **pyC<sub>5</sub>-CF<sub>3</sub>-tzH<sub>2</sub>**.

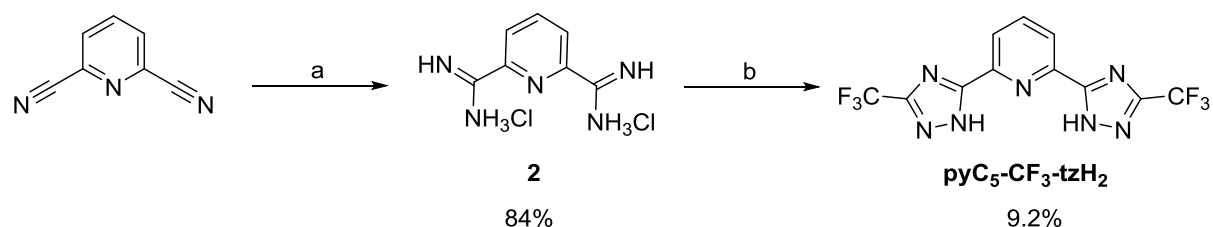
The synthesis of such type of ligands has been already reported by our group<sup>20</sup> and a general overview of this synthetic strategy is depicted in Scheme 3.1.



Scheme 3.1. General synthetic procedure for the tridentate ligands reported in literature<sup>20</sup>. a)  $NH_2NH_2 \cdot H_2O$ , EtOH, room temperature, overnight; b)  $RC(=O)Cl$ ,  $Na_2CO_3$ , DMF, 0 °C to room temperature, overnight; c) ethylene glycol, 180 °C, 2 hours.

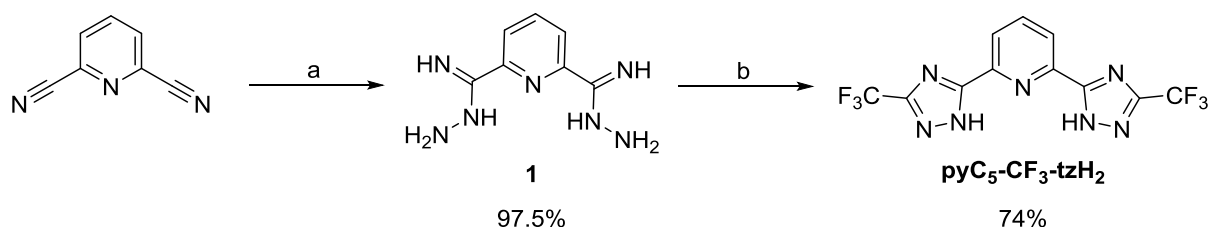
This synthetic strategy starts from the commercially available 2,6-pyridinebiscarbonitrile, pyridine-2,6-bis(carboximidhydrazide) (**1**) is then obtained upon reaction with hydrazine monohydrate in ethanol. This intermediate is first

condensed with the corresponding acyl chloride, either adamantanecarbonyl chloride or p-tolylcarbonyl chloride, directly leading to the 3-substituted 1,2,4-triazole precursors. The desired product is obtained through condensation reaction in ethylene glycol at 180 °C. This synthetic strategy is easy and straightforward and does not require any purification by chromatographic techniques leading to the final product in very good yield upon re-crystallization. Unfortunately, such strategy has not been found successful for the introduction of different moieties of interest such as CF<sub>3</sub> groups to yield ligand **pyC<sub>5</sub>-CF<sub>3</sub>-tzH<sub>2</sub>**. For this reason, a different synthetic strategy was employed and developed to achieve this purpose as shown in Scheme 3.2.<sup>21</sup>



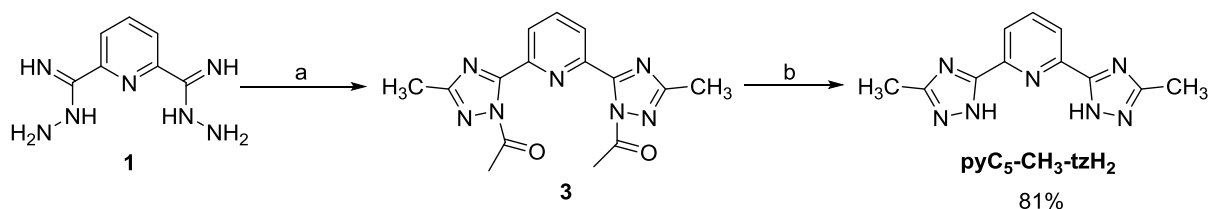
*Scheme 3.2. Synthetic pathway employed for ligand **pyC<sub>5</sub>-CF<sub>3</sub>-tzH<sub>2</sub>**. a) MeOH/MeONa, reflux, NH<sub>4</sub>Cl b) CF<sub>3</sub>COOEt, NH<sub>2</sub>NH<sub>2</sub>·H<sub>2</sub>O, THF, reflux.*

The synthetic strategy to afford **pyC<sub>5</sub>-CF<sub>3</sub>-tzH<sub>2</sub>** has been already reported in the literature and involves the synthesis of pyridine-2,6-bis(carboxamide) dihydrochloride **2** from the commercially available 2,6-pyridinedicarbonitrile (Scheme 3.2). **2** is then reacted in a three component condensation reaction with ethyl trifluoroacetate and hydrazine in the presence of sodium hydroxide in refluxing THF to afford **pyC<sub>5</sub>-CF<sub>3</sub>-tzH<sub>2</sub>**<sup>22,23</sup>. However, while the intermediate 2,6-bis(carboxamide) dihydrochloride **2** can be prepared in high yield without purification through chromatographic techniques, the condensation reaction is characterized by a very modest yield and the final product cannot be obtained in good quality without purification by chromatography techniques. Thus, the synthesis of **pyC<sub>5</sub>-CF<sub>3</sub>-tzH<sub>2</sub>** has been optimized as shown in Scheme 3.3.



*Scheme 3.3. New synthetic procedure for the tridentate ligand bearing CF<sub>3</sub> groups. a) NH<sub>2</sub>NH<sub>2</sub>·H<sub>2</sub>O, EtOH, room temperature, 3 days; b) Trifluoroacetic anhydride, diethylene glycol dimethyl ether, room temperature, 10 min then refluxed for 1 hour, aqueous HCl, 90 °C, overnight.*

In this modified synthetic strategy the yield of the intermediate pyridine-2,6-bis(carboximidhydrazide) **1** is almost quantitative upon optimization of the solvent and reagents ratio as well as reaction time when compared to the previously used procedure<sup>20</sup>. Further details can be found in the experimental section. By using this precursor, condensation reaction can be carried out by simply mixing the building block **1** with 2 equivalents of the desired anhydride followed by thermal treatment leading to acylation and ring closure without the need to isolate any intermediate. In particular, improvement in the condensation step was found when a water miscible and high boiling point solvent such as diethylene glycol dimethyl ether was used. The addition of water further induces precipitation of the desired product. However we have found that an acidic hydrolysis leads to an increase of both yield and purity which is probably due to the fact that a third condensation process can take place yielding to acylation of the triazole rings. A proof of this mechanism, which also allows an easy and straightforward synthesis of the methyl derivative, is depicted in Scheme 3.4.



*Scheme 3.4. Synthesis of the methyl derivate pyC<sub>5</sub>-CH<sub>3</sub>-tzH<sub>2</sub>. a) acetic anhydride, room temperature to 100 °C, overnight; b) H<sub>2</sub>O, aqueous HCl, 80 °C, overnight.*

This reaction can be carried out directly in acetic anhydride as solvent that act as both acylating and dehydrating agent and the diacylated product **3** can be precipitated upon addition of water. The cleavage of the triazole moieties can be performed in acidic aqueous media and the desired product can be isolated in high yield by filtration. The formation and the cleavage of the amide bonds on the triazole moieties can be monitored by  $^1\text{H-NMR}$  (Figure 3.2).

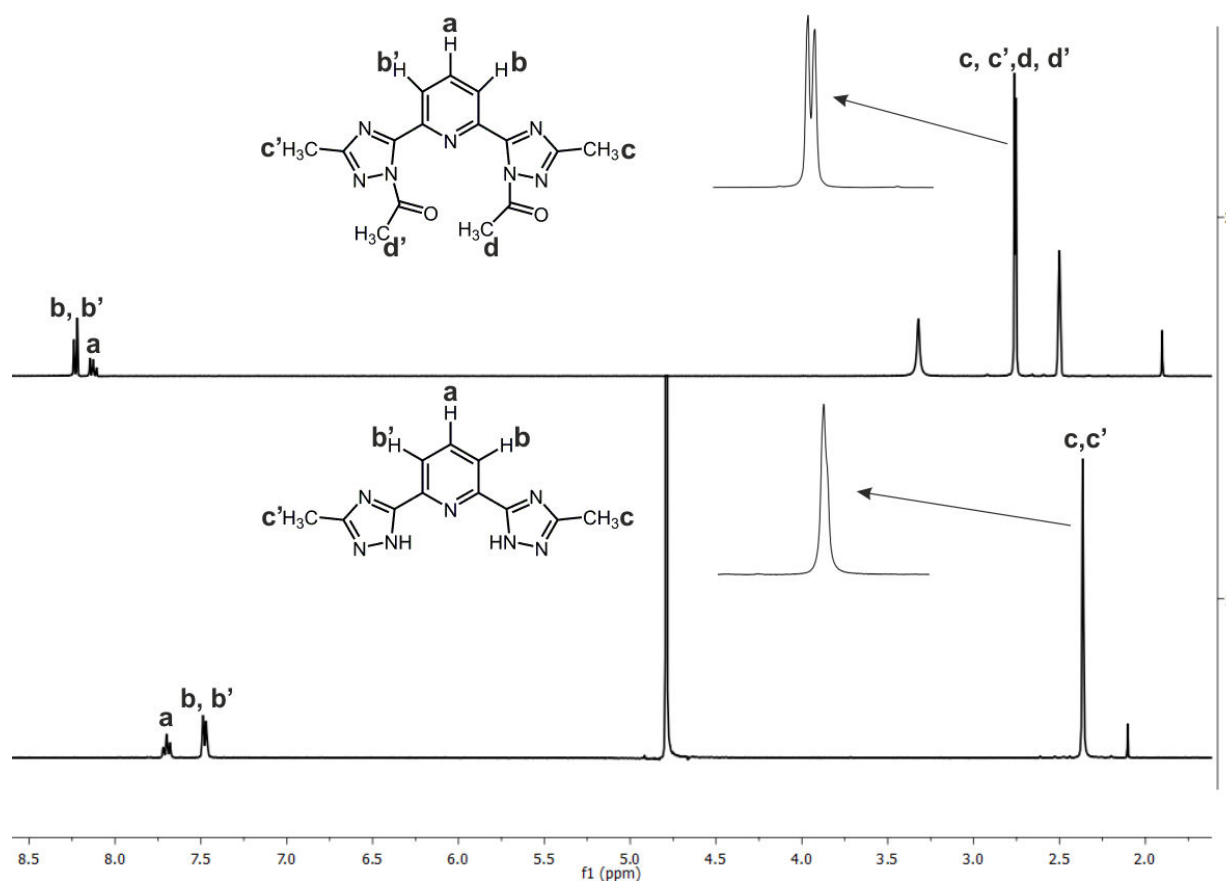
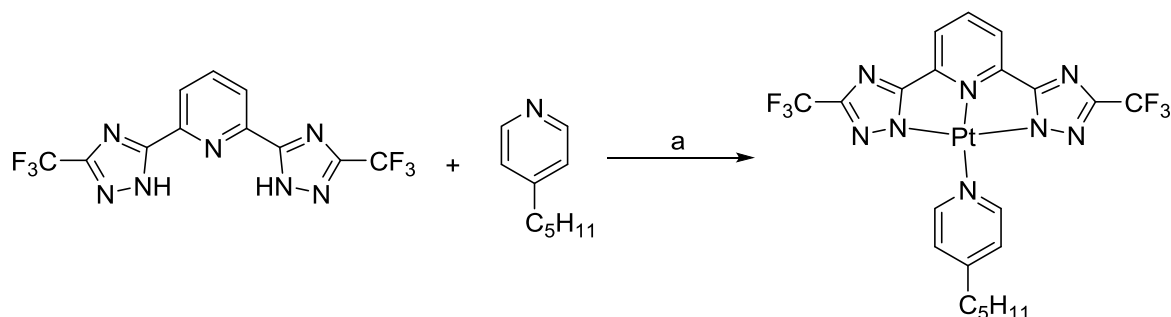


Figure 3.2. Comparison of the  $^1\text{H}$  NMR spectra of **3** (top), and **pyC<sub>5</sub>-CH<sub>3</sub>-trzH<sub>2</sub>** (bottom) in  $\text{DMSO-}d_6$  and  $\text{D}_2\text{O}$  respectively.

### 3.2.1.2 Synthesis of the platinum complexes

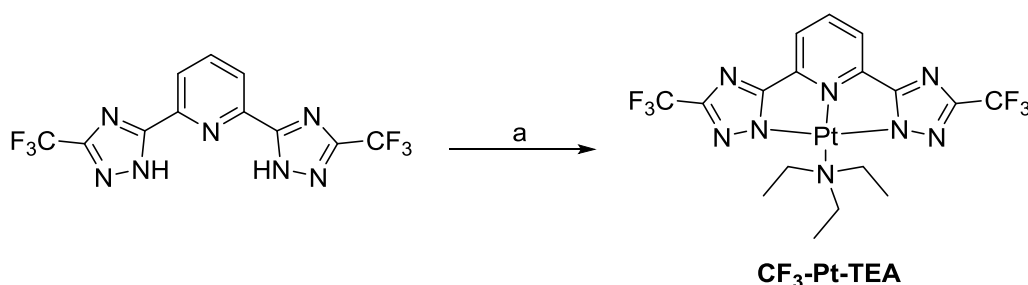
The general methodology to synthesize the complexes is described hereafter and it is in accordance to literature procedure previously reported by our group<sup>20</sup>. The general procedure for the complexation of this class of ligands consists in a one-pot reaction in which the tridentate ligand, a platinum precursor and an ancillary ligand, – the latter is generally a pyridine derivate – are partially dissolved in 2-methoxyethanol in

a 1:1.2:1-1.5 ratio, respectively, in presence of a base. The resulting mixture is then heated up from 50 to 85°C, depending on the ligands, under N<sub>2</sub> atmosphere. The synthesis of the complex **Pt-CF<sub>3</sub>tz-pyC<sub>5</sub>** is shown in Scheme 3.5.



*Scheme 3.5. Synthesis of complex **Pt-CF<sub>3</sub>tz-pyC<sub>5</sub>**. a) 2-methoxyethanol:H<sub>2</sub>O 3:1, diisopropylethylamine, 83 °C overnight, 75.5% yield.*

The choice of the Pt(II) source takes into account both solubility and reactivity and PtCl<sub>2</sub>(DMSO)<sub>2</sub> was employed according to literature<sup>13</sup>. At higher temperature and in presence of alcohol/water mixtures and/or strong bases such as alkoxide or hydroxyde salts, the formation of a black precipitate has been observed which is attributed due to the formation of metallic platinum. Upon reaction condition optimization, it turned out MeOH, ACN and CHCl<sub>3</sub> to be the better solvents than 2-methoxyethanol. Also, even if any mild base such as amines can be used, triethylamine (TEA) and N,N-diisopropylethylamine (DIPEA) were found to be the best choices. However, we have found that TEA can coordinate the metal center (Scheme 3.6) as demonstrated by single-crystal X-ray diffractometric analysis (Figure 3.3).



*Scheme 3.6. Synthesis of **CF<sub>3</sub>-Pt-TEA**. a) Pt(DMSO)<sub>2</sub>Cl<sub>2</sub>, TEA, CHCl<sub>3</sub>, reflux.*

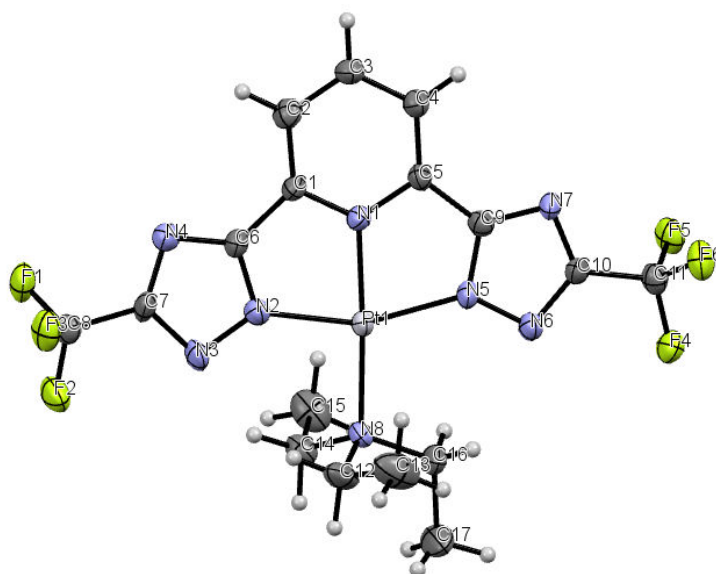


Figure 3.3. ORTEP diagram of complex **CF<sub>3</sub>-Pt-TEA** with thermal ellipsoids shown at 30% probability level with corresponding atom labelling. Selected bond lengths (Å) and angles (°): N(1)–Pt = 1.998(5), N(2)–Pt = 2.(6), N(5)–Pt = 2.025(6), N(8)–Pt = 2.107(5), N(1)–Pt– N(2) = 79.0(2), N(1)–Pt–N(5) = 79.1(2), N(2)–Pt–N(5) = 158.1(2), N(1)– Pt–N(8) = 178.4(2),. N(2)–Pt– N(8) = 102.5(2), N(5)–Pt– N(8) = 99.4(2).

### 3.2.2 Photophysical properties

The photophysical properties of complex **Pt-CF<sub>3</sub>tz-pyC<sub>5</sub>** have been investigated in both solution and solid state by means of steady-state and time-resolved techniques and the results are shown in Figure 3.4. In dilute (concentration  $5 \times 10^{-5}$  M) CHCl<sub>3</sub> solution at room temperature, the absorption spectrum of **Pt-CF<sub>3</sub>tz-pyC<sub>5</sub>** displays intense bands in the UV region ( $\lambda = 254$  nm,  $\epsilon = 2.3 \times 10^4$  M<sup>-1</sup> cm<sup>-1</sup>;  $\lambda = 302$  nm,  $\epsilon = 1.5 \times 10^4$  M<sup>-1</sup> cm<sup>-1</sup>; and  $\lambda = 337$  nm,  $\epsilon = 2.6 \times 10^3$  M<sup>-1</sup> cm<sup>-1</sup>). These transitions are mainly attributed to the intraligand (<sup>1</sup>IL) and metal-perturbed interligand charge transfer (<sup>1</sup>ILCT) states. At lower energy, a broad band in the region 350–450 nm ( $\epsilon$  ca.  $0.7 \times 10^3$  M<sup>-1</sup> cm<sup>-1</sup>) is ascribed to the admixture of spin-allowed metal-to-ligand charge transfer (<sup>1</sup>MLCT) and intra-ligand (<sup>1</sup>IL) transitions corresponding to the HOMO–LUMO excitation process, as supported by density functional calculations (data not shown). These assignments are further corroborated by the similarity with already reported Pt(II) complexes.<sup>20,24</sup> Upon photoirradiation a structured blue luminescence is observed, peaking at  $\lambda_{em} = 463, 493, 525$  and  $570$  (shoulder) nm, with a vibronical progression of  $1236$ – $1504$  cm<sup>-1</sup> attributable to the tridentate intraligand vibrational

modes. Such moderate (PLQY = 2%) luminescence is characterized by a very fast radiative decay, with a multi-exponential excited-state lifetime, being  $t_1 = 10$  ns (48%) and  $t_2 = 309$  ns (52%), that can be attributed to the  $T_1-S_0$  radiative transition with mainly metal-perturbed  $^3LC$  character.

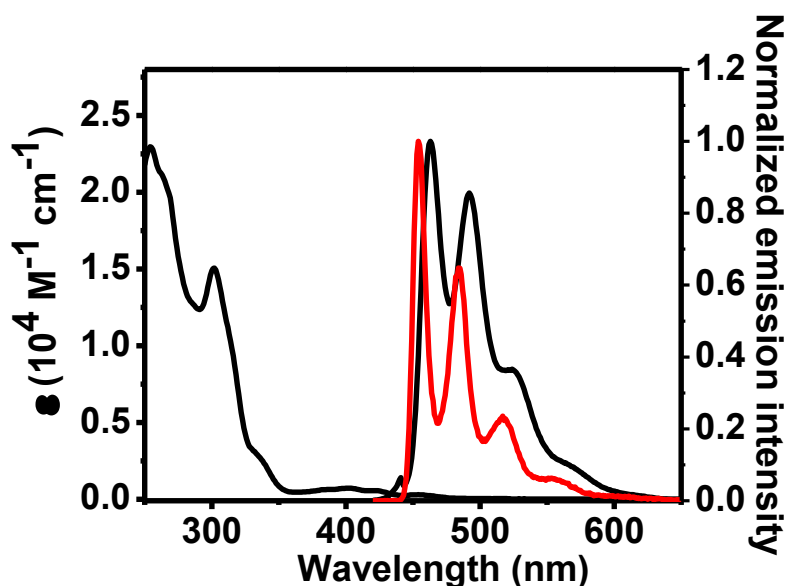


Figure 3.4. Absorption and emission spectra obtained for complex **Pt-CF<sub>3</sub>tz-pyC<sub>5</sub>** in CHCl<sub>3</sub> at room temperature (black traces) and at 77 K in 2-MeTHF glassy matrix (red trace).

Interestingly, the complex exhibits very different photo-physical behaviour in the solid state. In an attempt to crystallize the compound to obtain good quality single-crystals suitable for X-ray analysis, we have isolated yellow bright emissive microcrystalline fibers. The luminescent fibers, Figure 3.5, can be easily obtained when an acetone solution of **Pt-CF<sub>3</sub>tz-pyC<sub>5</sub>** is slowly concentrated by evaporation by drop-casting onto a quartz or glass substrate.

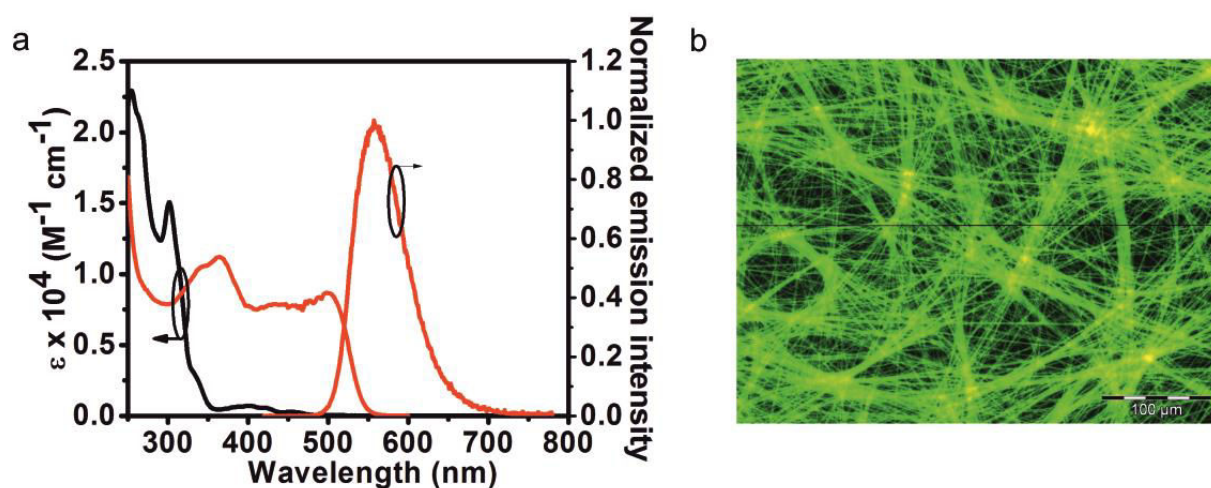


Figure 3.5. (a) Absorption and emission spectra obtained for complex **Pt-CF<sub>3</sub>tz-pyC<sub>5</sub>** in CHCl<sub>3</sub> at room temperature (black trace), excitation and emission ( $\lambda_{exc} = 300$  nm) spectra of the self-assembled fibers obtained from acetone at a concentration of 4 mg mL<sup>-1</sup> (red traces). Excitation spectrum was recorded at the maximum of the emission band. (b) The fluorescence microscopy image of the fibers obtained from acetone under irradiation at  $\lambda = 400$ –440 nm. Scale bar = 100  $\mu$ m.

Upon photo-irradiation with UV light, such discrete fibers showed intense and featureless emission centered at  $\lambda_{em,max} = 559$  nm with PLQY as high as 0.74. Such a great increase of the emission quantum yield is accompanied by a concomitant prolongation of the mono-exponential decay of the excited-state ( $\tau = 355$  ns). The sizeable bathochromic shift, the featureless emission profile, and the high emission quantum yield are already strong indications that the emissive state of the fibers is different from the luminescent state of the complex in solution. Furthermore, the outcome is not merely a rigidochromic effect since the nature of the emission is different.

It is well known that the square planar geometry of the compound can favor aggregate formation leading to Pt...Pt interactions, through the  $d_z^2$  orbitals of the metals that rise in energy and become the HOMO orbitals of the assemblies. As a consequence, the nature of the lowest electronic transitions can change from ligand centered to metal–metal ligand charge transfer, namely MMLCT.

The presence of such ground-state interaction through a strong coupling between the two platinum units is confirmed by the appearance of a lower energy band in the excitation spectrum of the fiber ( $\lambda = 501$  nm), as displayed in Figure 3.5a. The

electronic excitation transition involved has been ascribed as  $^1\text{MMLCT}$ . Excitation on this band, as well as in any other absorption band, leads to the yellow emission attributed to the radiative de-excitation of the triplet-manifold  $^3\text{MMLCT}$ . Furthermore, such metallophilic interactions are accounted to play a major role in the nanoscale organization and molecular propagation for the self-assembly of the **Pt-CF<sub>3</sub>tz-pyC<sub>5</sub>** complex, and in particular imparting the high directionality to the organization. Noteworthy, by investigating the emission with a fluorescence microscope equipped with a polarizer in the emission arm, it has been found that the intensity of the photoluminescence depends on the emission polarization angle.

### 3.2.3 Morphological characterization of the self-assembled fibers

Morphological and structural characterization of these Pt(II) aggregates has been performed by both scanning (SEM) and transmission electron microscopy (TEM) techniques and the results are shown in Figure 3.6.

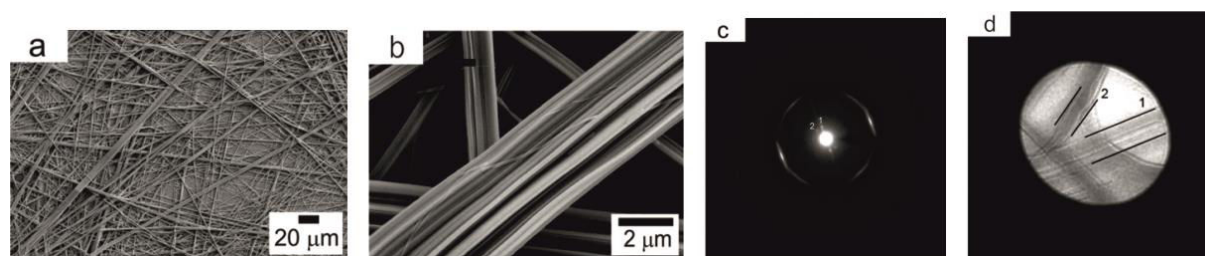


Figure 3.6. SEM images taken on a sample of fibers of complex **Pt-CF<sub>3</sub>tz-pyC<sub>5</sub>** obtained from acetone at a concentration of  $4 \text{ mg mL}^{-1}$  (a) and a zoom-in image (b); (c) the SAED pattern of a few fibers as shown in the corresponding shadow image (d).

As shown in the SEM images, the sample of the emissive soft-structures prepared from acetone (concentration  $4 \text{ mg mL}^{-1}$ ) is comprised of hundreds of micrometer long one-dimensional (1D) fibers. We hypothesize that such fibrous nanostructures is the result of a self-assembly process of thinner nanostructures such as nanofibrils. SEM analysis, however, could not give us any information on the packing and crystallinity of the assembly.

To explore the crystal structure of the Pt(II) aggregates prepared from acetone, selected area electron diffraction (SAED) patterns were acquired corresponding to a

local region with a few fibers present. In order to avoid damage of the crystal structure as a consequence of the electron beam, a very low dose rate was employed for the analysis (see experimental section for further details).

The morphology and orientation of the fibers contributing to electron diffraction were obtained by looking at the shadow image in the central disk of a strongly defocused diffraction pattern. Figure 3.6c–d show a representative diffraction pattern and the corresponding shadow image. In the diffraction pattern, two pairs of spots close to the central beam correspond to a lattice period of 1.33 nm.

The diffraction vectors are perpendicular to the two groups of fibers numbered in the shadow image, respectively. This indicates a periodic arrangement of the Pt complex alkyl chains perpendicular to the fiber long axis. In addition, strongly streaked diffraction spots corresponding to a lattice period of 3.44 Å were observed parallel to the fiber long axis. This lattice period is different from that obtained by X-ray scattering analysis and is most likely due to different sample preparation conditions required for the TEM analysis (lower concentration and fast evaporation rate). However, this periodicity can be attributed to the long-range order of the complex along the fiber axis.

The scattering pattern, obtained by SAXS/WAXS experiments, displays sharp peaks which confirms the high degree of long-range order within the self-assembled structures, as shown in Figure 3.7.

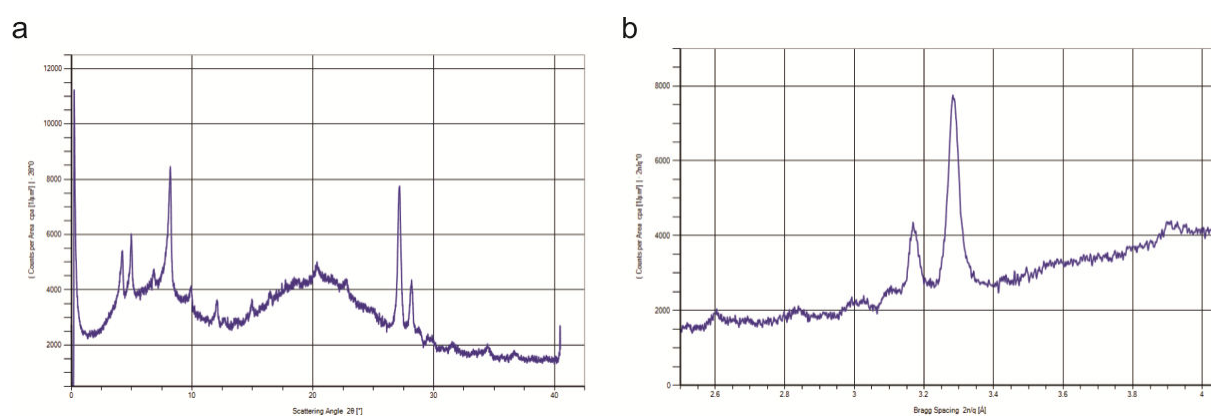


Figure 3.7. SAXS/WAXS pattern recorded as intensity [cps] vs. scattering angle  $2\theta$  [°] (a) and vs. Bragg spacing [Å] (b) on a drop-cast sample of fibers of complex **Pt-CF<sub>3</sub>tz-pyC<sub>5</sub>** obtained from acetone solution at concentration of  $4 \text{ mg mL}^{-1}$ .

Interestingly, it is possible to detect a scattering peak at 3.28 Å that can be most likely ascribed to the distance corresponding to  $d_z^2\pi \cdots d_z^2\pi$  intermolecular interaction leading to the strong bathochromic shift of the emission into the self-assembled fibers. As a result of this long-range order, light emission polarized parallel to the fiber growth axis is unambiguously observed.

### 3.2.4 Fluorescence anisotropy

In order to further characterize the properties of such luminescent fibers, several attempts to obtain fibers in an aligned fashion onto a substrate were carried out. This indeed represents a key-step for the characterization of the anisotropic features of the fibers as bulk material. In particular, alignment of the fibers has been successfully achieved by immersing a glass microscope slide into an acetone solution of **CF<sub>3</sub>tz-pyC<sub>5</sub>** complex and the solvent evaporated at room temperature. In this way, the platinum(II) fibers tend to grow aligned onto the glass surface following the direction of the air-solvent interface during solvent evaporation as shown in Figure 3.8a.

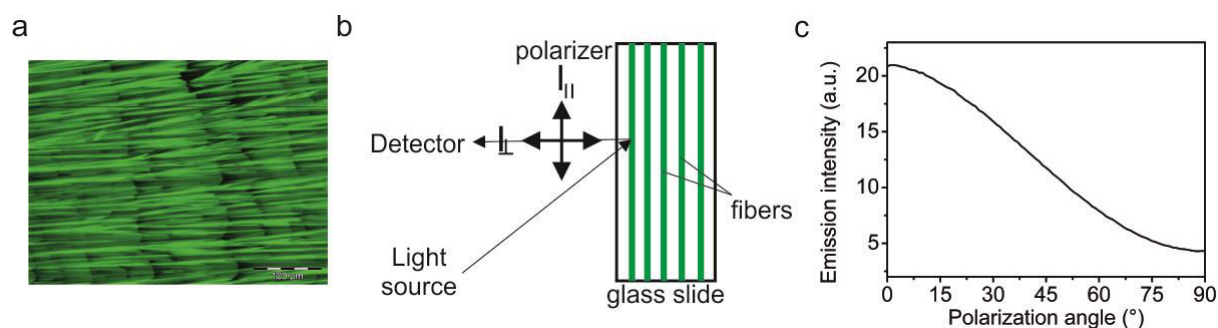


Figure 3.8. (a) The fluorescence microscopy image of the aligned fibers on the glass microscope slide under irradiation at  $\lambda = 400\text{--}440\text{ nm}$ . Scale bar = 100  $\mu\text{m}$ . (b) Schematic representation of the fluorescence anisotropy experiment performed on the aligned fibers. (c) Emission intensity recorded at  $\lambda_{em} = 555\text{ nm}$  upon variation of the emission polarization angle. The sample was excited by isotropic light source at  $\lambda_{exc} = 450\text{ nm}$ .

In this way anisotropy studies can be performed on the oriented fibers in order to elucidate the origin of such polarized emission and its correlation with the molecular packing and orientation within the fiber structure (Figure 3.8b). We found that the emitted light is maximized when the emission polarization is set parallel to the fiber long axis independently from wavelength and polarization angle of the excitation

source (Figure 3.8c). Such finding, along with the fact that the emission has a  $^3\text{MMLCT}$  nature, indicates that the radiative de-excitation process arises from a transition that is aligned along the fiber long axis on which also lies the Pt...Pt interactions.

More interestingly, anisotropy excitation spectra suggest that the transition dipole moment of the highest energy excitation band ( $^1\text{IL}/^1\text{ILCT}$ , 250-350 nm) is orthogonal with respect to the low energy lying excitation band ( $^1\text{MMLCT}$ , 350-530 nm), as shown in Figure 3.9b ( $I_{VV}$  and  $I_{HV}$ ).

Such orthogonal orientation of the lowest and highest energy band is further demonstrated by measuring the emission intensity profile upon variation of the excitation polarization angle at two different wavelengths, namely at  $\lambda_{\text{exc}} = 300$  nm for the IL/ILCT band and at  $\lambda_{\text{exc}} = 450$  nm for the MMLCT. The corresponding results are shown in Figure 3.9c.

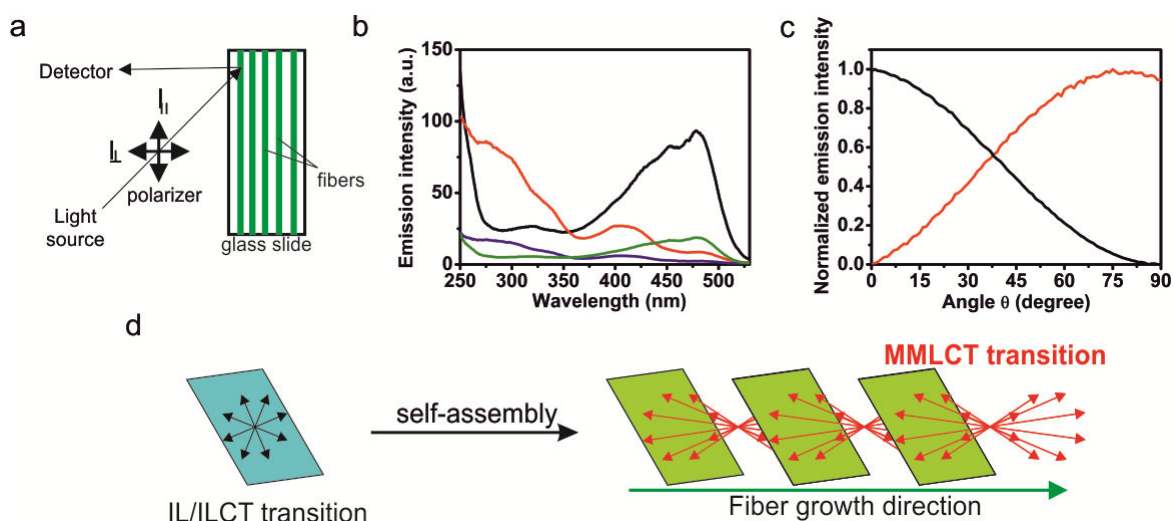


Figure 3.9. (a) Schematic representation of the fluorescence anisotropy experiment performed on the aligned fibers. (b) Excitation spectra ( $\lambda_{\text{em}} = 555$  nm),  $I_{VV}$  (black trace),  $I_{HV}$  (red trace),  $I_{HH}$  (blue trace),  $I_{VH}$  (green trace). (c) Normalized emission intensity profile recorded at  $\lambda_{\text{em}} = 555$  nm as a function of the excitation polarization angle upon irradiation at  $\lambda_{\text{exc}} = 450$  nm (black trace) and  $\lambda_{\text{exc}} = 300$  nm (red trace). (d) Schematic representation of the main electronic transition before and after self-assembly.

It is possible to observe that at  $\lambda = 300$  nm the maximum of the intensity is recorded when the polarizer is set at  $90^\circ$  – *i.e.*, perpendicularly to the fiber growth axis – while the minimum is recorded at  $0^\circ$  – *i.e.*, parallel to the fiber growth direction. On the

other hand, an opposite result is obtained by moving the excitation at 450 nm with maximum and minimum of the intensity recorded at 0° and 90°, respectively.

One should keep in mind that the MMLCT band is not present when the complex is molecularly dissolved, but it is formed upon self-assembly into fibers (Figure 3.5a) owing to  $d_z^2\pi \cdots d_z^2\pi$  intermolecular interactions between neighboring complexes.

On the basis of such findings and consideration, it is possible to conclude that the dipole moment of the MMLCT transition is thus oriented in such a way that lies onto the plane that contains the axial  $d_{z^2}\pi \cdots d_{z^2}\pi$  intermolecular interactions (the fiber growth axis). On the other hand, if we consider the transition at  $\lambda_{exc} = 300$  nm, also observed when the complex is molecularly dissolved, the associated transition dipole moment lies onto the molecular plane, which is oriented orthogonally with respect to the long fiber axis (Figure 3.9c).<sup>25,26</sup> The MMLCT band is indeed perpendicular to such plane and it follows that the square planar Pt(II) complexes pile on top of each other so the establishment of Pt $\cdots$ Pt metallophilic interaction provides high directionality to the fiber growth (Figure 3.9d).

### 3.3 Conclusion

The synthesis and characterization of a novel blue-emitting platinum(II) complex bearing a N<sup>N</sup>N pyridil-triazolate chromophoric ligand is reported. The compound shows a remarkable tendency to spontaneously assemble into highly ordered structures, such as fibers, through metal $\cdots$ metal and  $\pi$ - $\pi$  interactions.

The assemblies efficiently emit polarized yellow light with a remarkably high PLQY value of 74%, which might find application in polarized light-emitting devices and 3D OLED displays.

To gain insight onto the structural properties of the self-assembled structures SAED and SAXS/WAXS experiments were performed, which displayed an intermolecular distance of 3.44 and 3.28 Å, respectively, attributable to the  $d_z^2\pi \cdots d_z^2\pi$  interactions along the growth axis of the fibers.

Comprehensive steady-state fluorescence anisotropic measurements were carried out to elucidate the nature and orientation of the transition responsible of the

emission of the aligned fibers. Anisotropy measurements have clearly shown, for the first time, that the new electronic transition dipole moment, originated from the  $d_z^2\pi\cdots d_z^2\pi$  interactions, is indeed oriented along the fiber growth axis, while both wavelength- and polarization-dependent excitation and emission properties are observed and elucidated.

### 3.4 Experimental section

#### 3.4.1 Synthesis and characterization

All the reactions were carried out under inert atmosphere (Schlenk technique). All the solvents were used as received from Aldrich or Fluka without any further purification. 4-pentylpyridine was bought from TCI Europe. All the chemicals were purchased and used as received. The compounds were purified by column chromatography by using silica gel 60 (230–400 mesh) as stationary phase.  $^1\text{H}$ ,  $^{13}\text{C}$  and  $^{19}\text{F}$  NMR spectra were recorded on a Bruker Avance 400 spectrometer. The  $^1\text{H}$  NMR chemical shifts ( $\delta$ ) are given in ppm and referred to residual protons on the corresponding deuterated solvent. All deuterated solvents were used as received without any further purification. All coupling constants (J) are given in Hertz (Hz). Electrospray ionization mass (ESI-MS) spectra were recorded on a Bruker Daltonics (Bremen, Germany) MicroTof with loop injection. Elemental analyses were recorded by the analytical service of physical measurements and optical spectroscopy at the University of Strasbourg.

##### 3.4.1.1 Pyridine-2,6-bis(carboxamidinium) dihydrochloride (2)

In a 500 mL round bottom flask 2,6-dicarbonitrile (20.0 g, 154.9 mmol, 1.0 eq.) and MeONa (1.67 g, 30.98 mmol, 0.2 eq) were dissolved in 180 mL of dry methanol. After refluxing for 6 h, ammonium chloride (12.8 g, 340.8 mmol, 2.2 eq.) was added to the reaction mixture and kept overnight under reflux. After cooling, the solid was filtered over a Buchner, washed with  $\text{Et}_2\text{O}$ , dried and collected as pure compound (30.6 g, 130.2 mmol, yield 84.0%)  $^1\text{H}$  NMR (400 MHz,  $\text{D}_2\text{O}$ )  $\delta$ : 8.43 (m). HR-ESI-MS (m/z):  $[\text{M}-2\text{HCl}+\text{H}]^+$  calcd. 164.0933; found 164.0931.

#### **3.4.1.2 2,6-bis(3-(trifluoromethyl)-1H-1,2,4-triazol-5-yl)pyridine (pyC<sub>5</sub>-CF<sub>3</sub>-tzH<sub>2</sub>)**

In a 500 mL round-bottom flask, ethyltrifluoroacetate (13.7 mL, 114.4 mmol, 1.8 eq.) was dissolved in 150 mL of THF and hydrazine monohydrate (6.15 mL, 126.7 mmol, 2.0 eq.) was added. The reaction mixture was refluxed for 2 h, followed by the addition of pyridine-2,6-bis(carboximidine dihydrochloride (15.0 g, 63.5 mmol, 1 eq.) and sodium hydroxide (2.54 g, 63.5 mmol, 1 eq.). The reaction mixture was kept overnight refluxing under N<sub>2</sub>. After cooling, the desired product, pyC<sub>5</sub>-CF<sub>3</sub>-tzH<sub>2</sub>, was purified from the crude on column chromatography by using silica gel as stationary phase and dichloromethane and acetone 9:1 as eluent (2.04 g, 5.84 mmol, yield 9.2%). <sup>1</sup>H NMR (400 MHz, CD<sub>2</sub>Cl<sub>2</sub>) δ: 13.82 (2H), 8.21 (2H), 8.06 (1H); <sup>19</sup>F{<sup>1</sup>H} NMR (376 MHz, CD<sub>2</sub>Cl<sub>2</sub>, δ): -65.61 (6F). HR-ESI-MS (m/z): [M+Na]<sup>+</sup> calcd. 372.0395; found 372.0403.

#### **3.4.1.3 Pyridine-2,6-bis(carboximidhydrazide) (1)**

In a 500 mL round bottom flask 2,6-pyridinedicarbonitrile (10.0 g, 77.45 mmol) was dissolved in 200 mL of ethanol then 80 mL of hydrazine monohydrate were added and the flask closed with a rubber septum. The resulting solution was stirred for three days at room temperature. The solution was then filtered and the slightly yellowish solid washed with ethanol (50 mL) and dried. The compound was used without further purification. Yield 14.6 g (97.5%).

#### **3.4.1.4 2,6-bis(3-(trifluoromethyl)-1H-1,2,4-triazol-5-yl)pyridine (pyC<sub>5</sub>-CF<sub>3</sub>-tzH<sub>2</sub>) (Optimized version)**

Compound **1** (2.28 g, 11.8 mmol) was suspended in 25 mL of diethylene glycol dimethyl ether and sonicated until a fine white suspension was formed. Trifluoroacetic anhydride (3.6 mL, 26 mmol) was slowly added to the mixture at room temperature. Upon addition, the suspension dissolves and the solution turns yellow in color. The solution was stirred for ten minutes at room temperature then slowly heated up using a silicon oil bath until reflux. The progress of the reaction was

followed by TLC using acetone as the eluent and was complete within one hour from reflux. After cooling down to room temperature, 70 mL of distilled water followed by 2 mL of concentrated HCl were added and the mixture overnight heated at 90 °C. The solution was then cooled down to room temperature and stirred for additional two hours. The white precipitate was filtered and abundantly washed with water and petroleum ether, then dried overnight at 70 °C. The compound was used without further purification. Yield (3.0 g, 74.5%). <sup>1</sup>H NMR (acetone-*d*<sub>6</sub>, 400 MHz, ppm) δ: 8.33–8.40 (m); <sup>19</sup>F NMR (acetone-*d*<sub>6</sub>, 376 MHz, ppm) δ: 65.80 (s, CF<sub>3</sub>); <sup>13</sup>C NMR (acetone-*d*<sub>6</sub>, 100 MHz, ppm) δ: 156.42 (s), 156.04–154.88 (q, *J* = 39 Hz), 146.05 (s), 141.36 (s), 124.55–116.53 (q, *J* = 268 Hz), 123.82 (s). HR-ESI-MS (*m/z*): C<sub>11</sub>H<sub>5</sub>F<sub>6</sub>N<sub>7</sub>Na [M+Na]<sup>+</sup>, calcd. 372.040, found 372.035.

#### 3.4.1.5 2,6-bis(3-methyl-1H-1,2,4-triazol-5-yl)pyridine (pyC<sub>5</sub>-CH<sub>3</sub>-tzH<sub>2</sub>)

To a stirred solution of acetic anhydride (30 ml) in a 50 mL one neck round bottom flask, 2,6-bis(carboximidhydrazide)-pyridine (3 g; 15.5 mmol) was added slowly at room temperature. The resulting suspension was heated up to 100°C overnight and subsequently stirred for 24 hours at room temperature. The resulting precipitate was filtered and washed with water (20 ml). The filtrate was filtered again since more precipitate is formed and washed again until no more precipitate was formed (**3**). The resulting solid (**3**) was suspended in a mixture of EtOH/Water 1:1 (v/v; 100 mL) and few drops of HCl (37%) were added. The mixture was heated at 80°C overnight. Upon heating, the precipitate dissolved fully and the reaction mixture became transparent. The solvent was removed completely under vacuum. The residue was dissolved in a minimum amount of EtOH (few ml) and diethyl ether (excess) was added to precipitate the product. The solid formed was filtered off, washed with diethyl ether and dried in vacuo. The product was obtained as a white solid. Yield: 3.05 g; 12.6 mmol; 81.4 %. <sup>1</sup>H NMR (400 MHz, D<sub>2</sub>O) δ 7.47 (t, 1H, *J* = 7.6 Hz), 7.18 (d, 2H, *J* = 6.8 Hz), 2.25 (s, 6H) ppm. <sup>13</sup>C NMR (100 MHz, D<sub>2</sub>O): δ 155.01, 154.80, 143.98, 138.60, 120.88, 10.30. MS (*m/z*-ESI-MS): Found: 264.0957 [M+Na]<sup>+</sup>, calculated for [C<sub>11</sub>H<sub>11</sub>N<sub>7</sub>Na]<sup>+</sup>: 264.0968. Anal. Calcd for C<sub>11</sub>H<sub>11</sub>N<sub>7</sub>·2/3(H<sub>2</sub>O)·HCl: C, 45.60; H, 4.64; N,

33.84. Found: C, 45.41; H, 4.84; N, 33.58. (**3**)  $^1\text{H}$  NMR (400 MHz, DMSO- $d_6$ )  $\delta$  8.22 (d, 2H,  $J = 6$  Hz), 8.10 (t, 1H,  $J = 7.8$  Hz), 2.75 (d, 12H) ppm.

#### **3.4.1.6 Platinum [2,6-bis[5-(trifluoromethyl)-1,2,4-triazol-3-yl- $\kappa\text{N}^2$ ]pyridinato(2-)- $\kappa\text{N}$ ](4-pentylpyridine- $\kappa\text{N}$ ) (Pt-CF<sub>3</sub>tz-pyC<sub>5</sub>)**

In a 50 mL round-bottom flask, compound pyC<sub>5</sub>-CF<sub>3</sub>-tzH<sub>2</sub> (200.0 mg, 0.573 mmol, 1.5 eq.), PtCl<sub>2</sub>(DMSO)<sub>2</sub> (230.0 mg, 0.546 mmol, 1 eq.), 4-pentylpyridine (90.5  $\mu\text{L}$ , 0.546 mmol, 1.0 eq.) and 100  $\mu\text{L}$  of DIPEA were suspended in 20 mL of a 3:1 2-methoxyethanol:water. The reaction mixture was heated overnight at 83 °C under nitrogen atmosphere. A yellowish-green precipitate appeared few minutes after the heating. The desired compound (Pt-CF<sub>3</sub>tz-pyC<sub>5</sub>) was purified on column chromatography using silica gel as stationary phase and 1:1 THF:cyclohexane mixture as eluent, and obtained as greenish-yellow solid (285 mg, 0.412 mmol, yield 75.5%).  $^1\text{H}$  NMR (400 MHz, CD<sub>2</sub>Cl<sub>2</sub>, ppm)  $\delta$ : 9.38 (2H), 8.04 (1H), 7.75 (2H), 7.40 (2H), 2.76 (2H), 1.73 (2H), 1.38 (4H), 0.92 (3H);  $^{19}\text{F}\{^1\text{H}\}$  NMR (376 MHz, CH<sub>2</sub>Cl<sub>2</sub>)  $\delta$ : -64.78 (6F);  $^{13}\text{C}$  NMR (100 MHz, CD<sub>2</sub>Cl<sub>2</sub>)  $\delta$ : 164.61 (s), 157.63 (s), 153.08 (s), 149.26 (s), 143.70 (s), 126.93 (s), 118.77 (s), 35.81 (s), 31.77 (s), 29.91 (s), 22.90 (s), 14.21 (s). HR-ESI-MS (positive scan,  $m/z$ ):  $[\text{M}+\text{H}]^+$  calcd. 692.1280; found 692.1376 Elemental analysis calcd. for C<sub>21</sub>H<sub>18</sub>F<sub>6</sub>N<sub>8</sub>Pt C 36.48%, H 2.62%, N 16.20%, found C 36.88%, H 2.93%, N 15.85%.

#### **3.4.2 Fluorescence microscopy**

Fluorescence microscopy was performed with an Olympus BX51 microscope using a 20x objective and an Olympus U-MWBV BP 400–440 nm, dichroic 455 nm, and LP 475 nm as excitation and emission filter cubes, respectively; images and movies were recorded with a Olympus XC-10 color camera.

#### **3.4.3 Small-angle/Wide-angle X-ray Scattering (SAXS/WAXS)**

SAXS/WAXS measurements of samples were performed with SAXSess Small-angle X-Ray Scattering instrument (Anton Paar GmbH, Austria). The Kratky type camera is

attached to a laboratory X-Ray generator (PW3830, PANalytical), and was operated with a fine focus glass sealed X-Ray tube at 40 kV and 50 mA (Cu K $\alpha$ ,  $\lambda = 0.1542$  nm). Detection was performed with the 2D imaging plate and analyzed by an imaging plate reader Cyclone<sup>®</sup> (Perkin Elmer). Measurements were performed with standard solid sample holder for 30 min. The two-dimensional intensity data were converted to one-dimensional data with SASXQuant software (Anton Paar GmbH, Austria). The scattering intensities were corrected for background noise, detector efficiency, empty cell scattering and sample transmission, and were placed on an absolute scale using beam flux measurements. The samples were prepared by drop-cast technique of an acetone solution of the complex at concentration of 4 mg mL<sup>-1</sup> onto the sample holder. The solution was left aging overnight in order to allow the formation of the self-assembled fibers.

#### **3.4.4 Scanning electron microscopy (SEM)**

The SEM images on the fibers were recorded using a Zeiss 1540 EsB dual beam/field emission SEM with a working distance of 8 mm and an electronic high tension (EHT) of 3kV.

#### **3.4.5 Transmission electron microscopy (TEM)**

The TEM analyses were performed using an aberration (image) corrected FEI Titan 80-300 electron microscope at an accelerating voltage of 300 kV, with 50  $\mu$ m C2 condenser aperture and spot size 11 to reach a very low current density (150 e nm<sup>-2</sup> s<sup>-1</sup>). TEM and SAED patterns were acquired using a Gatan US1000 slowscan CCD camera. Samples for TEM analysis were prepared by deposition of the needles from organic suspension onto Quantifoil copper grids coated with holey carbon film and removing of the residual solvent after 30 sec. A series of 28 pairs of diffraction spots were also acquired on fibers prepared by using the same method employed for the photophysically characterized samples, and an average lattice spacing of  $3.44 \pm 0.02$  Å has been found.

### 3.5 References

- [1] D. M. Roundhill; H. B. Gray; C. M. Che, *Acc. Chem. Res.*, **1989**, *22*, 55-61.
- [2] P. Pyykkö, *Chem. Rev.*, **1997**, *97*, 597-636.
- [3] V. H. Houlding; V. M. Miskowski, *Coord. Chem. Rev.*, **1991**, *111*, 145-152.
- [4] S. Y.-L. Leung; W. H. Lam; V. W.-W. Yam, *Proc. Natl. Acad. Sci. U.S.A.*, **2013**, *110*, 7986-7991.
- [5] Y. Tanaka; K. Man-Chung Wong; V. Wing-Wah Yam, *Chem. Sci.*, **2012**, *3*, 1185-1191.
- [6] X. Zhang; B. Cao; E. J. Valente; T. K. Hollis, *Organometallics*, **2013**, *32*, 752-761.
- [7] V. N. Kozhevnikov; B. Donnio; D. W. Bruce, *Angew. Chem. Int. Ed.*, **2008**, *47*, 6286-6289.
- [8] M. Krikorian; S. Liu; T. M. Swager, *J. Am. Chem. Soc.*, **2014**, *136*, 2952-2955.
- [9] M.-Y. Yuen; V. A. L. Roy; W. Lu; S. C. F. Kui; G. S. M. Tong; M.-H. So; S. S.-Y. Chui; M. Muccini; J. Q. Ning; S. J. Xu; C.-M. Che, *Angew. Chem. Int. Ed.*, **2008**, *47*, 9895-9899.
- [10] W. Zhang; W. Jin; T. Fukushima; N. Ishii; T. Aida, *Angew. Chem. Int. Ed.*, **2009**, *48*, 4747-4750.
- [11] Y. Chen; K. Li; W. Lu; S. S.-Y. Chui; C.-W. Ma; C.-M. Che, *Angew. Chem. Int. Ed.*, **2009**, *48*, 9909-9913.
- [12] M. A. Daniele; S. H. North; J. Naciri; P. B. Howell; S. H. Foulger; F. S. Ligler; A. A. Adams, *Adv. Funct. Mater.*, **2013**, *23*, 698-704.
- [13] C. A. Strassert; C.-H. Chien; M. D. Galvez Lopez; D. Kourkoulos; D. Hertel; K. Meerholz; L. De Cola, *Angew. Chem. Int. Ed.*, **2011**, *50*, 946-950.
- [14] M. C.-L. Yeung; V. W.-W. Yam, *Chem. Sci.*, **2013**, *4*, 2928.
- [15] T. Masatsugu; Y. Takuma; A. Chihaya, *Appl. Phys. Express*, **2011**, *4*, 071602.
- [16] M.-Y. Yuen; V. a. L. Roy; W. Lu; S. C. F. Kui; G. S. M. Tong; M.-H. So; S. S.-Y. Chui; M. Muccini; J. Q. Ning; S. J. Xu; C.-M. Che, *Angew. Chem. Int. Ed.*, **2008**, *47*, 9895-9899.
- [17] L.-M. Huang; G.-M. Tu; Y. Chi; W.-Y. Hung; Y.-C. Song; M.-R. Tseng; P.-T. Chou; G.-H. Lee; K.-T. Wong; S.-H. Cheng; W.-S. Tsai, *J. Mater. Chem. C*, **2013**, *1*, 7582-7592.
- [18] C.-M. Che; C.-F. Chow; M.-Y. Yuen; V. A. L. Roy; W. Lu; Y. Chen; S. S.-Y. Chui; N. Zhu, *Chem. Sci.*, **2011**, *2*, 216-220.
- [19] M. Grell; D. D. C. Bradley, *Adv. Mater.*, **1999**, *11*, 895-905.
- [20] M. Mydlak; M. Mauro; F. Polo; M. Felicetti; J. Leonhardt; G. Diener; L. De Cola; C. A. Strassert, *Chem. Mater.*, **2011**, *23*, 3659-3667.
- [21] D. Septiadi; A. Aliprandi; M. Mauro; L. De Cola, *RSC Advances*, **2014**, *4*, 25709-25718.
- [22] K. Funabiki; N. Noma; G. Kuzuya; M. Matsui; K. Shibata, *J. Chem. Res., Synop.*, **1999**, 300-301.
- [23] X. Huixia; Y. Yan; Q. Litao; H. Yuying; W. Hua; C. Liuqing; X. Bingshe, *Dyes and Pigments*, **2013**, *99*, 67-73.
- [24] C. Cebrian; M. Mauro; D. Kourkoulos; P. Mercandelli; D. Hertel; K. Meerholz; C. A. Strassert; L. De Cola, *Adv. Mater.*, **2013**, *25*, 437-442.
- [25] *Principles of Fluorescence Spectroscopy*, ed. Springer, **2007**
- [26] *Molecular Fluorescence: Principles and Applications*, ed. Wiley, **2013**



# Chapter 4

## Chiral amplification by self-assembly of neutral platinum(II) complexes

**Abstract:** This chapter describes the synthesis and the characterizations of two novel enantiomerically pure chiral ligands and the corresponding Pt(II) complexes. The self-assembly properties have been characterized by different morphological and photophysical techniques. The two enantiomeric complexes show a tendency to self-assemble into chiral supramolecular aggregates with right (P) and left-handed (M) helical configuration, respectively, as proved by SEM and CD. The formation of such organized structures is driven by the formation of metallophilic and  $\pi$ - $\pi$  interactions between spatially close platinum complexes with an enhancement of the chiro-optical properties.

## 4.1 Introduction

The use of self-assembly in chemistry is a very powerful tool for the bottom-up preparation of systems and architectures that can mimic biological functions as well as to create nano-organized materials with superior properties than the single components or the bulk materials, with controlled spatial disposition and organization of molecules.<sup>1-3</sup> The concept of self-assembly is tightly engaged with biology and in particular with biological structures such as membranes, proteins, enzymes, and DNA, just to cite some.

It is possible to distinguish two levels of chirality. The first, at the molecular scale, which concerns atoms arranged in one unique fashion in the space due to the presence of a chiral center. The second, at the supramolecular level, which involves the nonsymmetric arrangement of molecules in a non-covalent assembly.<sup>4</sup> Hence, there is currently growing interest towards the preparation of synthetic chiral functional structures for application in asymmetric catalysis, molecular recognition, chiro-optical switches, optoelectronics, and sensing. Some examples of platinum complexes showing chiro-optical properties in solution have been reported, mostly focused on cycloplatinated helicenes<sup>5,6</sup>

In this chapter we describe the preparation of long-range, ordered, functional supramolecular chiral assemblies onto surfaces using the already described non-covalent  $\pi$ - $\pi$  and platinum...platinum interactions. The self-assembly properties of a series of charge-neutral platinum complexes forming highly luminescent, chiral supramolecular aggregates were investigated. They display very interesting chiro-optical properties,<sup>7-9</sup> making them very interesting for applications in chiro-optical switches<sup>10</sup> and polarized light-emitting devices such as 3D organic light-emitting diodes (3D OLEDs).<sup>11</sup>

To this purpose, we have synthesized two enantiomeric Pt(II) complexes in which the ancillary pyridine ligand has been functionalized with a chiral moiety to introduce just one asymmetric carbon atom.

The characterization of the formed chiral self-assembled solid-state structures has been performed using different steady-state and time-resolved photophysical

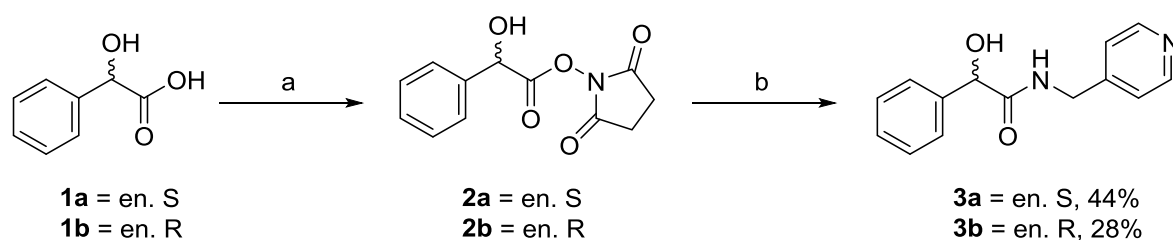
techniques, such as electronic absorption, steady-state and time-resolved luminescence, circular dichroism (CD), electron scanning microscopy (SEM) and fluorescent microscopy.

As it will be here described, the self-assembly of the luminescent complexes onto surfaces, driven by Pt...Pt interactions, led to the formation of a chiral supramolecular structure with enhanced chiro-optical properties.<sup>12</sup>

## 4.2 Result and discussion

### 4.2.1 Synthesis and characterization

The synthetic strategy employed for the preparation of two chiral pyridine derivatives is shown in Scheme 4.1.

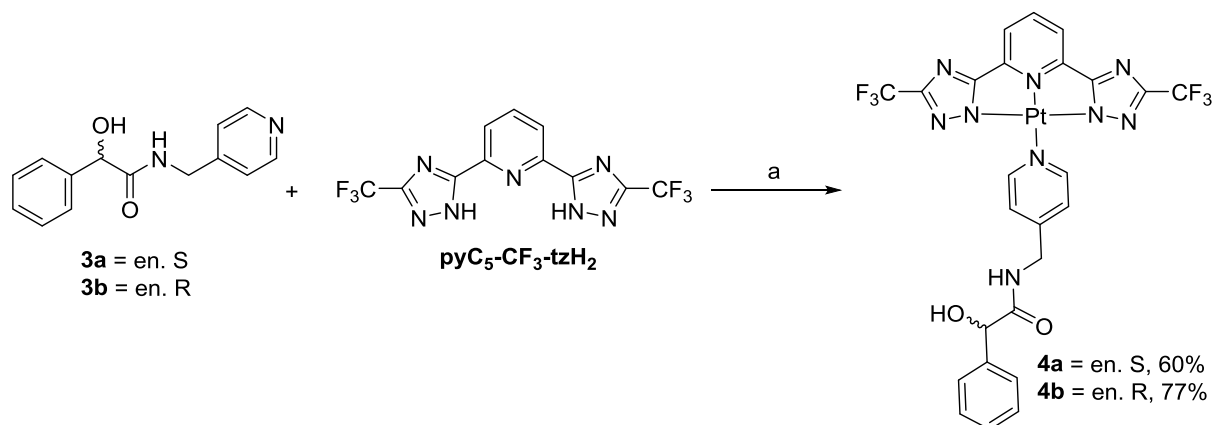


*Scheme 4.1. Synthesis of the chiral pyridine derivatives. (a) NHS, DCC, 1,4-dioxane, r.t, N<sub>2</sub>, overnight. (b) 4-Picolylamine, 1,4-dioxane, 50 °C, N<sub>2</sub>, overnight.*

The procedure we have used in this study starts from the synthesis of the chiral ancillary ligands, which is a derivate of the mandelic acid. We have decided to use mandelic acid because both enantiomers are commercially available as optically pure compounds, as well as to introduce moieties able to engage hydrogen bonding (C=ONH and OH) and  $\pi$ - $\pi$  stacking (benzyl ring). We expect that such interactions will provide a driving force for the chiral amplification at the supramolecular level.

Mandelic acid either S(-) or R(+), **1a** and **1b**, was priory activated by esterification with N-hydroxysuccinimide (NHS) in the presence of N,N'-dicyclohexylcarbodiimide (DCC) in 1,4-dioxane to give the corresponding succinimidyl esters **2a** and **2b**.<sup>13</sup> The reaction mixture was filtered in order to remove N,N'-dicyclohexylurea (DCU) and the obtained filtrate, **2a** and **2b**, was directly condensed with 4-picolylamine. The compound **3a** was purified by chromatographic techniques while compound **3b** was

purified by recrystallization from ethyl acetate. Both purification methods provide the desired product in good purity as proved by NMR, however the recrystallization method has lower yield (28% versus 44%). The complexation reaction is shown in Scheme 4.2.



Scheme 4.2. Synthesis of the Pt(II) complexes. (a)  $\text{PtCl}_2\text{DMSO}_2$ , TEA, MeOH,  $\text{N}_2$ , 8h, reflux.

The platinum(II) complexes were prepared, according to the general procedure discussed in chapter 3 by reacting  $\text{pyC}_5\text{-CF}_3\text{-tzH}_2$  with the prepared ancillary ligands (either **3a** or **3b**),  $\text{PtCl}_2(\text{DMSO})_2$  in refluxing methanol for 8 hours in presence of TEA as the base. A plentiful solid precipitated during the reaction which was washed several times with methanol to purify, finally isolating the complexes as yellow solids. All the prepared ligands and final complexes have been characterized by high-resolution mass spectrometry (HR-MS) and NMR spectroscopy. For both complexes the elemental analysis has been carried out as prove of purity. The complexes resulted to be poorly soluble in various organic solvents such as ethyl acetate, dichloromethane or chloroform. On the other hand, the complexes resulted to be slightly soluble in THF, thus this solvent has been used for NMR spectroscopy. Also, DMSO seemed to solubilize the compounds, yet giving badly resolved NMR spectra.

#### 4.2.2 Photophysical properties

The absorption spectra of both complexes **4a** and **4b** in THF solution at a  $5.1 \times 10^{-5}$  M concentration are presented in Figure 4.1. Upon irradiation with unpolarized light, these two enantiomers have as expected, the same spectroscopic properties due to

the fact that their different chirality (being enantiomers) has no effect on the absorption and the emission spectra.

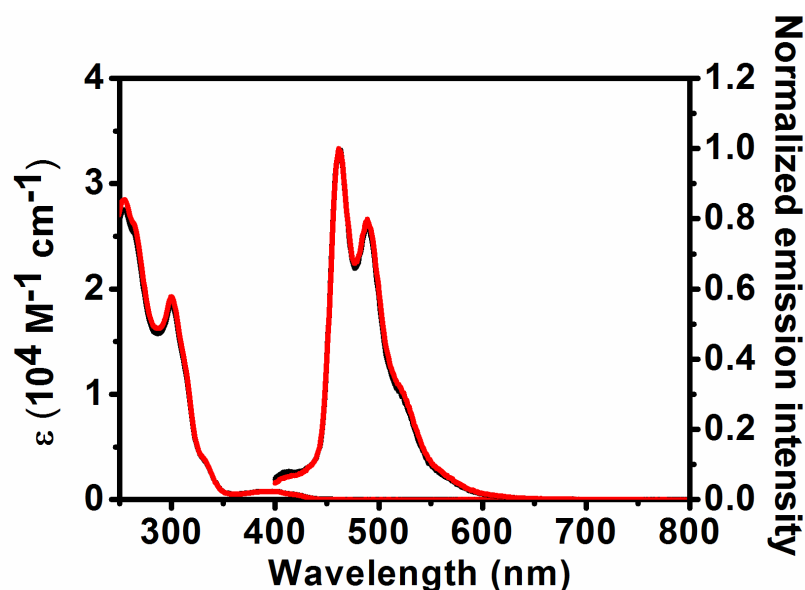


Figure 4.1. Absorption and emission spectra ( $\lambda_{exc} = 300$  nm) of **4a** (black line) and **4b** (red line) in THF at concentration  $5.1 \times 10^{-5}$  M.

As show in Figure 4.1, in dilute THF solution ( $5.1 \times 10^{-5}$  M) at room temperature, the absorption spectra displays intense bands in the UV region with  $\lambda_{max}$  abs 254 ( $\epsilon = 28451 \text{ M}^{-1} \text{ cm}^{-1}$ ), 300 ( $\lambda = 18706 \text{ M}^{-1} \text{ cm}^{-1}$ ) and 332 ( $\lambda = 3725 \text{ M}^{-1} \text{ cm}^{-1}$ ) nm attributed to singlet intraligand ( $^1\text{IL}$ ),  $\pi \rightarrow \pi^*$  of the tridentate ligand and metal-perturbed charge transfer transitions. A broad, featureless and weaker band ( $\epsilon = 784 \text{ M}^{-1} \text{ cm}^{-1}$ ) is observed in the region between 340–440 nm. It can be tentatively attributed to the HOMO  $\rightarrow$  LUMO transition and described as metal-to-ligand charge transfer ( $^1\text{MLCT}$ ) and intraligand ( $^1\text{IL}$ ) transition on the basis of other achiral and closely related reported complexes.<sup>14,15</sup>

Photoexcitation of **4a** and **4b** in THF solution ( $5.1 \times 10^{-5}$  M) at room temperature at any absorption band gave a structured blue emission with maximum at 462, 490 and 527 nm, with low intensity due to the fact that the measured PLQY was only 0.2%. Such low emission intensity was also accompanied by very short excited state lifetimes. Lifetime measurements showed a multi-exponential decay with  $\tau_1 = 2.8$  ns

(54%) and  $\tau_2 = 1.4$  ns (43%) for complex **4a**. Similar results have been obtained for the other enantiomer **4b**.

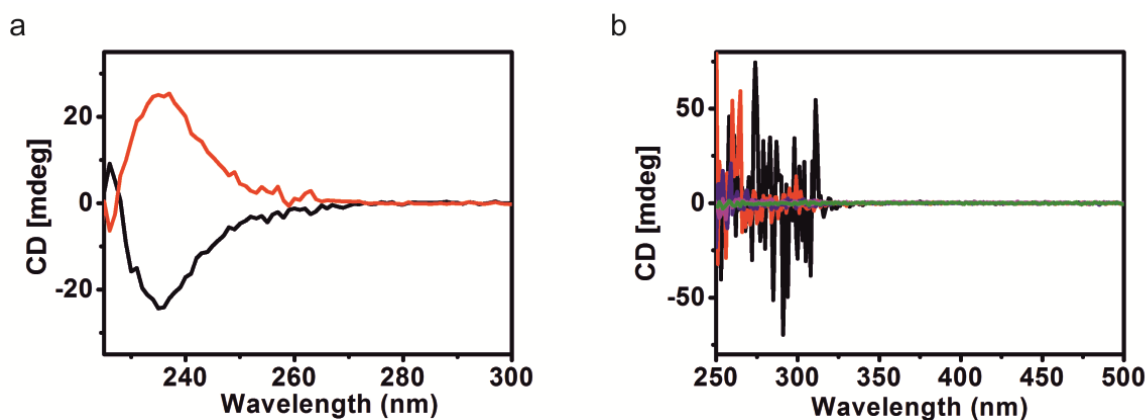


Figure 4.2. (a) CD spectra obtained for the ligands **3a** (black trace) and **3b** (red trace) in methanol solution at concentration of  $1.03 \times 10^{-3}$  M at room temperature; (b) CD spectra for the complex **4a** in THF solution (concentration range:  $2.78 \times 10^{-6}$  -  $4.00 \times 10^{-4}$  M) showing the absence of circular polarization of the light.

The circular dichroic (CD) spectrum gives us information about the chirality of the system. As expected, the chiral ligands **3a** and **3b** in MeOH solution ( $1.03 \times 10^{-3}$  M) give a clear signal and the resulting spectra are the mirror image of each other (Figure 4.2a). This finding demonstrates that the two ligands are enantiomers, confirming that the chirality, priority present in the starting corresponding mandelic acid (**1a** and **1b**) has been preserved during the synthesis process. We can thus expect that the chirality is also maintained for the complexes **4a** and **4b**.

The CD spectra of **4a** and **4b** have been recorded in THF solution. Surprisingly no CD signal was detected at any concentration in the range  $2.78 \times 10^{-6}$  -  $4.00 \times 10^{-4}$  M (Figure 4.2b). The absence of CD signal in solution can be explained by the origin of the transitions observed in the unpolarized absorption spectra of the two enantiomeric complexes (Figure 4.1). In the same region of the recorded CD spectra, the UV-Vis transitions are mainly due to the  $^1\text{LC}$  bands of the terdentate ligand, as well as, the MLCT and ILCT bands involving both the terdentate ligand and the heavy metal center. On such moieties there is no chirality present. In the same spectral region, only little contribution of the ancillary ligand to the absorption spectra can be expected. As a result the strength of the CD signal, which can be only caused by the

single asymmetric carbon of the mandelic acid moiety, is too weak if compared to the overall light absorption of the complex. The increase of the concentration is expected to increase the strength of the CD signal. However, the saturation of the detector occurs before detecting the CD signal.

Upon drop-casting a  $1.03 \text{ mg mL}^{-1}$  THF solution of either **4a** or **4b** onto quartz substrates, the compounds tend to aggregate into highly luminescent fibers (Figure 4.3b). Photoexcitation of such fibers yield an intense featureless emission broad band, which is now strongly bathochromically-shifted with a maximum at 560 nm with PLQY as high as 57% for **4a** and 37% for **4b** (Figure 4.3a).

In contrast with the THF solutions, samples of the self-organized fibers showed much longer excited state lifetimes with multi-exponential decays, where the longest components are 582 and 631 ns for **4a** and **4b**, respectively. The multi-exponential decay, as well as the different PLQY can be attributed to the absence of homogeneity of the samples.

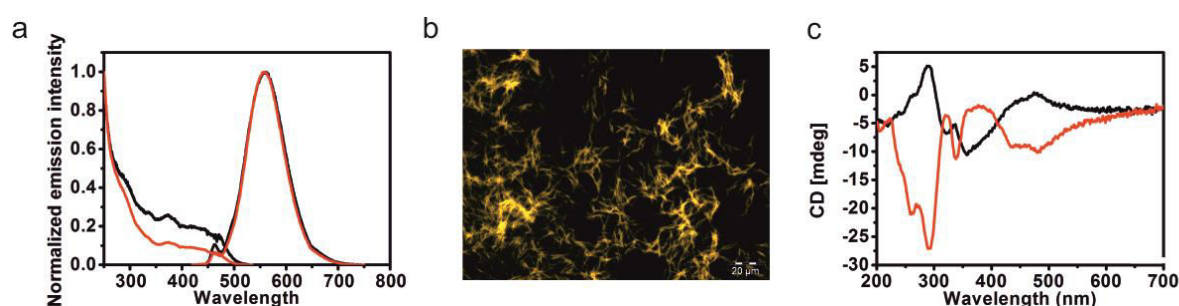


Figure 4.3. (a) Emission and excitation spectra obtained for the self-assembled fibers of **4a** (black trace) and **4b** (red trace) prepared by drop-casting onto a quartz substrate a  $1.03 \text{ mg mL}^{-1}$  THF solution.  $\lambda_{exc}$  and  $\lambda_{em}$  were 560 and 400 nm, for emission and excitation spectra, respectively. (b) Fluorescence microscopy images of the fibers obtained from **4b** as example upon irradiation at 400 - 440 nm and imaged with a long-pass emission filter at 455 nm. Scale bar = 20  $\mu\text{m}$ . (c) CD spectra obtained for the fibers made by complex **4a** (black line) and **4b** (red line).

The bathochromic shift in the emission profile and the higher PLQY are strong indications that the nature of the emitting excited state is most likely different from the luminescent excited state for the complexes in solution. The square planar geometry leads to the formation of Pt...Pt interactions, through the  $d_{z^2}$  orbitals of the metals that rise the energy of the HOMO orbitals upon assembling and lead the

lowest electronic transitions to become a triplet metal-metal to ligand charge transfer ( $^3\text{MMLCT}$ ).

The formation of such new excited state is also clearly visible looking at the excitation spectra recorded at  $\lambda_{\text{em}} = 560 \text{ nm}$ , which shows a strong bathochromic shift with respect to the absorption spectra of the solution. This shift is due to the formation of a new band with  $^1\text{MMLCT}$  character upon establishment of Pt...Pt interactions.

Noteworthy, when the CD spectra were recorded on samples of the self-organized fibers made by either **4a** or **4b**, a strong CD signal was detected as shown in Figure 4.3c. For the two enantiomers, such signal appears to be the mirror image, even though the intensity was not the same due to the fact that the amount of deposited fibers can be different. In contrast to the THF fluid solutions of **4a** and **4b**, mirrored CD spectra between the two enantiomers with maxima at 260, 290, 322, 337, 370, 472 nm can be observed in the aggregates. While the CD signals of the ancillary chiral ligands (Figure 4.2a) display a single peak and an onset at around 270 nm, the CD signal of the assembled fibers possess several bands with an onset at 580 nm (MMLCT band).

Such findings suggest that the asymmetric carbon located on the ancillary pyridine induces the formation of large chiral supramolecular architectures as shown in Figure 4.4.

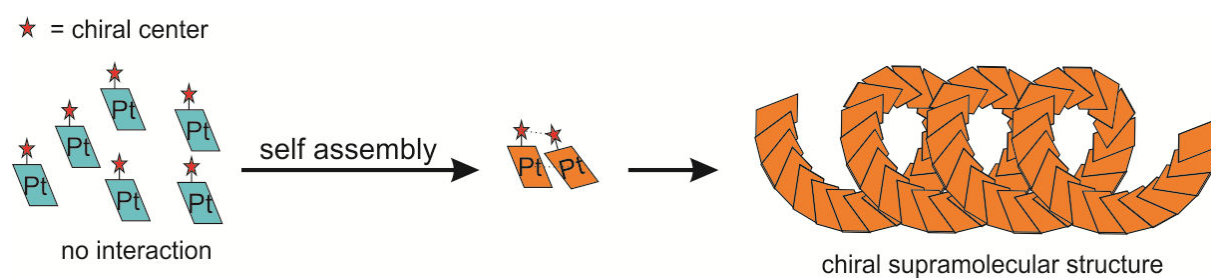


Figure 4.4. Schematic representation of the supramolecular self-assembly of the chiral Pt(II) complex.

### 4.2.3 Morphological characterization of the self-assembled fibers

To deeper explore the formation of these fibers, scanning electron microscopy (SEM) was performed on the self-assembled structures (Figure 4.5). The SEM analyses were performed on samples prepared from the same solution used for the other

characterizations ( $1.03 \text{ mg mL}^{-1}$  THF solution) onto a glass substrate sputtered with Au/Ag.

As shown in the images of the fibers for both complexes **4a** (Figure 4.5a-b) and **4b** (Figure 4.5c-d), the samples showed interconnected fibers with a clear helicity as a consequence of the supramolecular chiral organization of the complexes in the assemblies.

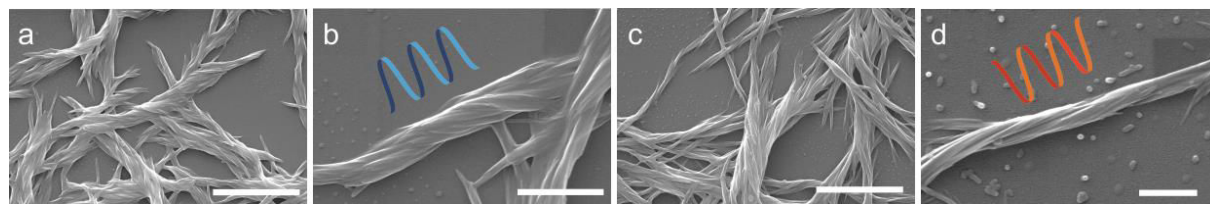


Figure 4.5. SEM images taken on samples of fibers of complex **4a** showing *P* configuration (a) scale bar =  $4 \mu\text{m}$  (b) scale bar =  $1 \mu\text{m}$  and **4b** complex showing *M* configuration (c) scale bar =  $4 \mu\text{m}$  (d) scale bar =  $500 \text{ nm}$ . All the samples were prepared from THF at concentration of  $1.03 \text{ mg mL}^{-1}$ .

In particular, complexes **4a** and **4b** aggregate in a clockwise and counterclockwise arrangement, respectively, yielding self-assembled aggregates with right-handed (*P*) and left-handed (*M*) helical configuration, respectively. We hypothesize that in both cases, the fibrous nanostructures are the result of the self-assembly of thinner nanostructures such as nanofibrils.

This observation clearly proves the formation of chiral supramolecular structures onto a substrate starting from the enantiomerically pure complexes prepared.

### 4.3 Conclusion

The synthesis and the characterizations of two novel enantiomerically pure Pt(II) complexes and their corresponding chiral ligands has been presented, and the compounds characterized by different morphological and photophysical techniques. The two enantiomeric complexes, **4a** and **4b**, show a tendency to self-assemble into chiral supramolecular aggregates with right (*P*) and left-handed (*M*) helical configuration, respectively, as proved by SEM and CD. Surprisingly, both complexes **4a** and **4b** did not show any detectable CD signal in solution at any concentration

investigated, while a huge enhancement of the CD signal was observed upon formation of self-assembled long-range organized fibers in the solid state. Photoluminescence investigation helped to demonstrate that the formation of such organized structures is driven by the formation of metallophilic and  $\pi$ - $\pi$  interactions among spatially close platinum complexes. These results represent the first examples of enhancement of the chiro-optical properties driven by metallophilic interactions in the solid state and can pave the way to design supramolecular chiral functional materials.

#### 4.4 Experimental section

##### 4.4.1 Synthesis and characterization

All chemicals were obtained from Sigma-Aldrich except for **pyC<sub>5</sub>-CF<sub>3</sub>-tzH<sub>2</sub>**, which was synthesized as described in chapter 3.

##### 4.4.1.1 S(+)-hydroxy-N-(4-pyridinylmethyl)-benzeneacetamide (3a)

S(+)-mandelic acid (1 eq., 1.011 g, 6.64 mmol) and NHS (1 eq., 757 mg, 6.58 mmol) were dissolved in 1,4-dioxane (20 ml) under nitrogen. DCC (1.358 g, 6.58 mmol) was added to the mixture at room temperature, and the mixture was stirred for 22 hours, then filtered. The filtrate was added on a two neck round bottom flask, then 1 eq. of 4-(aminomethyl)-pyridine (714 mg, 6.60 mmol) was added and the solution was stirred for 1.5 hours under nitrogen at 50 °C. Then the solvent was evaporated and then the crude product was purified by column chromatography over silica gel (SiO<sub>2</sub>, ethyl acetate/methanol: 97/3 then 95/5) to give the S(+)-hydroxy-N-(4-pyridinylmethyl)-benzeneacetamide as a white solid (704 mg, 2.90 mmol) in 44% yield. <sup>1</sup>H NMR (400 MHz, MeOD)  $\delta$  (ppm) : 8.41 (d, 2H), 7.50 (d, 2H), 7.35 (m, 3H), 7.27 (d, 2H), 5.11 (s, 1H), 4.47 (s, 2H). <sup>13</sup>C NMR (100 MHz, MeOD)  $\delta$  (ppm) = 149.98; 129.42; 129.17; 127.63; 123.75; 75.59; 42.51. ESI-TOF-MS (+) (m/z): [M + H]<sup>+</sup> calcd. 243.1128; found 243.1121.

#### 4.4.1.2 R(-)-hydroxy-N-(4-pyridinylmethyl)-benzeneacetamide (3b)

R(-)-mandelic acid (1 eq., 1.003 g, 6.59 mmol) and NHS (1 eq., 757 mg, 6.58 mmol) were dissolved in 1,4-dioxane (50 ml) under nitrogen. DCC (1.359 g, 6.59 mmol) was added to the mixture at room temperature, and the mixture was stirred for overnight, then filtered. The filtrate was added on a two neck round bottom flask, then 1 eq. of 4-(aminomethyl)-pyridine (722 mg, 6.68 mmol) was added and the solution was stirred overnight under nitrogen at 50 °C. The solution was dried and the crude solid was recrystallized from ethyl acetate to give the R(-)-hydroxy-N-(4-pyridinylmethyl)-benzeneacetamide as a white solid (450 mg, 1.86 mmol) in 28% yield. <sup>1</sup>H NMR (400 MHz, MeOD) δ (ppm) : 8.41 (d, 2H), 7.50 (d, 2H), 7.35 (m, 3H), 7.27 (2H), 5.11 (s, 1H), 4.47 (s, 2H). ESI-TOF-MS (+) (m/z): [M + H]<sup>+</sup> calcd. 243.1128; found 243.1105

#### 4.4.1.3 Platinum [2,6-bis[5-(trifluoromethyl)-1,2,4-triazol-3-yl-κN<sup>2</sup>]pyridinato(2-)-κN][S(+)-hydroxy-N-(4-pyridinylmethyl)-benzeneacetamide-κN] (4a)

In a 50 ml two necks round-bottom flask were added pyC<sub>5</sub>-CF<sub>3</sub>-tzH<sub>2</sub> (201 mg, 576 μmol), PtCl<sub>2</sub>(DMSO)<sub>2</sub> (246 mg, 583 μmol) and 20 mL of methanol under nitrogen. 160 μL of triethylamine was added to the mixture with a syringe, the mixture become yellow bright. Then S(+)-hydroxy-N-(4-pyridinylmethyl)-benzeneacetamide **3a** (142 mg, 586 μmol) was added and the mixture was heated to 66 °C for 6 hours . The mixture was filtrated and washed several time with methanol to give a yellow solid (347 mg, 442 μmol, yield 77%). <sup>1</sup>H NMR (400 MHz, THF-*d*<sub>8</sub>) δ (ppm) : 9.58 (br. d, 2H), 8.23 (t, 2H), 7.93 (d, 2H), 7.54 (t, 4H), 7.34-7.24 (m, 3H), 5.51 (d, 1H), 5.12 (d, 1H), 4.62-4.47 (dd, 2H). <sup>19</sup>F NMR (376 MHz, THF-*d*<sub>8</sub>) δ (ppm) : 65.14. ESI-TOF-MS(+) (m/z): [M + Na]<sup>+</sup> calcd. 807.0951; found 807.0855. Elemental Analysis Calcd. for C<sub>25</sub>H<sub>17</sub>O<sub>2</sub>N<sub>9</sub>F<sub>6</sub>Pt: C 38.27%, H 2.18%, N 16.07%. Found: C 38.20%, H 2.29%, N 16.10%.

#### 4.4.1.4 Platinum [2,6-bis[5-(trifluoromethyl)-1,2,4-triazol-3-yl-κN<sup>2</sup>]pyridinato(2-)-κN][R(-)-hydroxy-N-(4-pyridinylmethyl)-benzeneacetamide-κN] (**4b**)

In a 50 ml two necks round-bottom flask were added pyC<sub>5</sub>-CF<sub>3</sub>-tzH<sub>2</sub> (201 mg, 576 μmol), PtCl<sub>2</sub>(DMSO)<sub>2</sub> (246 mg, 583 μmol) and 20 mL of methanol under nitrogen. 160 μL of triethylamine was added to the mixture with a syringe, the mixture become yellow bright. Then R(-)-hydroxy-N-(4-pyridinylmethyl)-benzeneacetamide **3b** (142 mg, 586 μmol) was added and the mixture was heated to 66 °C for 6 hours . The mixture was filtrated and washed several time with methanol to give a yellow solid (347 mg, 442 μmol, yield 77%). <sup>1</sup>H NMR (400 MHz, THF-*d*<sub>8</sub>) δ (ppm) : 9.58 (br. d , 2H), 8.23 (t, 2H), 7.93 (d, 2H), 7.54 (t, 4H), 7.34-7.24 (m, 3H), 5.51 (d, 1H), 5.12 (d, 1H), 4.62-4.47 (dd, 2H). <sup>19</sup>F NMR (376 MHz, THF-*d*<sub>8</sub>) δ (ppm): 65.14. ESI-TOF-MS(+) (m/z): [M + Na]<sup>+</sup> calcd. 807.0951; found 807.0855 Elemental Analysis. Calcd for C<sub>25</sub>H<sub>17</sub>O<sub>2</sub>N<sub>9</sub>F<sub>6</sub>Pt: C 38.27%, H 2.18%, N 16.07%. Found: C 38.20%, H 2.29%, N 16.10%.

#### 4.4.2 SEM analysis

SEM characterization was performed employing a FEI scanning electron microscope Quanta FEG 250, at an acceleration voltage of 10 kV. Samples were prepared by drop-casting a THF solution onto a glass slide, and subsequent plasma-induced deposition of a 5 nm thick layer of Au.

#### 4.4.3 Emission microscopy

Fluorescence microscopy was performed with an Olympus BX51 microscope using a 20x objective and an Olympus U-MWBV BP 400–440 nm, dichroic 455 nm, and LP 475 nm as excitation and emission filter cubes, respectively; images and movies were recorded with a Olympus XC-10 color camera.

#### 4.4.4 Photophysical measurements

Absorption spectra were measured on a Shimadzu UV-3600 spectrophotometer double-beam UV–VIS–NIR spectrometer and baseline corrected. Steady-state emission spectra were recorded on a Horiba Jobin–Yvon IBH FL-322 Fluorolog 3

spectrometer (see chapter 2). Time-resolved measurements were performed on a PicoQuant FluoTime 300 (PicoQuant GmbH, Germany). Circular dichroic experiments were performed on Jasco J-810. Photoluminescence quantum yield measurements (PLQY) in solution were recorded at a fixed excitation wavelength ( $\lambda_{\text{exc}} = 400 \text{ nm}$ ) using a Hamamatsu Photonics absolute PLQY measurement Quantaaurus.

#### 4.5 References

- [1] J.-M. Lehn, *Angew. Chem. Int. Ed. Engl.*, **1990**, *29*, 1304-1319.
- [2] G. M. Whitesides; B. Grzybowski, *Science*, **2002**, *295*, 2418-2421.
- [3] D. N. Reinhoudt; M. Crego-Calama, *Science*, **2002**, *295*, 2403-2407.
- [4] M. A. Mateos-Timoneda; M. Crego-Calama; D. N. Reinhoudt, *Chem. Soc. Rev.*, **2004**, *33*, 363-372.
- [5] C. Shen; E. Anger; M. Srebro; N. Vanthuyne; K. K. Deol; T. D. Jefferson; G. Muller; J. A. G. Williams; L. Toupet; C. Roussel; J. Autschbach; R. Reau; J. Crassous, *Chem. Sci.*, **2014**, *5*, 1915-1927.
- [6] L. Norel; M. Rudolph; N. Vanthuyne; J. A. G. Williams; C. Lescop; C. Roussel; J. Autschbach; J. Crassous; R. Réau, *Angew. Chem. Int. Ed. Engl.*, **2010**, *122*, 103-106.
- [7] Y. Wang; J. Xu; Y. Wang; H. Chen, *Chem. Soc. Rev.*, **2013**, *42*, 2930-2962.
- [8] F. Garcia; L. Sanchez, *J. Am. Chem. Soc.*, **2012**, *134*, 734-742.
- [9] F. Aparicio; F. Vicente; L. Sanchez, *Chem. Commun.*, **2010**, *46*, 8356-8358.
- [10] P. Guo; L. Zhang; M. Liu, *Adv. Mater.*, **2006**, *18*, 177-180.
- [11] M. Grell; D. D. C. Bradley, *Adv. Mater.*, **1999**, *11*, 895-905.
- [12] M. J. Mayoral; C. Rest; V. Stepanenko; J. Schellheimer; R. Q. Albuquerque; G. Fernández, *J. Am. Chem. Soc.*, **2013**, *135*, 2148-2151.
- [13] J. P. Ley; H.-J. Bertram, *Tetrahedron*, **2001**, *57*, 1277-1282.
- [14] M. Mydlak; M. Mauro; F. Polo; M. Felicetti; J. Leonhardt; G. Diener; L. De Cola; C. A. Strassert, *Chem. Mater.*, **2011**, *23*, 3659-3667.
- [15] M. Mauro; A. Aliprandi; C. Cebrian; D. Wang; C. Kübel; L. De Cola, *Chem. Commun.*, **2014**, *50*, 7269-7272.



# Chapter 5

## Controlling and imaging biomimetic self-assembly processes

**Abstract:** This chapter describes the synthesis of an amphiphilic Pt(II) compound and its self-assembly properties in different solvent mixtures. We have found a complex system comprising with three different self-assembly process. The full chemical management of such complex landscape is successfully achieved by the proper use of supramolecular and photochemical approaches. The monitoring of the different emission properties, used as fingerprint for each of the assembled species, allowed an unprecedented real-time visualization of the evolving self-assemblies. Finally, preliminary results on the role of the molecular design on the self-assembly processes are shown.

## 5.1 Introduction

Supramolecular chemistry represents a powerful tool for the creation of large functional complex architectures.<sup>1-7</sup> The driving force for creating self-assembled objects stems from the ability of small and discrete entities to spontaneously arrange into more organized systems by establishing reversible dynamic interactions and using chemically-encoded information.<sup>8,9</sup> Such approach is ubiquitous in nature, where it allows efficient synthesis of complex biological structures out of their thermodynamic equilibrium. Initial studies on self-assembly focused on thermodynamic control of the reversible bonds formation to create defined supramolecular architectures with possibility of inherent error correction.<sup>1-9</sup> However, organic and biological chemistry has clearly shown that both thermodynamic and kinetic controls are essential for accessing a wider range of chemical species.<sup>10</sup> The ability of managing such complex pathways in supramolecular chemistry opens the possibilities to prepare out-of-equilibrium self-assembled functional nanostructures with different morphologies and properties.<sup>11-16</sup> In this respect, Meijer and co-workers<sup>16</sup> recently reported on the control of helicity of synthetic supramolecular polymers by controlling both thermodynamic and kinetic aggregation pathway. Remarkably, the conversion of kinetic structures into the thermodynamic assembly mimics biological infection processes, it resemble. It resemble, indeed, the nucleation-elongation mechanisms observed in misfolded proteins, such as amyloid- $\beta$ , responsible of several neurodegenerative diseases.<sup>17</sup> Such findings inspired the work of Takeuchi *et al.*<sup>18</sup> that reported an example of living supramolecular polymerization. By studying the assembly phenomenon involving the monomers and the analogies with conventional chain growth polymerization, they were able to synthesize supramolecular polymers with controlled length and narrow polydispersity. However, unravelling complex dynamics involving more than two different assemblies is still a challenge to date. Furthermore, real-time visualization of these interlocked events has never been reported.

Herein, we demonstrate the possibility of comprehensively control the self-assembling processes of a platinum(II) complex in a complex supramolecular system. Recently, we have reported a class of luminescent neutral platinum(II) complexes able to self-assemble into highly emissive species.<sup>19,20</sup> In these compounds, establishment of highly directional metallophilic interactions between neighbor molecules, also supported by face-to-face  $\pi$ - $\pi$  stacking, induces dramatic changes in the electronic spectroscopic properties.<sup>19-25</sup> As a consequence of the  $d_z^2$  interaction new molecular orbitals are formed leading to metal-metal-to-ligand charge transfer (MMLCT) states. In particular, the larger is the Pt...Pt interaction (distances in the range 3.0–3.5 Å) the more bathochromically shifted is the MMLCT bands. We use the modulation of such metallophilic interaction, and therefore of the emitting <sup>3</sup>MMLCT state energy, to probe the evolution of complex supramolecular processes.

In this work, the studied complex is an amphiphilic luminescent square-planar platinum(II) complex able to self-assemble through different aggregation pathways leading to the formation of two distinct metastable assemblies, **A** and **B**, and a stable isoform **C** (Figure 5.1).

Taking advantage of its luminescent properties, we unravel the self-assembling processes visualizing them in real-time, by following the concomitant changes of photophysical properties with the associated self-assembled arrangements. Noteworthy, deep understanding of the system allows us to selectively entrap each of the kinetic species **A** and **B**. Moreover, we achieve size control of the aggregates by seeded growth under living supramolecular polymerization condition.

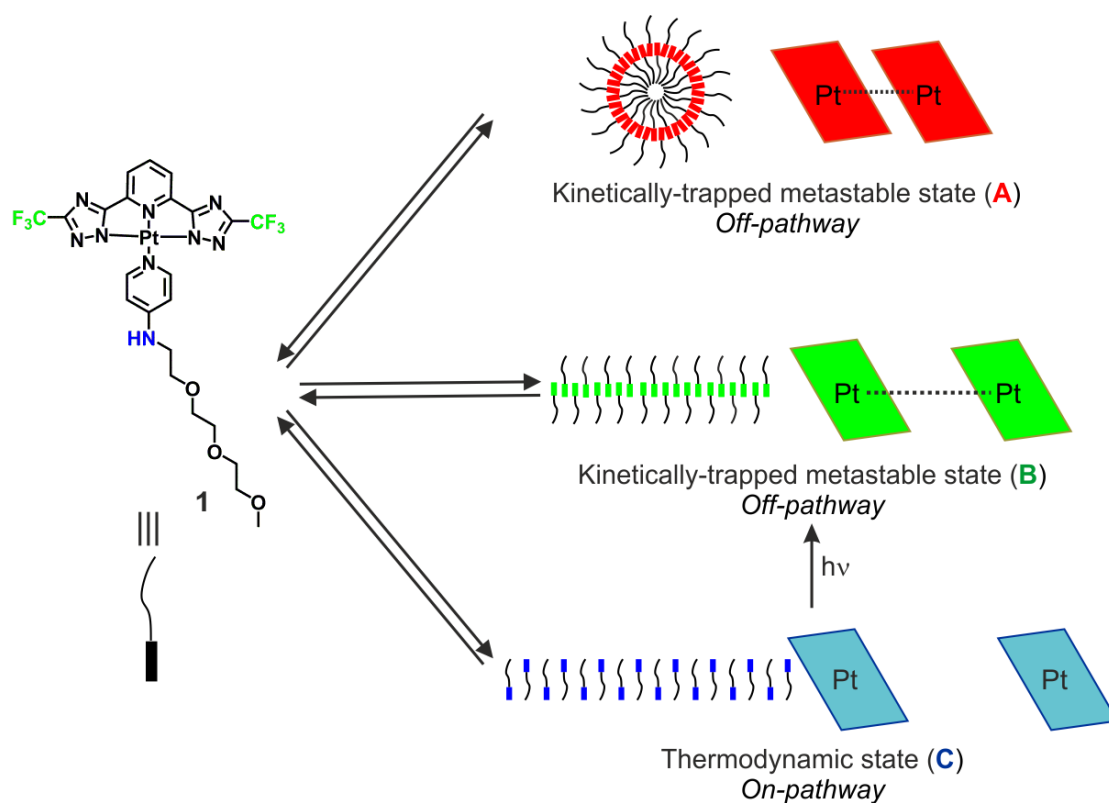


Figure 5.1. Chemical formula of the platinum(II) complex **1** and landscape of its supramolecular self-assemblies **A**, **B**, and **C** in dynamic equilibrium with the monomeric form. It is important to note that the Pt-Pt interaction decreases going from **A** to **B** and it is not present in **C**. A schematic representation of the assemblies is also shown to summarize the processes.

## 5.2 Result and discussion

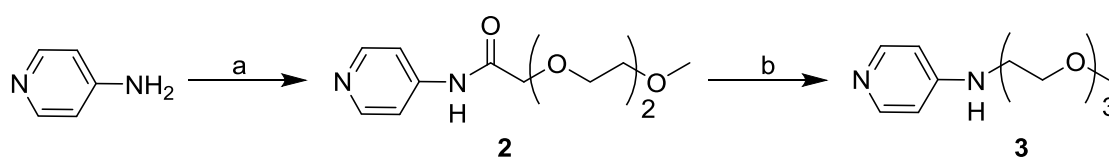
### 5.2.1 Synthesis and characterization

Pt(II) complexes with tridentate ligand bearing two triazole or tetrazole have been deeply studied in the literature thanks to their very interesting photophysical properties.<sup>19</sup> However they suffer of the drawback of poor solubilities. In order to overcome this issue without influencing the photophysical properties the only possible strategy is to modify the ancillary ligand. Aiming to maintain the pyridine motifs for stability issues, we have designed a straightforward way to introduce linear or branched glycol chains in the system. A judicious design of these moieties allowed us to prepare systems able to engage directional hydrogen bonds (such as NH).

In particular, we chose the 4-amino pyridine as substrate and a hydrophilic triethylene glycol pendant as chain. Also this is useful to increase the amphiphilic character of the molecule and play an important role in the self-assembly. Depending

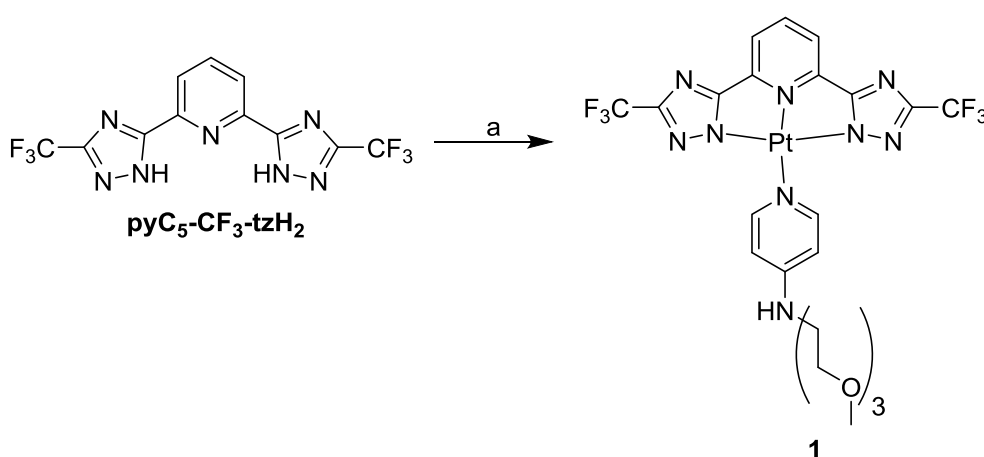
on the experimental condition (solvent, temperature, ionic strength, etc.) the interplay between the hydrophobic and hydrophilic is expected to lead different self-assembly behaviors.

The synthesis of the ancillary ligand is depicted in Scheme 5.1. The first step consist in the condensation of 2-[2-(2-methoxyethoxy)ethoxy]acetic with 4-amino pyridine in the presence of a coupling agent such as dicyclohexylcarbodiimide (DCC). The reduction of the resulting amide into amine was performed in order to avoid a possible hydrolysis and increase stability.



*Scheme 5.1. Synthesis of the ancillary ligand. a) 2-[2-(2-methoxyethoxy)ethoxy]acetic acid, DCC,  $\text{CHCl}_3$ , reflux overnight. b)  $\text{LiAlH}_4$ , THF,  $0^\circ\text{C}$  to room temperature overnight.*

The platinum complex **1** was synthesized as shown in Scheme 5.2 using  $\text{PtCl}_2(\text{DMSO})_2$  as a platinum source and **pyC<sub>5</sub>-CF<sub>3</sub>-tzH<sub>2</sub>** in presence of triethylamine (TEA) in ACN at  $60^\circ\text{C}$  under nitrogen atmosphere. After flash chromatography purification, the desired complex was obtained in modest yield (37%).



*Scheme 5.2. Synthesis of the platinum complex 1. a)  $\text{PtCl}_2(\text{DMSO})_2$ , TEA,  $\text{CH}_3\text{CN}$ ,  $60^\circ\text{C}$  (Yield 37%).*



PtCl<sub>2</sub>(DMSO)<sub>2</sub>, the terdentate ligand (either **pyC<sub>5</sub>-CF<sub>3</sub>-tzH<sub>2</sub>** or **pyC<sub>5</sub>-tolyl-tzH<sub>2</sub>**),<sup>19</sup> the ancillary ligand and 2 equivalents of TEA in refluxing MeOH overnight under inert atmosphere (see experimental section).

### 5.2.2 Photohysical properties

In order to gain deeper insights onto the self-assembling properties of such derivative in solvent/non-solvent mixtures we undertook a systematic study and chose 1,4-dioxane:H<sub>2</sub>O as solvent mixtures due to the following considerations:

- i)* monomer **1** is well solubilized by 1,4-dioxane, thus allowing us to study the system over a larger range of concentrations;
- ii)* the miscibility of the two solvents is complete at any desired ratio;
- iii)* the steady variation of the dioxane:H<sub>2</sub>O – the latter acting as the non-solvent for compound **1** – composition mirrors the linear modulation of the dielectric constant within a wide range of solvent ratios, thus prompting for easy and precise control over polarity of the media.<sup>20-22</sup>

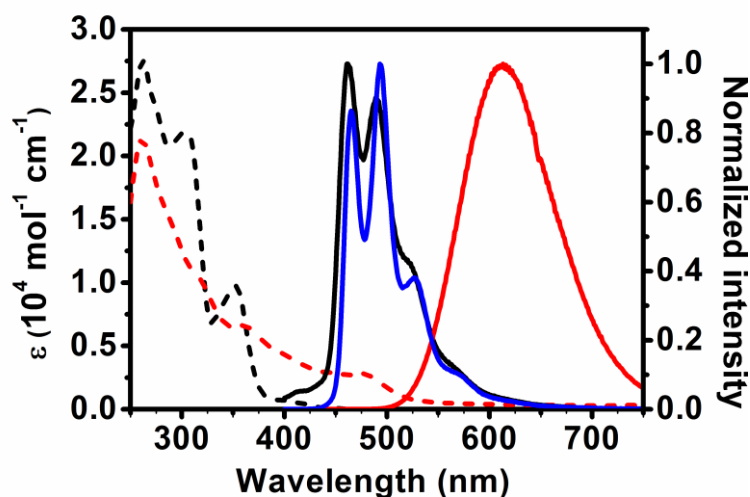


Figure 5.3. Electronic absorption (dotted trace) and emission (solid trace) spectra of complex **1** in pure 1,4 dioxane ( $c = 1 \times 10^{-4}$  M, black), after flash-injection into water to form assembly **A** ( $c = 1 \times 10^{-4}$  M, 95% water content, red trace) and assembly **C** (blue trace).

It should be also noticed that all the photophysical properties hereafter presented and investigated are carried out in air-equilibrated conditions.

As shown in Figure 5.3 when **1** is molecularly dissolved in air-equilibrated 1,4-dioxane ( $c = 0.1\text{--}200 \times 10^{-5}$  M) only a weak blue emission is detected with photoluminescence quantum yield (PLQY) of about 1% and short excited state lifetime (intensity weighted lifetime,  $\tau_{av} = 2.6$  ns) arising from an excited state with mainly triplet ligand centered ( $^3\text{LC}$ ) character.<sup>23</sup> Upon flash-injecting a 1,4-dioxane solution of **1** ( $c = 2 \times 10^{-3}$  M) into water – the latter acting as the non-solvent – we noticed the formation of an emissive species namely assembly **A**. The final H<sub>2</sub>O:dioxane ratio was 95:5 and the resulting platinum complex concentration was  $1 \times 10^{-4}$  M. The formation of Pt...Pt interaction leads to the formation of a new band in the absorption spectrum between 400 and 550 nm assigned to a transition with  $^1\text{MMLCT}$  character. More importantly, such assemblies are characterized by strong orange phosphorescence with longer lifetime (PLQY = 84%,  $\lambda_{em} = 615$  nm,  $\tau = 646$  ns) despite the air-equilibrated condition, which instead should promote an efficient quenching of the triplet manifold excited state by the dioxygen molecules (Figure 5.3). Such emission is indeed due to the establishment of a sizeable extent of close Pt...Pt metallophilic interactions between neighbor molecules of **1**,<sup>23-29</sup> due to the fast – i.e., kinetically controlled – formation of the emitting nanoparticles (Figure 5.4). Dynamic light scattering (DLS) analysis have indeed shown the formation of soft nanoparticles with relatively narrow distribution ( $D_h = 126.2$  nm, PDI = 0.059) and their size and spherical shape was confirmed by scanning electron microscopy (SEM) analysis (Figure 5.4c). In these aggregates, hydrophilic ethylene oxide tails are expected to face the highly polar media and be solvated by water molecules intercalated within the  $-\text{CH}_2\text{CH}_2\text{O}-$  tails upon engagement with H-bonds, whereas the platinum complex cores tightly pack in the inner core of the assembly most likely as consequence of hydrophobic effect. Samples of this metastable state **A** do not show any change in the photoluminescence properties up to 10 hours (Figure 5.4a) even if a slight increase of hydrodynamic diameter and its distribution was observed (Figure 5.4b).

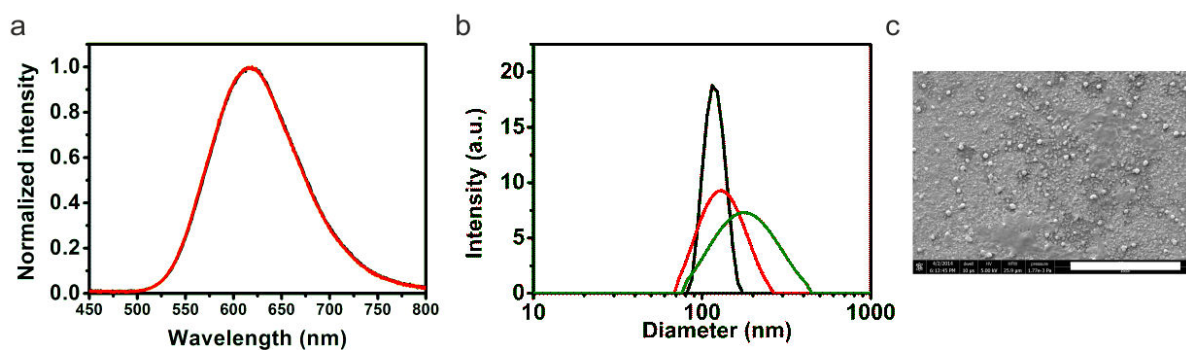


Figure 5.4. (a) Normalized emission spectra recorded at  $t_0$  and after 10 hours aging showing no detectable changes ( $\lambda_{exc} = 405$  nm). (b) DLS analysis of the solution of metastable assembly **A** ( $c = 1 \times 10^{-4}$  M, 95% water content) at  $t_0$  (black trace), and after one hour (red trace) and 8 hours (green trace) of aging. (c) SEM images obtained for drop-casted samples onto glass of samples of assembly **A**.

Therefore we hypothesize that the observed aggregate is a metastable kinetically entrapped state named as **A**. We found indeed that the sample tend to spontaneously interconvert into a thermodynamically stable isoform (assembly **C**) over three weeks at room temperature. Interestingly, **C** displays completely different morphological and optical properties than **A**. SEM analysis revealed the formation of micrometer-long ribbon-like structures (Figure 5.5a) that possess the same emission energy and profile as the monomeric species **1** (Figure 5.3), but with much higher PLQY (up to 20%) and longer lifetime ( $\tau_{av} = 1.08$   $\mu$ s). The fact that the energy and profile of the emission spectra for **1** and for **C** are identical suggests absence of any Pt...Pt and  $\pi$ - $\pi$  interactions. The higher PLQY is therefore due to an increased rigidity and to the shielding towards the oxygen quenching exerted by the packing into fiber structures.

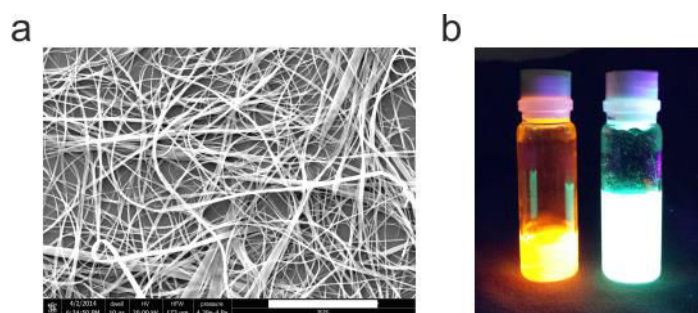


Figure 5.5. (a) SEM images obtained for drop-casted samples onto glass of samples of assembly **C** (scale bar = 50  $\mu$ m). (b) Digital camera photograph of the solution of assembly **A** (left) and **C** (right) under top-bench UV lamp irradiation ( $\lambda_{exc} = 365$  nm).

On the basis of the large changes in terms of emission spectra (Figure 5.3 and Figure 5.5b) and quantum yields observed for the different assemblies, we have undertaken studies of the system evolution with an innovative approach, by using an integrating sphere setup equipped with an EM-CCD camera. The monitoring of the excited state properties with this equipment turned out to be a successful way for unraveling the assembly processes, different from the commonly used techniques such as electronic absorption and/or circular dichroism.<sup>30,31</sup>

While performing these studies, it's important to keep in mind that factors that control the self-assembly process are expected to be manifold. In particular, *environment* (such as solvent and solvent polarity), *temperature*, *concentration* and *time* are expected to play an important role and to have an impact on the final properties of the self-assembled structure. Therefore, we decided to carry out a series of systematic experiments in which all these parameters have been varied to a certain extent one by one.

### 5.2.3 Depolymerization curves

We started by examining the evolution of the system upon changing solvent mixture composition, in particular the H<sub>2</sub>O:dioxane ratio. We thus studied the corresponding changes in emission profile and intensities, upon normalization for the total number of absorbed photons by the system, as well as PLQY upon excitation in the isoabsorptive point observed at  $\lambda_{\text{abs}} = 362$  nm). This is the wavelength where molecularly dissolved **1** and assembly **A** have the same molar absorptivity at the concentration used for the experiments (Figure 5.3). The method simply consists of titrating a known volume of a 95:5 water:dioxane mixture of the pure kinetically-trapped aggregate **A** ( $c = 1 \times 10^{-4}$  M) with a dioxane solution of molecularly dissolved **1** at the same concentration.<sup>32</sup> This was important in order to keep the concentration constant during the experiment. Upon aliquots addition, spectra were recorded after 10 seconds of stirring and 50 seconds of equilibration in order to keep the time constant (see experimental section). The experiments were conducted at room

temperature. The variation of the emission profile of the system is displayed in Figure 5.6a. In Figure 5.6b instead is shown the solvent-dependent changes of the luminescence intensity of assembly **C** at  $\lambda_{em} = 464$  nm ( $I_{em,C}$ , blue line), assembly **A** at 720 nm ( $I_{em,A}$ , red line) and of the overall system (black line). These different traces can be considered as depolymerization curves.<sup>32</sup>

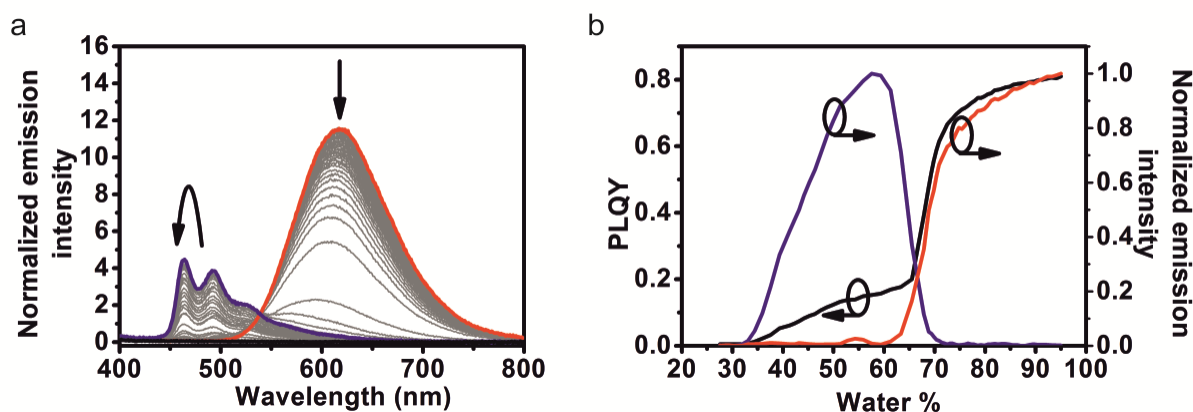


Figure 5.6. (a) Emission spectra normalized by the number of absorbed photons recorded for samples at different solvents composition (grey line) showing the evolution from assembly **A** into **C** and molecularly dissolved **1** (red, blue and black trace, respectively). Black arrows show the emission changes upon increasing dioxane content. The curved arrow indicates an increase followed by a decrease of the emission. (b) PLQY (black line) and normalized emission intensity profile at  $\lambda_{em} = 720$  nm ( $I_{em,A}$ , red line) and  $\lambda_{em} = 464$  nm ( $I_{em,C}$ , blue trace) characteristics of assembly **A** and **C** as function of the solvent composition.

The addition of dioxane solution of **1** to the sample containing **A** leads to a gradual decrease in the recorded PLQY values. When 75% of water content is reached, a fast drop of the emission intensity of **A** is observed together with the concomitant formation of **C**. Assembly **C** quickly grows reaching its maximum at around 60% of water; where it is present as pure isoform. Further addition of dioxane solution of **1** to the mixture leads to a gradual decrease of the emission intensity of **C** which starts to gradually dissolve. Below 30% of water content the PLQY as well as the emission intensity of **C** drops at the constant value of 1%. However, it maintains its characteristic emission profile in the blue region, confirming that **C** is now completely disassembled into monomeric units of **1** (Figure 5.6b).

### 5.2.4 Thermodynamic studies

Afterwards, we carried out thermodynamic investigations on pure isoform assemblies **A** and **C** at fixed concentration and solvent composition. In particular we used 95% water content for assembly **A** and 60% water content for assembly **C** and we run UV-vis experiments under thermodynamic control (cooling rate  $1 \text{ K min}^{-1}$ , temperature region 288.9–358.29 K, 30 seconds of equilibration) as shown in Figure 5.7.

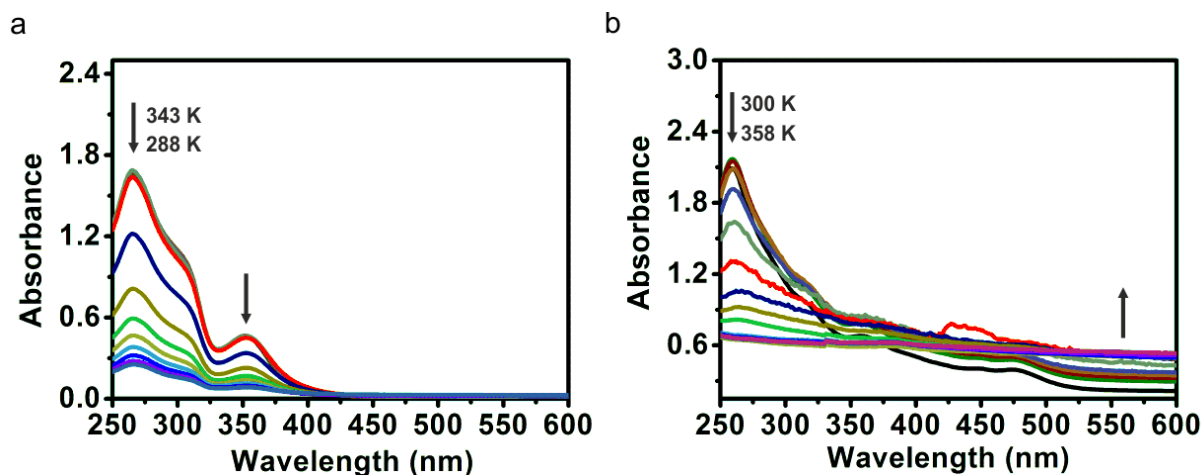


Figure 5.7. Temperature-dependent absorption spectra. of samples of assembly **C** (box a) at 60% water content ( $c = 6 \times 10^{-5} \text{ M}$  of **1**) and assembly **A** (box b) at 95% water content ( $c = 1 \times 10^{-4} \text{ M}$  of **1**) showing the change in the absorption (black arrows) upon cooling and heating, respectively.

We observed that assembly **C** ( $c = 6 \times 10^{-5} \text{ M}$  in 60:40 water:dioxane) is molecularly dissolved at high temperature (343 K) with the absorption spectra resembling the one of the compound in pure dioxane (Figure 5.3). Interestingly, negligible changes in the absorption value are observed upon reaching a critical temperature (318 K). Then a fast decrease in the absorption is observed which is due to the formation of **C**. Similar thermodynamic studies on the kinetically trapped form **A** in 95:5  $\text{H}_2\text{O}$ :dioxane mixture ( $c = 1 \times 10^{-4} \text{ M}$ ) showed an opposite behavior. Upon heating a decrease of the intensity of the UV band ( $\lambda_{\text{max}} = 260 \text{ nm}$ ) is observed with a concomitant increase of scattering ( $\lambda_{\text{max}} = 600 \text{ nm}$ , Figure 5.7b).

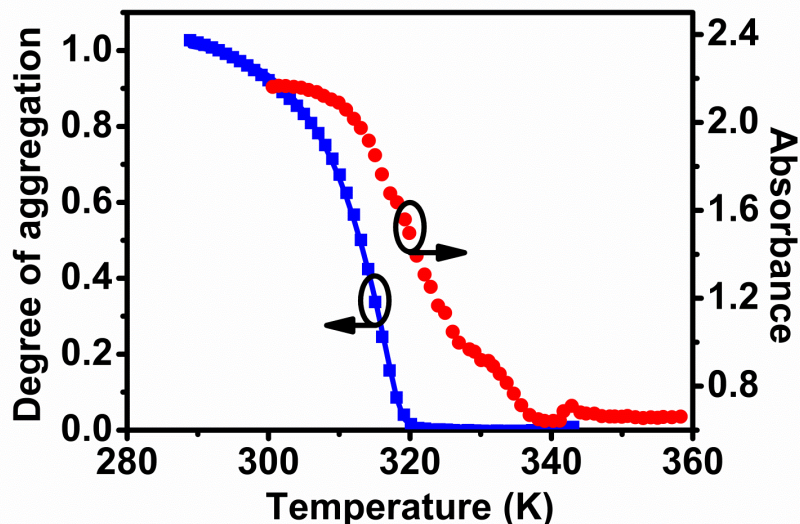


Figure 5.8. Temperature-dependent study of assembly **A** ( $\bullet$ ,  $c = 1 \times 10^{-4}$  M, 95% water content,  $\lambda_{abs} = 260$  nm) and **C** ( $\blacktriangle$ ,  $c = 6 \times 10^{-5}$  M, 60% water content,  $\lambda_{abs} = 362$  nm) fitted with cooperative model<sup>33</sup> (solid trace).

From the experimental data recorded for **C** at  $\lambda_{abs} = 362$  nm as a function of temperature (Figure 5.8) it is possible to demonstrate that assembling of **C** ( $c = 6 \times 10^{-5}$  M in 60:40 water:dioxane) occurs via a cooperative nucleation-elongation mechanism. The process is characterized by a disfavored nucleation step and a subsequent favored elongation process with an abrupt variation of the UV-vis features when the elongation temperature,  $T_e$ , of 318 K is reached. The fitting of the data with Eikelder-Markoort-Meijer model<sup>33</sup> associates enthalpy values of  $\Delta_{nucl}H^0 = -18.2$  kJ mol<sup>-1</sup> and  $\Delta_{el}H^0 = -102.5$  kJ mol<sup>-1</sup> for the nucleation and elongation process respectively. This indicates that the growth of the fibers **C** is strongly cooperative characterized by two different equilibrium constants for the nucleation and the elongation processes respectively. The different behavior observed for assembly **A** is attributable to the thermal-induced, diffusion-controlled, increase of the nanoparticles size already observed to occur slowly at room temperature (Figure 5.4b). Furthermore, the high water content ratio (95%) needed to kinetically entrap **A** largely shifts the chemical equilibrium towards formation of assembled species, reducing the concentration of dissolved monomer **1**. On the basis of the tentative fit of the experimental data (Figure 5.8) and also from the shape of the depolymerization curve, obtained<sup>32</sup> (Figure 5.6b), we could describe that the

formation of assembly **A** is arising from a non-cooperative mechanism characterized by a single equilibrium constant (i.e. isodesmic mechanism).

### 5.2.5 Kinetic studies

We also monitored the evolution in time of the systems keeping fixed all the other parameters (such as concentration, solvent mixture and temperature) fixed. We expect that the solvent/non-solvent ratio, which affects the kinetic interconversion energy barrier, allow us to kinetically control the **A**  $\rightarrow$  **C** transformation.

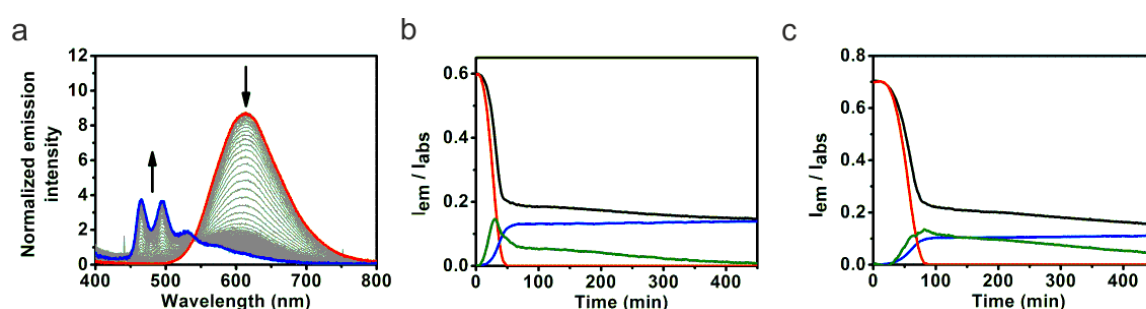


Figure 5.9. **a)** Emission spectra of the system at 79% water content showing the time-dependent transformation of **A** at  $t_0$  into **C** at  $t_\infty$  (red and blue trace, respectively). Overall PLQY (black line) and weighted intensity contributions of assembly **A** (red trace,  $\lambda_{em} = 750$  nm), **C** (blue trace,  $\lambda_{em} = 464$  nm) and **B** (green trace) at 79% (box b) and 83% (box c) water content upon  $\lambda_{exc} = 362$  nm.

Hence, we prepared a fresh suspensions of metastable **A** ( $c = 1 \times 10^{-4}$  M, 95% water) and we added molecularly dissolved **1** in pure dioxane ( $c = 1 \times 10^{-4}$  M) in order to slightly lower the water content ratio and thus decrease the trapping barrier for **A**. We chose 83:17 and 79:21 as the ratio for the water:1,4-dioxane mixture and we recorded the photoluminescence properties – emission spectra and PLQY – as function of time with an integrating sphere setup ( $\lambda_{exc} = 362$  nm, Figure 5.9a for sample at 79% water). These two solvent/non solvent ratios have been judiciously chosen in order to slow down the process to such an extent to be able to observe the system evolution. The resulting spectra show clearly how the solvent composition affects **A**  $\rightarrow$  **C** transformation, which expectantly becomes faster upon lowering the water content (Figure 5.9).

Furthermore, we can assume that at the first instant,  $t_0$ , only **A** is present, while at thermodynamic equilibrium,  $t_\infty$ , **C** is the only existing species and contributing to the overall luminescence of the system. Moreover, we can consider that at  $\lambda_{em} = 464$  and 750 nm the contribution to the emitted photons arises from **A** and **C** only, respectively. On this basis, we were able to estimate the contribution of each of the two species to the total amount of emitted photons (Figure 5.9b-c) and follow the kinetics of the two assemblies. In principle, we expect that the sum of the two intensity components, namely  $I_A$  and  $I_C$ , will traces out the overall PLQY recorded. As a matter of fact, a time-dependent number of residual photons,  $I_B$ , were surprisingly observed for both the investigated solvent mixtures (Figure 5.9b-c). The kinetics of  $I_B$  shows a solvent-dependent profile. As shown in Figure 5.9b-c,  $I_B$  is not detected at  $t_0$ ; it reaches a maximum after a certain time, then a gradual decrement is observed when approaching the thermodynamic equilibrium ( $t_\infty$ ). Such findings strongly pointed towards the presence of a transient species (assembly **B**) that represents a second off-pathway isoform. At this stage, the emission of such novel assembly could not be resolved in a clear manner due to large spectral overlap.

It is worth to notice that the time-dependent evolution of the emitted photons  $I_B$  and  $I_C$  is not linear (Figure 5.9b and c). Indeed, the profiles display an initial lag time whose duration depends on solvent composition, being the longer observed for higher water content, and corresponds to the nucleation step. After such period of time, rapid growth – elongation step – of the emission intensity, with an ascending sigmoidal profile, indicates that the formation of the assemblies **B** and **C** follows an autocatalytic process.<sup>32-34</sup> This is mirrored by the descending sigmoidal profile of  $I_A$  recorded for the metastable **A** that is being consumed, which acts as feedstock reservoir.

In order to deeply understand the mechanism of the described complex pathway dynamics and how the equilibria here at work are interplayed by common species, we carried out similar kinetic experiments at different initial concentrations of the metastable **A**, whereas the solvent composition has been kept constant at the value of 83:17 water:dioxane ratio (Figure 5.10a).

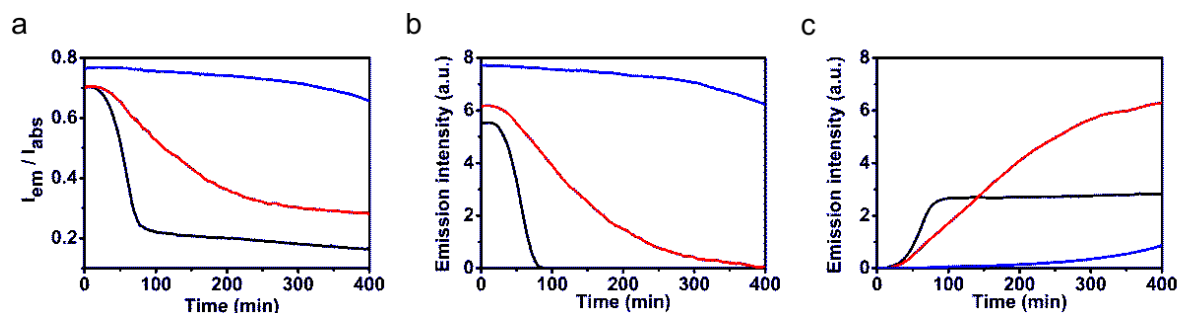


Figure 5.10. Time-dependent evolution of the metastable assembly **A** at different initial concentration in 83:17 H<sub>2</sub>O:dioxane ratio upon excitation at 362 nm. (a) Overall PLQY profile at  $c = 1 \times 10^{-4}$  M (black line),  $2.5 \times 10^{-4}$  M (red line) and  $3.5 \times 10^{-4}$  M (blue line); (b) Intensity profile of assembly **A** ( $\lambda_{em} = 750$  nm) at  $c = 1 \times 10^{-4}$  M (black line),  $2.5 \times 10^{-4}$  M (red line) and  $3.5 \times 10^{-4}$  M (blue line); (c) Intensity profile of assembly **C** ( $\lambda_{em} = 464$  nm) at  $c = 1 \times 10^{-4}$  M (black line),  $2.5 \times 10^{-4}$  M (red line) and  $3.5 \times 10^{-4}$  M (blue line).

Upon increasing the initial concentration of **A**, obtained by increasing the overall concentration of **1**, we observed a higher PLQY at  $t_0$ . This indicates that higher concentrations of **1** affects the equilibria between **A** and **1** in such way that formation of **A** is now favored (Figure 5.10a). Interestingly, this is followed by a slower kinetic of disappearance of **A** (Figure 5.10b) mirrored by a slower appearance of the thermodynamic product **C** (Figure 5.10c). These findings confirm the fact that the formation of **C** occurs through the nucleation of the monomeric compound **1** instead of structural reorganization of **C**. The molecularly dissolved **1** is the chemical node of the interplayed equilibria network between the different assemblies, *i.e.* the common feedstock.<sup>16</sup>

### 5.2.6 Real-time imaging of the self-assembly process

The comprehensive kinetic control of the system jointly with the unique photophysical properties of each of the assemblies allowed real-time imaging of the system evolution by fluorescence confocal microscopy. To this end, we drop-casted freshly prepared samples of **A** at 79% and 83% H<sub>2</sub>O content onto a closed quartz petri dish, in similar conditions employed for the kinetic experiments, and monitored the samples over time at room temperature upon excitation at  $\lambda_{exc} = 405$  nm. In this way

we were able to clearly observe the presence of three different self-assembled isoforms with three different emission spectra. Figure 5.11

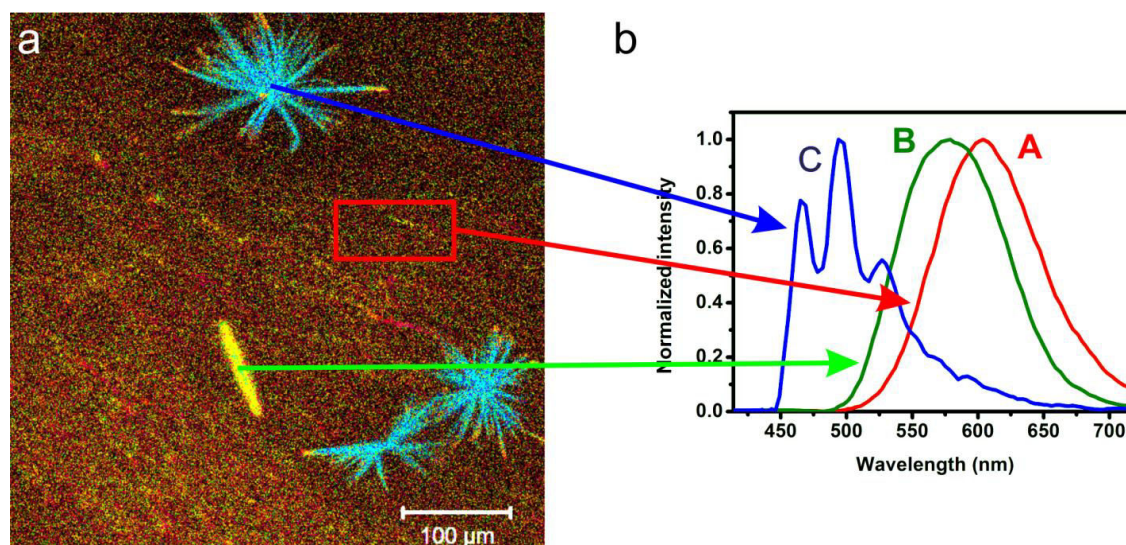


Figure 5.11. (a) Confocal microscopy image of the supramolecular assemblies showing their true-color emission obtained by using lambda-mode option. (b) Normalized emission spectra of the assemblies upon  $\lambda_{exc} = 405$  nm.

The emission spectra of these three distinct assemblies show clearly a hypsochromic shift going in the series **A** to **B** and finally to **C**. As previously described for **A**, the green photoluminescence observed for assembly **B**, arises from an emitting  $^3\text{MMLCT}$  excited as consequence of axial Pt...Pt interactions between neighbor platinum complexes arranged in a face-to-face fashion. The change in the emission color indicates that the metal...metal distance is slightly larger than that expected for the metastable assembly **A** while in assembly **C** no interactions between platinum complexes are present.

As it can be seen in figure 5.11, at  $t_0$  the scenario is dominated by the diffusion of red-emitting nanoparticles corresponding to assembly **A**. After few minutes, confocal images typically show appearance of both assemblies **B** and **C** (Figure 5.12).

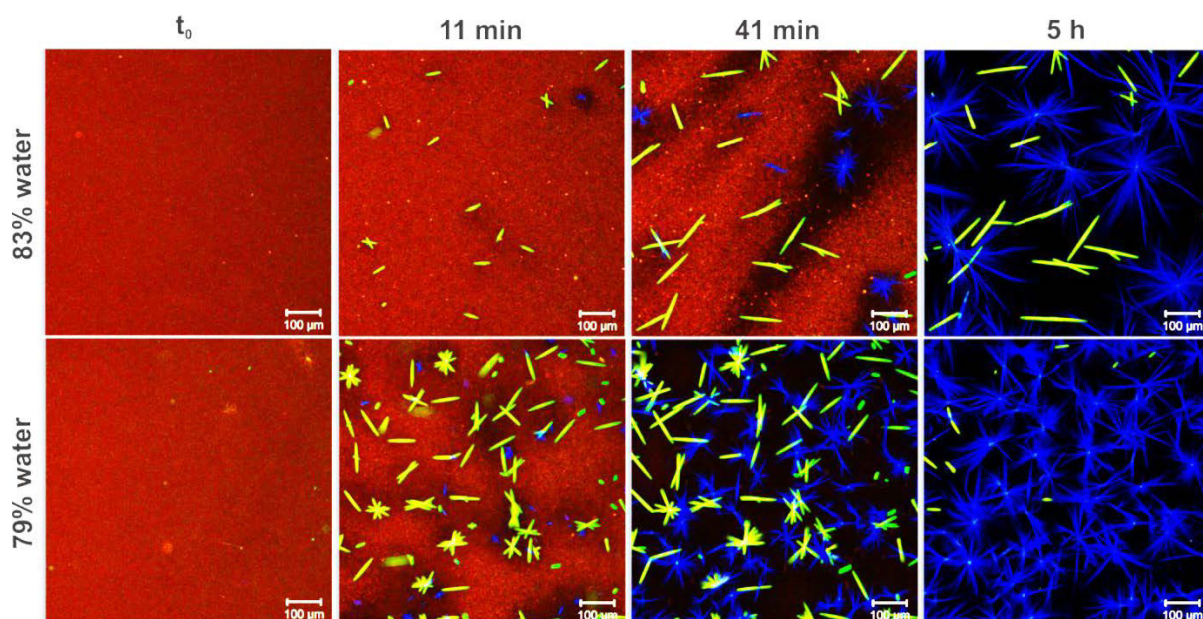


Figure 5.12. Snapshots taken from the movies at 83% and 79% water content showing time-dependent evolution of assembly **A** (red) into **B** (green) and **C** (blue).  $\lambda_{exc} = 405 \text{ nm}$ , scale bar  $100 \mu\text{m}$ .

We attribute such aggregates being the result of nucleation processes of monomers **1** on the basis of the nucleation-elongation models developed for supramolecular polymers and proteins.<sup>7,16,34,35</sup> Afterwards, nuclei of both assembly **B** and **C** appear to quickly grow in a highly anisotropic fashion at the expenses of the surrounding nanoparticles of assembly **A**, which act as a metastable reservoir of **1**. Such step, which nicely resembles biological infection process observed for prions and insulin<sup>36</sup>, yields micrometers-long emissive supramolecular architectures and represents the cooperative elongation process of **B** and **C**. Once **A** is entirely consumed, we observe slow disappearance of **B** while **C** keeps growing until an almost complete conversion of the system is reached as the thermodynamic equilibrium approaches. Interestingly even big assemblies of **B** are consumed by much smaller aggregates of the thermodynamic favored **C** as shown in Figure 5.13 which exclude Ostwald ripening.

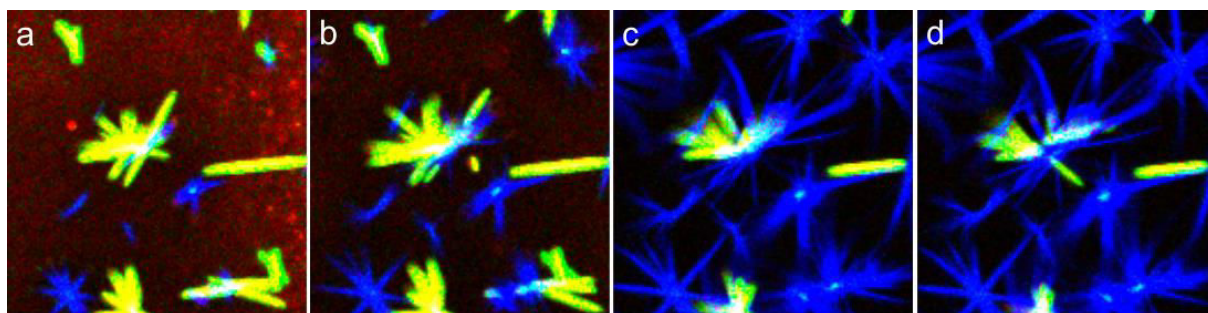


Figure 5.13. Magnification of some pictures taken from our movie at 79% water content showing assembly **B** (green) slowly eaten by assembly **C** (blue) after a) 13 min, b) 23 min, c) 56 min and d) 63 min.

All these findings demonstrate that the thermodynamic product **C** is not formed by mere structural rearrangement of either **A** or **B**, but that all the species are products of delicate interplays between different on- and off-pathways interconnected by chemical equilibria with monomeric **1**. Remarkably, the kinetic control of the evolution of the overall system is achieved by fine tuning the solvent:non-solvent ratio. Indeed, upon increasing water content (79%  $\rightarrow$  83%) we are able to slow down the kinetics of the observed self-assembly processes as we previously predicted by means of the above described kinetic studies (Figure 5.9b and c). As a control experiment, we monitored the sample at 95% water content, which shows a very slow formation of small amount of **B** and **C** while **A** still dominates the system even after more than 10 hours observation (Figure 5.14).

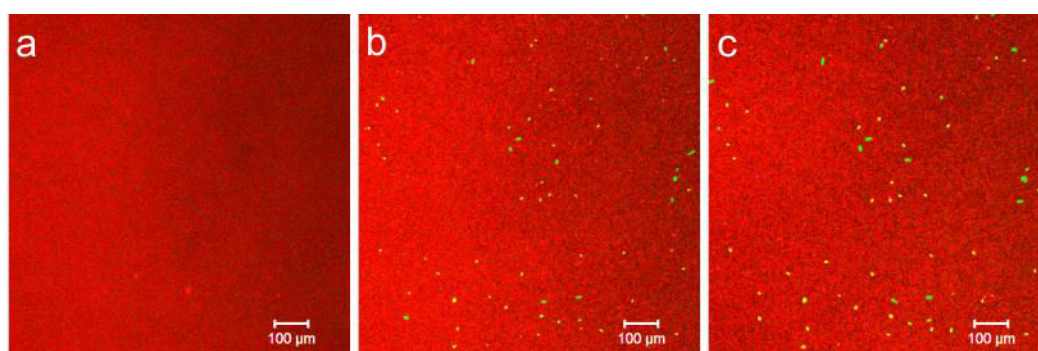


Figure 5.14. Snapshots taken from the movies at 95% water at a) 0 min b) 6 h 10min and c) 12h 25 min showing no significant changes.  $\lambda_{exc} = 405 \text{ nm}$ , scale bar  $100 \mu\text{m}$ .

### 5.2.7 Seeded living supramolecular polymerization

At solvent composition of 95:5 water:dioxane, the very slow nucleation–elongation processes of **B** and **C**, while **A** is trapped, prompted us to investigate about the possibility to control the cooperative growth of **C** using the seeded living supramolecular polymerization.<sup>15,18,37-39</sup> To this end, we started with pure assembly **A** at 95% water ( $c = 5 \times 10^{-5}$  M,  $D_h = 114.4$  nm, PDI = 0.188) and we sonicated for 3 hours, selectively obtaining seeds of **C** in a rather good size distribution ( $D_h = 265.3$  nm, PDI = 0.150) (Figure 5.15).

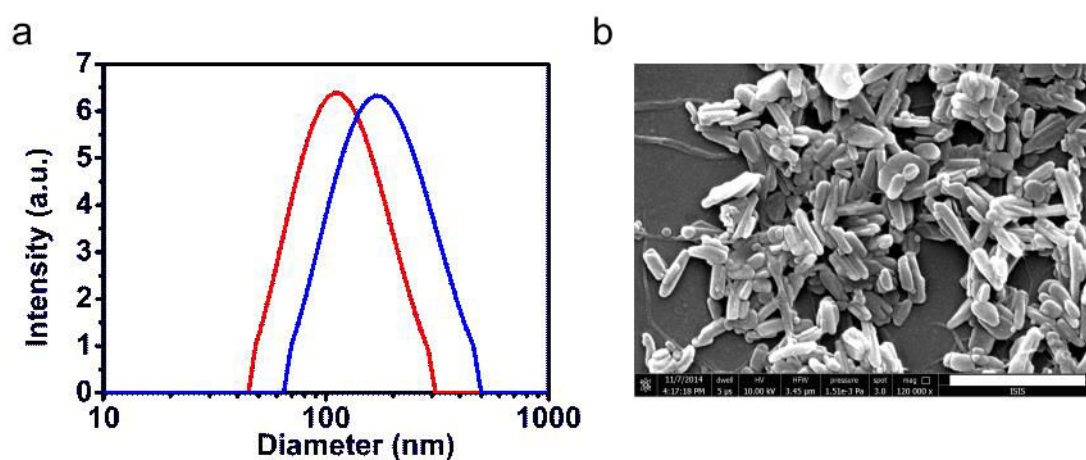


Figure 5.15. a) Dynamic light scattering (DLS) data showing the intensity-averaged hydrodynamic diameter ( $D_h$ ) of the assembly **A** (red trace,  $c = 5 \times 10^{-5}$  M) and assembly **C** (blue trace) obtained after sonication of the sample. b) SEM images obtained for samples of seeds of assembly **C** obtained after sonication of assembly **A**. Samples were drop-casted onto glass. Scale bar =  $1 \mu\text{m}$ .

The addition of different aliquots of such suspension of seeds **C** to pure metastable **A** (95%  $\text{H}_2\text{O}$ ) leads to changes in its electronic absorption spectra in time (Figure 5.16a). Noteworthy, similarly to what observed before for metastable **A** (Figure 5.9), the evolution of the absorption is not linear as expected for an autocatalytic process. Nonetheless, the absence of lag time is now the direct consequence of the externally seeded growth of the assembly **C**. However, by plotting the logarithm of the polymerization rate at the initial step,  $\log[d\varepsilon_{362}/dt]$ , versus the concentration of the added seed of **C**  $\log[\text{seed C}]$  we obtain a linear relationship with slope of 0.94. This

value is very close to that of an apparent first-order kinetics with respect to the concentration of seed **C**, as it is typical for chain growth polymerization.<sup>40</sup>

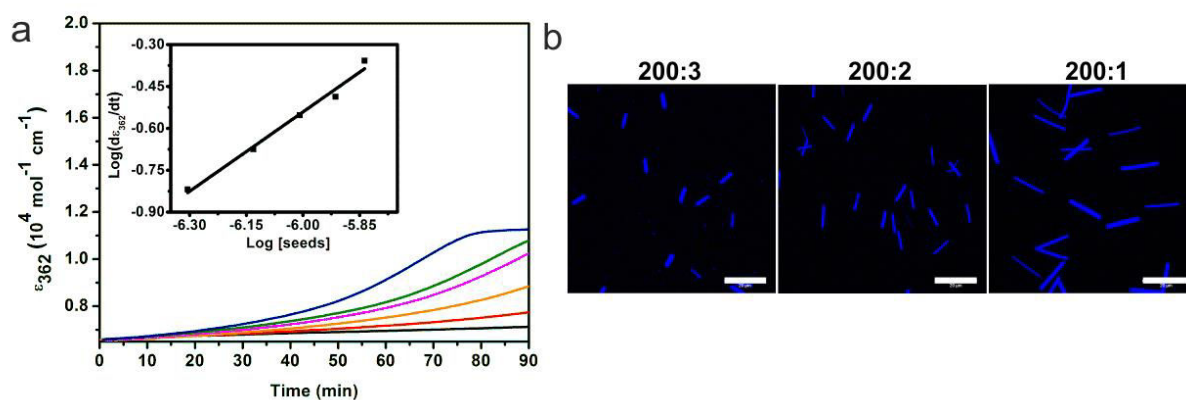


Figure 5.16. (a) Time course of supramolecular polymerization of assembly **A** initiated by the addition of seeds of **C** under conditions of  $[A]/[C] = 200:1$  (-),  $200:2$  (-),  $200:3$  (-),  $200:4$  (-),  $200:5$  (-) and  $200:6$  (-). The overall concentration of **1** is  $5 \times 10^{-5}$  M. Inset: Log-log plot of the initial increase of  $\epsilon_{362}$  ( $s^{-1}$ ) as function of seed concentration ( $[M]$ ), showing a linear relationship (correlation coefficient 0.980) with a slope of 0.94. (b) Confocal images of fibers obtained from seeded polymerization as from box a.  $\lambda_{exc} = 405$  nm. Scale bar  $20 \mu m$ .

Confocal microscopy investigation showed the formation of blue-emissive rods with uniform length that increases upon decreasing the amount of seeds (Figure 5.16b).

### 5.2.8 Photoconversion

The size control of assembly **C** is achieved, however full management for obtaining off-pathway assembly **B** as pure isoform seems to be still precluded. This is due to the intrinsically transient nature of **B** as well as to the concomitant formation of **C**.

Therefore we decide to try using an external stimulus such as light to locally induce **C**  $\rightarrow$  **B** transformation. We found out that it was possible to perform a fast **C**  $\rightarrow$  **B** interconversion in 95:5%  $H_2O$ :dioxane with good spatial resolution, while keeping the structural features intact, upon irradiating **C** with a laser power higher than that used for imaging (Figure 5.17b). The externally triggered and spatiotemporally controlled interconversion of a thermodynamic assembly back to one of the kinetic intermediate, **C**  $\rightarrow$  **B**, is unprecedented to the best of our knowledge.

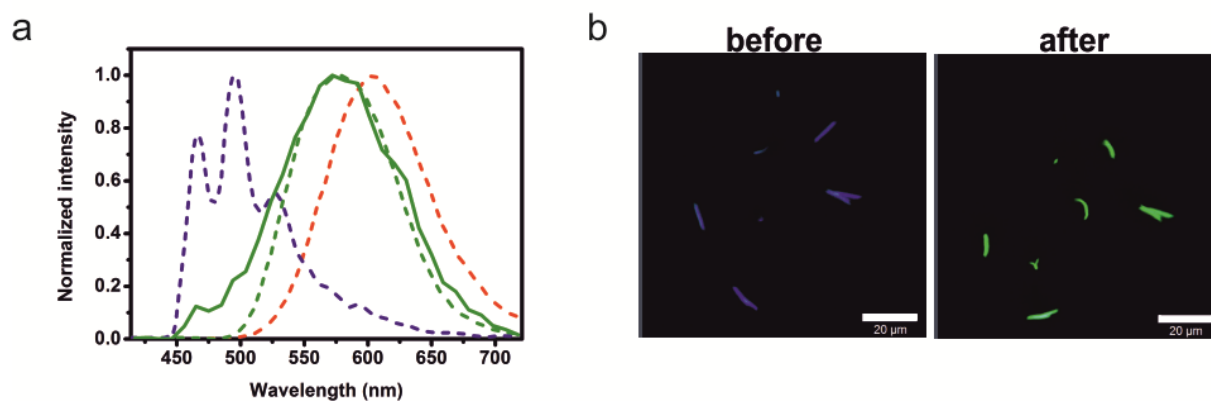


Figure 5.17. a) Emission spectra of the assembly obtained upon irradiating assembly C ( $\lambda_{exc} = 405$  nm) with higher laser power (green, solid line). The emission spectra of assembly **A** (red), **B** (green) and **C** (blue) obtained during confocal imaging experiments at lower laser power ( $\lambda_{exc} = 405$  nm) are displayed as dotted traces (see Figure 5.11). b) Confocal pictures of fibers before (left) and after (right) 5 minutes of irradiation at  $\lambda_{exc} = 405$  nm. Scale bar 20  $\mu$ m.

We believe that the mechanism responsible for such structural rearrangement of the platinum complexes within the fibers is due to a photoinduced effect (i.e., radiationless deactivation pathways) either through a photochemical or a local thermal process. The conversion of the blue emitting fibers in green emissive assemblies is completed in ca. 5 minutes and the emission spectrum recorded for the obtained fibers traces out the profile obtained from the abovementioned confocal imaging experiments (Figure 5.17) confirming that the photochemical product is indeed the transient species **B**.

### 5.2.9 Effect of the molecular design on the self-assembly process

At this stage, it was not possible to identify secondary supramolecular interactions involved in our system in addition to the Pt...Pt bond formation, which are taking place within the different assemblies **A**, **B** and **C**. Nonetheless, the main interactions that can be at play between spatially-closed complexes are the following:

- i) hydrophobic interactions, in which  $CF_3$  moieties are expected to play an important role;
- ii)  $\pi$ - $\pi$  stacking between the extended  $\pi$ -conjugated ligands;
- iii) strength of the H-bonding (amine vs. amide);

To answer these questions, we started to investigate the correlation between the molecular design, the self-assembly properties and the features of the resulting

assemblies. The corresponding structures of the prepared complexes are depicted in Figure 5.2.

### 5.2.9.1 Photophysical properties

The photophysical properties of complexes **6-9** have been investigated similarly as complex **1** in 1,4-dioxane/water mixture.

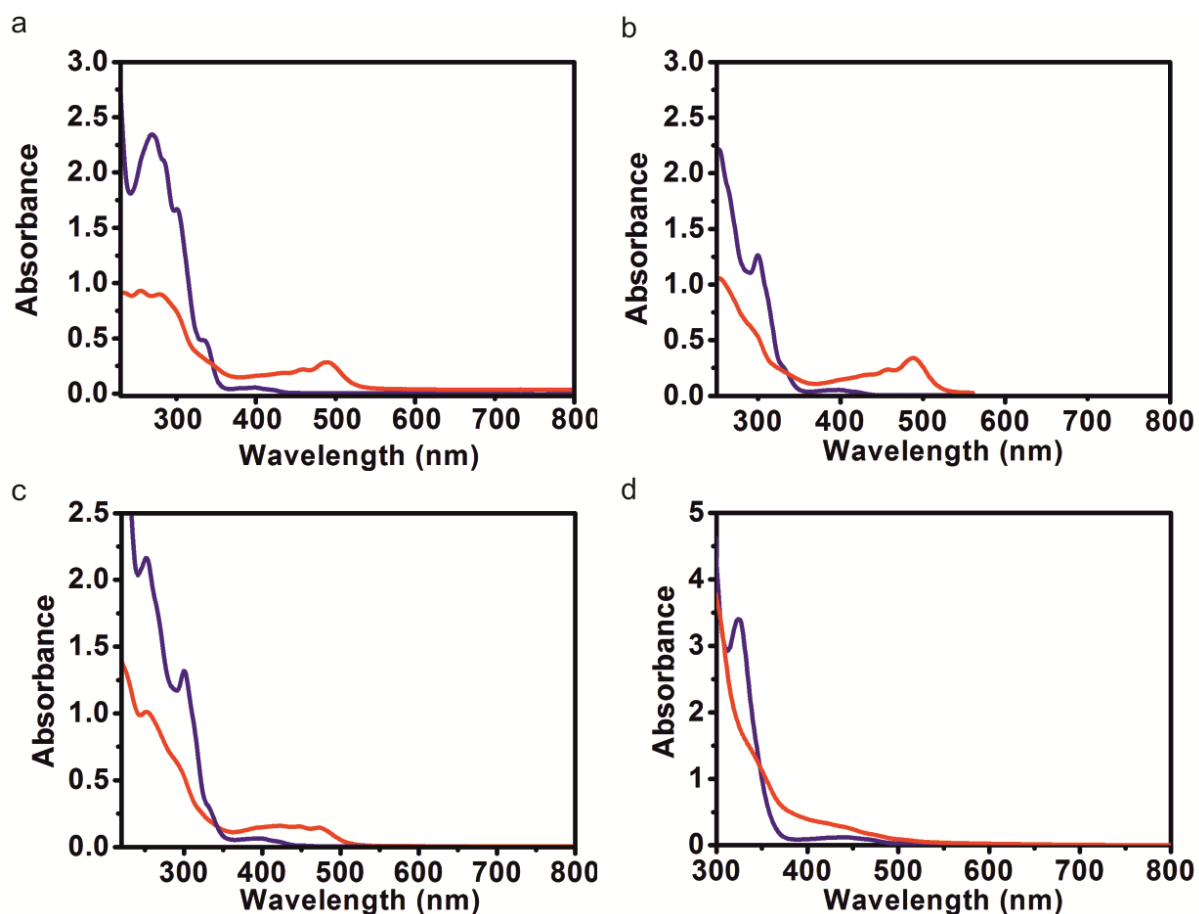


Figure 5.18. Absorption spectra of complex **6** (a), **7** (b), **8** (c) and **9** (d) in pure 1,4-dioxane (blue trace) and after flash-injection into water (95% water content, red trace). The concentration of the complexes **6-8** is  $5 \times 10^{-5}$  M while for complex **9** is  $1 \times 10^{-4}$  M.

We have first examined the absorption spectrum of each compound in pure 1,4-dioxane (Figure 5.18) and after in a 95:5 water:dioxane ratio obtained by flash injection in water. As expected the absorption spectra for complexes **6-8** ( $c = 5 \times 10^{-5}$  M) is rather similar to complex **1**, with typical features for the monomeric form in pure dioxane, and the formation of a new absorption band at lower energy ( $^1\text{MMLCT}$ )

after flash injection in water, revealing the formation Pt...Pt metallophilic interactions. In the case of **9**, in which the CF<sub>3</sub> moieties on the chromophoric terdentate ligand has been replaced with tolyl groups, the absorption spectrum in pure dioxane (Figure 5.18d) displays a clear bathochromic shift being the onset of the <sup>1</sup>MMLCT at lower energy (500 nm). Upon flash injection of **6-8** into water we observed a change in the absorption spectrum with a shift of the onset at 550 nm.

### 5.2.9.2 Depolymerization curves

Then we have examined the changes in emission profile and intensities (normalized for the total number of absorbed photons by the system) and in PLQY as a function of the solvents mixture composition (H<sub>2</sub>O:dioxane ratio). As excitation wavelength, we have chosen as excitation point the isoabsorptive point of molecularly dissolved complexes (**6-9**) in pure dioxane and the assembled systems in 95% water at the same concentration in Pt(II) complex ( $c = 5 \times 10^{-5}$  M).

As already described, the method consists in a titration of a known volume of a 95:5 water:dioxane mixture of the aggregate ( $c = 5 \times 10^{-5}$  M) with a dioxane solution containing Pt(II) complex at identical concentration,<sup>32</sup> in order to keep the concentration variable fixed and constant during the experiment. Spectra were recorded after 10 seconds of stirring and 50 seconds of equilibration in order to fix the time variable and the experiment were conducted at room temperature.

Interestingly, only complex **6** seems to behave similarly to **1**, forming two different assemblies, namely **A<sub>6</sub>** and **C<sub>6</sub>**, **A<sub>6</sub>**, is characterized by a bathochromically shifted emission ( $\lambda_{em,max} = 574$  nm, PLQY = 80%) arising from the establishment of strong metallophilic interactions amongst closely-packed platinum complexes. Similarly to what found for complex **1**, the second assembly, named **C<sub>6</sub>**, possesses an emission energy and profile, which resemble that of the monomeric species (Figure 5.19a), yet with higher PLQY (up to 20%).

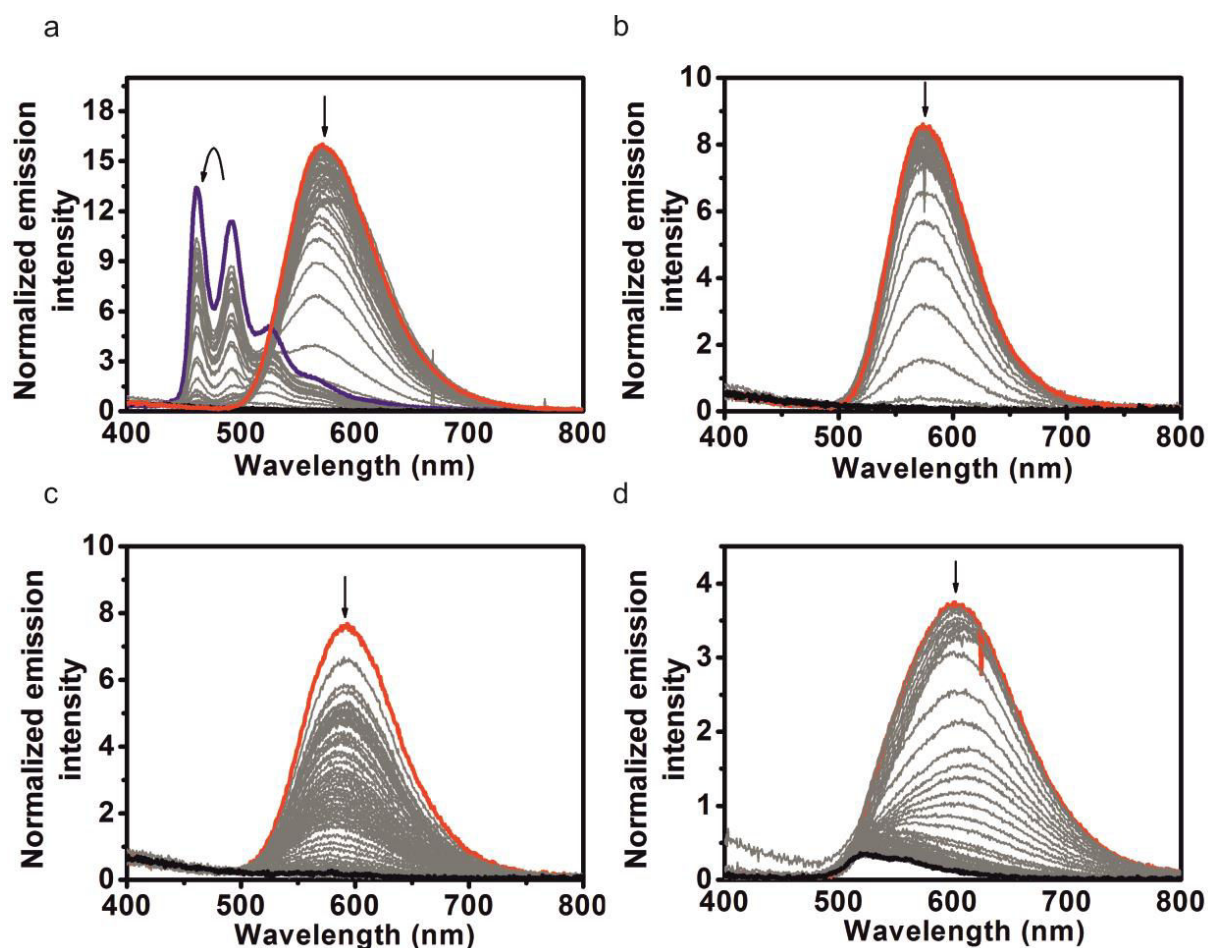


Figure 5.19. Emission spectra normalized by the number of absorbed photons recorded for samples at different solvents composition (grey line) showing the spectral change from 95% water content (red trace) till the molecularly dissolved complex (black trace) for complex **6** (a), **7** (b), **8** (c) and **9** (d.) In the case of **7** blue fibers are formed (blue trace) . Black arrows show the emission changes upon increasing dioxane content. The curved arrow indicates an increase followed by a decrease of the emission. The concentration of the complexes **6-9** is  $5 \times 10^{-5}$  M.

On the other hand, at high water content complexes **7** and **8** have similar emission properties to **1** and **6** due to the establishment of strong Pt...Pt metallophilic interactions ( $\lambda_{em,max} \approx 574$  nm and PLQY  $\approx 40\%$ ); whereas, addition of the monomer leads only to a decrease of the emission intensity till molecular dissolution. Likewise, for complex **9** it is possible to observe a change in the emission properties from the molecularly dissolved state in pure dioxane ( $\lambda_{em,max} \approx 520$  nm and PLQY  $\approx 2\%$ ) to the assembled state at high water content ( $\lambda_{em,max} = 602$  nm and PLQY  $\approx 28$ ).

We now consider the overall PLQY of the system as a function of the solvent composition (Figure 5.20) in a similar manner to what recorded for complex **1** (Figure 5.6b).

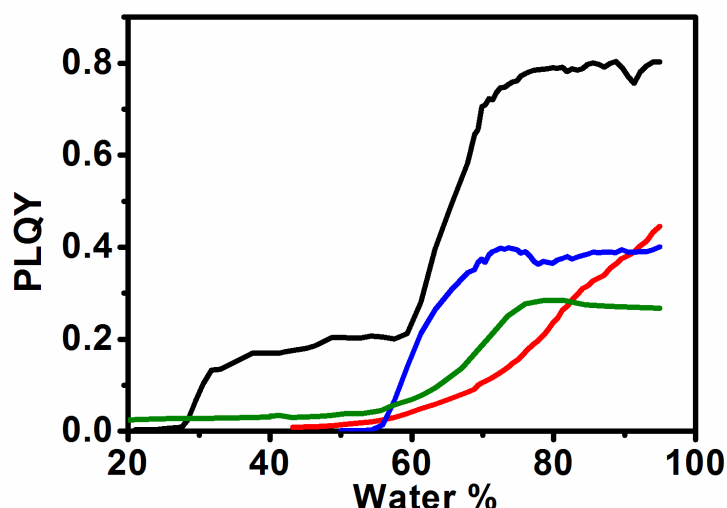


Figure 5.20. Depolymerization curve<sup>32</sup> showing the PLQY as a function of the solvent composition for complexes **6** (black line), **7** (blue line), **8** (red line) and **9** (green line).

As far as compound **6** is concerned, it is possible to notice the presence of three well-defined regions. The first region, between 95 and 70% water content, with constant PLQY around 80%; a second region between 60% and 30% water content, with PLQY around 20% and a third region below 30% water content in which **6** is molecularly dissolved (constant PLQY of 1%).

On the other hand, depolymerization curve for complex **7** is characterized by the presence of only two regions. At 95% the value of the PLQY (41%) is rather constant until the water content is above 70%, then it quickly drops to a constant value of 1%, which is attributed to the molecular dissolution of the compound.

In the case of complex **8**, which differs from **7** only for the nature of the hydrogen-bonding moiety (amine vs. amide for **8** and **7**, respectively), the depolymerization curve displays the absence of a critical solvent composition since no sharp transition is observed (see red trace in Figure 5.20). For this complex, a gradual decrease of the PLQY upon increasing the amount of good solvent is recorded till the PLQY reaches the constant value of 1% at about 50% water content, which indicates dissolution into molecular species.

Finally, upon changing the substituent group on the terdentate ligand from trifluoromethyl to tolyl, namely complex **9**, a depolymerization curve characterized by only one abrupt variation of the PLQY is recorded. In particular, the curve is

characterized by an overall lower PLQY, being 20% at water content as high as 95%. Such PLQY values were found rather constant until approximately 75% water content. Then, an initial abrupt decrease of the PLQY followed by a more gradual variation is observed, similarly to what observed for complex **8**, till the constant value of 2% is reached as characteristic of the platinum complex **9** in the molecularly dissolved state in air-equilibrated condition.

It seems that the presence of both the CF<sub>3</sub> groups on the terdentate ligand as well as the absence of a methylene spacer in the ancillary pyridine (Figure 5.2) are both required to observe the formation of the blue emitting fibers. Furthermore, the shape of the depolymerization curve is appear to be affected by the nature of the hydrogen-bonding motif showing sharp transition for the amide and more gradual changes in the presence of the amine. As already discussed, sharp transitions in the depolymerization curve suggest the presence of cooperativity, however thermodynamic studies must be carry out to confirm such hypothesis.

### **5.2.9.3 Real-time imaging of the self-assembly process**

As above described, the dramatic change in the photophysical properties of these materials upon self-assembly allows confocal imaging of the supramolecular polymerization processes in real-time. The experiments were carried in a similar manner to what above described for complex **1** at a solvent composition of 74:26 water:dioxane.

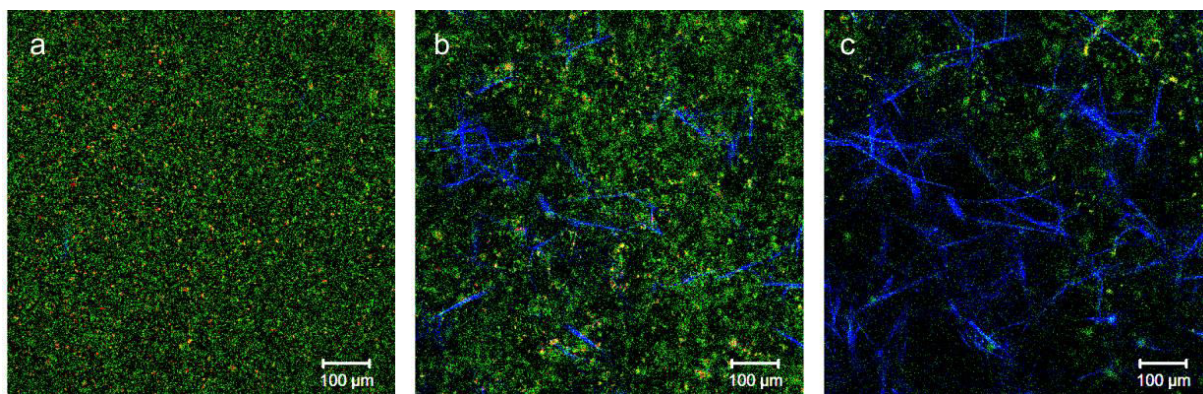


Figure 5.21. Confocal microscopy snapshots taken from the movies recorded at 74% water content. The images show the supramolecular polymerization of complex **7** after (a) 0 min (b) 80 min (c) 160 min.  $\lambda_{exc} = 405 \text{ nm}$ , scale bar = 100  $\mu\text{m}$ .

Preliminary confocal results have confirmed that **6** can self-assemble into two kinetic species and the thermodynamic product as in the case of **1**. For compound **7**, the formation of the thermodynamic product only was observed and it is constituted by long, green emissive, rod-like structures (Figure 5.22).

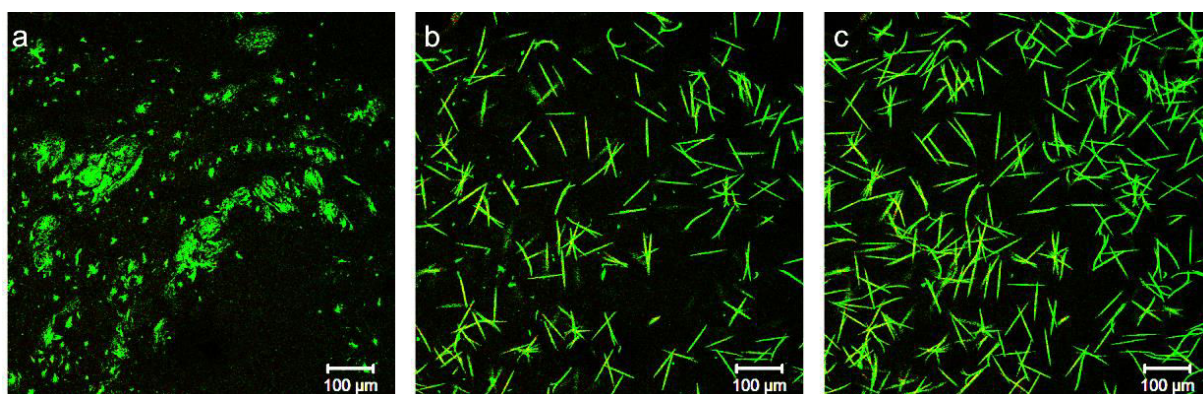


Figure 5.22. Confocal microscopy snapshots taken from the movies recorded at 74% water content. The images show the supramolecular polymerization of complex **8** after a) 0 min b) 15 min c) 30 min.  $\lambda_{exc} = 405 \text{ nm}$ , scale bar = 100  $\mu\text{m}$ .

At this stage, it was not possible to detect any microscopic self-assembled structures for complexes **8** and **9**.

Nonetheless, for better elucidating the energetic landscape and equilibria at play between the different assembled species and monomer, a deeper investigation of the thermodynamics and kinetics of formation of such assemblies is required for each of the complexes **6–9**. Such investigation will be subject of future works.

### 5.3 Conclusion

Our results showed that it is possible to manage with interlocked dynamic pathways comprising more than two assemblies by judiciously playing with different stimuli such as solvents composition and light, allowing a real-time visualization of the events involved. In particular, environment and environmental condition play fundamental roles in the self-assembly processes and in presence of cooperativity this is reflected by the presence of critical points in the depolymerization curve<sup>32</sup>. Such findings open the possibility not only to tune the size of the assemblies but also to prepare out-of-equilibrium supramolecular functional structures able to respond to specific stimuli such as environmental changes, which are important in biological systems.

### 5.4 Experimental section

#### 5.4.1 Synthesis and characterization

All the reactions were carried out under an inert atmosphere of nitrogen (Schlenk technique). All the solvents and chemicals were used as received from Aldrich or Fluka without any further purification. The compounds were purified by column chromatography by using either silica gel 60 (70–230 mesh) or neutral alumina as stationary phase. <sup>1</sup>H, <sup>13</sup>C, and <sup>19</sup>F NMR spectra were recorded on a Bruker Avance 400 spectrometer. The <sup>1</sup>H NMR chemical shifts ( $\delta$ ) are given in ppm and referred to residual protons on the corresponding deuterated solvent. All deuterated solvents were used as received without any further purification. All coupling constants ( $J$ ) are given in Hertz (Hz). Electrospray ionization mass spectrometry (ESI-MS) was recorded on a MicroTOF (Bruker) mass spectrometer equipped with an electrospray source by the mass spectrometry service of the Institut de Chimie at the University of Strasbourg. Elemental analyses were recorded by the analytical service of physical measurements and optical spectroscopy at the University of Strasbourg.

#### 5.4.1.1 N-(4-pyridyl)2-[2-(2-methoxyethoxy)ethoxy]acetic acid amide (2)

2-[2-(2-methoxyethoxy)ethoxy]acetic acid (19.88 g, 111.57 mmol) and 4-aminopyridine (7.0 g, 74.38 mmol) were dissolved in 150 mL of  $\text{CHCl}_3$ , then N,N'-dicyclohexylcarbodiimide (DCC), 23.0 g, 111.57 mmol) was added in consecutive little aliquots. During the addition the solution warmed up and a white precipitate was formed. The solution was stirred for one hour at room temperature then refluxed for four hours. After cooling down to room temperature, the solution was filtered and the filtrate concentrated in vacuo. The crude yellow oil was purified by column chromatography on silica gel using AcOEt to AcOEt:MeOH 9:1 obtaining the pure product as light yellow oil. Yield 12.0 g, 63%.  $^1\text{H}$  NMR ( $\text{CD}_2\text{Cl}_2$ , 400 MHz, ppm)  $\delta$ : 9.04 (s, broad, 1H), 8.51 (d,  $J = 8$  Hz, 2H), 7.62 (d,  $J = 8$  Hz, 2H), 4.14 (s, 2H), 3.72–3.80 (m, 6H), 3.60–3.62 (m, 2H), 3.38 (s, 3H);  $^{13}\text{C}$  NMR ( $\text{CD}_2\text{Cl}_2$ , 100 MHz, ppm)  $\delta$ : 169.92, 151.18, 145.10, 114.28, 72.27, 72.00, 71.24, 70.94, 70.52, 59.15. HR-ESI-MS ( $m/z$ ):  $\text{C}_{12}\text{H}_{18}\text{N}_2\text{O}_4$  [ $\text{M}+\text{Na}$ ] $^+$ , calcd. 277.115, found 277.115.

#### 5.4.1.2 N-(2-(2-(2-methoxyethoxy)ethoxy)ethyl)pyridin-4-amine (3)

Under strong nitrogen flux, a solution of **4** (5.5 gr, 21.62 mmol) in anhydrous THF (5 mL) was dropwise added to 30 mL suspension of  $\text{LiAlH}_4$  in THF 1 M at 0 °C. After the addition the ice bath was removed and the mixture was stirred overnight. Then the solution was cooled down at 0 °C and methanol was added slowly (30 mL) under strong flux of nitrogen. The resulting suspension was filtered through a pad of neutral alumina and the filtrate was evaporated under reduced pressure. The product was obtained as yellowish oil purifying the crude by column chromatography on neutral alumina using acetone/10%MeOH as eluent. Yield 2.5 g (48%) as.  $^1\text{H}$  NMR ( $\text{CD}_2\text{Cl}_2$ , 400 MHz, ppm)  $\delta$ : 8.12 (d,  $J = 8$  Hz, 2H), 6.45 (d,  $J = 8$  Hz, 2H), 4.74 (s, broad, 1H), 3.65–3.70 (m, 2H), 3.64–3.58 (m, 6H), 3.52–3.50 (m, 2H), 3.34–3.28 (m, 5H);  $^{13}\text{C}$  NMR ( $\text{CD}_2\text{Cl}_2$ , 100 MHz, ppm)  $\delta$ : 154.01, 150.53, 108.16, 72.52, 71.02, 70.94, 69.61, 59.18, 42.86. HR-ESI-MS ( $m/z$ ):  $\text{C}_{12}\text{H}_{20}\text{N}_2\text{O}_3$  [ $\text{M}+\text{H}$ ] $^+$ , calcd. 241.154, found 241.115.

#### 5.4.1.3 Platinum [2,6-bis[5-(trifluoromethyl)-1,2,4-triazol-3-yl-κN<sup>2</sup>]pyridinato (2)-κN][N-[2-[2-(2-methoxyethoxy)ethoxy]ethyl]-4-pyridinamine-κN] (Pt-CF<sub>3</sub>tz-pyPEG) (1)

In a 100 mL round bottom flask compound **3** (400 mg, 1.145 mmol) and PtCl<sub>2</sub>(DMSO)<sub>2</sub> (483.7 mg, 1.145 mmol) was dissolved in 20 mL of acetonitrile then N,N-diisopropylethylamine (DIPEA) (400 μL, 2.29 mmol) was added and the resulting suspension stirred for 10 minutes. Compound **5** (357.8 mg, 1.489 mmol) dissolved in a minimum amount of MeCN was added to the solution and the resulting mixture stirred overnight at 60 °C under nitrogen. A yellow precipitate was formed during the course of the reaction. The crude was purified by column chromatography using cyclohexane:AcOEt 1:4 and then AcOEt:acetone 4:1. The product was then recrystallized by dissolving it in the minimum amount of hot MeCN upon cooling it down to room temperature overnight. A yellow cotton-like solid was formed and filtered. Yield 370 mg, 37%. <sup>1</sup>H NMR (CD<sub>2</sub>Cl<sub>2</sub>, 400 MHz, ppm) δ: 9.03 (d, *J* = 8 Hz, 2H), 8.05 (t, *J* = 8Hz, 1H), 7.79 (d, *J* = 8Hz, 2H), 5.88 (m, 1H), 3.78–3.76 (m, 2H), 3.70–3.61 (m, 6H), 3.57–3.54 (m, 2H), 3.47–3.43 (m, 2H), 3.37 (s, 3H); <sup>19</sup>F NMR (CD<sub>2</sub>Cl<sub>2</sub>, 376 MHz, ppm) δ: 64.54 (s). HR-ESI-MS (*m/z*): C<sub>23</sub>H<sub>23</sub>F<sub>6</sub>N<sub>9</sub>NaO<sub>3</sub>Pt [M+Na]<sup>+</sup>, calcd. 805.137, found: 805.136. Elemental analysis: calcd. C 35.30 %; H 2.96%; N 16.11%; found C 35.14%; H 3.04%; N 15.78%.

#### 5.4.1.4 2-(2-(2-methoxyethoxy)ethoxy)-N-(pyridin-4-ylmethyl)acetamide (4)

The amide was synthesized through acyl chloride coupling. In a typical experiment, to a toluene solution (80 ml) of 22-[2-(2-methoxyethoxy)ethoxy]acetic acid (1 g, 1 eq, 0.0056 mol), oxalyl chloride (0.95 ml, 2 eq, 0.011 mol, d= 1.5 g/ml) was added dropwise under N<sub>2</sub> at r.t. After 15 minutes, 6 drops of DMF on molecular sieves were added and a slight effervescence was noted. The solution was stirred for 6 hours at r.t. Then the solvent was evaporated and the residue was dissolved in 30ml of dry THF and added to a solution of 4-picolylamine (0.606 g, 1 eq, 0.0056 mol of amine in 100 ml of dry THF) and TEA (1.56 ml, 2 eq, 0.011 mol, d = 0.725 g/ml) under N<sub>2</sub> at 0°C. The mixture was stirred overnight, thus the solvent was evaporated to yield a

yellowish waxy solid (TLC in AcOEt/MeOH 95:5: amide R<sub>f</sub> = 0.52), which was purified by solvent extraction (DCM/water) and then by column chromatography (Al<sub>2</sub>O<sub>3</sub>: AcOEt/MeOH from 97:3 to 95:5). Collected: 859mg; yield = 57%.

<sup>1</sup>H NMR (CD<sub>2</sub>Cl<sub>2</sub> 400 MHz, ppm) δ: 3.21 (s, 3H, CH<sub>3</sub>O), 3.42 (m, 8H, CH<sub>2</sub>CH<sub>2</sub>-O-CH<sub>2</sub>CH<sub>2</sub>-O), 4.04 (s, 2H, CH<sub>2</sub>CO), 4.46 (d, J = 6.3Hz, 2H, CH<sub>2</sub>), 7.22 (d, J = 5.6 Hz, 2H, Ar-H), 8.51 (dd, 2H, Ar-H).

#### 5.4.1.5 2-(2-(2-methoxyethoxy)ethoxy)-N-(pyridin-4-ylmethyl)ethan-1-amine (5)

To a 2 necks round-bottom 100 ml flask LiAlH<sub>4</sub> (2ml of a solution 1M in THF, 1 eq) were added and stirred at 0°C under nitrogen. **4** in dry THF was added dropwise. The suspension was stirred overnight. Afterwards LiAlH<sub>4</sub> was quenched with few drops of water and AcOEt and stirred for 1h; the mixture was filtered over porous septum filter and the organic phase was evaporated. The product was purified through column chromatography (SiO<sub>2</sub>: AcOEt/MeOH 8:2, then Me<sub>2</sub>CO/MeOH 8:2).

<sup>1</sup>H NMR (CD<sub>2</sub>Cl<sub>2</sub>, 400 MHz, ppm) δ: 2.76 (t, J = 5.1Hz, 2H, CH<sub>2</sub>N), 3.32 (s, 3H, CH<sub>3</sub>), 3.47-3.58 (m, 10H, CH<sub>2</sub>CH<sub>2</sub>-O-CH<sub>2</sub>CH<sub>2</sub>-O-CH<sub>2</sub>), 3.81 (s, 2H, pyCH<sub>2</sub>), 7.27 (d, J = 5.3Hz, 2H, Ar-H), 8.49 (d, J = 5.8Hz, 2H, Ar-H).

#### 5.4.1.6 Platinum [2,6-bis[5-(trifluoromethyl)-1,2,4-triazol-3-yl-κN<sup>2</sup>]pyridinato (2)-κN][N-(4-pyridyl)2-[2-(2-methoxyethoxy)ethoxy]acetic acid amide-κN] (6)

pyC<sub>5</sub>-CF<sub>3</sub>-tzH<sub>2</sub> (0.3 g, 1 eq, 0.86 mmol) and PtCl<sub>2</sub>DMSO<sub>2</sub> (0.362 g, 1 eq, 0.86 mmol) were suspended and stirred in MeOH under N<sub>2</sub> and a yellow suspension was obtained; then TEA (0.25 ml, 2 eq, 1.72 mmol) was added and the suspension became a yellow solution after 10 minutes. Afterwards **2** (0.22 g, 1 eq, 0.86 mmol) was added dropwise and the mixture was heated up at 60°C overnight. A yellow precipitate was isolated through decantation and purified through column chromatography (SiO<sub>2</sub>: Cyclohexane/AcOEt 2:8, then AcOEt/Me<sub>2</sub>CO 7:3).

<sup>1</sup>H NMR (CD<sub>2</sub>Cl<sub>2</sub>, 400 MHz, ppm) δ: 3.46 (s, 3H, CH<sub>3</sub>), 3.63-3.80 (m, CH<sub>2</sub>CH<sub>2</sub>-O-CH<sub>2</sub>CH<sub>2</sub>-O), 4.18 (s, 2H, CH<sub>2</sub>CO), 7.86 (d, J = 8.0Hz, 2H, Ar-H), 8.02 (d, J = 7.1Hz, 2H, Ar-H), 8.09 (t, J = 8.1Hz, 1H, Ar-H), 9.58 (d, J = 7.1Hz, 3H, Ar-H and N-H). m/z: 819.1175 [M+Na]<sup>+</sup>

Elemental analysis C, H, N for C<sub>23</sub>H<sub>21</sub>F<sub>6</sub>N<sub>9</sub>O<sub>4</sub>Pt – calculated: C, 34.68; H, 2.66; F, 14.31; N, 15.83;; found: C, 34.57; H, 2.41; N, 15.50.

**5.4.1.7 Platinum [2,6-bis[5-(trifluoromethyl)-1,2,4-triazol-3-yl-κN<sup>2</sup>]pyridinato (2)-κN][2-(2-(2-methoxyethoxy)ethoxy)-N-(pyridin-4-ylmethyl)acetamide-κN] (7)**

pyC<sub>5</sub>-CF<sub>3</sub>-tzH<sub>2</sub> (0.250 g, 1 eq, 0.72 mmol) and PtCl<sub>2</sub>DMSO<sub>2</sub> (0.302 g, 1 eq, 0.72 mmol) were dissolved and stirred in MeOH under N<sub>2</sub> and a yellow suspension was obtained; then TEA (0.2 ml, 2 eq, 1.4 mmol) was added and the suspension became a yellow solution after 10 minutes. Afterwards **4** (0.193 g, 1 eq, 0.72 mmol) was added dropwise and the mixture was heated up at 60°C overnight. Hence, the solvent was evaporated and an orange waxy luminescent solid was obtained (TLC in DCM/MeOH: R<sub>f</sub> = 0.73). It was then purified through column chromatography (SiO<sub>2</sub>: DCM/MeOH from 95:5 to 90:10).

<sup>1</sup>H NMR (CD<sub>2</sub>Cl<sub>2</sub>, 400 MHz, ppm) δ: 3.25 (s, 3H, CH<sub>3</sub>), 3.49 (m, 2H, CH<sub>2</sub>), 3.64 (m, 2H, CH<sub>2</sub>), 3.67 (m, 2H, CH<sub>2</sub>), 3.76 (m, 2H, CH<sub>2</sub>), 4.10 (s, 2H, CH<sub>2</sub>CO), 4.60 (d, J = 6.3Hz, 2H, CH<sub>2</sub>N), 7.54 (d, J = 6.7Hz, 2H, Ar-H), 7.79 (d, J = 7.9Hz, 2H, Ar-H), 8.04-8.07 (t, J = 7.9Hz, 1H, Ar-H), 9.52 (d, J = 6.7Hz, 2H, Ar-H). <sup>13</sup>C NMR (CD<sub>2</sub>Cl<sub>2</sub>, 100 MHz, ppm) δ: 30.30, 42.17, 59.05, 70.63, 70.85, 70.98, 72.12, 72.33, 118.92, 125.34, 130.20, 143.87, 144.68, 149.63, 153.81, 164.72, 171.52. <sup>19</sup>F NMR (CD<sub>2</sub>Cl<sub>2</sub>, 376 MHz, ppm) δ: 64.60. m/z: 833.13 [M+Na]<sup>+</sup> Elemental analysis C, H, N for C<sub>24</sub>H<sub>23</sub>F<sub>6</sub>N<sub>9</sub>O<sub>4</sub>Pt – calculated: C, 35.56; H, 2.86; N, 15.55; found: C, 36.76; H, 3.21; N, 14.53.

**5.4.1.8 Platinum [2,6-bis[5-(trifluoromethyl)-1,2,4-triazol-3-yl-κN<sup>2</sup>]pyridinato (2)-κN][2-(2-(2-methoxyethoxy)ethoxy)-N-(pyridin-4-ylmethyl)ethan-1-amine-κN] (8)**

pyC<sub>5</sub>-CF<sub>3</sub>-tzH<sub>2</sub> (0.229 g, 1 eq, 0.66 mmol) and PtCl<sub>2</sub>DMSO<sub>2</sub> (0.277g, 1 eq, 0.66 mmol) were suspended and stirred in MeOH under N<sub>2</sub> and a yellow suspension was obtained; then TEA (0.18 ml, 2 eq, 1.3 mmol) was added and the suspension became a yellow solution after 10 minutes. Afterwards, **5** (0.167 g, 1 eq, 0.66 mmol) was

added dropwise and the mixture was heated up at 60°C overnight. Hence, the solvent was evaporated and an orange waxy luminescent solid was obtained (TLC in AcOEt/Me<sub>2</sub>CO 1:1: R<sub>f</sub> = 0.45). It was then purified through column chromatography (SiO<sub>2</sub>: AcOEt/Me<sub>2</sub>CO 1:1).

<sup>1</sup>H NMR (CD<sub>2</sub>Cl<sub>2</sub> 400 MHz, ppm) δ: 2.85 (t, 2H, CH<sub>2</sub>), 2.85 (s, 3H, CH<sub>3</sub>), 3.33-3.62 (m, 10H, CH<sub>2</sub>CH<sub>2</sub>-O-CH<sub>2</sub>CH<sub>2</sub>-O-CH<sub>2</sub>), 4.00 (s, 2H, CH<sub>2</sub>CO), 7.63 (d, J = 6.2Hz, 2H, Ar-H), 7.76 (d, J = 7.9Hz, 2H, Ar-H), 8.04 (t, J = 8.0, 1H, Ar-H), 9.45 (d, J = 6.6Hz, 2H, Ar-H). <sup>13</sup>C NMR (CD<sub>2</sub>Cl<sub>2</sub>, 100MHz, ppm) δ: 153.41, 149.45, 143.77, 125.84, 117.51, 72.51, 71.05, 71.00, 70.94, 59.19, 50.50, 49.44. m/z: 797.17 [M+H]<sup>+</sup> Elemental analysis C, H, N for C<sub>24</sub>H<sub>25</sub>F<sub>6</sub>N<sub>9</sub>O<sub>3</sub>Pt – calcd: C, 36.19; H, 3.16; N, 15.83; found: C, 35.26; H, 2.96; N, 15.67.

#### 5.4.1.9 Platinum [2,6-bis[3-(4-methylphenyl)-1,2,4-triazol-5-yl-κN<sup>2</sup>]pyridinato(2-)-κN][N-[2-[2-(2-methoxyethoxy)ethoxy]ethyl]-4-pyridinamine-κN] (9)

In a 100 mL round bottom flask pyC<sub>5</sub>-tol-tzH<sub>2</sub> (200 mg, 0.508 mmol) and PtCl<sub>2</sub>(DMSO)<sub>2</sub> (214.7 mg, 0.508 mmol) were dissolved in 20 mL of acetonitrile (ACN) then N,N-Diisopropylethylamine (DIPEA) (177 uL, 1.016 mmol) was added and the resulting suspension stirred for 10 minutes. **3** (158 mg, 0.660 mmol) dissolved in a minimum amount of ACN was added and the solution refluxed overnight under nitrogen. The mixture was then dried under vacuum at 45°C and the crude purified by column chromatography on SiO<sub>2</sub>, using cyclohexane/ethylacetate 2/1 to pure ethylacetate then ethylacetate/acetone to pure acetone. Yield 100 mg (23.7%) as yellow solid. <sup>1</sup>H NMR (CD<sub>2</sub>Cl<sub>2</sub>, 400 MHz, ppm) δ = 9.57 (2H), 8.07 (4H), 7.86 (1H), 7.66 (2H), 7.26 (4H), 6.70 (2H), 5.68 (1H), 3.75-3.39 (10H), 3.44-3.39 (5H), 2.41 (6H). <sup>13</sup>C NMR (CD<sub>2</sub>Cl<sub>2</sub>, 100 MHz, ppm) δ = 163.91, 161.05, 154.40, 152.93, 149.55, 141.61, 138.43, 130.80, 129.58, 126.46, 116.30, 72.54, 71.05, 71.02, 70.93, 69.11, 59.23, 42.67, 21.73. HR-ESI-MS: C<sub>23</sub>H<sub>23</sub>F<sub>6</sub>N<sub>9</sub>NaO<sub>3</sub>Pt (M+Na)<sup>+</sup>, Calcd: 805.137; Found: 805.136. CHN Analysis – calcd. C 35.30 %; H 2.96%; N 16.11%; found C 35.14%; H 3.04%; N 15.78%.

#### 5.4.2 Photophysical measurements

Absorption spectra were measured on a Shimadzu UV-3600 double-beam UV–VIS–NIR spectrophotometer and baseline corrected. Time- and temperature-dependent absorption spectra were recorded on a JASCO V-650 UV–VIS spectrophotometer equipped with cell holder and temperature control. Steady-state emission spectra were recorded on a Horiba Jobin–Yvon IBH FL-322 Fluorolog 3. The absolute photoluminescence quantum yields (PLQY) were measured on a Hamamatsu Quantaurus-QY integrating sphere in air-equilibrated condition using an empty quartz tube as a reference. The following procedures have been described for complex **1** as example of the class.

#### 5.4.3 Samples preparation

Compound **1** was dissolved in 2 mL of 1,4-dioxane in order to obtain a solution at concentration of  $2 \times 10^{-3}$  M. 250  $\mu$ L of the solution were taken and poured into a volumetric flask (5 mL) which was brought to volume with 1,4-dioxane (solution of monomeric **1**) or flash injected into 4750  $\mu$ L of pure distilled water (solution of metastable assembly **A**) in order to achieve a final concentration of  $1 \times 10^{-4}$  M.

#### 5.4.4 Depolymerization curves and kinetic experiments

For the depolymerization curves 1 mL of solution of metastable assembly **A** (95% water content,  $c = 1 \times 10^{-4}$  M) was poured into a quartz tube and PLQY values were measured at  $\lambda_{\text{exc}} = 362$  nm. Aliquots of 1,4-dioxane solution containing molecularly dissolved **1** ( $c = 1 \times 10^{-4}$  M) were then added and stirred 10 sec using an analog vortex mixer at 1600 rpm and measured after 50 seconds of equilibration at  $\lambda_{\text{exc}} = 362$  nm (isoabsorptive point). Kinetic experiments were carried out in a similar manner by using freshly prepared solutions of assembly **A** from the same stock solution. The measurements were carried out at single scan mode of the integrating sphere using as reference an empty quartz tube before the first measurement. Then, the sample was monitored for 450 minutes upon  $\lambda_{\text{exc}} = 362$  nm by measuring every 90 seconds. A

single point measurement was performed after 10 hours aging ( $t_{\infty}$ ) when the thermodynamic equilibrium was reached.

#### 5.4.5 Thermodynamic studies

Assembly **A** was prepared in a similar manner as described above. The sample was placed in a quartz cuvette equipped with a magnetic stirrer and a temperature control. The solution was then stirred at 500 rpm and the absorption spectra were recorded in the range 250–600 nm with a heating step of 1 K and heating rate of 1 K min<sup>-1</sup> after 30 seconds of equilibration. Assembly **C** was directly prepared inside a quartz cuvette equipped with a magnetic stirrer by mixing the solution of assembly **A** (95% water content,  $c = 1 \times 10^{-4}$  M) and the solution of 1,4-dioxane containing molecularly dissolved **1** ( $c = 1 \times 10^{-4}$  M) in order to obtain a final mixture at 60% water according to the depolymerization curve, where assembly **C** is present at room temperature as pure isoform. The solution was further diluted with H<sub>2</sub>O:1,4-dioxane 60:40 to obtain  $6 \times 10^{-5}$  M as the final concentration. The solution was then stirred at 500 rpm and heated up to 343 K. The solution was left at this temperature for 10 minutes and the absorption spectra were recorded with a heating step of 1 K and heating rate of 1 K min<sup>-1</sup> with 30 seconds of equilibration time.

Parameters	[1] = $6 \times 10^{-5}$ M water:dioxane 60:40	[1] = $1 \times 10^{-4}$ M water:dioxane 95:5
$\Delta H^0$ (kJ mol <sup>-1</sup> )	-102.5	-180.7
$\Delta H^0_{\text{STD}}$ (kJ mol <sup>-1</sup> )	2.26	14.74
$\Delta S^0$ (kJ mol <sup>-1</sup> )	-0.2	-0.5
$\Delta S^0_{\text{STD}}$ (kJ mol <sup>-1</sup> )	0.00725	0.048
$\Delta H^0_{\text{mucl}}$ (kJ mol <sup>-1</sup> )	-18.2	-0.2
$\Delta H^0_{\text{mucl\_STD}}$ (kJ mol <sup>-1</sup> )	0.95	1.4
$T_e$ (K)	318.0	321.2
$T_e_{\text{STD}}$ (K)	0.14	1.29

Table 5.1. Thermodynamic parameters obtained by fitting the curves in Fig. 5.8 with the Eikelder-Markoort-Meijer model<sup>33</sup>.

#### 5.4.6 Real-time confocal imaging

Fluorescence confocal images were recorded by using a Zeiss LSM 710 confocal microscope system with a 10× magnification objective. The samples were excited by continuous wave laser at  $\lambda_{\text{exc}} = 405$  nm. The emission of the assemblies was collected in the range from 414 to 721 nm with 9.7 nm resolution by using the lambda-mode option. Images were taken every 10 sec over a total five-hour time window by time-series experiment. The emission profiles of the three assemblies were recorded at a resolution of 3.2 nm. The raw data recorded by means of the lambda-mode were processed by using linear un-mixing tool option available in the ZEN 2011 software package (Zeiss GmbH, Germany). False colors were used to better distinguish the different assemblies, in particular, red, green and blue was used for assembly **A**, **B** and **C**, respectively.

The sample was prepared by mixing appropriate volumes of a freshly prepared solution of metastable **A** with 1,4-dioxane solution containing molecularly dissolved **1** at identical concentration ( $c = 1 \times 10^{-4}$  M) in a glass vial and then mixed gently using a syringe. A couple of drops were casted on a quartz petri dish and closed with a quartz cap for time-dependent experiments.

#### 5.4.7 Living supramolecular polymerization

Compound **1** was dissolved in 2 mL of 1,4-dioxane in order to obtain a solution at  $c = 1 \times 10^{-3}$  M then 250  $\mu\text{L}$  of the solution were flash-injected into 4750  $\mu\text{L}$  of pure distilled water (solution of metastable **A**, 95% water content) in order to achieve a final concentration of  $5 \times 10^{-5}$  M. Size distribution was then measured by DLS. The solution was sonicated for 3 hours (45 kHz, 120 W). The total conversion of assembly **A** into assembly **C** was confirmed by recording emission and excitation spectra, while size distribution was measured by DLS. To 2 mL of freshly prepared assembly **A** ( $c = 5 \times 10^{-5}$  M), aliquots of solution containing seeds of assembly **C** (10, 20, 30, 40, 50 and 60  $\mu\text{L}$ ,  $c = 5 \times 10^{-5}$  M) was added, and the resulting mixture was manually shaken for few

seconds and monitored through absorption spectroscopy at room temperature at  $\lambda_{\text{abs}} = 362$  nm. An aliquot of the resulting solution was drop casted onto a glass cover slip and the drop removed with a syringe. The luminescent assemblies deposited onto glass were easily imaged by using the confocal microscopy.

#### 5.4.8 Photoconversion experiments

Few drops of a solution obtained from living supramolecular polymerization (95 % water content) were casted onto a glass substrate and irradiated at  $\lambda_{\text{exc}} = 405$  nm with high power. The images were taken every second for 5 minutes by time-series experiment. The raw data recorded by means of the lambda-mode were preceded by using linear un-mixing tool option available in the ZEN 2011 software package (Zeiss GmbH, Germany). False colors were used to better distinguish the different assemblies, in particular, green and blue were used for assembly **B** and **C**, respectively.

### 5.5 References

- [1] J.-M. Lehn, *Science*, **2002**, *295*, 2400-2403.
- [2] D. N. Reinhoudt; M. Crego-Calama, *Science*, **2002**, *295*, 2403-2407.
- [3] G. M. Whitesides; B. Grzybowski, *Science*, **2002**, *295*, 2418-2421.
- [4] G. Whitesides; J. Mathias; C. Seto, *Science*, **1991**, *254*, 1312-1319.
- [5] T. Aida; E. W. Meijer; S. I. Stupp, *Science*, **2012**, *335*, 813-817.
- [6] G. M. Whitesides; M. Boncheva, *Proc. Natl. Acad. Sci. U.S.A*, **2002**, *99*, 4769-4774.
- [7] P. Jonkheijm; P. van der Schoot; A. P. Schenning; E. W. Meijer, *Science*, **2006**, *313*, 80-83.
- [8] J. M. Lehn, *Proc. Natl. Acad. Sci. U.S.A*, **2002**, *99*, 4763-4768.
- [9] J.-M. Lehn, *Angew. Chem. Int. Ed. Engl.*, **1990**, *29*, 1304-1319.
- [10] E. Busseron; Y. Ruff; E. Moulin; N. Giuseppone, *Nanoscale*, **2013**, *5*, 7098-7140.
- [11] Y. Mai; A. Eisenberg, *Chem. Soc. Rev.*, **2012**, *41*, 5969-5985.
- [12] P. A. Korevaar; C. J. Newcomb; E. W. Meijer; S. I. Stupp, *J. Am. Chem. Soc.*, **2014**, *136*, 8540-8543.
- [13] F. Rodriguez-Llansola; E. W. Meijer, *J. Am. Chem. Soc.*, **2013**, *135*, 6549-6553.
- [14] A. Lohr; M. Lysetska; F. Wurthner, *Angew. Chem. Int. Ed. Engl.*, **2005**, *44*, 5071-5074.
- [15] H. Cui; Z. Chen; S. Zhong; K. L. Wooley; D. J. Pochan, *Science*, **2007**, *317*, 647-650.
- [16] P. A. Korevaar; S. J. George; A. J. Markvoort; M. M. Smulders; P. A. Hilbers; A. P. Schenning; T. F. De Greef; E. W. Meijer, *Nature*, **2012**, *481*, 492-496.
- [17] E. T. Powers; D. L. Powers, *Biophys. J.*, **2008**, *94*, 379-391.
- [18] S. Ogi; K. Sugiyasu; S. Manna; S. Samitsu; M. Takeuchi, *Nat. Chem.*, **2014**, *6*, 188-195.
- [19] M. Mydlak; M. Mauro; F. Polo; M. Felicetti; J. Leonhardt; G. Diener; L. De Cola; C. A. Strassert, *Chem. Mater.*, **2011**, *23*, 3659-3667.

- [20] G. Åkerlöf; O. A. Short, *J. Am. Chem. Soc.*, **1936**, *58*, 1241-1243.
- [21] F. Hovorka; R. A. Schaefer; D. Dreisbach, *J. Am. Chem. Soc.*, **1936**, *58*, 2264-2267.
- [22] G. Lukinavicius; K. Umezawa; N. Olivier; A. Honigmann; G. Yang; T. Plass; V. Mueller; L. Reymond; I. R. Correa, Jr.; Z. G. Luo; C. Schultz; E. A. Lemke; P. Heppenstall; C. Eggeling; S. Manley; K. Johnsson, *Nat. Chem.*, **2013**, *5*, 132-139.
- [23] M. Mauro; A. Aliprandi; C. Cebrian; D. Wang; C. Kübel; L. De Cola, *Chem. Commun.*, **2014**, *50*, 7269-7272.
- [24] C. A. Strassert; C. H. Chien; M. D. Galvez Lopez; D. Kourkoulos; D. Hertel; K. Meerholz; L. De Cola, *Angew. Chem. Int. Ed. Engl.*, **2011**, *50*, 946-950.
- [25] V. W.-W. Yam; K. M.-C. Wong; N. Zhu, *J. Am. Chem. Soc.*, **2002**, *124*, 6506-6507.
- [26] B. Ma; J. Li; P. I. Djurovich; M. Yousufuddin; R. Bau; M. E. Thompson, *J. Am. Chem. Soc.*, **2005**, *127*, 28-29.
- [27] C. Po; A. Y. Tam; K. M. Wong; V. W. Yam, *J. Am. Chem. Soc.*, **2011**, *133*, 12136-12143.
- [28] M. Krikorian; S. Liu; T. M. Swager, *J. Am. Chem. Soc.*, **2014**, *136*, 2952-2955.
- [29] A. Aliprandi; D. Genovese; M. Mauro; L. D. Cola, *Chem. Lett.*, in press.
- [30] M. M. J. Smulders; A. P. H. J. Schenning; E. W. Meijer, *J. Am. Chem. Soc.*, **2008**, *130*, 606-611.
- [31] C. Schaefer; I. K. Voets; A. R. A. Palmans; E. W. Meijer; P. van der Schoot; P. Besenius, *ACS Macro Letters*, **2012**, *1*, 830-833.
- [32] P. A. Korevaar; C. Schaefer; T. F. de Greef; E. W. Meijer, *J. Am. Chem. Soc.*, **2012**, *134*, 13482-13491.
- [33] H. M. ten Eikelder; A. J. Markvoort; T. F. de Greef; P. A. Hilbers, *J. Phys. Chem. B*, **2012**, *116*, 5291-5301.
- [34] A. M. Morris; M. A. Watzky; R. G. Finke, *Biochimica et biophysica acta*, **2009**, *1794*, 375-397.
- [35] D. Zhao; J. S. Moore, *Org. Biomol. Chem.*, **2003**, *1*, 3471-3491.
- [36] I. V. Baskakov; G. Legname; M. A. Baldwin; S. B. Prusiner; F. E. Cohen, *The Journal of biological chemistry*, **2002**, *277*, 21140-21148.
- [37] Z. M. Hudson; C. E. Boott; M. E. Robinson; P. A. Rugar; M. A. Winnik; I. Manners, *Nat. Chem.*, **2014**, *6*, 893-898.
- [38] P. A. Rugar; L. Chabanne; M. A. Winnik; I. Manners, *Science*, **2012**, *337*, 559-562.
- [39] J. B. Gilroy; T. Gadt; G. R. Whittell; L. Chabanne; J. M. Mitchels; R. M. Richardson; M. A. Winnik; I. Manners, *Nat. Chem.*, **2010**, *2*, 566-570.
- [40] *Principles of Polymerization*, ed. John Wiley & Sons, Inc., **2004**



# Chapter 6

## Bioimaging by self-assembling Pt(II) complexes

**Abstract:** This chapter describes how the establishment of Pt...Pt interactions between neighboring Pt(II) complexes can be advantageously used to obtain dynamic labels for imaging application. The assemblies possess enhanced and tunable properties with distinct features respect to the molecularly dissolved Pt(II) complexes. Such assemblies have been internalized inside HeLa cells giving Stable, highly emissive and long-lived aggregates and the assembly and disassembly process can be explored as a tool to obtain dynamic labels for imaging application. We have found that the molecular design and the conditions used for the incubation determine cell internalization of the platinum complexes, as well as, their eventual expulsion in the media.

## 6.1 Introduction

Even though Pt(II) complexes have been extensively studied for cancer therapy<sup>1</sup> due to their high toxicity, much less work has been done for their application as bio-imaging probes compared to the compounds discussed previously. Organometallic complexes of Pt(II) possess attractive properties and several groups have reported luminescent Pt(II) complexes able to enter into living cells and, in some cases, to selectively stain specific compartments<sup>2</sup>. Williams group<sup>3,4</sup> shows how highly emissive and photostable Pt(II) complexes can be used in bioimaging using a combination of confocal one-photon excitation or nonlinear two photon excitation (TPE) with time-resolved emission imaging microscopy (TREM) on a hitherto uncharted microsecond time scale. The long lifetime up to  $\mu\text{s}$  allows an easy separation of the signal coming from the phosphorescent complex from fluorescent signals such as from a solution of fluorescein in 1M concentration,<sup>3</sup> in addition lifetime mapping can be used to image live cells and tissue section with a wealth of detail within the cell, illuminating, in particular, nuclear and cell membranes. The general trend observed is the increase of the excited state lifetimes when moving from the cell membrane, through the cytoplasm and into the nucleolus, which has been assigned to a variable degree of protection from quenching. The self-assembly of Pt(II) complexes into supramolecular structures with enhanced photochemical properties, induced by the establishment of metallophilic interactions (MMLCT band), can be advantageously used for shifting both the excitation and the emission in more biologically interesting spectral windows, such as red and NIR regions. Furthermore the dynamic formation of such assemblies, often followed by an increase of the PLQY, as well as, a prolongation of the excited state lifetime, may results in the creation of a new class of bright dynamic probes.

## 6.2 Results and discussion

The cell is the basic functional unit of life. All cells have a membrane that envelops the cell and separates its interior from the surrounding environment. This membrane is made mostly from the amphiphilic phospholipid bilayer. A variety of protein

molecules are embedded in this membrane. They act as channels and pump for different molecules to move into and out of the cell. In addition, the membrane maintains the electric potential of the cell. As a result, for small- molecule-based heavy-metal complexes, the cellular uptake and compartmentalization behaviors are usually related to their charge, size, substitute group and hydrophobicity/hydrophilicity.<sup>5</sup> Before discussing the effect of chemical structures on cellular uptake of phosphorescent heavy-metal complexes, it is necessary to understand the role of incubated media with permeabilizing organic solvent in cell imaging experiments. DMSO and short chain alcohols have been for long time in biochemistry as the cell permeabilization agents at a concentration of approximately 1% v/v. In fact, DMSO makes the membrane significantly floppy, even induces the formation of water pores in the membrane for high concentration of DMSO, and permeabilizes the phospholipid membrane, corresponding to membrane permeability enhancement particularly for hydrophilic molecules. In order to be usefully applied in fluorescence microscopy these complexes must have certain attributes in particular:

- i. *Stability and solubility* in aqueous buffers or growth media.
- ii. *Low Toxicity*. Must be non-toxic to the organism at least over the course of the experiment; should not show phototoxicity (i.e. generate fatal levels of toxic species such as  $^1\text{O}_2$ ).
- iii. *Fast uptake*. Must be readily taken up into the cells, preferably without the addition of chemical agents to assist membrane permeability (DMSO). Often this requires high lipophilicity in the lumophore.
- iv. *Localisation*. Either show preferential localisation in a certain organelle of the cell, or be easily adaptable by bioconjugation to endow this property upon a basic structure.<sup>6</sup>

As previously described in chapter 1, some of these properties are in conflict with each other like the water solubility and the fast internalization, which generally requires, instead, a lipophilic character in order to cross the phospholipidic membrane of the cells. Many of these features such as localization as well as the photophysical properties under physiological conditions cannot be predicted a priori

so most of the novel luminescent molecules were discovered serendipitously or by screening library of compounds.<sup>7-9</sup> However all the Pt(II) complexes described so far were not water soluble at all, even the complexes described in chapter 5, that possess an hydrophilic PEG chain, were not uptake by the cells in the typical experimental conditions (see experimental part).

### 6.2.1 Synthesis of the platinum complexes

Initially, 4-hydroxypyridine has been chosen as the ancillary ligand to provide an amphiphilic character to the complexes while keeping the overall charge neutral in nature and the size small. Neutral square-planar platinum complexes are indeed expected to show higher aggregation tendency than charged counterparts, due to the fact that the latters might experience much higher repulsive electrostatic interactions when spatially near.<sup>10</sup>

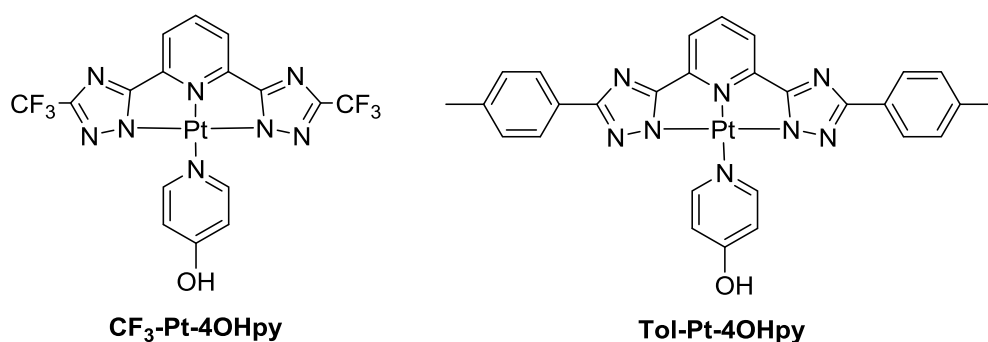
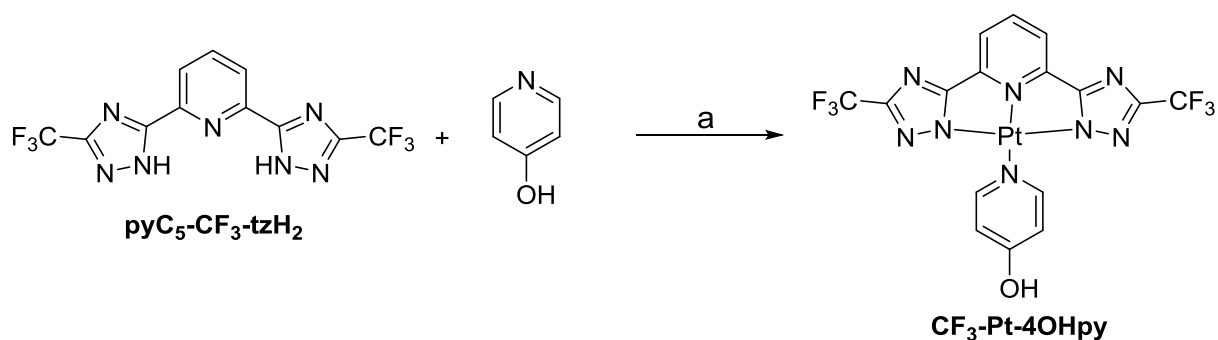


Figure 6.1. Structure of the platinum complexes.

The complexation reaction consists in a one pot reaction in which the tridentate ligand, a platinum precursor and an ancillary ligand, in presence of a base are heated up from 50 to 85°C under N<sub>2</sub> atmosphere (see chapter 3). The synthesis of the complex **CF<sub>3</sub>-Pt-4OHpy** is shown in Scheme 6.1.



Scheme 6.1. Synthesis of  $\text{CF}_3\text{-Pt-4OHpy}$ . (a)  $\text{Pt}(\text{DMSO})_2\text{Cl}_2$ , TEA, 3 : 1 2-methoxyethanol: water, 85°C, 15.7% yield.

The complex **Tol-Pt-4OHpy** was prepared in similar conditions described above, by employing  $\text{pyC}_5\text{-tol-tzH}_2$ <sup>11</sup> as tridentate ligand (see experimental part for details). Unfortunately, due to the absence of solubilizing chains in the ancillary pyridine, both complexes display very low solubility in organic solvents<sup>11-14</sup> and no solubility in polar media such as water.

## 6.2.2 Photophysical properties

The absorption spectra of both complexes in DMSO solution are shown in Figure 6.2.

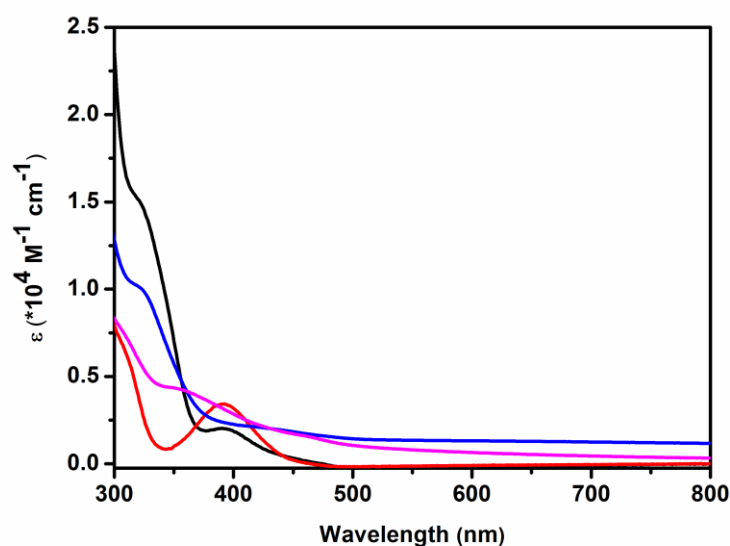


Figure 6.2. Electronic absorption spectra for complex **Tol-Pt-4OHpy** in DMSO (black trace) and DMSO:H<sub>2</sub>O 1:99 v/v (blue trace) and for complex **CF<sub>3</sub>-Pt-4OHpy** in DMSO (red trace) and DMSO:H<sub>2</sub>O 1:99 v/v (magenta trace).

The compounds display broad and featureless weak bands ( $\epsilon = 3.4 \times 10^3 \text{ M}^{-1} \text{ cm}^{-1}$  and  $2.2 \times 10^3 \text{ M}^{-1} \text{ cm}^{-1}$  for **CF<sub>3</sub>-Pt-4OHpy** and **Tol-Pt-4OHpy**, respectively) centered at

around 390 nm, which can be attributed to spin-allowed metal-to-ligand charge-transfer ( $^1\text{MLCT}$ ) transitions, as already reported for closely related complexes<sup>2,11,13</sup>, that mainly involve the platinum d orbitals partially mixed with the terdentate-ligand-centered  $\pi$  and  $\pi^*$  orbitals. Complex **Tol-Pt-4OHpy** presents a strong featureless band at about 320 nm attributed to ligand-centered ( $^1\text{LC}$ )  $\pi \rightarrow \pi^*$  transitions involve the tolyl groups. However only **Tol-Pt-4OHpy** shows an emission at room temperature when excited at any of the absorption bands, with a maximum at 534 nm, while the trifluoro-methyl derivative is not emissive in this condition (Figure 6.3)

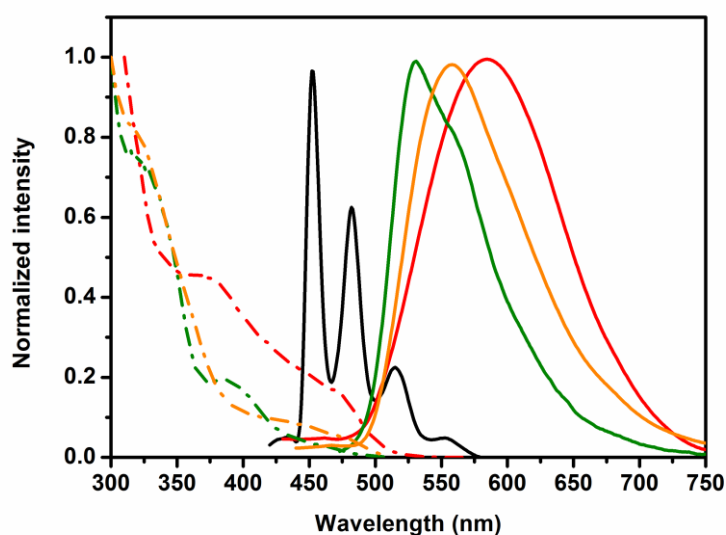


Figure 6.3. Emission (solid traces) and excitation (---) spectra for complexes **Tol-Pt-4OHpy** and **CF<sub>3</sub>-Pt-4OHpy** in different conditions. Emission and excitation for **Tol-Pt-4OHpy** in pure DMSO (green traces) and in DMSO:H<sub>2</sub>O solutions (1 : 99 v/v) (orange trace); **CF<sub>3</sub>-Pt-4OHpy** at 77 K in 2-MeTHF glassy matrix (black trace) and in DMSO: H<sub>2</sub>O(1 : 99 v/v) (red trace). The samples were excited at  $\lambda_{exc}=330$  nm.

The excitation spectrum, also depicted in Figure 6.3, is very similar to the absorption spectrum recorded in the same conditions. Interestingly, the addition of water in the DMSO solution, DMSO:H<sub>2</sub>O (1 : 99 v/v), causes the formation of aggregates for both complexes. For the **Tol-Pt-4OHpy** the emission shifts to lower energy reaching a maximum at 562 nm, while the **CF<sub>3</sub>-Pt-4OHpy** displays now an emission at 587 nm. The fact that aggregates are formed is also visible looking at the excitation spectra as clearly demonstrated by the formation of a new broad band around 450 nm for **Tol-Pt-4OHpy** while for the **CF<sub>3</sub>-Pt-4OHpy** the onset shifts to very low energy reaching

520 nm. These low energy bands, which are absent in pure DMSO solutions, are attributed to the transitions involving a new excited state, namely  $^3\text{MMLCT}$ , which is promoted by metallophilic interactions between platinum centers. The emission of the molecularly dissolved complex **CF<sub>3</sub>-Pt-4OHpy**, can be detected only at 77 K in 2-MeTHF glassy matrix. The structured emission presents vibrational sharp peaks at 452, 482 and 515 nm, it is attributed mainly to the ligand centered (LC) transitions. At room temperature, the excited state lifetimes of the complexes show multi-exponential kinetics and, for **Tol-Pt-4OHpy**, they become longer going from pure DMSO to DMSO/H<sub>2</sub>O solutions (Table 6.1). The elongation of the lifetimes is due to a synergic effect between the establishment of metallophilic interactions that lead to the formation of a new excited state with  $^3\text{MMLCT}$  character and rigidochromic effect due to the high packing of the molecule which decreases non radiative pathways and protects the lumophore from quenching. In fact the emission quantum yield for **CF<sub>3</sub>-Pt-4OHpy** reaches a value as high as 36% in the aggregate form in air-equilibrated DMSO:H<sub>2</sub>O (1 : 99 v/v) condition.

Compound	$\lambda_{\text{abs}} (\epsilon)$ [nm, $\times 10^3 \text{ M}^{-1} \text{ cm}^{-1}$ ] 1]	$\lambda_{\text{em}}$ [nm]	$\tau$ [ns]	PLQY (%)	DMSO:H <sub>2</sub> O 1:99		
					$\lambda_{\text{em}}$ [nm]	$\tau$ [ns]	PLQY (%)
<b>CF<sub>3</sub>-Pt-4OHpy</b>	392 (3.4) <sup>a</sup>	452, 482, 515 <sup>b</sup>	–	–	587	163 (57%) 22 (28%) 365 (14%)	36
<b>Tol-Pt-4OHpy</b>	322 (14.9), 390 (2.0) <sup>a</sup>	534 <sup>a</sup>	5.1 (26%) 205 (67%) 476 (7%)	1.2 <sup>a</sup>	562	662 (55%) 139 (27%) 1772 (19%)	2.8

Table 6.1. Most meaningful photophysical data for complexes **Tol-Pt-4OHpy** and **CF<sub>3</sub>-Pt-4OHpy** in DMSO and DMSO:H<sub>2</sub>O (1 : 99 v/v) solutions.

### 6.2.3 Bioimaging

The platinum complexes were dissolved in a minimum amount of DMSO and the respective solutions were diluted into phosphate buffer saline, PBS, resulting in a 50  $\mu\text{M}$  solution with less than 1% content in DMSO. HeLa cells were incubated for 4 hours at 37 °C under 5% CO<sub>2</sub> atmosphere with the complexes, washed with complex-

free PBS, followed by cell fixation using 4% paraformaldehyde (PFA) solution. The two complexes show bright emission coming from different cellular compartments indicating cell internalization. The emission of **Tol-Pt-4OHpy** was mainly observed from cytoplasmic region while **CF<sub>3</sub>-Pt-4OHpy**, was partially distributed in the cytoplasmic region but bright aggregates were observed inside the nucleus. At this stage we have no evidence if the metal complexes are internalized as monomeric species and then aggregate inside cells or they are uptaken as small aggregates. The emission spectra taken from the highly emissive spots clearly demonstrate that for both complexes the emission energy and shape correspond to the assembled systems in DMSO:water solution (Figure 6.4 and Figure 6.5).

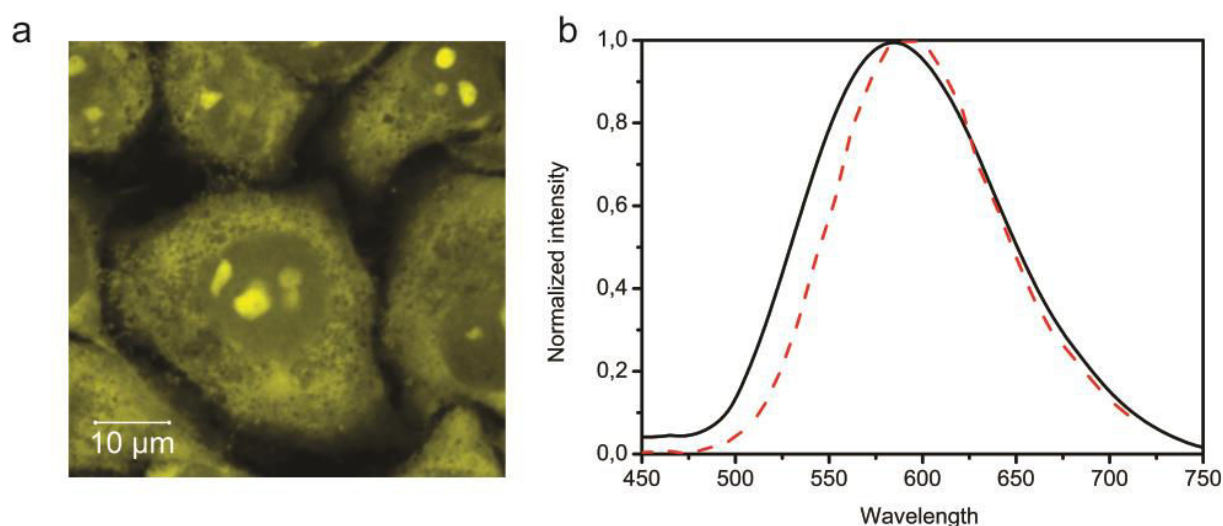


Figure 6.4. (a) Luminescence confocal microscopy images show the distribution of **CF<sub>3</sub>-Pt-4OHpy** inside HeLa cells; (b) emission spectra recorded in DMSO:H<sub>2</sub>O solution (black solid trace) and from the bright aggregate inside the nuclear region (dashed red trace). The samples were excited at  $\lambda_{exc} = 330$  and 405 nm for solvents and cell experiments, respectively.

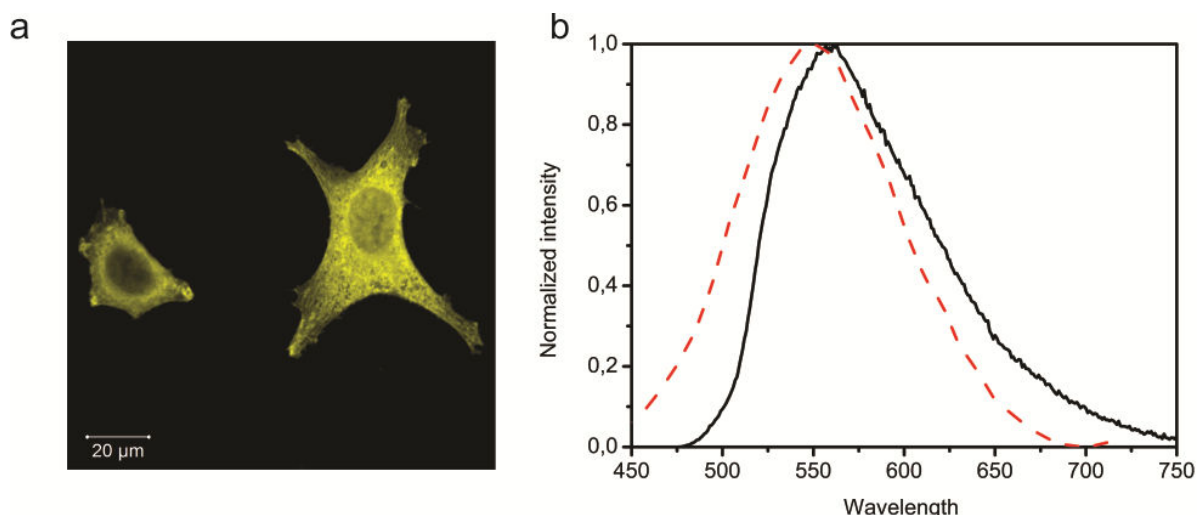


Figure 6.5. (a) Luminescence confocal microscopy images show the distribution of complex **Tol-Pt-4OHpy** inside HeLa cells; (b) emission spectra recorded for DMSO:H<sub>2</sub>O solution (solid black trace) and collected from the cytoplasmic region of the cells (dashed red trace). The samples were excited at  $\lambda_{exc} = 330$  and 405 nm for solvents and cell experiments, respectively.

To better understand the localization of the **CF<sub>3</sub>-Pt-4OHpy** complex, co-localization studies were performed by staining the three regions where we observe the orange emission. The cells were labelled with 40,6-diamidino-2-phenylindole-6-carboxamide (DAPI) (nucleus label), Phalloidin Alexa Fluor® 568 (F-actin stain) and SYTO® RNASelect™ Green Fluorescent Cell Stain (nucleoli stain).

As depicted in Figure 6.6a,b, **CF<sub>3</sub>-Pt-4OHpy** is able to localize into cytoplasm and also inside the nucleus. The perfect overlap of the emission of the complex and the SYTO® RNASelect™ green fluorescence indicates that the assemblies are present in the nucleoli (Figure 6.6b). To prove that the complex is really inside the cell we have also done z-scan acquisitions by means of a confocal microscope and the results are displayed in Figure 6.6c.

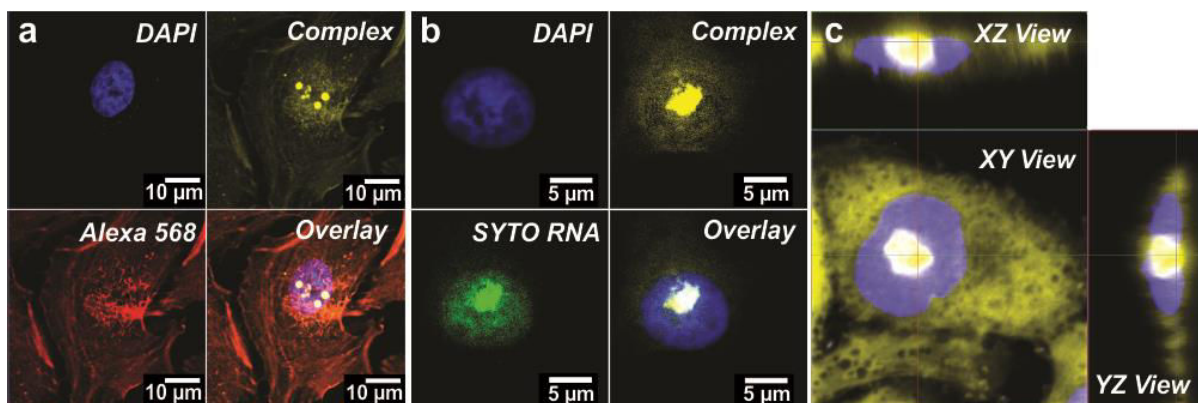


Figure 6.6. Confocal microscopy images of the distribution of **CF<sub>3</sub>-Pt-4OHpy** inside HeLa cells. (a) DAPI staining of nucleus, complex **CF<sub>3</sub>-Pt-4OHpy**, Phalloidin Alexa Fluor® 568 stains F-actin inside cytoplasmic region, overlay of three images. The excitation wavelength for DAPI and **CF<sub>3</sub>-Pt-4OHpy** was 405 nm, while Phalloidin Alexa Fluor® 568 was excited at 594 nm. Localization experiments (b) show DAPI staining the nucleus, SYTO® RNASelect™ Green Fluorescent Cell Stain labels the nucleoli ( $\lambda_{exc} = 488$  nm), and in yellow the emission of **CF<sub>3</sub>-Pt-4OHpy**. The overlay image suggests that the aggregates are confined in the nucleoli. (c) Orthogonal view of the image show a very bright signal (yellow) due to **CF<sub>3</sub>-Pt-4OHpy** aggregates coming from inside the nuclear region and co-localized into the nucleoli. Blue color is due to the DAPI staining.

Interestingly, these complexes show aggregation process through (extended) ground-state  $d_{z^2}-d_{z^2}$  metallophilic interactions possess low-lying  $^1\text{MMLCT}$  state. As can be clearly seen from Figure 6.3 we should be able to excite the systems also in the visible region since the excitation spectrum extend to almost 550 nm. To prove that excitation can be as low as 543 nm, we have recorded emission images upon different excitation wavelengths thus showed that we can efficiently use this complex and overcome the problem related to the excitation energy as shown for **CF<sub>3</sub>-Pt-4OHpy** in Figure 6.7.

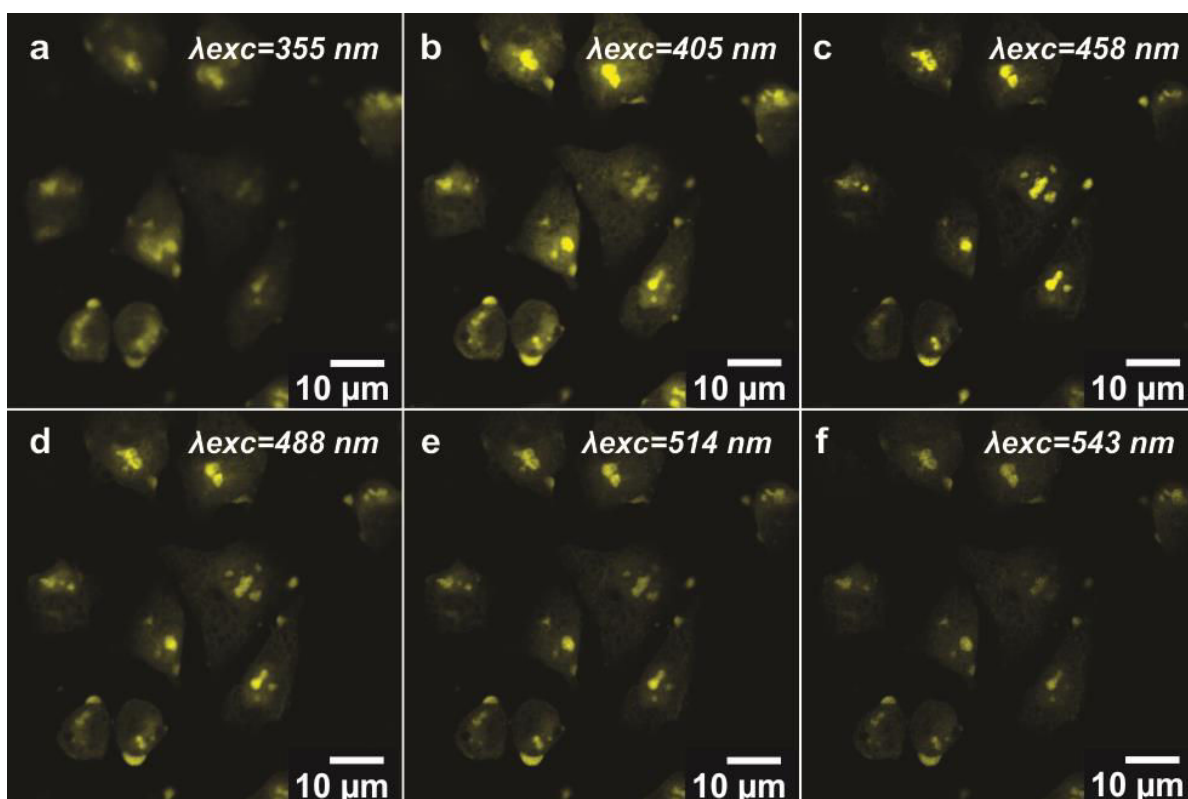


Figure 6.7. Fluorescence confocal microscopy images of **CF<sub>3</sub>-Pt-4OHpy** internalized in HeLa cells after 4 hours incubation in PBS. The samples were excited at 355 nm (a), 405 nm (b), 458 nm (c), 488 nm (d), 514 nm (e), and 543 nm (f).

The aggregation process is not only leading to the protection of the platinum complexes and prevents oxygen quenching, as already discussed above, but also to reduced photobleaching. In order to estimate, to a certain extent, the degree of photostability of the investigated systems inside the nucleus of cells, we have compared the photobleaching time of DAPI, used to stain nuclear region, with our platinum complexes upon excitation at the same wavelength, 405 nm. The results are displayed in Figure 6.8 and clearly suggest that our label is more photostable than the organic dye.

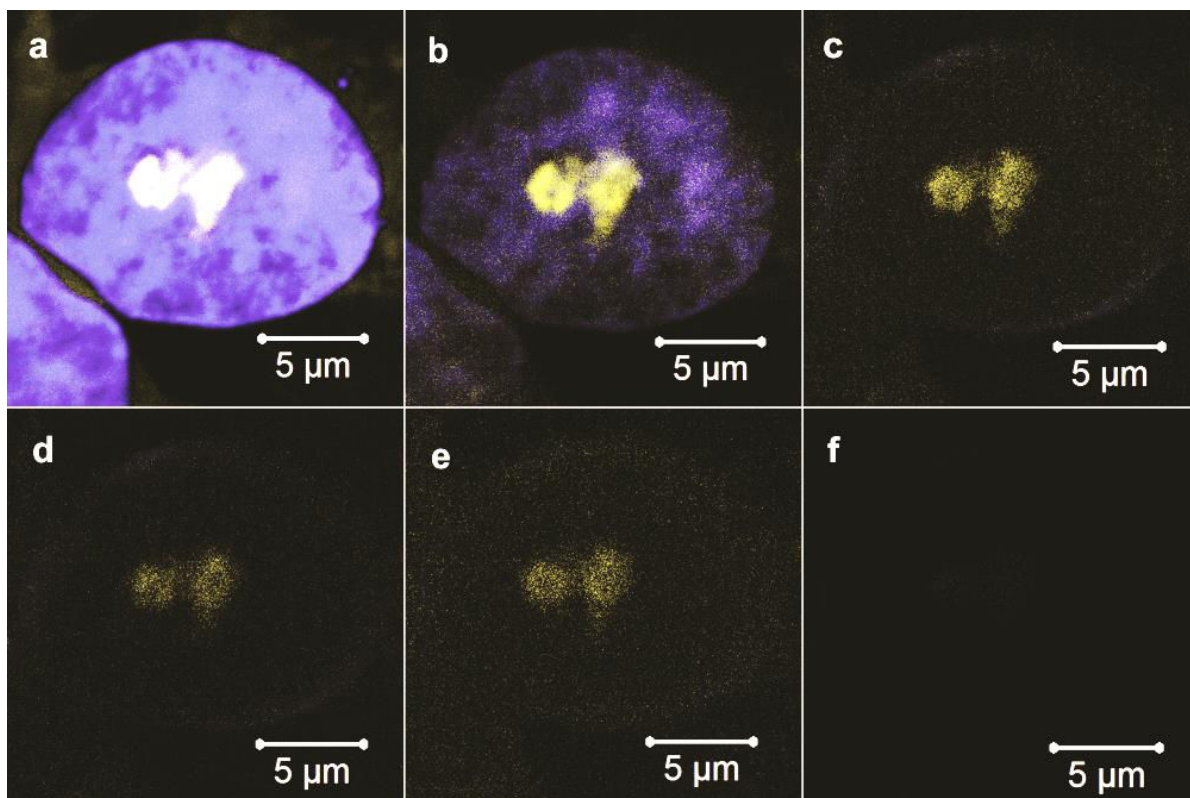


Figure 6.8. Fluorescence confocal microscopy images show the photostability of **CF<sub>3</sub>-Pt-4OHpy** towards photobleaching relative to DAPI. Panels (c-e) show that DAPI (blue) has been already photobleached meanwhile **CF<sub>3</sub>-Pt-4OHpy** (yellow) still maintains its emission even after 20 minutes of continuous UV irradiation at 405 nm. The sample was continuously excited with high power laser (32 mW) for 5 minutes and subsequently imaged at low power acquisition (1.2 mW) every 5 minutes for a total time of 25 minutes.

It's important to point out that the uptake of the platinum complexes and their internalization in HeLa cells occur only when PBS is used as incubation media. Indeed, the replacement of PBS with cell culture media prevented the complexes to be internalized by the cells. Figure 6.9 shows the experiments carried out for the complex **CF<sub>3</sub>-Pt-4OHpy**. The data obtained suggest that the platinum complex is somehow sequestered by the culture media, most likely because of an interaction with one of the proteins, and therefore is not uptaken by the cells even if the incubation time is extended to 24 hours.

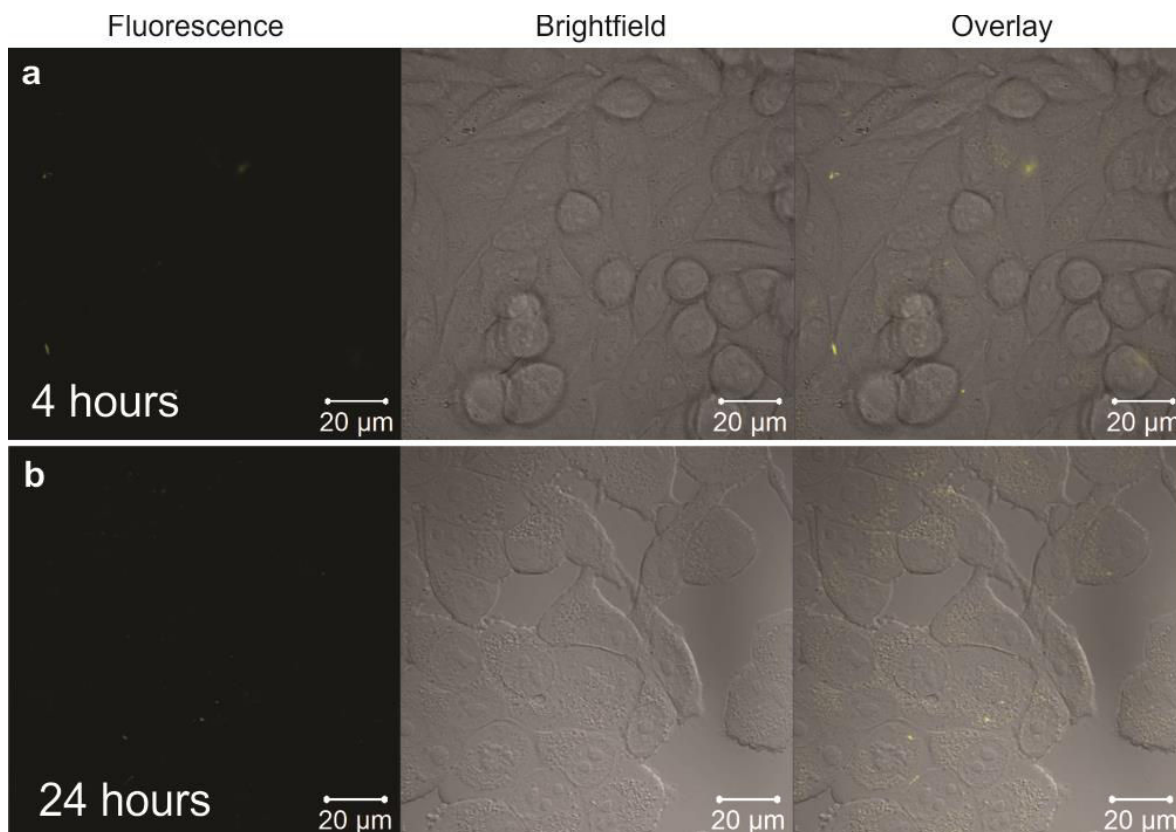


Figure 6.9. Fluorescence confocal microscopy images show no uptake of **CF<sub>3</sub>-Pt-4OHpy** in HeLa cells even after (a) 4 and (b) 24 hours incubation time in culture media. Cells were excited at 405 nm.

Furthermore, to confirm this hypothesis, the complex was incubated for 20 minutes in PBS solution with cells and, as expected, internalization occurred (Figure 6.10). At this point, the cells were washed several times with PBS to eliminate the excess of the complex and the PBS was replaced by normal culture media. After several minutes (Figure 6.10b and c), the luminescence slowly disappears from inside the cells and surprisingly it has been detected in bright small spots surrounding the cells, but clearly in the cell culture media.

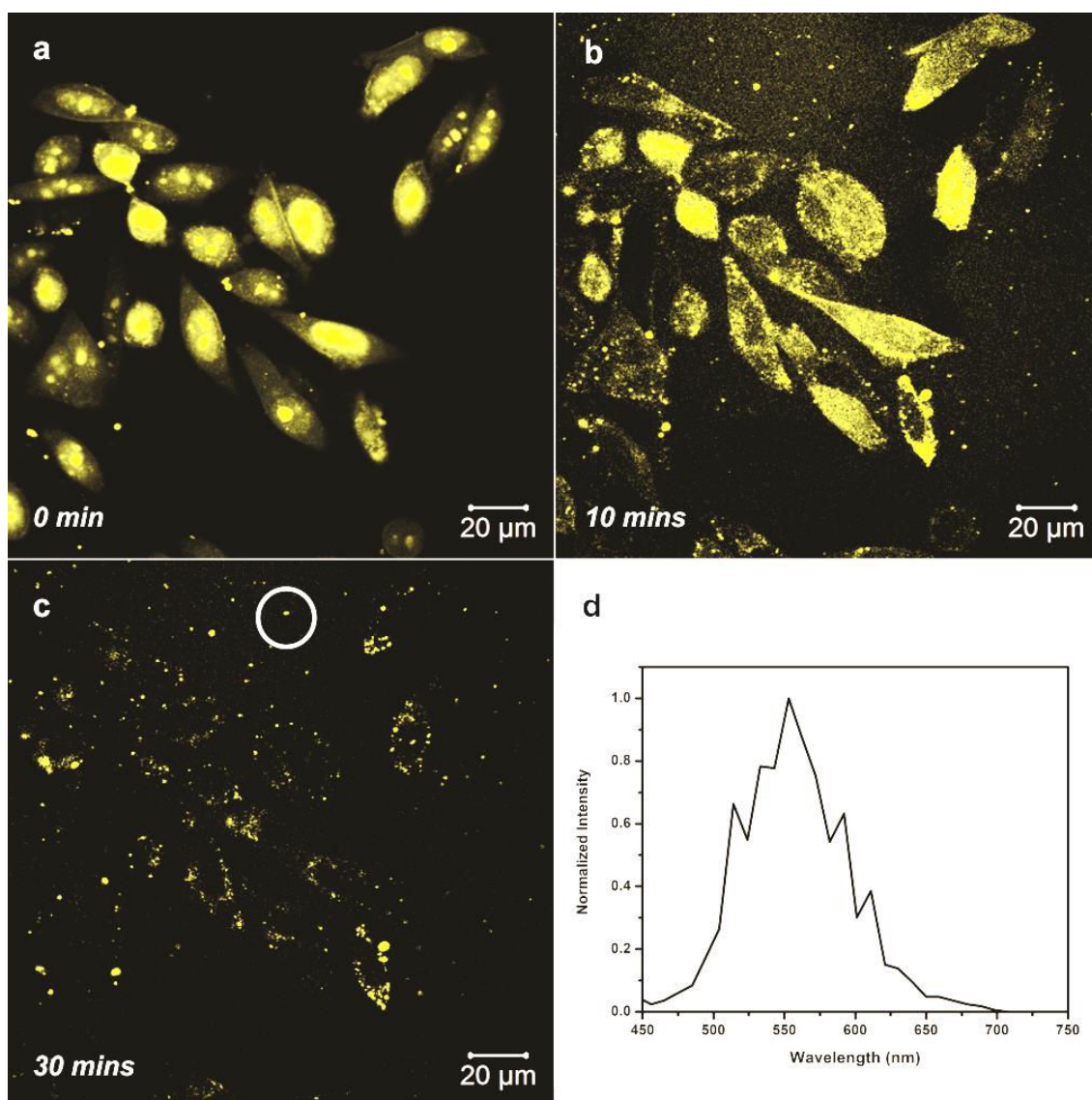


Figure 6.10. The complex **CF<sub>3</sub>-Pt-4OHpy** is aggregated inside the nucleus after 20 min incubation in PBS and replacement of the PBS with cell culture media causes its externalization in few minutes: (a) 0 minute, (b) 10 minutes, and (c) 30 minutes. (d) Emission spectrum recorded from the small aggregates in the white circle region, showing a maximum centered at 550 nm.

In addition, the emission profile collected from several of these aggregates confirms that photoluminescence is coming from the platinum compounds, but the wavelength ( $\lambda_{em} = 550$  nm) is hypsochromically shifted compared to the platinum aggregates inside the cells. This observation supports the hypothesis that the platinum complexes experience a different environment and therefore change their emission properties. However, internalization of the platinum complexes using cell culture media as the incubating media can occur if the cells are dying or cell membrane is partly damaged. Live cell imaging was performed on HeLa cells

incubated with **CF<sub>3</sub>-Pt-4OHpy** in cell culture media using time-lapse acquisition mode. The complex was excited at 405 nm and the emission signal was collected with one-minute acquisition time for a total duration of 75 minutes. The slices of time-lapse images for 0 to 75 minutes can be seen in Figure 6.11.

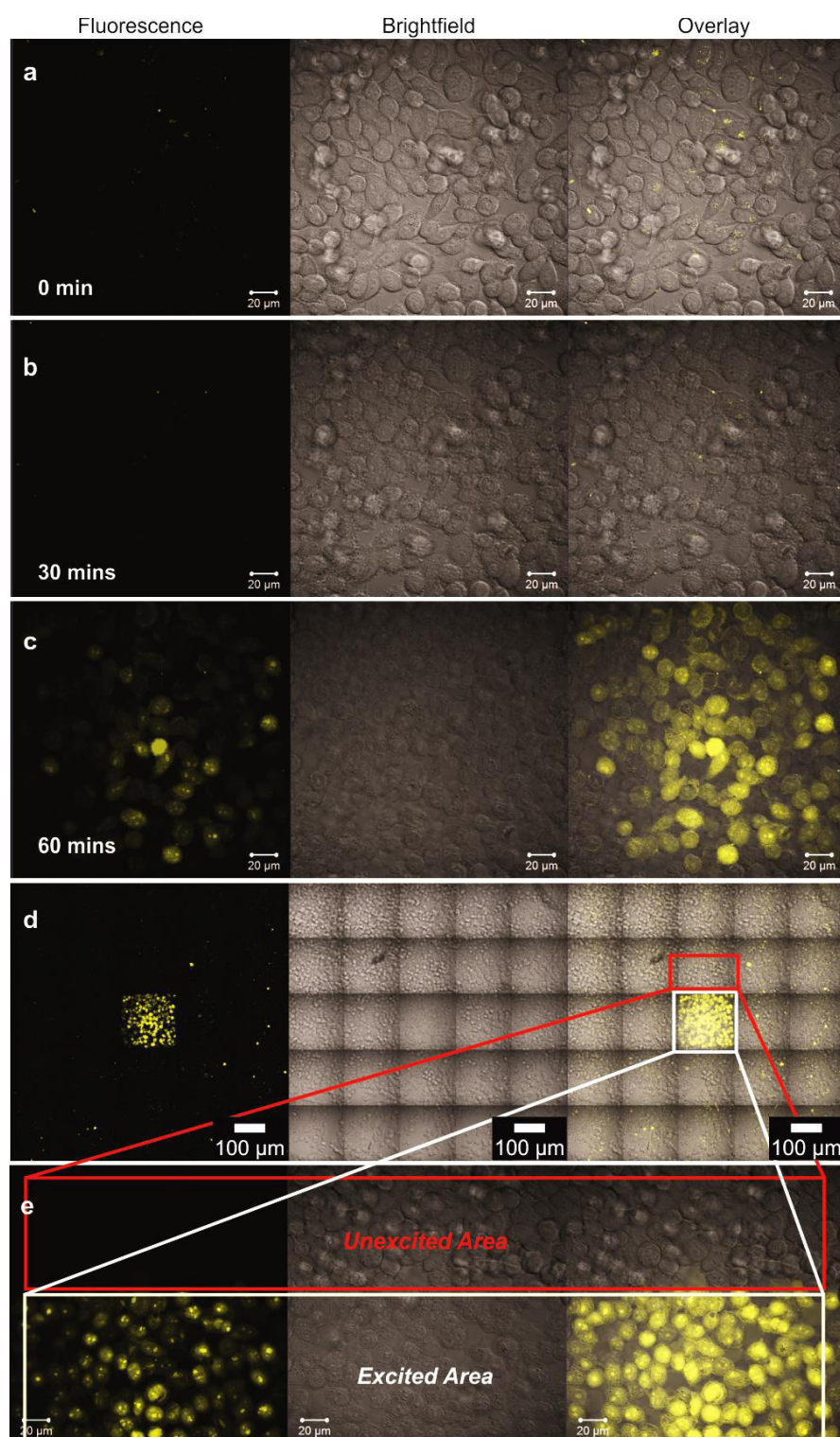


Figure 6.11. Time-lapse images show the light-induced internalization of **CF<sub>3</sub>-Pt-4OHpy** in culture media after different irradiation times: (a) 0 minute, (b) 30 minutes, and (c) 60

minutes. (d) zoom-out view; (e) zoom-in view showing the unexcited region and the area exposed to the 405 nm laser irradiation.

Our findings reveal that there was no uptake occurring before the first 30 minutes, but surprisingly the uptake of the complex starts very rapidly only when the cells were dying due to the long exposure to UV light (see formation of apoptotic sign in brightfield image, after one hour). This is not surprising since, as already reported, long exposure to UV light can harm the cell, break cell membrane, damage DNA and damage other cellular organelles and later induce cell death<sup>15</sup>. In fact, this specific uptake phenomenon has been observed especially in the development of dead cell labelling molecules. As shown in Figure 6.11d, this observation is also strongly supported by the fact that only area irradiated with UV light shows cellular uptake of the complex while cells in the surrounding do not exhibit any internalization since they have not been damaged. A control experiment to proving that the platinum complex is not responsible for the cell damage, due to the formation of singlet oxygen or other reactive species, was performed by irradiating the system, in the same conditions, at 455 and 488 nm, where the platinum complexes absorb light.

#### **6.2.4 Role of the ancillary ligand**

The investigated complexes suffer of several drawbacks such as no uptake in healthy HeLa cells (in cell culture media), the absence of specific localization and water solubility. Unfortunately such aspects are crucial in the application of metal-based fluorophores as imaging agents, thus bioconjugation is probably the easiest and straightforward strategy to improve these properties (chapter 7).<sup>16,17</sup> However we have preliminary tested if it's possible to improve the solubility and the internalization of the compounds by changing of the ancillary ligand (Figure 6.12). In particular, vitamin B<sub>6</sub> is expected to increase the hydrophilic character while keeping the size of the molecule small. A biologically active ancillary ligand could also provide a better uptake and localization due to its intrinsic activity. We have also tested the effect of the change of the nature of the ancillary ligand from pyridine to aliphatic amine; in particular, we have chosen diethanolamine (DEA). The replacement of the pyridine moiety with DEA should decrease the  $\pi$ - $\pi$  interaction in favor of the

solubility still keeping the overall charge neutral. At this stage we have decided to employ  $\text{pyC}_5\text{-CF}_3\text{-tzH}_2$  as terdentate ligand since the resulting complexes have possessed the best known photophysical properties.

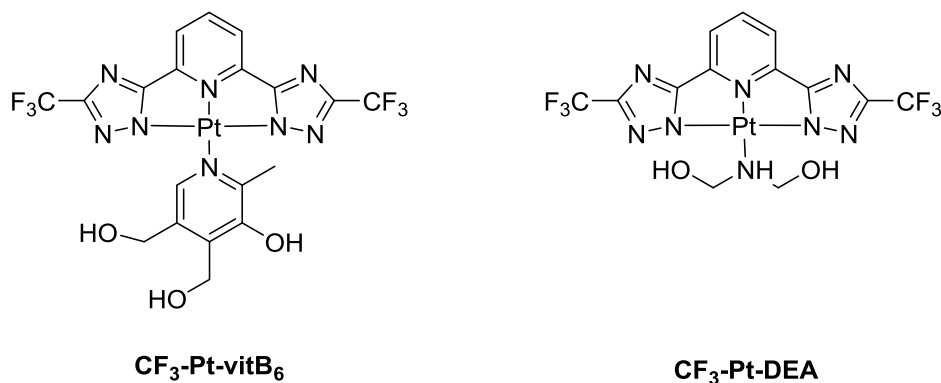


Figure 6.12. Chemical structures of the platinum complexes.

The complex **CF<sub>3</sub>-Pt-vitB<sub>6</sub>** and **CF<sub>3</sub>-Pt-DEA** were synthesized as described above for **CF<sub>3</sub>-Pt-4OHpy** and fully characterized by NMR techniques (<sup>1</sup>H, <sup>13</sup>C, <sup>19</sup>F), HR mass and elemental analysis (see experimental part). Interestingly, **CF<sub>3</sub>-Pt-DEA** displays a higher solubility than **CF<sub>3</sub>-Pt-4OHpy** which is soluble even in rather polar media such methanol and ethanol as well as halogenated solvents, while the change in solubility is less pronounced for **CF<sub>3</sub>-Pt-vitB<sub>6</sub>**. However the newly synthesized complexes require the addition of a solubilizing agent (DMSO) due to their negligible solubility in water.

#### 6.2.4.1 Bioimaging

**CF<sub>3</sub>-Pt-vitB<sub>6</sub>** seems to behave similarly to **CF<sub>3</sub>-Pt-4OHpy**, with no internalization in cell culture media. However, if the platinum complex is incubated in DMSO/PBS ( $c = 50 \mu\text{M}$ , < 1% DMSO v/v), after 4 hours of incubation (37 °C, 5% CO<sub>2</sub>), an emission attributable to aggregates formed upon establishment of Pt...Pt interaction has been observed inside HeLa cells (Figure 6.13).

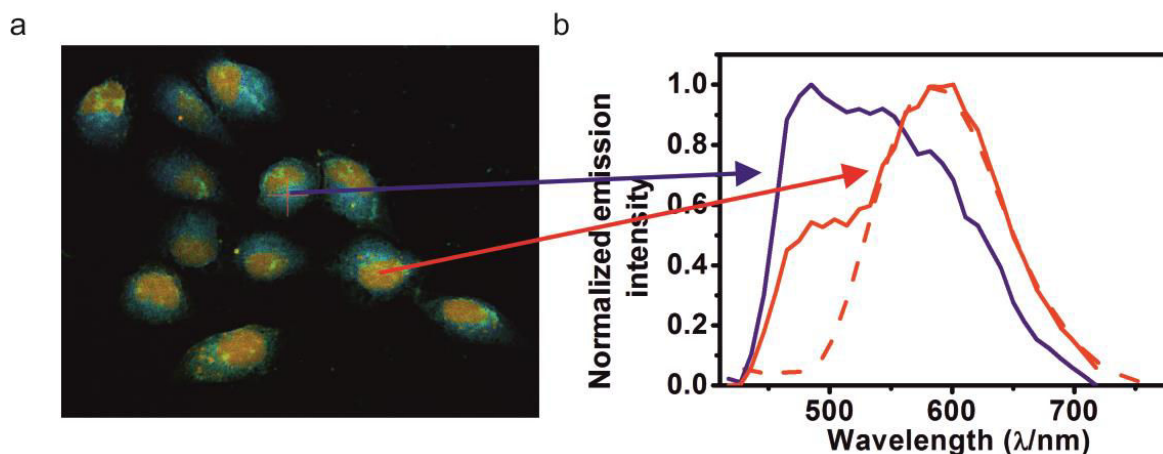


Figure 6.13. (a) Confocal microscopy image of HeLa cells after incubation with  $\text{CF}_3\text{-Pt-vitB}_6$  shows true-color emission of the cell compartments by using lambda-mode option. (b) Corresponding normalized emission spectra recorded from the cytoplasmic region (blue line) and the nuclear region (red trace) as indicated by the arrows. The emission of  $\text{CF}_3\text{-Pt-4OHpy}$  in the nuclear region (Figure 6.4b) is also depicted as red dashed trace. The samples were excited at  $\lambda_{\text{exc}} = 405 \text{ nm}$ .

As shown in Figure 6.13, the maximum of the emission in the nuclear region is detected at 600 nm and the emission profile in such region traces out the emission of the  **$\text{CF}_3\text{-Pt-4OHpy}$**  aggregates in similar conditions (Figure 6.13b); indeed an emission at these wavelengths can only be ascribed to the formation of luminescent aggregates of Pt(II) complexes. Moving to the cytoplasmic region, the emission maximum shifts to 485 nm and this emission band, which is also observed in the nuclear region, can be attributed to endogenous fluorophores. The use of vitamin B<sub>6</sub> as ancillary ligand has somehow improved the nuclear localization already present in  **$\text{CF}_3\text{-Pt-4OHpy}$**  without changing dramatically the uptake kinetics. As already mentioned, internalization of the complex has been observed only in the absence of cell culture media which makes such compound not suitable for biological application.  **$\text{CF}_3\text{-Pt-DEA}$**  the first compound which is internalized in the presence of cell culture media (<1% DMSO) as shown in Figure 6.14.

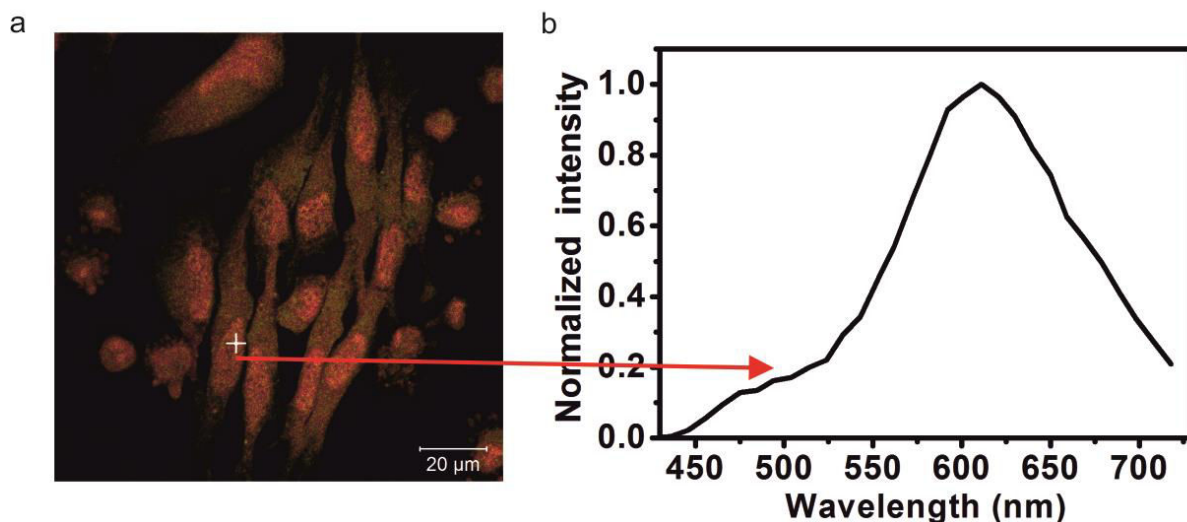


Figure 6.14. (a) Confocal microscopy image of HeLa cells after incubation with  $CF_3$ -Pt-DEA shows true-color emission by using lambda-mode option. (b) Corresponding normalized emission spectra. The sample was excited at  $\lambda_{exc} = 405$  nm.

Indeed an emission spectrum, attributable to the formation of luminescent aggregates of Pt(II), is detected inside the cells ( $\lambda_{max} = 610$  nm) after only 25 minutes of incubation in the cell culture media which is extraordinary fast if compared with the previous investigated compounds, but no preferential localization has been observed (Figure 6.14a). These results suggest that decrease of the  $\pi$ - $\pi$  interaction obtained by replacing the ancillary pyridine with an aliphatic amine has a positive effect not only on the solubility of the complex but also on the cellular uptake.

### 6.3 Conclusion

We have demonstrated the use of metal complexes and in particular of luminescent Pt(II) systems for bio-imaging. Their square planar geometry can induce self-assembly into supramolecular architectures possessing interesting photo-physical properties together with an enhanced stability. Such aggregates can be indeed considered a new class of dynamic probes, since the emission can be easily modulated and their long-live emission easily detected. The investigated complexes have shown uptake only when specific incubation conditions were used. By designing the coordinating ligands it is possible to internalize and localize the complexes in specific parts of the cells. The investigated complexes are internalized only when specific incubation conditions are used (e.g. PBS), in fact the presence of proteins or other biomolecules can inhibit or

even sequester the platinum complexes forcing expulsion from cells after their internalization (culture media). Irradiation of the cells with 405 nm light causes fast uptake of the compounds due to cell damage. Preliminary results have shown that the use of an aliphatic amine (DEA) as ancillary ligand significantly improves the cellular uptake, which occurs even in cell culture media.

## 6.4 Experimental Section

### 6.4.1 Synthesis and characterization

All the reactions were carried out under an inert atmosphere of nitrogen (Schlenk technique). All the solvents and chemicals were used from Aldrich or Fluka without any further purification. The compounds were purified by column chromatography by using silica gel 60 (70-230 mesh) as stationary phase.  $^1\text{H}$ ,  $^{13}\text{C}$  and  $^{19}\text{F}$  NMR spectra were recorded on a Bruker Advance 400 spectrometer. The  $^1\text{H}$  NMR chemical shifts ( $\delta$ ) are given in ppm and referred to residual protons on the corresponding deuterated solvent. All deuterated solvents were used without any further purification. All coupling constants (J) are given in Hertz (Hz). Electrospray ionization mass (ESI-MS) spectra were recorded on a Bruker Daltonics (Bremen, Germany) MicroTof with loop injection. Elemental analysis was realized by the Service d'analyses, de mesures physiques et de spectroscopie optique at the université de Strasbourg

#### 6.4.1.1 Platinum [2,6-bis[5-(trifluoromethyl)-1,2,4-triazol-3-yl- $\kappa\text{N}^2$ ]pyridinato(2-)- $\kappa\text{N}$ ](4-pyridinol- $\kappa\text{N}$ ) ( $\text{CF}_3\text{-Pt-4OHpy}$ )

Ligand py- $\text{CF}_3\text{-trzH}_2$  (230.0 mg, 0.660 mmol, 1.0 eq.),  $\text{PtCl}_2(\text{DMSO})_2$  (306.0 mg, 0.73 mmol, 1.1 eq.), 4-hydroxypyridine (63 mg, 0.660 mmol, 1.0 eq.) and 200  $\mu\text{L}$  of  $\text{Et}_3\text{N}$  were suspended in 20 mL of a 3 : 1 2-methoxyethanol and water. The reaction mixture was heated overnight at 85 °C. A yellowish-green precipitate appeared few minutes after the heating. The desired compound was purified on column chromatography using silica gel as stationary phase and 3 : 1 THF–n-hexane mixture as eluent, and obtained as greenish-yellow solid (66.1 mg, 0.104 mmol, yield 15.7%).

$^1\text{H}$  NMR (THF- $d^8$ , 400 MHz, ppm)  $\delta$ : 9.31 (2H), 8.14 (1H), 8.72 (2H), 6.95 (2H);  $^{19}\text{F}\{1\text{H}\}$  NMR (THF- $d^8$ , 376 MHz, ppm)  $\delta$ : 65.10 (1F). HR-ESI-MS(-)(m/z):  $[\text{M}-\text{H}]^-$  calculated 636.03246; found 636.03002.

#### **6.4.1.2 Platinum [2,6-bis[3-(4-methylphenyl)-1,2,4-triazol-5-yl- $\kappa\text{N}^2$ ]pyridinato(2-)- $\kappa\text{N}$ ] (4-pyridinol- $\kappa\text{N}$ ) (Tol-Pt-4OHpy)**

The platinum(II) complex was prepared in similar conditions described above for **CF<sub>3</sub>-Pt-4OHpy**, by employing py-tol-trzH<sub>2</sub> as tridentate ligand. The complex was purified on column chromatography using silica gel as stationary phase and ethylacetate:ethanol 1:1 as eluent, and obtained as yellow solid (yield 7%).  $^1\text{H}$  NMR (DMSO- $d^6$ , 400 MHz, ppm)  $\delta$ : 9.10 (2H), 8.17 (1H), 8.01 (4H), 7.80 (2H), 7.29 (4H), 6.50 (2H), 2.36 (6H); HR-ESI-MS (m/z):  $[\text{M} + \text{H}]^+$  calculated 682.16388; found 682.16471.

#### **6.4.1.3 Platinum [2,6-bis[5-(trifluoromethyl)-1,2,4-triazol-3-yl- $\kappa\text{N}^2$ ]pyridinato(2-)- $\kappa\text{N}$ ][4,5-Bis(hydroxymethyl)-2-methylpyridin-3-ol- $\kappa\text{N}$ ] (CF<sub>3</sub>-Pt-vitB<sub>6</sub>)**

Ligand py-CF<sub>3</sub>-trzH<sub>2</sub> (200 mg, 0.572 mmol, 1 eq.), PtCl<sub>2</sub>(DMSO)<sub>2</sub> (242 mg, 0.572 mmol, 1 eq.), Pyridoxine hydrochloride (141 mg, 0.687 mmol, 1.2 eq.) and 250  $\mu\text{L}$  of Et<sub>3</sub>N were suspended in 20 mL of a 3 : 1 2-methoxyethanol and water. The reaction mixture was heated overnight at 85 °C. A yellowish-green precipitate appeared few minutes after the heating. The desired compound was purified on column chromatography using silica gel as stationary phase and ethylacetate:acetone 8:2 mixture as eluent, and obtained as greenish-yellow solid (170 mg, 0.239 mmol, yield 41.7%).  $^1\text{H}$  NMR (THF- $d^8$ , 400 MHz, ppm)  $\delta$ : 8.48 (1H), 8.22 (1H), 7.91 (2H), 5.14 (2H), 4.71 (1H) 4.60 (2H), 2.90 (3);  $^{13}\text{C}$  NMR (THF- $d^8$ , 100 MHz, ppm)  $\delta$ : 165.53, 155.35-154.2 (q, J =4 Hz), 154.43, 150.75, 150.65, 144.86, 143.39, 136.34, 135.02, 125.38-117.35 (q, J =27 Hz), 119.3, 61.00, 60.14, 20.84.  $^{19}\text{F}\{1\text{H}\}$  NMR (THF- $d^8$ , 376 MHz, ppm)  $\delta$ : 66.84. HR-ESI-MS(+)(m/z):  $[\text{M}-\text{Na}]^+$  calcd. 712.0814; found 712.0834. Elemental analysis calcd. for C<sub>19</sub>H<sub>14</sub>F<sub>6</sub>N<sub>8</sub>O<sub>3</sub>Pt C 32.08%, H 1.98%, N 15.75%, found C 31.63%, H 2.23%, N 15.89%.

#### 6.4.1.4 Platinum [2,6-bis[5-(trifluoromethyl)-1,2,4-triazol-3-yl-κN<sup>2</sup>]pyridinato(2-)-κN](diethanolamine-κN) (CF<sub>3</sub>-Pt-DEA)

Ligand py-CF<sub>3</sub>-trzH<sub>2</sub> (178 mg, 0.51 mmol, 1 eq.), PtCl<sub>2</sub>(DMSO)<sub>2</sub> (215 mg, 0.51 mmol, 1 eq.), DEA (160 mg, 1.53 mmol, 3 eq.) in 20 mL of methanol and water. The reaction mixture was refluxed 4 hours. The desired compound was purified on column chromatography using silica gel as stationary phase and cyclohexane:ethylacetate 2:1 mixture as eluent and obtained as greenish-yellow solid (245 mg, 0.38 mmol, yield 74.5%). <sup>1</sup>H NMR (CD<sub>2</sub>Cl<sub>2</sub>, 400 MHz, ppm) δ: 8.15 (1H), 7.88 (2H), 6.06 (1H), 4.41 (2H), 3.94 (2H) 3.79 (4H), 3.39 (2H); <sup>13</sup>C NMR (THF-d<sup>8</sup>, 100 MHz, ppm) δ: 165.13, 154.63-153.61 (q, J =4 Hz), 149.45, 143.98, 124.36-116.32 (q, J =27 Hz), 119.42. <sup>19</sup>F{<sup>1</sup>H} NMR (THF-d<sup>8</sup>, 376 MHz, ppm) δ: 64.84. HR-ESI-MS(+)(m/z): [M-Na]<sup>+</sup> calcd. 648.0865; found 648.0901. Elemental analysis calcd. for C<sub>15</sub>H<sub>15</sub>F<sub>6</sub>N<sub>8</sub>O<sub>2</sub>Pt C 32.08%, H 1.98%, N 15.75%, found C 31.63%, H 2.23%, N 15.89%.

#### 6.4.2 Cell culture media

All materials for cell tests were purchased from Gibco. HeLa cells were cultured inside media which contains 88% Dulbecco's Modified Eagle Medium (DMEM), 10% Fetal Bovine Serum (FBS), 1% penicillin–streptomycin and 1% L-glutamine 200mM under 37°C and 5% of CO<sub>2</sub> condition for 48 hours until reaching 70 to 80% cell confluence. Subsequently, the cells were washed twice with Phosphate Buffer Solution (PBS), trypsinated and approximately 50 000 cells were reseeded on the monolayer glass cover slip inside six-well plate culture dish and glass bottom dishes (MatTek). Fresh culture media (2 mL) was added gently and cells were grown overnight.

#### 6.4.3 Platinum complexes incubation with PBS

The culture media was removed and 2 mL of new staining solution containing the corresponding platinum complex (50 μM in less than 1% DMSO containing PBS) were gently added onto cells. After incubation at 37 °C for 4 hours, the incubating media was removed and the cell layer on glass cover slips was gently washed (3 ×) with PBS and fixed with 4% paraformaldehyde (PFA) solution for 10 min.

#### **6.4.4 Incubation with cell culture media**

The cell culture media was removed and 50  $\mu\text{M}$  of the corresponding platinum complex (in less than 1% DMSO containing culture media) was added to the cells grown onto glass bottom dishes. After incubation at 37 °C for either 4 or 24 hours, the media was removed and the cell layer on glass cover slips was gently washed (3  $\times$ ) with PBS and 2 mL of fresh culture media was added.

#### **6.4.5 Organelle staining**

The cell layer was washed twice with PBS and kept in 0.1% Triton X-100 in PBS for 10 minutes, afterwards in 1% bovine serum albumin, BSA (Sigma Aldrich), and finally in PBS for 20 min. The cell layer on glass cover slip was stained with Phalloidin Alexa Fluor<sup>®</sup> 568 (Invitrogen), for F-actin/membrane staining, for 20 min, in the dark at room temperature, and washed twice with PBS. For nucleoli staining purpose, 500 nM of SYTO<sup>®</sup> RNASelect™ Green Fluorescent Cell Stain (Invitrogen) solution were added on the top of cells for 20 minutes followed by PBS washing. For visualizing nuclear region, cell nucleus was stained with 40,6-diamidino-2-phenylindole carboxamide (DAPI) and washed twice with PBS. The cover slips were mounted onto glass slides for microscopy measurements.

#### **6.4.6 Photobleaching experiments**

Photobleaching experiments were carried out on fixed cells stained with **CF<sub>3</sub>-Pt-4OHpy** and DAPI. The sample was continuously excited with high power 405 nm laser (32 mW) for 5 minutes and subsequently imaged at low power acquisition (1.2 mW) every 5 minutes for a total time of 25 minutes.

#### **6.4.7 Kinetic of internalization of the complex in cell culture media**

The cell culture media of living cells grown onto glass bottom dish was removed and 2mL of CF<sub>3</sub>-Pt-4OHpy staining solution (50  $\mu\text{M}$  in less than 1% DMSO containing

culture media) was added. The cells were subsequently imaged by confocal microscopy setup or one minute acquisition time for a total duration of 75 minutes.

#### **6.4.8 Kinetic of cellular expulsion of the complex after cell culture media addition**

Cells growing on glass bottom dish were incubated with 2 mL of CF<sub>3</sub>-Pt-4OHpy staining solution (50 μM in less than 1% DMSO containing PBS) for 20 minutes. Subsequently, cells were quickly washed three times with PBS to eliminate the excess of the complex and PBS media was replaced by normal cell culture media. Confocal microscopy experiments were directly performed for 2 minutes acquisition time for a total duration of 40 minutes.

#### **6.4.9 Fluorescence confocal microscopy**

All of the fluorescence images were taken by using Zeiss LSM 710 confocal microscope system with 63 × magnification, numerical aperture, NA, 1.3 of Zeiss LCI Plan-NEOFLUAR water immersion objective lens (Zeiss GmbH). The samples were excited by continuous wave (cw) laser at 405 nm. The emission of the complexes was collected in the range from 500 to 620 nm. In addition, the lambda-mode acquisition technique was performed to observe the emission spectra of the two complexes after cell internalization. In this case, the complexes were excited at 405 nm and emission spectra were collected from 412 to 723 nm. For co-localization experiments, the samples priorly co-stained with different dyes, DAPI (excitation/emission wavelength: 358 nm/461 nm), SYTO<sup>®</sup> RNASelect<sup>™</sup> Green Fluorescent Cell Stain (excitation/emission wavelength: 490 nm/ 530 nm) and Alexa Fluor<sup>®</sup> 568 Phalloidin (excitation/emission wavelength: 578 nm/600 nm) were excited at 405 nm and 594 nm, respectively. The emission spectra of the complexes together with the different dyes employed were also collected by using lambda-mode acquisition of the confocal setup. The raw data, taken by the lambda-mode, were processed by using linear un-mixing tool available in ZEN 2011 software package (Zeiss GmbH). All images were performed by using the same software. False colour images were adjusted to better

distinguish of the complexes from cellular organelles, e.g. yellow corresponds to complex, blue to DAPI that stains nucleus, green to nucleoli, and red to F-actin.

## 6.5 References

- [1] T. C. Johnstone; J. J. Wilson; S. J. Lippard, *Inorg. Chem.*, **2013**, *52*, 12234-12249.
- [2] M. Mauro; A. Aliprandi; D. Septiadi; N. S. Kehr; L. De Cola, *Chem. Soc. Rev.*, **2014**, *43*, 4144-4166.
- [3] S. W. Botchway; M. Charnley; J. W. Haycock; A. W. Parker; D. L. Rochester; J. A. Weinstein; J. A. G. Williams, *Proc. Natl. Acad. Sci. U.S.A.*, **2008**, *105*, 16071-16076.
- [4] E. Baggaley; S. W. Botchway; J. W. Haycock; H. Morris; I. V. Sazanovich; J. A. G. Williams; J. A. Weinstein, *Chem. Sci.*, **2014**, *5*, 879-886.
- [5] Q. Zhao; C. Huang; F. Li, *Chem. Soc. Rev.*, **2011**, *40*, 2508-2524.
- [6] V. Fernandez-Moreira; F. L. Thorp-Greenwood; M. P. Coogan, *Chem. Commun.*, **2010**, *46*, 186-202.
- [7] E. Kim; M. Koh; J. Ryu; S. B. Park, *J. Am. Chem. Soc.*, **2008**, *130*, 12206-12207.
- [8] A. Samanta; M. Vendrell; R. Das; Y.-T. Chang; A. Samanta; M. Vendrell; R. Das; Y.-T. Chang, *Chem. Commun.*, **2010**, *46*, 7406-7408.
- [9] Y. Kawazoe; H. Shimogawa; A. Sato; M. Uesugi, *Angew. Chem. Int. Ed. Engl.*, **2011**, *50*, 5478-5481.
- [10] N. K. Allampally; C. G. Daniliuc; C. A. Strassert; L. De Cola, *Inorg. Chem.*, **2015**, *54*, 1588-1596.
- [11] M. Mydlak; M. Mauro; F. Polo; M. Felicetti; J. Leonhardt; G. Diener; L. De Cola; C. A. Strassert, *Chem. Mater.*, **2011**, *23*, 3659-3667.
- [12] C. A. Strassert; C. H. Chien; M. D. Galvez Lopez; D. Kourkoulos; D. Hertel; K. Meerholz; L. De Cola, *Angew. Chem. Int. Ed. Engl.*, **2011**, *50*, 946-950.
- [13] C. Cebrian; M. Mauro; D. Kourkoulos; P. Mercandelli; D. Hertel; K. Meerholz; C. A. Strassert; L. De Cola, *Adv. Mater.*, **2013**, *25*, 437-442.
- [14] N. K. Allampally; C. A. Strassert; L. De Cola, *Dalton Trans.*, **2012**, *41*, 13132-13137.
- [15] K. V. Bogdanov; A. B. Chukhlovin; A. Y. Zaritskey; O. I. Frolova; B. V. Afanasiev, *Br. J. Haematol.*, **1997**, *98*, 869-872.
- [16] G. Crivat; J. W. Taraska, *Trends Biotechnol.*, **2012**, *30*, 8-16.
- [17] C. Y.-S. Chung; K. H.-Y. Chan; V. W.-W. Yam, *Chem. Commun.*, **2011**, *47*, 2000-2002.



# Chapter 7

## **$\beta$ -lactam bioconjugates bearing luminescent platinum(II) tags: synthesis and photophysical characterization**

**Abstract:** Two novel neutral Pt(II) complexes bearing a  $\beta$ -lactam unit on the ancillary pyridine ligand have been synthesized and their photophysical properties investigated. The complexes show interesting emission properties that, in the solid state, are dominated by the formation of aggregates due to the square-planar geometry of the Pt(II) species. Interestingly, the formation of closed-shell metal...metal interactions in such aggregates lead to new excited states that conveniently allow excitation in the visible region. The combination of the biologically active azetidinone agent and the intense and long-lived emission are of particular interest for developing efficient multifunctional biomedical systems.

## 7.1 Introduction

$\beta$ -Lactam compounds are historically well-known as one of the most important class of antimicrobial agents since the discovery of the naturally occurring bicyclic penicillin and cephalosporin compounds.<sup>1</sup> It was recognized early on that the four-membered azetidinone ring represents the pharmacophoric core of  $\beta$ -lactams, as attested by the discovery of the monocyclic and potent Aztreonam antibiotic.<sup>2</sup> However, the treatment of bacterial infections has been hindered by the increasing emergence of multidrug-resistant microorganisms, which is one of the greatest challenges in the clinical management of infectious diseases.<sup>3</sup> Resistance is an inevitable side effect of antibiotic use and requires a continuous search for new bacterial targets and novel therapeutic agents to treat drug-resistant microorganisms.<sup>4,5</sup> Research in this field remains active, and reports of new  $\beta$ -lactam derivatives against resistant bacteria continue to appear.<sup>6</sup>

In a recent contribution from our group, a series of new azetidinones were tested in vitro against Gram-positive and Gram-negative clinical isolates. In particular, the new  $\beta$ -lactams were found to be active against methicillin-resistant and methicillin-susceptible *Staphylococcus Aureus* strains, MRSA and MSSA respectively, isolated from patients with cystic fibrosis.<sup>7-9</sup>

The biological activity of monocyclic  $\beta$ -lactams is not limited to their antibacterial properties, and specific activities are continuously emerging from new azetidinone derivative. The design and synthesis of new azetidinones thus has resulted in the discovery of valuable inhibitors of serine proteases including elastase,  $\beta$ -lactamase, phospholipase A2, and bacterial signal peptidase, inhibitors of HFAAH, HDAC, Cathepsin K, and vasopressin, anticancer, antitubercular, and anti-inflammatory agents.<sup>10,11</sup>

The study of transition-metal-bioconjugates is an active field of research that has led to potential therapeutics. Such compounds can function as tracers in immunological analysis based on several analytical methods.<sup>12</sup> Furthermore, the possibility of combining therapeutic properties with diagnostics tools making compounds with dual functionality (i.e., theranostic agents) has recently blossomed. These compounds can

be simultaneously used as powerful imaging tools to unveil real-time biochemical processes, compound accumulation, drug activity and interaction, and to gather information about the fate of the compounds.<sup>13-19</sup> In this respect, much effort is currently devoted to the preparation of luminescent complexes based on second- and third-row transition metals such as iridium(III), rhenium(I), ruthenium(II), and platinum(II), for applications in bioimaging *in vitro*, *in cellulo* and *in vivo*.<sup>20-24</sup> Such increasing scientific interest is driven by the fact that the judicious choice of coordinating ligands together with the presence of the heavy metals might provide enhanced physicochemical properties, such as photostability, large Stokes shifts, tunable emission colors, and high photoluminescence quantum yield.<sup>20-24</sup> Furthermore, as a consequence of the formally spin-forbidden nature of the radiative processes, such transition-metal complexes (TMCs) possess long-lived excited states with lifetimes that span over greater orders of magnitude when compared to widely used organic fluorophores,<sup>25-27</sup> allowing the successful employment of time-gated microscopy techniques for imaging purposes.<sup>28,29</sup> However, TMCs typically show excitation bands in the deep-blue and ultraviolet region, which severely hampers their use in real applications for *in cellulo* and *in vivo* experiments.

Among all the investigated complexes, luminescent platinum(II) derivatives possess the tendency to aggregate into self-assembled nanostructures by means of weak  $\pi$ - $\pi$  and closed-shell metallophilic ( $d_{z^2} \cdots d_{z^2}$ ) interactions.<sup>30-36</sup> The establishment of such intermolecular interactions leads to the formation of lower-lying excited states, namely metal-metal-to-ligand charge transfer (MMLCT).

We have very recently demonstrated that it is possible to take advantage of the formation of such aggregates to obtain luminescent TMC-based labels that are able to self-assemble in cellular compartments, forming highly emitting aggregates as a consequence of their protection from quenchers (e.g., dioxygen) in biologically relevant environments.<sup>20,37</sup> More interestingly, the formation of MMLCT bands leads to sizeable bathochromic shift of both excitation and emission, allowing easy excitation of the probe with visible light.<sup>37,38</sup>

The  $\beta$ -lactams have seldom been studied as ligands for metal complexes,<sup>39-41</sup> and most of the examples deal with metallocene derivatives. Recently, examples of Pd and Pt complexes with azetidinones<sup>42</sup> and bio-organometallic Ir and Rh with  $\beta$ -lactam ligands were reported.<sup>43</sup> However, specifically designed metal complex bioconjugates should allow the possibility to couple the multifaceted biological activities of  $\beta$ -lactams with photoactive metal complexes. This could represent an interesting combination because among the new strategies to combat antibiotic-resistant infections, antimicrobial photodynamic therapy appears promising for the treatment of local infections caused by both Gram-positive and Gram-negative bacteria.<sup>44,45</sup>

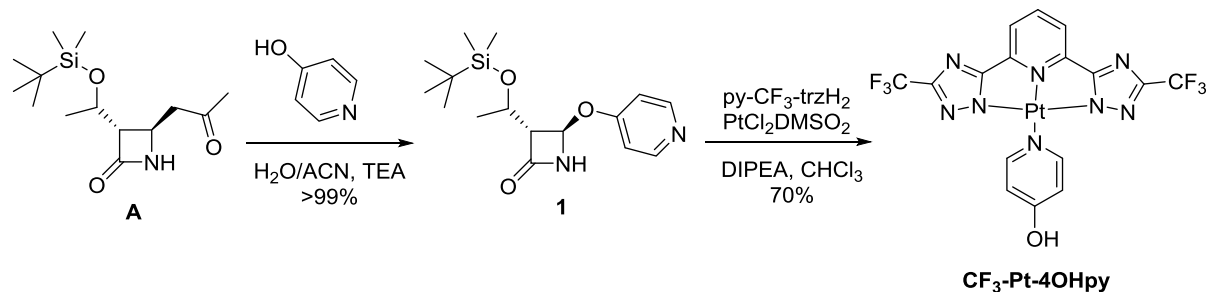
In this chapter we propose the first step towards the development of bioconjugates between azetidinones and luminescent platinum complexes. We have chosen platinum compounds because of their interesting photophysics, which can be tuned upon the formation of aggregates. Furthermore, platinum complexes are widely used in biomedical applications due to their anticancer activity,<sup>46-50</sup> and their ability to recognize proteins.<sup>51-54</sup> We can envisage that the molecules reported and here characterized here could therefore be parent compounds of a novel set of bioimaging probes with self-assembling properties for particular biological targets, such as bacteria, proteins, or receptors.

## 7.2 Results and discussion

### 7.2.1 Synthesis and characterization

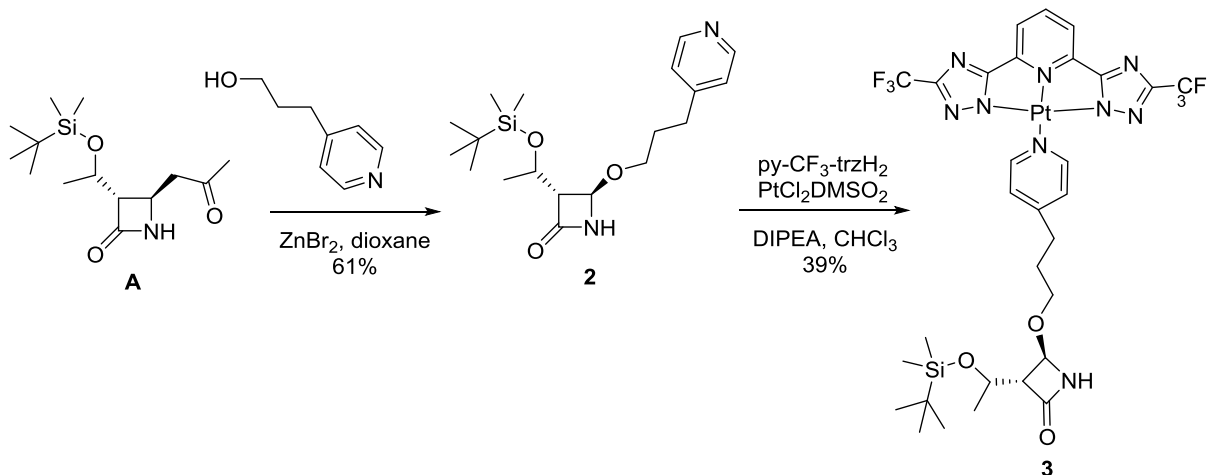
Starting from the commercially available (3R,4R)-4-acetoxy-3-[(1R)-1-(tert-butyl)dimethylsilyloxy]ethyl]azetidin-2-one (**A**), a nucleophilic substitution reaction was performed to insert on the C-4 position of the  $\beta$ -lactam ring a pyridine residue that would act as ancillary ligand. As a first attempt, 4-OH-pyridine was chosen as a nucleophile and the corresponding azetidinone **1** was obtained in quantitative yields. On attempting the complexation of **1** with Pt(II)Cl<sub>2</sub>(DMSO)<sub>2</sub> as the platinum precursor, and py-CF<sub>3</sub>-trzH<sub>2</sub> as the tridentate ligand in CHCl<sub>3</sub>, and in the presence of DIPEA at 50 °C, only the **CF<sub>3</sub>-Pt-4OHpy** was obtained. A tentative explanation is that the C4 position of the expected  $\beta$ -lactam **B** could become activated by the direct

conjugation of the phenolic moiety with the pyridine coordinated to platinum. Thus, in the aqueous work-up, displacement of the ligand from the azetidinone intermediate **B** occurred and only **CF<sub>3</sub>-Pt-4OHpy** was isolated (Scheme 7.1).



*Scheme 7.1. Synthetic strategy used to access the new  $\beta$ -lactam platinum conjugate.*

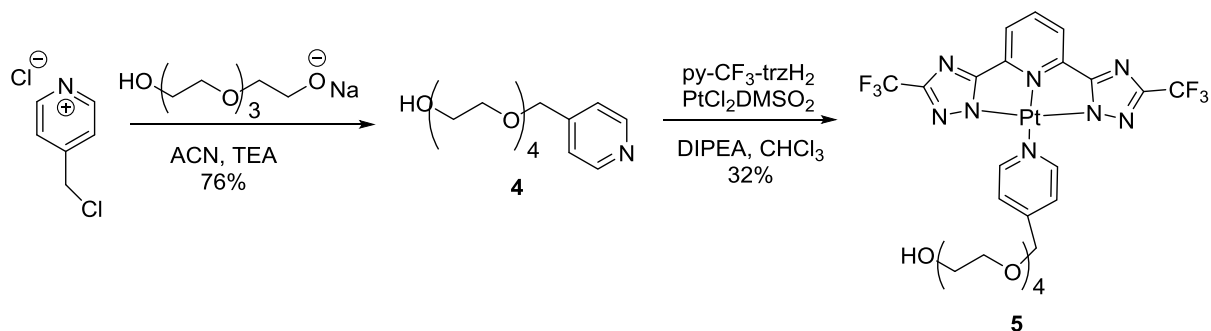
To avoid the electronic coupling between the pyridine and the azetidinone moiety, a short alkyl chain was introduced as a spacer. Thus, 3-pyridylpropanol and the 4-acetoxy-azetidinone **A** were coupled (Scheme 7.2) to give azetidinone **2**. Compound **2** was then treated with the platinum(II) precursor and py-CF<sub>3</sub>-trzH<sub>2</sub>, in the presence of DIPEA in CHCl<sub>3</sub> at 50 °C, leading to the  $\beta$ -lactam complex **3** (Scheme 7.2). The new platinum-based bioconjugate was purified by column chromatography and fully characterized.



*Scheme 7.2. Synthetic strategy used to access the new  $\beta$ -lactam platinum conjugate **3**.*

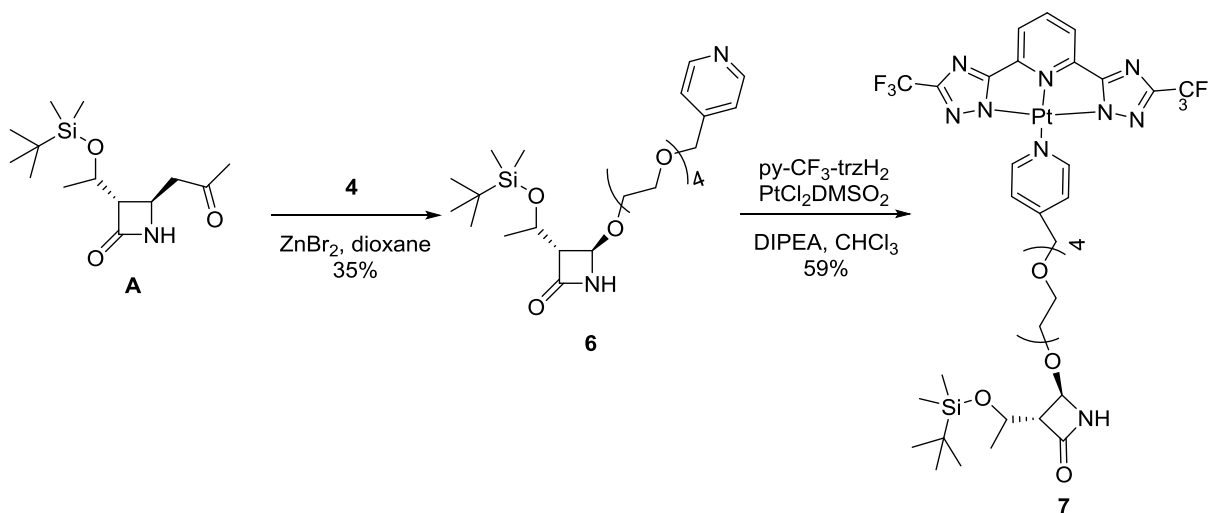
However, complex **3** was poorly soluble in organic solvents and completely insoluble in water. To improve its solubility, we then inserted a short tetraethylene glycol (TEG) chain as spacer between the pyridine and the  $\beta$ -lactam moieties. The synthetic

pathway is depicted in Scheme 7.2 *Figure 7.3* and started from the reaction of 4-(chloromethyl)pyridine hydrochloride with tetraethylene glycol to give **4**. The new tetraethyleneglycol-pyridyl ligand **4** was preliminarily evaluated as platinum ligand in reaction with the Pt(II) precursor, obtaining successfully complex **5** (Scheme 7.3).



*Scheme 7.3. Synthetic strategy for TEG platinum conjugate 5.*

Treatment of the starting 4-acetoxy-azetidinone **A** with **4** gave the  $\beta$ -lactam conjugate **6**, which was treated with the Pt(II) precursor, py-CF<sub>3</sub>- trzH<sub>2</sub> and DIPEA in CHCl<sub>3</sub> at 50 °C to give the desired  $\beta$ -lactam complex **7**.



*Scheme 7.4. Synthetic route to azetidinone-PtII complex 7.*

The  $\beta$ -lactam conjugate **7** was obtained in 59% yield after flash chromatography purification and was fully characterized. Complex **7** is very soluble in several organic solvents (CH<sub>2</sub>Cl<sub>2</sub>, CHCl<sub>3</sub>, THF, MeOH, ethyl acetate, and acetone), and in water it rapidly formed a colloidal suspension.

The purified complexes **3** and **7** were fully characterized by mass spectrometry (ESI), IR, and NMR spectroscopy. The  $^1\text{H}$  NMR spectra of compounds **2**, **3** and **7** are compared in Figure 7.1. The successful complexation of the  $\beta$ -lactam **2** to platinum in compounds **3** and **7** was confirmed by the downfield shift of the ortho-aromatic pyridine protons of the C4 side chain of the  $\beta$ -lactam, which moved from 8.5 ppm in compound **2** to 9.4 ppm for **3** and **7**. In contrast, resonance peaks relative to the peculiar hydrogen atoms on the  $\beta$ -lactam ring b, c, and d (Figure 7.1) were influenced by complexation to a much lesser extent. Therefore, the  $\beta$ -lactam ring should not be involved in platinum complexation and it could retain its own characteristics and properties. This is an important observation in view of the possible application of the conjugation described here to biologically active azetidinones.

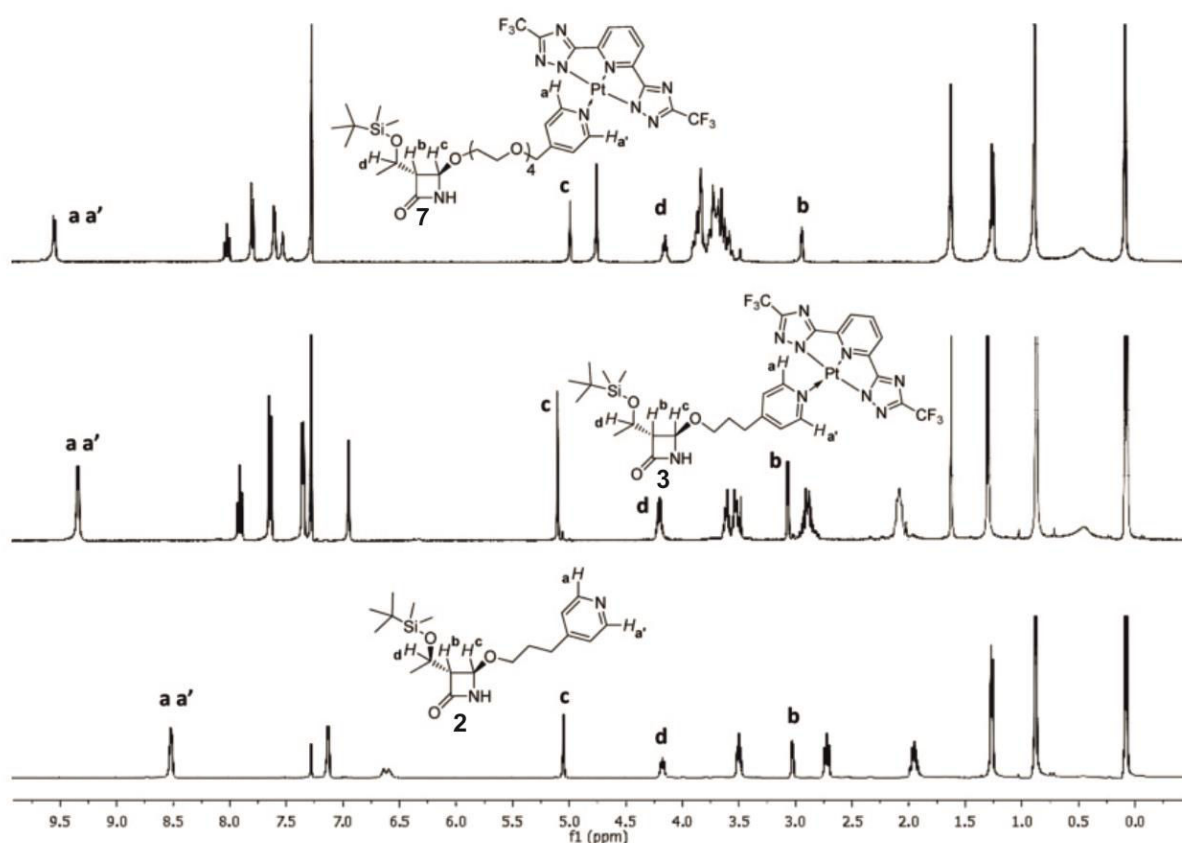


Figure 7.1 Comparison of the  $^1\text{H}$  NMR (400 MHz) spectra of **2** (bottom), **3** (middle), and **7** (top) in  $\text{CDCl}_3$ .

## 7.2.2 Photophysical Characterization

The absorption and emission spectra in dilute  $\text{CHCl}_3$  solution (concentration  $1 \times 10^{-5}$  M) at room temperature and at a concentration of  $5 \times 10^{-5}$  M in 2-MeTHF glassy matrix at 77 K are displayed in Figure 7.2. As shown in the electronic absorption spectrum in dilute  $\text{CHCl}_3$  fluid solution, both compounds **3** and **7** display absorption features in two main regions. At lower energy in the region 360–400 nm, a weak broad and featureless band with molar extinction coefficient,  $\epsilon$ , of  $0.8$  and  $1.1 \times 10^3$   $\text{M}^{-1}\text{cm}^{-1}$  (at  $\lambda_{\text{abs}} = 403$  nm) for compound **3** and **7**, respectively, is attributable to the overlap of energetically lower-lying spin-allowed singlet-manifold metal-to-ligand charge transfer,  $^1\text{MLCT}$ , and ligand-centered,  $^1\text{LC}$ , excitation processes as typical of similar reported cyclometalated platinum(II) complexes.<sup>30,37,55-59</sup> Such excitation can be mainly described as a shift of electron density from the filled d metal-based molecular orbitals to the empty MOs of the tridentate ligand with  $\pi^*$  character,  $d\pi(\text{Pt}) \rightarrow \pi^*$ .

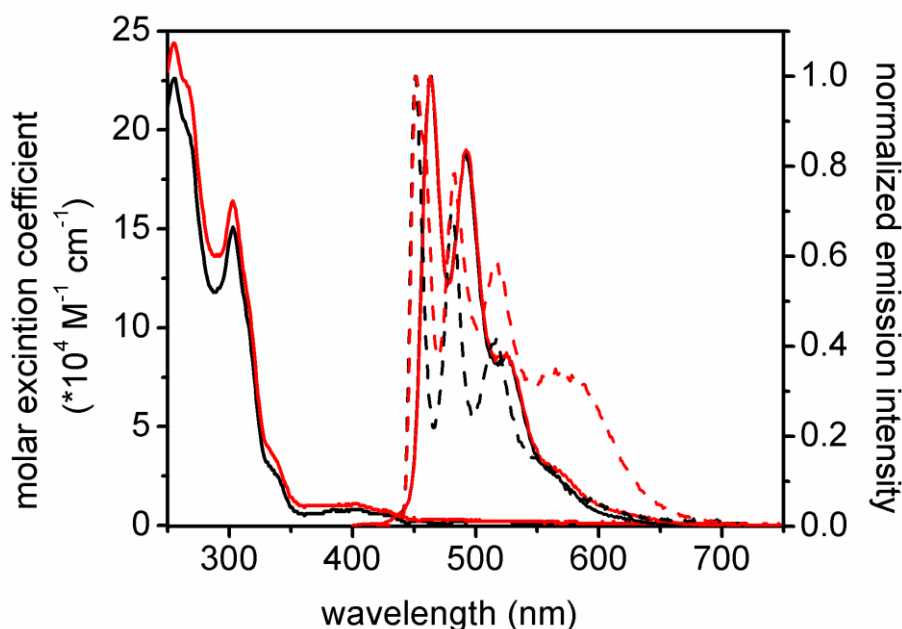


Figure 7.2. Room temperature (solid traces) absorption and normalized emission spectra for samples of compound **3** (black) and **7** (red) at  $1 \times 10^{-5}$  M in  $\text{CHCl}_3$  and low temperature (77 K) emission spectra (dashed traces) at  $5 \times 10^{-5}$  M in 2-MeTHF glassy matrix. Emission spectra were collected upon  $\lambda_{\text{exc}} = 300$  nm.

On the other hand, the more intense ( $\epsilon = 0.26\text{--}2.44 \times 10^4 \text{ M}^{-1}\text{cm}^{-1}$ ) and structured absorption features present at higher energy ( $\lambda_{\text{abs}} = 250\text{--}340 \text{ nm}$ ) can be attributed to  $^1\text{LC}$  bands. Unfortunately, the low solubility of the complexes in solvents with a wide range of polarity hampered studies on solvent dependence.

As shown in Figure 7.2, upon photoexcitation in the range of 300–400 nm, diluted fluid air-equilibrated solutions in  $\text{CHCl}_3$  of both complexes display moderate (PLQY = 2%) and structured emission in the blue region of the visible spectrum with a maximum at 464, and vibrational bands at 492, 525, and a shoulder at 567 nm. The observed emission band with vibronic progression is similar to other reported platinum(II) derivatives bearing N $\wedge$ N $\wedge$ N tridentate chelating motifs and is attributed to  $\pi\text{--}\pi^*$  transitions involving the tridentate ligand.<sup>30,58</sup> All the complexes possess bi-exponential radiative deactivation kinetics:  $\tau_1 = 278 \text{ ns}$  and  $\tau_2 = 13 \text{ ns}$  for compound **4** and  $\tau_1 = 239 \text{ ns}$  and  $\tau_2 = 14 \text{ ns}$  for compound **7** (see Table 7.1 for more details).

Table 7.1. Photophysical data for **3** and **7** in fluid solution at room temperature, 77 K glassy matrix, and solid state.

	Room temperature $\text{CHCl}_3$				77 K 2MeTHF glassy matrix				Solid state			
	$\lambda_{\text{abs}}$ ( $\epsilon$ ) [nm, ( $\times 10^3 \text{ M}^{-1}\text{cm}^{-1}$ ) <sup>1</sup> ]	$\lambda_{\text{em}}$ [nm] <sup>[a]</sup>	$\tau$ [ns]	PLQY (%)	$\lambda_{\text{em}}$ [nm] <sup>[a]</sup>	$\tau$ ( $\langle\tau\rangle$ ) <sup>[b]</sup> [ $\mu\text{s}$ ]	$\lambda_{\text{em}}$ [nm]	$\tau$ [ns]	PLQY (%)			
<b>3</b>	255 (22.6), (19.8), 303 (15.1), 338 (2.6), 402 (0.8)	267 464, 492, 525, 567 (sh)	278 (77%) 13 (23%)	2	451, 480, 517, 554 (sh)	4.2, 69% 10.7, 31% (6.2) <sup>[c]</sup> 3.6, 96% 7.7, 4% (3.8) <sup>[d]</sup>	596	321	55			
<b>7</b>	255 (24.4), (22.2), 303 (16.4), 338 (3.3), 402 (1.1)	266 464, 492, 525, 567 (sh)	239 (66%) 14 (34%)	2	451, 483, 517, 571	4.0, 71% 9.6, 29% (5.6) <sup>[c]</sup> 3.5, 97% 7.7, 3% (3.6) <sup>[d]</sup>	589	341	56			

[a] 'sh' denotes shoulder. [b] Amplitude-weighted lifetimes. [c] Recorded at 450 nm. [d] Recorded at 585 nm.

Such bi-exponential de-excitation kinetics can be attributed either to the formation of aggregates, even in diluted solution, meaning the coexistence of different species in solution, or to the presence of two close-lying excited states, an emissive state with  $^3\text{MLCT}/^3\text{LC}$  nature, and an energetically close-lying nonemitting (quenching) state.<sup>30,58</sup> To clarify the photophysical behavior, low-temperature and solid-state measurements have been performed. At 77K in 2-MeTHF glassy matrix ( $c = 5 \times 10^{-5} \text{ M}$ ),

the emission spectra display a slight hypsochromic shift of only  $621\text{ cm}^{-1}$  with an enhancement of the band structure, featuring maxima at 451, 480, 517 and a shoulder at 554 nm for compound **3**, whereas an additional band is clearly visible for compound **7** at approximately 571 nm. The emission at higher energy (ca. 450 nm) has an amplitude- weighted lifetime of 6.2 and 5.6  $\mu\text{s}$  (for **3** and **7**, respectively). On the other hand, at longer wavelengths ( $\lambda_{\text{em}} = 585\text{ nm}$ ), the amplitude-weighted lifetime reduces to 3.8 and 3.6  $\mu\text{s}$ , for **3** and **7**, respectively. As shown by the excitation spectra at 585 nm for both compounds (Figure 7.3), the presence of a lower-energy excitation band extending towards 500 nm suggests partial aggregation through formation of closed-shell metallophilic Pt...Pt interactions.

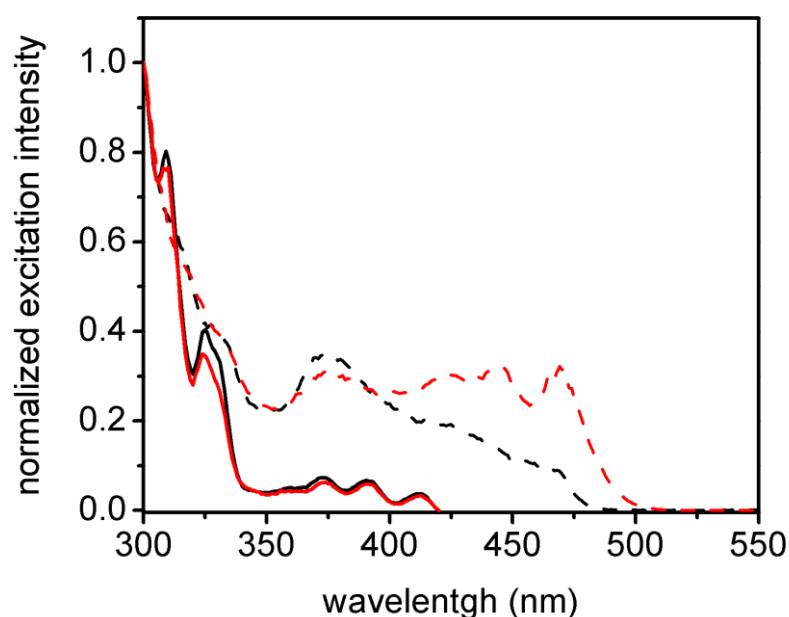


Figure 7.3. Normalized excitation spectra recorded at 77 K for samples of compound **3** (black) and **7** (red) at  $5 \times 10^{-5}\text{ M}$  in in 2-MeTHF glassy matrix. Spectra were recorded at 445 (solid lines) and 585 (dashed lines) nm.

This effect is even stronger for compound **7**, indicating that the emissive excited state is generated by aggregation, with the formation of the luminescent  $^3\text{MMLCT}$  state. To further support the assignment of the nature of the emitting excited states, a concentration- dependent emission study was conducted in the range  $0.1\text{--}5 \times 10^{-5}\text{ M}$  at low temperature (77 K) for the derivative that showed higher tendency toward aggregation, i.e., compound **7**.

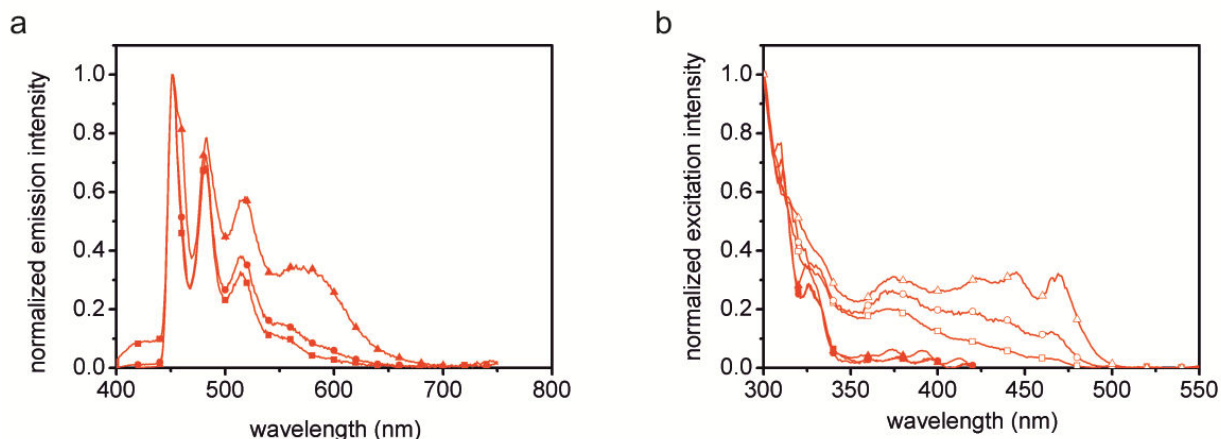


Figure 7.4. Normalized emission (a) and excitation (b) spectra for samples of compound **7** at concentration of  $0.1 \times 10^{-5}$  (squares),  $1 \times 10^{-5}$  (circles) and  $5 \times 10^{-5}$  M (triangles) in 2-MeTHF glassy matrix. Emission spectra were recorded at  $\lambda_{exc} = 300$  nm while excitation spectra were recorded at  $\lambda_{em} = 450$  (filled symbols) and 585 nm (empty symbols).

The resulting emission and excitation spectra are displayed in Figure 7.4, respectively, and the corresponding lifetimes are listed in Table 7.2.

Sample concentration [ $\mu$ M]	450 nm		585 nm	
	$\tau$ [ $\mu$ s]	$\tau$ [ $\mu$ s]	$\tau$ [ $\mu$ s]	$\tau$ [ $\mu$ s]
1	3.7 (24%)	10.0 (76%)	Not detectable	
10	4.0 (40%)	10.0 (60%)	3.2 (84%)	5.8 (16%)
50	4.0 (71%)	9.6 (29%)	3.5 (97%)	7.4 (3%)

Table 7.2. Lifetime data for compound **7** at 77 K in 2-MeTHF glassy matrix at different concentration in the range  $0.1$ – $5 \times 10^{-5}$  M recorded at  $\lambda_{em} = 450$  and 585 nm, upon  $\lambda_{exc} = 375$  nm.

As expected from radiative transition attributed to a  $^3$ MMLCT emission of the ground state aggregated platinum complexes, we observed that, upon increasing the concentration, both low-energy emission and excitation (recorded at  $\lambda_{em} = 585$  nm) bands increase their relative intensity. On the other hand, the excitation spectra recorded at higher energy (i.e., 450 nm) show a negligible concentration dependency. Concomitantly, in the time-resolved emission decay recorded at 585 nm, the shorter lifetime component (i.e., 4.0  $\mu$ s) attributed to  $^3$ MMLCT increases its relative weight. A

mirrored trend is obtained upon monitoring the lifetime at the higher energy band ( $\lambda_{em} = 450$  nm), for which the longer lifetime component (i.e., 10.0  $\mu$ s) attributed to the  $^3LC/^3MLCT$  excited state of the monomeric species increases its weight upon dilution. Similar consideration can be made for complex **3**. Therefore, we can conclude that at 77 K and even at room temperature in dilute solution the multiexponential decays are due to the formation of small aggregates. For the latter case, i.e., in dilute  $CHCl_3$  solution, we attribute the short component to the monomeric species and to the longer excited-state lifetime to the aggregates. The assembling formation for the  $\beta$ -lactam-platinum conjugates **3** and **7** have also been investigated in the solid state, and the corresponding normalized excitation and emission spectra are reported in Figure 7.5. Interestingly, upon photoexcitation between 300 and 400 nm, the solid-state samples display a very intense emission band centered at 596 and 589 nm with PLQY as high as 55 and 56% for compound **3** and **7**, respectively. The excited-state lifetimes decay with monoexponential kinetics and are 321 and 341 ns for complex **3** and **7**, respectively. Similar to the 77 K spectra, such bright emission is attributable to the  $^3MMLCT$  emitting excited-state established upon aggregation of the complex in the solid state.

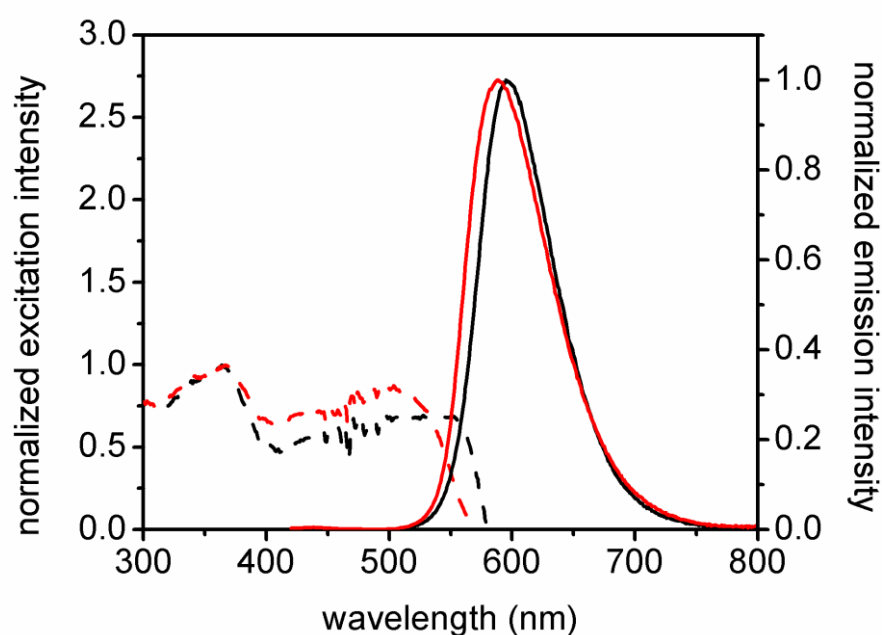


Figure 7.5. Normalized excitation (dotted traces) and emission (solid traces) spectra for solid-state samples of **3** (black) and **7** (red). Excitation and emission spectra were collected at the  $\lambda_{em}$  maximum and upon  $\lambda_{exc}$  at 350 nm, respectively.

Even more interestingly, the excitation spectra recorded at the maximum of emission wavelength display a typical <sup>1</sup>MMLCT band with onset wavelength as long as 580 nm for compound **3**, allowing the possibility to excite such luminescent probes in their aggregated form with visible light with a wavelength that approaches the so-called biological window (600– 1300 nm). Overall, the several nanosecond lifetime scale, the very bright emission in air-equilibrated conditions of the aggregated compounds, as well as the excellent stability of the compounds, are valuable properties that should facilitate further exploration of the behavior of such species for bioapplications and as theranostic agents.

### **7.3 Conclusions**

New luminescent Pt(II) complexes bearing a  $\beta$ -lactam unit were successfully synthesized and the new  $\beta$ -lactam platinum conjugates showed interesting photophysical properties. Furthermore, the formation of aggregates, due to the square-planar geometry of the Pt(II) species, leads to new excited states that allow excitation in the visible region. The combination of a biologically active agent (the  $\beta$ -lactam unit) and an intense and long-lived emission (platinum complex) are of particular interest for the development of biomedical systems in which imaging and antimicrobial properties are combined in a single compound.

### **7.4 Experimental Section**

#### **7.4.1 Synthesis and characterization**

Commercial reagents were used as received without additional purification. <sup>1</sup>H, <sup>13</sup>C, and <sup>19</sup>F NMR spectra were recorded with an INOVA 400 or a Bruker Avance 400 instrument with a 5 mm probe. All chemical shifts are quoted relative to deuterated solvent signals ( $\delta$  in ppm and J in Hz). TLC was performed with Merck 60 F254 plates. Column chromatography was performed with Merck silica gel 200–300 mesh. HPLC-MS were recorded with an Agilent Technologies HP1100 instrument, equipped with a ZOB- RAX-Eclipse XDB-C8 Agilent Technologies column (mobile phase: H<sub>2</sub>O/ACN, 0.4 mL/min, gradient from 30 to 80% ACN in 8 min, 80% ACN until 25 min), coupled with

an Agilent Technologies MSD1100 single-quadrupole mass spectrometer, full scan mode from  $m/z$  50 to 2600, scan time 0.1 s in positive ion mode, ESI spray voltage 4500 V, nitrogen gas 35 psi, drying gas flow 11.5 mL/min, fragmentor voltage 20 V. Elemental analysis were performed with a Thermo Flash 2000 CHNS/O Analyzer.

#### **7.4.1.1 (3R,4R)-3-((R)-1-((tert-Butyldimethylsilyl)oxy)ethyl)-4-(pyridin-4-yloxy)azetidin-2-one (1)**

In a 25 mL flask, to a stirred solution of **A** (143 mg, 0.5 mmol) in acetonitrile (1.0 mL) were slowly added H<sub>2</sub>O (4.0 mL), then 4-hydroxypyridine (95 mg, 1.0 mmol) and finally TEA (154  $\mu$ L, 1.1 mmol). The reaction was followed by TLC (EtOAc/cyclohexane, 8:2) and after 1 h stirring, the mixture was extracted with CH<sub>2</sub>Cl<sub>2</sub> (3 $\times$ 10 mL), dried with Na<sub>2</sub>SO<sub>4</sub>, and evaporated in vacuo. After flash-chromatography purification (acetone to acetone/MeOH, 95:5), the desired product **1** (144 mg, 100%) was obtained as a white solid;  $[\alpha]_D = 29.8$  ( $c = 0.62$ , CH<sub>2</sub>Cl<sub>2</sub>). <sup>1</sup>H NMR (400 MHz, CDCl<sub>3</sub>):  $\delta = 0.10$  (s, 3 H, MeSi), 0.12 (s, 3 H, MeSi), 0.89 (s, 9 H, tBuSi), 1.25 (d,  $J = 7.4$  Hz, 3 H, Me), 3.20 (dd,  $J = 1.5, 4.2$  Hz, 1 H, CHCONH), 4.28 (m, 1 H, CHOTBS), 5.43 (s, 1 H, CHOPyr), 6.37 (d,  $J = 7.6$  Hz, 2 H, ArH), 7.55 (d,  $J = 7.6$  Hz, 2H, ArH), 7.88 (s, 1 H, NH) ppm. <sup>13</sup>C NMR(100.6 MHz, CDCl<sub>3</sub>):  $\delta = -5.0, -4.3, 17.9, 22.5, 25.7, 64.4, 68.1, 68.5, 118.9, 136.3, 165.7, 179.6$  ppm. IR (neat):  $\tilde{\nu} = 3391, 2956, 2929, 2857, 1784, 1634, 1549, 1386, 1257, 1174, 1099, 982, 836, 776$  cm<sup>-1</sup>. HPLC-MS (ESI+):  $R_t = 6.70$  min;  $m/z = 323$  (100) [M+H]<sup>+</sup>, 645 (59) [2M+H]<sup>+</sup>, 667 (23) [2M+Na]<sup>+</sup>.

#### **7.4.1.2 Platinum [2,6-bis[5-(trifluoromethyl)-1,2,4-triazol-3-yl- $\kappa$ N<sup>2</sup>]pyridinato(2-)- $\kappa$ N](4-pyridinol- $\kappa$ N) (CF<sub>3</sub>-Pt-4OHpy)**

In a 25 mL two-neck flask with a Liebig condenser under a nitrogen atmosphere, to a stirred solution of **2** (84 mg, 0.23 mmol) in CHCl<sub>3</sub> (10.0 mL) were added py-CF<sub>3</sub>-trzH<sub>2</sub> (80 mg, 0.23 mmol), PtCl<sub>2</sub>(DMSO)<sub>2</sub> (97 mg, 0.23 mmol), and DIPEA (80  $\mu$ L, 0.46 mmol). The mixture was heated at 50 °C, stirred overnight and then analyzed by TLC (EtOAc/acetone, 8:2). Direct evaporation afforded a crude reaction mixture that was purified by flash-chromatography (EtOAc/acetone, 9:1 to acetone) to give complex

**CF<sub>3</sub>-Pt-4OHpy** (102 mg, 70%) as a yellow luminescent waxy solid. Spectroscopic characterization was in accordance to the previously reported.

**7.4.1.3 (3R,4R)-3-((R)-1-((t-butyltrimethylsilyloxy)ethyl)-4-(3-(pyridin-4-yl)propoxy)azetidin-2-one (2)**

In a 25 mL two-neck flask dried and under nitrogen atmosphere, to a stirred solution of **A** (143 mg, 0.5 mmol) in 5.0 mL of dioxane, 3-pyridine-propanol (274 mg, 2.0 mmol) and ZnBr<sub>2</sub> (450 mg, 2.0 mmol) were added. The reaction was monitored by TLC (AcOEt/cyclohexane 8/2) and after 56 h quenched by stirring with a NaHCO<sub>3</sub> saturated aqueous solution (5 mL), extracted with DCM (3×10 mL), dried over Na<sub>2</sub>SO<sub>4</sub> and evaporated in vacuum. After flash-chromatography purification with a polarity gradient eluent from AcOEt/cyclohexane 4/6 to 8/2, compound **3** was obtained as a colorless oil in a 61% yield (111 mg).

$[\alpha]_D = -1.9$  ( $c = 0.76$ , CH<sub>2</sub>Cl<sub>2</sub>). <sup>1</sup>H NMR (400 MHz, CDCl<sub>3</sub>):  $\delta$  0.06 (s, 3H, MeSi), 0.08 (s, 3H, MeSi), 0.87 (s, 9H, tBuSi), 1.25 (d,  $J = 6.2$  Hz, 3H, Me), 1.94 (m, 2H, OCH<sub>2</sub>CH<sub>2</sub>), 2.71 (t,  $J = 7.6$  Hz, 2H, OCH<sub>2</sub>CH<sub>2</sub>CH<sub>2</sub>), 3.02 (d,  $J = 4.2$  Hz, 1H, CHCONH), 3.49 (t,  $J = 6.4$  Hz, 2H, OCH<sub>2</sub>), 4.17 (m, 1H, CHOTBS), 5.04 (s, 1H, CHNH), 6.61 (bs, 1H, NH), 7.12 (d,  $J = 4.0$  Hz, 2H, Arom), 8.50 (d,  $J = 4.0$  Hz, 2H, Arom) ppm. <sup>13</sup>C NMR (100.6 MHz, CDCl<sub>3</sub>):  $\delta$  -5.1, -4.4, 17.9, 22.5, 25.7, 29.9, 31.5, 64.2, 65.5, 66.6, 80.5, 124.0, 149.3, 150.9, 167.9 ppm. IR:  $\tilde{\nu} = 3227, 2955, 2929, 2857, 1767, 1605, 1463, 1417, 1361, 1255, 1120, 1098, 836$  cm<sup>-1</sup>. HPLC-MS (ESI<sup>+</sup>):  $R_t = 9.65$  min;  $m/z = 365$  [M+H]<sup>+</sup>

**7.4.1.4 Platinum [2,6-bis[5-(trifluoromethyl)-1,2,4-triazol-3-yl-κN<sup>2</sup>]pyridinato(2-)-κN] [(3R,4R)-3-((R)-1-((t-butyltrimethylsilyloxy)ethyl)-4-(3-(pyridin-4-yl)propoxy)azetidin-2-one-κN] (3)**

In a 25 mL two-neck flask with a Liebig refrigerator under nitrogen atmosphere, to a stirred solution of **2** (60 mg, 0.165 mmol) in 7.2 mL of CHCl<sub>3</sub> py-CF<sub>3</sub>-trzH<sub>2</sub> (58 mg, 0.165 mmol), PtCl<sub>2</sub>DMSO<sub>2</sub> (67 mg, 0.165 mmol) and DIPEA (69 μL, 0.396 mmol) were added. The mixture was heated at 50°C overnight and monitored by TLC with AcOEt as eluent. The crude, obtained after evaporation of the reaction solvent, was purified

by flash-chromatography with CH<sub>2</sub>Cl<sub>2</sub>/AcOEt 3/7, to obtain the compound **3** as a yellow to orange fluorescent waxy solid in a 39% yield (58 mg).

[ $\alpha$ ]<sub>D</sub> = -2.8 (c = 0.87, DCM). <sup>1</sup>H NMR (400 MHz, CDCl<sub>3</sub>):  $\delta$  0.07 (s, 3H, MeSi), 0.09 (s, 3H, MeSi), 0.87 (s, 9H, tBuSi), 1.29 (d, J = 6.4 Hz, 3H, Me), 2.03 – 2.12 (m, 2H OCH<sub>2</sub>CH<sub>2</sub>), 2.75–2.99 (m, 2H, OCH<sub>2</sub>CH<sub>2</sub>CH<sub>2</sub>), 3.06 (d, J = 3.6 Hz, 1H, CHCONH), 3.50–3.55 (m, 1H, OCHAHB), 3.56–3.66 (m, 1H, OCHAHB), 4.12–4.26 (m, 1H, CHOTBS), 5.09 (s, 1H, CHNH), 6.94 (s, 1H, NH), 7.34 (d, J = 6.2 Hz, 2H, Arom), 7.63 (d, J = 8.0 Hz, 2H, Arom), 7.90 (t, J = 8.0 Hz, 1H, Arom), 9.33 (d, J = 6.2 Hz, 2H, Arom) ppm. <sup>13</sup>C NMR (100.6 MHz, CDCl<sub>3</sub>):  $\delta$  -5.1, -4.3, 17.9, 22.5, 25.7, 28.9, 31.7, 64.3, 65.6, 66.0, 80.5, 118.1, 119.6 (q, <sup>1</sup>J<sub>C-F</sub> = 270 Hz), 121.0, 126.4, 143.0, 148.4, 152.5, 152.6 (q, <sup>2</sup>J<sub>C-F</sub> = 38 Hz), 155.4, 163.5, 167.8 ppm. <sup>19</sup>F NMR (376 MHz, CDCl<sub>3</sub>):  $\delta$  -64.1 ppm. IR:  $\tilde{\nu}$  = 3286, 2958, 2930, 2858, 1767, 1628, 1482, 1202, 1156, 1132, 1098 cm<sup>-1</sup>. MS (ESI<sup>+</sup>): m/z 907 [M+H]<sup>+</sup>, 929 [M+Na]<sup>+</sup>, 1836 [2M+Na]<sup>+</sup>. Found C, 39.65; H, 4.21; N, 12.44 %; C<sub>30</sub>H<sub>35</sub>F<sub>6</sub>N<sub>9</sub>O<sub>3</sub>SiPt requires C, 39.73; H, 3.89; N, 13.90 %

#### 7.4.1.5 1-(pyridin-4-yl)-2,5,8,11-tetraoxatridecan-13-ol (**4**)

In a 100 mL two-neck flask under nitrogen atmosphere, to a stirred solution of 4-chloromethyl-pyridine hydrochloride (820 mg, 5.0 mmol) in 40.0 mL of ACN were added tetraethylene glycole (949  $\mu$ L, 6.5 mmol) and TEA (1.4 mL, 10.0 mmol). After 1 hour stirring NaH 60% in mineral oil (400 mg, 10.0 mmol) was added and the mixture was stirred overnight at room temperature. The progress of the reaction was monitored by TLC (AcOEt/cyclohexane 8/2) and the reaction mixture was concentrated under vacuum. The obtained crude was then purified by flash-chromatography with acetone/MeOH 95/5, obtaining the alcohol **4** as a colorless oil in a 76% yield (217 mg).

<sup>1</sup>H NMR (400 MHz, CDCl<sub>3</sub>):  $\delta$  3.60–3.73 (m, 16H, OCH<sub>2</sub>CH<sub>2</sub>O), 4.61 (s, 2H, OCH<sub>2</sub>Arom), 7.36 (d, J = 5.2 Hz, 2H, Arom), 8.60 (d, J = 5.2 Hz, 2H, Arom) ppm. <sup>13</sup>C NMR (100.6 MHz, CDCl<sub>3</sub>):  $\delta$  60.8, 69.5, 69.6, 69.7, 69.9, 70.0, 70.8, 72.2, 72.3, 121.3, 147.4, 148.9 ppm. IR:  $\tilde{\nu}$  = 3375, 2969, 2925, 2879, 1465, 1419, 1378, 1301, 1127, 1106, 952 cm<sup>-1</sup>. HPLC-MS (ESI<sup>+</sup>): R<sub>t</sub> = 1.28 min; m/z 286 [M+H]<sup>+</sup>.

#### 7.4.1.6 Platinum [2,6-bis[5-(trifluoromethyl)-1,2,4-triazol-3-yl- $\kappa$ N<sup>2</sup>]pyridinato(2-)- $\kappa$ N] [1-(pyridin-4-yl)-2,5,8,11-tetraoxatridecan-13-ol- $\kappa$ N] (5)

In a 25 mL two-neck flask equipped with a Liebig refrigerator under nitrogen atmosphere, to a stirred solution of **4** (48 mg, 0.17 mmol) in 7.4 mL of CHCl<sub>3</sub>, py-CF<sub>3</sub>-trzH<sub>2</sub> (59 mg, 0.17 mmol), PtCl<sub>2</sub>DMSO<sub>2</sub> (72 mg, 0.17 mmol) and DIPEA (71  $\mu$ L, 0.408 mmol) were added. The mixture was heated at 50°C, left stirring overnight and then monitored by TLC (acetone/AcOEt 8/2). The crude was purified by CombiFlash using silica as stationary phase with CH<sub>2</sub>Cl<sub>2</sub>/MeOH 98/2 to obtained **5** as a yellow to orange fluorescent waxy solid in a 32% yield (45 mg).

<sup>1</sup>H NMR (400 MHz, CDCl<sub>3</sub>):  $\delta$  3.56–3.87 (m, 16H, OCH<sub>2</sub>CH<sub>2</sub>O), 4.76 (s, 2H, OCH<sub>2</sub>Arom), 7.68 (d, J = 6.0 Hz, 2H, Arom), 7.89 (d, J = 8.0 Hz, 2H, Arom), 8.08 (t, J = 8.0 Hz, 1H, Arom), 9.62 (d, J = 6.0 Hz, 2H, Arom). <sup>13</sup>C NMR (100.6 MHz, CDCl<sub>3</sub>):  $\delta$  61.6, 70.3, 70.4, 70.5, 70.6, 70.6, 70.7, 70.7, 72.5, 117.8, 119.4 (q, <sup>1</sup>J<sub>C-F</sub> = 269 Hz), 123.5, 142.7, 147.7, 152.0, 152.1 (q, <sup>2</sup>J<sub>C-F</sub> = 38 Hz), 152.6, 163.0 ppm. <sup>19</sup>F NMR (376 MHz, CDCl<sub>3</sub>):  $\delta$  -64.3 ppm. IR [ $\tilde{\nu}$ ]: 3423, 3062, 2922, 2363, 1629, 1482, 1463, 1132 cm<sup>-1</sup>. MS (ESI+): m/z 850 [M+Na]<sup>+</sup>, 1677 [2M+Na]<sup>+</sup>. Found C, 35.99; H, 3.52; N, 11.90 %; C<sub>25</sub>H<sub>26</sub>F<sub>6</sub>N<sub>8</sub>O<sub>5</sub>Pt requires C, 36.28; H, 3.17; N, 13.54 %.

#### 7.4.1.7 (3R,4R)-3-((R)-1-((t-butyldimethylsilyl)oxy)ethyl)-4-((1-(pyridin-4-yl)-2,5,8,11-tetraoxatridecan-13-yl)oxy)azetidin-2-one (6)

In a 25mL two-necked flask equipped with a Liebig refrigerator, dried and under nitrogen atmosphere, to a stirred solution of **A** (143 mg, 0.5 mmol) in 4.0 mL of dioxane, **5** (142 mg, 0.5 mmol) and ZnBr<sub>2</sub> (112 mg, 0.5 mmol) were added. The reaction was warm to 50°C and monitored by TLC (AcOEt). After 30 hours stirring the reaction was quenched with a NaHCO<sub>3</sub> saturated aqueous solution (5 mL) and evaporated under vacuum. The solid mixture was treated with 10 mL of ACN/MeOH 1/1, filtered and the liquid phase concentrated under vacuum. After a flash-chromatography purification with a polarity gradient eluent from AcOEt to AcOEt/MeOH 95/5, product **6** was obtained as a colorless oil in a 35% yield (90 mg).

$[\alpha]_D = 4.4$  ( $c = 1.00$ , DCM).  $^1\text{H NMR}$  (400 MHz,  $\text{CDCl}_3$ ):  $\delta$  0.06 (s, 3H, MeSi), 0.07 (s, 3H, MeSi), 0.88 (s, 9H, tBuSi), 1.25 (d,  $J = 6.4$  Hz, 3H, Me), 2.94 (dd,  $J = 1.2, 4.0$  Hz, 1H, CHCONH), 3.44–3.96 (m, 16H,  $\text{OCH}_2\text{CH}_2\text{O}$ ), 4.11–4.18 (m, 1H, CHOTBS), 4.60 (s, 2H,  $\text{OCH}_2\text{Arom}$ ), 5.00 (d,  $J = 1.2$  Hz, 1H, CHNH), 7.29 (d,  $J = 5.6$  Hz, 2H, Arom), 7.51 (s, 1H, NH), 8.57 (d,  $J = 5.6$  Hz, 2H, Arom) ppm.  $^{13}\text{C NMR}$  (100 MHz,  $\text{CDCl}_3$ )  $\delta$  -5.1, -4.2, 17.9, 22.4, 25.7, 26.5, 64.5, 65.4, 69.9, 70.2, 70.3, 70.4, 70.5, 70.7, 71.2, 71.5, 82.8, 122.2, 148.1, 149.9, 167.6 ppm. IR:  $\tilde{\nu} = 3330, 2955, 2928, 2858, 1764, 1462, 1375, 1253, 1103, 949, 778, 732$   $\text{cm}^{-1}$ . HPLC-MS ( $\text{ESI}^+$ ):  $R_t = 1.45$  min;  $m/z$  513  $[\text{M} + \text{H}]^+$ .

**7.4.1.8 Platinum [2,6-bis[5-(trifluoromethyl)-1,2,4-triazol-3-yl- $\kappa\text{N}^2$ ]pyridinato(2-)- $\kappa\text{N}$ ] [(3R,4R)-3-((R)-1-((t-butyl)dimethylsilyl)oxy)ethyl)-4-((1-(pyridin-4-yl)-2,5,8,11-tetraoxatridecan-13-yl)oxy)azetid-2-one- $\kappa\text{N}$ ] (7)**

In a 25 mL two-neck flask with a Liebig refrigerator under nitrogen atmosphere, to a stirred solution of **6** (44 mg, 0.086 mmol) in 7.2 mL of  $\text{CHCl}_3$ ,  $\text{py-CF}_3\text{-trzH}_2$  (30 mg, 0.086 mmol),  $\text{PtCl}_2\text{DMSO}_2$  (36 mg, 0.086 mmol) and DIPEA (36  $\mu\text{L}$ , 0.206 mmol) were added. The mixture was heated at 50°C overnight and then monitored by TLC with AcOEt/acetone (8/2). The crude, obtained after evaporation of the reaction solvent was purified by flash-chromatography with AcOEt/acetone 95/5 to obtain **7** as a yellow to orange luminescent waxy solid in a 59% yield (54 mg).

$[\alpha]_D = -0.4$  ( $c = 0.91$ , THF).  $^1\text{H NMR}$  (400 MHz,  $\text{CDCl}_3$ ):  $\delta$  -0.01 (s, 3H, MeSi), 0.00 (s, 3H, MeSi), 0.80 (s, 9H, tBuSi), 1.17 (d,  $J = 6.4$  Hz, 3H, Me), 2.88 (d,  $J = 4.4$  Hz, 1H, CHCONH), 3.46–3.85 (m, 16H,  $\text{OCH}_2\text{CH}_2\text{O}$ ), 4.02–4.14 (m, 1H, CHOTBS), 4.68 (s, 2H,  $\text{OCH}_2\text{Arom}$ ), 4.91 (s, 1H, CHNH), 7.46 (s, 1H, NH), 7.53 (d,  $J = 6.0$  Hz, 2H, Arom), 7.72 (d,  $J = 8.0$  Hz, 2H, Arom), 7.95 (t,  $J = 8.0$  Hz, 1H, Arom), 9.48 (d,  $J = 6.0$  Hz, 2H, Arom).  $^{13}\text{C NMR}$  (50.3 MHz,  $\text{CDCl}_3$ ):  $\delta$  -3.7, -3.6, 14.0, 22.6, 23.8, 25.6, 61.7, 66.3, 66.9, 67.4, 67.6, 70.4, 70.7, 70.8, 72.5, 82.5, 118.0, 120.8 (q,  $^1J_{\text{C-F}} = 265$  Hz), 123.7, 142.9, 148.4, 152.6, 152.7 (q,  $^2J_{\text{C-F}} = 40$  Hz), 152.8, 160.9, 163.5 ppm.  $^{19}\text{F NMR}$  (376 MHz,  $\text{CDCl}_3$ ):  $\delta$  -64.2 ppm. MS ( $\text{ESI}^+$ ):  $m/z$  1077  $[\text{M} + \text{Na}]^+$ . Found C, 40.88; H, 4.20; N, 12.30%;  $\text{C}_{36}\text{H}_{47}\text{F}_6\text{N}_9\text{O}_7\text{SiPt}$  requires C, 40.99; H, 4.49; N, 11.95 %.

## References

- [1] K. M. G. O'Connell; J. T. Hodgkinson; H. F. Sore; M. Welch; G. P. C. Salmond; D. R. Spring, *Angew. Chem. Int. Ed. Engl.*, **2013**, *52*, 10706-10733.
- [2] R. B. Sykes; C. M. Cimarusti; D. P. Bonner; K. Bush; D. M. Floyd; N. H. Georgopapadakou; W. H. Koster; W. C. Liu; W. L. Parker; P. A. Principe; M. L. Rathnum; W. A. Slusarchyk; W. H. Trejo; J. S. Wells, *Nature*, **1981**, *291*, 489-491.
- [3] *Antibiotics*, ed. American Society of Microbiology, **2003**
- [4] R. R. Watkins; M. Z. David; R. A. Salata, *J. Med. Microbiol.*, **2012**, *61*, 1179-1193.
- [5] D. J. Payne, *Science*, **2008**, *321*, 1644-1645.
- [6] B. Bhattacharya; E. Turos, *Tetrahedron*, **2012**, *68*, 10665-10685.
- [7] R. Cervellati; P. Galletti; E. Greco; C. E. A. Cocuzza; R. Musumeci; L. Bardini; F. Paolucci; M. Pori; R. Soldati; D. Giacomini, *Eur. J. Med. Chem.*, **2013**, *60*, 340-349.
- [8] P. Galletti; C. E. A. Cocuzza; M. Pori; A. Quintavalla; R. Musumeci; D. Giacomini, *ChemMedChem*, **2011**, *6*, 1919-1927.
- [9] F. Broccolo; G. Cainelli; G. Caltabiano; C. E. A. Cocuzza; C. G. Fortuna; P. Galletti; D. Giacomini; G. Musumarra; R. Musumeci; A. Quintavalla, *J. Med. Chem.*, **2006**, *49*, 2804-2811.
- [10] N. Arya; A. Y. Jagdale; T. A. Patil; S. S. Yeramwar; S. S. Holikatti; J. Dwivedi; C. J. Shishoo; K. S. Jain, *Eur. J. Med. Chem.*, **2014**, *74*, 619-656.
- [11] P. D. Mehta; N. P. S. Sengar; A. K. Pathak, *Eur. J. Med. Chem.*, **2010**, *45*, 5541-5560.
- [12] A. Monney; M. Albrecht, *Coord. Chem. Rev.*, **2013**, *257*, 2420-2433.
- [13] G. Chen; H. Qiu; P. N. Prasad; X. Chen, *Chem. Rev.*, **2014**, *114*, 5161-5214.
- [14] M. Montalti; L. Prodi; E. Rampazzo; N. Zaccheroni, *Chem. Soc. Rev.*, **2014**, *43*, 4243-4268.
- [15] Z. Li; J. C. Barnes; A. Bosoy; J. F. Stoddart; J. I. Zink, *Chem. Soc. Rev.*, **2012**, *41*, 2590-2605.
- [16] J. Khandare; M. Calderon; N. M. Dagia; R. Haag, *Chem. Soc. Rev.*, **2012**, *41*, 2824-2848.
- [17] C. S. Cutler; H. M. Hennkens; N. Sisay; S. Huclier-Markai; S. S. Jurisson, *Chem. Rev.*, **2013**, *113*, 858-883.
- [18] E. Terreno; D. D. Castelli; A. Viale; S. Aime, *Chem. Rev.*, **2010**, *110*, 3019-3042.
- [19] J. Yao; M. Yang; Y. Duan, *Chem. Rev.*, **2014**, *114*, 6130-6178.
- [20] M. Mauro; A. Aliprandi; D. Septiadi; N. S. Kehr; L. De Cola, *Chem. Soc. Rev.*, **2014**, *43*, 4144-4166.
- [21] V. Fernandez-Moreira; F. L. Thorp-Greenwood; M. P. Coogan, *Chem. Commun.*, **2010**, *46*, 186-202.
- [22] E. Baggaley; J. A. Weinstein; J. A. G. Williams, *Coord. Chem. Rev.*, **2012**, *256*, 1762-1785.
- [23] Q. Zhao; C. Huang; F. Li, *Chem. Soc. Rev.*, **2011**, *40*, 2508-2524.
- [24] K. K.-W. Lo; A. W.-T. Choi; W. H.-T. Law, *Dalton Trans.*, **2012**, *41*, 6021-6047.
- [25] R. Y. Tsien, *Angew. Chem. Int. Ed. Engl.*, **2009**, *48*, 5612-5626.
- [26] J. O. Escobedo; O. Rusin; S. Lim; R. M. Strongin, *Curr. Opin. Chem. Biol.*, **2010**, *14*, 64-70.
- [27] S. A. Hilderbrand; R. Weissleder, *Curr. Opin. Chem. Biol.*, **2010**, *14*, 71-79.
- [28] S. W. Botchway; M. Charnley; J. W. Haycock; A. W. Parker; D. L. Rochester; J. A. Weinstein; J. A. G. Williams, *Proc. Natl. Acad. Sci. U.S.A.*, **2008**, *105*, 16071-16076.
- [29] E. Baggaley; S. W. Botchway; J. W. Haycock; H. Morris; I. V. Sazanovich; J. A. G. Williams; J. A. Weinstein, *Chem. Sci.*, **2014**, *5*, 879-886.

- [30] M. Mauro; A. Aliprandi; C. Cebrian; D. Wang; C. Kübel; L. De Cola, *Chem. Commun.*, **2014**, *50*, 7269-7272.
- [31] V. W.-W. Yam; K. M.-C. Wong; N. Zhu, *J. Am. Chem. Soc.*, **2002**, *124*, 6506-6507.
- [32] Y. Sun; K. Ye; H. Zhang; J. Zhang; L. Zhao; B. Li; G. Yang; B. Yang; Y. Wang; S.-W. Lai; C.-M. Che, *Angew. Chem. Int. Ed. Engl.*, **2006**, *118*, 5738-5741.
- [33] W. Zhang; W. Jin; T. Fukushima; N. Ishii; T. Aida, *Angew. Chem. Int. Ed. Engl.*, **2009**, *48*, 4747-4750.
- [34] Y. Li; E. S.-H. Lam; A. Y.-Y. Tam; K. M.-C. Wong; W. H. Lam; L. Wu; V. W.-W. Yam, *Chem. Eur. J.*, **2013**, *19*, 9987-9994.
- [35] S. Yu-Lut Leung; V. Wing-Wah Yam, *Chem. Sci.*, **2013**, *4*, 4228-4234.
- [36] K. M.-C. Wong; V. W.-W. Yam, *Acc. Chem. Res.*, **2011**, *44*, 424-434.
- [37] D. Septiadi; A. Aliprandi; M. Mauro; L. De Cola, *RSC Advances*, **2014**, *4*, 25709.
- [38] M. Mauro; A. Aliprandi; D. Septiadi; N. S. Kehr; L. De Cola, *Chem. Soc. Rev.*, **2014**, *43*, 4144-4166.
- [39] K. Kumar; P. Singh; L. Kremer; Y. Guerardel; C. Biot; V. Kumar, *Dalton Trans.*, **2012**, *41*, 5778-5781.
- [40] N. E. A. El-Gamel, *J. Coord. Chem.*, **2009**, *63*, 534-543.
- [41] Z. H. Chohan; C. T. Supuran; A. Scozzafava, *J. Enzyme Inhib. Med. Chem.*, **2004**, *19*, 79-84.
- [42] D. Pellico; M. Gómez-Gallego; P. Ramírez-López; M. J. Mancheño; M. A. Sierra; M. R. Torres, *Chem. Eur. J.*, **2009**, *15*, 6940-6952.
- [43] J. G. Muntaner; L. Casarrubios; M. A. Sierra, *Org. Biomol. Chem.*, **2014**, *12*, 286-297.
- [44] C. A. Strassert; M. Otter; R. Q. Albuquerque; A. Höne; Y. Vida; B. Maier; L. De Cola, *Angew. Chem. Int. Ed. Engl.*, **2009**, *48*, 7928-7931.
- [45] R. Dosselli; R. Ruiz-González; F. Moret; V. Agnolon; C. Compagnin; M. Mognato; V. Sella; M. Agut; S. Nonell; M. Gobbo; E. Reddi, *J. Med. Chem.*, **2014**, *57*, 1403-1415.
- [46] X. Wang; Z. Guo, *Chem. Soc. Rev.*, **2013**, *42*, 202-224.
- [47] K. D. Mjos; C. Orvig, *Chem. Rev.*, **2014**, *114*, 4540-4563.
- [48] T. C. Johnstone; J. J. Wilson; S. J. Lippard, *Inorg. Chem.*, **2013**, *52*, 12234-12249.
- [49] F. Arnesano; M. Losacco; G. Natile, *Eur. J. Inorg. Chem.*, **2013**, *2013*, 2701-2711.
- [50] F. Arnesano; G. Natile, *Coord. Chem. Rev.*, **2009**, *253*, 2070-2081.
- [51] T. Zou; C.-N. Lok; Y. M. E. Fung; C.-M. Che, *Chem. Commun.*, **2013**, *49*, 5423-5425.
- [52] C. Y.-S. Chung; V. W.-W. Yam, *J. Am. Chem. Soc.*, **2011**, *133*, 18775-18784.
- [53] C.-M. Che; F.-M. Siu, *Curr. Opin. Chem. Biol.*, **2010**, *14*, 255-261.
- [54] P. Wu; E. L.-M. Wong; D.-L. Ma; G. S.-M. Tong; K.-M. Ng; C.-M. Che, *Chem. Eur. J.*, **2009**, *15*, 3652-3656.
- [55] J. Brooks; Y. Babayan; S. Lamansky; P. I. Djurovich; I. Tsyba; R. Bau; M. E. Thompson, *Inorg. Chem.*, **2002**, *41*, 3055-3066.
- [56] S.-Y. Chang; J. Kavitha; S.-W. Li; C.-S. Hsu; Y. Chi; Y.-S. Yeh; P.-T. Chou; G.-H. Lee; A. J. Carty; Y.-T. Tao; C.-H. Chien, *Inorg. Chem.*, **2006**, *45*, 137-146.
- [57] S. Develay; O. Blackburn; A. L. Thompson; J. A. G. Williams, *Inorg. Chem.*, **2008**, *47*, 11129-11142.
- [58] C. Cebrian; M. Mauro; D. Kourkoulos; P. Mercandelli; D. Hertel; K. Meerholz; C. A. Strassert; L. De Cola, *Adv. Mater.*, **2013**, *25*, 437-442.
- [59] M. Mydlak; M. Mauro; F. Polo; M. Felicetti; J. Leonhardt; G. Diener; L. De Cola; C. A. Strassert, *Chem. Mater.*, **2011**, *23*, 3659-3667.

# Chapter 8

## Mechanochromism: from bulk material to the nanoscale

**Abstract:** Luminescence mechanochromism is a phenomenon in which a mechanical action on solids leads to a change in the photoluminescent properties. Such phenomenon is studied from bulk materials for a family of pegylated Pt(II) to the nanoscale for a Pt(II) complex self-assembling in ultra-long ribbons. At the nanoscale, atomic force microscopy (AFM) is used to modulate the mechanical stress from pure pressure (piezochromism) to high friction (tribochromism), while confocal spectral imaging is used as the detection system. We design and achieve high-density information writing with AFM nanolithography on individual self-assembled ribbons. Moreover, we report that ribbons show changes in the emission spectrum upon exposure to light (photochromism) that can be used to conceal information previously written with nanolithography.

## 8.1 Introduction

Luminescence mechanochromism<sup>1-4</sup> is defined as a change of emission spectrum upon mechanical stresses. Depending on the nature of the mechanical means, the terms piezochromism and tribochromism are often used to distinguish respectively the effect of pressure from friction or grinding.<sup>5</sup>

The phenomenon of mechanochromism has recently emerged as a powerful new tool for a variety of applications, ranging from sensing<sup>6</sup> and tracking of mechanical stresses to data storage<sup>7</sup> and security<sup>8</sup>. In particular, data storage and data encryption<sup>9</sup> based on optical reading have attracted enormous interest, because miniaturization of memory units, eventually down to a single molecule, can lead to massive increase in information density and capacity.<sup>10</sup>

The race for miniaturization and read-out speed demands high brightness and large signal difference between two or more states. In the most desirable case, a switchable system should feature two forms both providing bright signals, which should be clearly distinguishable from one another and could be possibly probed separately.<sup>11,12</sup> As a consequence, an ideal mechanochromic system would thus feature high quantum yield of both “relaxed” (R) and “mechanically stressed” (MS) forms, large differences between their emission spectra, and large differences in excitation spectra, so that each form can be selectively excited and efficiently detected.<sup>13,14</sup> In recent years, quite a broad selection of Pt(II) complexes has been prepared showing mechanochromism, and responding to some of these requirements.<sup>4,15,16</sup> Conversely, the possibility of using them in novel high density memory was never explored. The use of microcrystalline mechanochromic powders for operations such as exposure, writing and reading at the submicron scale poses indeed serious problems in terms of obtaining a microscopically homogeneous memory substrate.<sup>17,18</sup>

However the possibility to prepare ultra-long ribbons of controlled size (see chapter 5) prone us to investigate on the possibility to directly employ them as microdevices for data storage and security.

In this chapter we correlate the mechanochromic properties of the bulk materials with single fibers at the nanoscale. In particular we have monitored the change in the photoluminescent properties upon mechanical grinding (tribochromism) and by pressure dependent studies (piezochromism). At the nanoscale we have used an AFM tip to modulate the mechanical stress from pure pressure to high friction in a single self-assembled fiber. Moreover, we have found that an AFM tip can be used to write submicron features with high fidelity on individual ribbons, which are individually used as homogeneous memory substrates. The information written by AFM can also be hidden upon irradiation. The photoconversion of the fiber (in R form) into a yellow emitting form (PC), featuring similar luminescence as MS, reduces the luminescence contrast with the unwritten region of the ribbon.

## 8.2 Result and discussion

### 8.2.1 Mechanochromic properties of the bulk materials

The synthesis of the compounds, their self-assembly properties, as well as the photophysical property in solution have been discussed in details in chapter 5. In this chapter we will focus on the solid state properties and on their responsiveness to mechanical and photochemical stimuli. Molecular structures of the complexes investigated in this chapter are depicted in Figure 8.1.

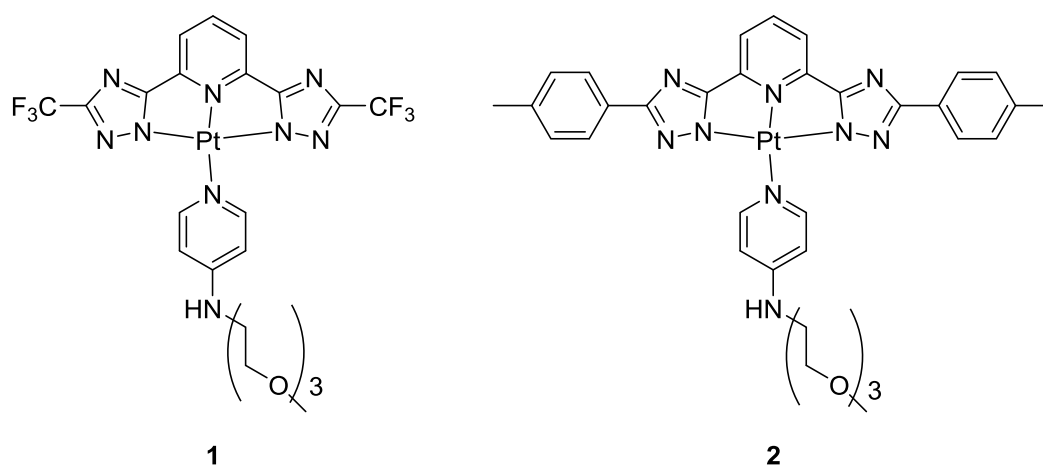


Figure 8.1. Molecular structures of the investigated platinum complexes.

Complex **1** displays bright blue emission in solid state (R form) peaking at  $\lambda_{em} = 465, 494, 527$  nm with a multi-exponential excited-state lifetime, being  $\tau_{av} = 1.08$   $\mu$ s. After

a gentle grinding using a pestle, the complex becomes bright yellow (MS form) and the emission spectra is characterized by a broad band centered at  $\lambda_{\text{max}} = 598 \text{ nm}$  with PLQY up to 51% and bi-exponential excited state lifetime with  $\tau_{\text{av}} = 514 \text{ ns}$ . The lifetime observed for R form is ascribable to the triplet nature of the  $^3\text{LC}/^3\text{MLCT}$  excited state of the monomeric species; by contrast, the decrease of the excited state lifetime after grinding (MS form) is due to a larger influence of the heavy metal in the nature of the new  $^3\text{MMLCT}$  excited state. Upon treatment of the ground powder with a few drops of acetone, the yellow luminescence from this complex changes back to the original blue luminescence after drying of the solid in air for a few minutes (Figure 8.2).

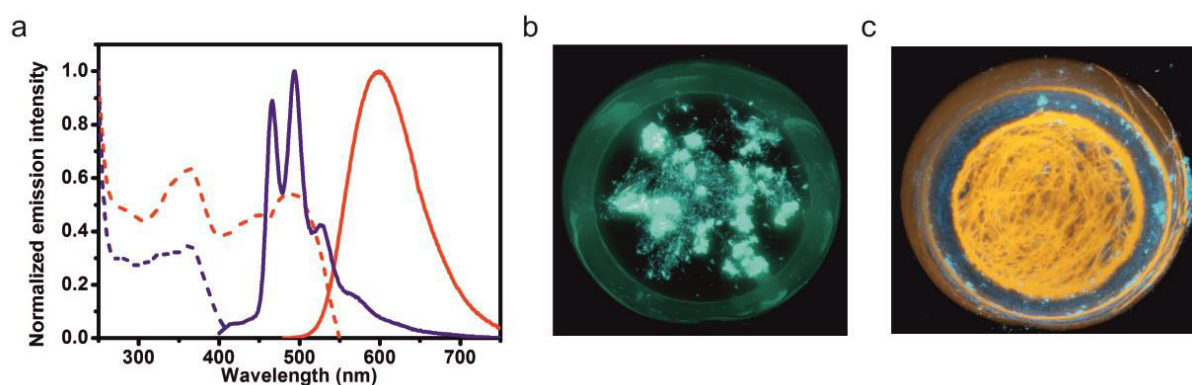


Figure 8.2. (a) Solid state emission (line) and excitation (dashed line) spectra of complex **1** before (blue) and after grinding (red) with a pestle. Photographs showing **1** on an agate mortar under UV irradiation ( $\lambda_{\text{exc}}=365 \text{ nm}$ ) before (b) and after (c) grinding.

Also complex **2** exhibits a similar mechanochromic response: before grinding the compound is characterized by an intense green emission (R form) with PLQY up to 46%  $\tau_{\text{av}} = 2.207 \mu\text{s}$  and  $\lambda_{\text{max}} = 542 \text{ nm}$  while, after grinding (MS form), the emission spectrum becomes broader with  $\lambda_{\text{max}} = 602 \text{ nm}$  PLQY up to 35% and  $\tau_{\text{av}} = 1.186 \mu\text{s}$  (Figure 8.3). Like complex **1** upon treatment of the ground powder with a few drops of acetone, the yellow luminescent turns back into the original green luminescent after drying the solid.

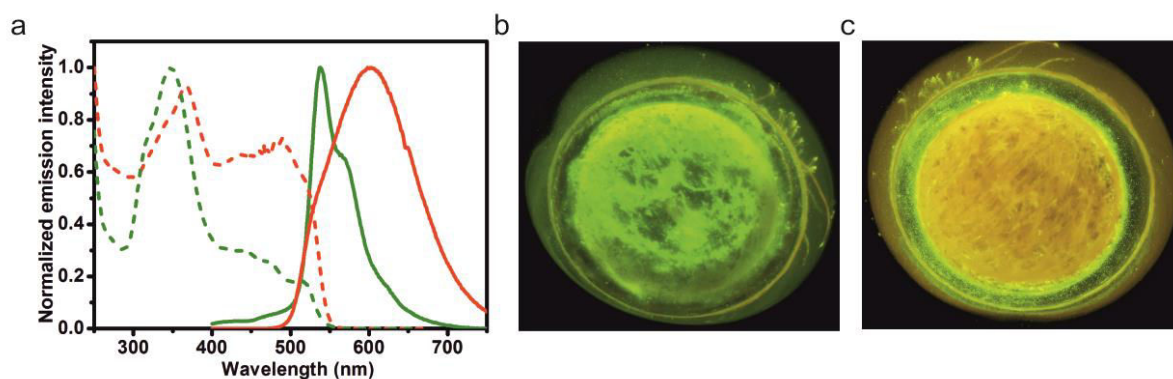


Figure 8.3. (a) Solid state emission (line) and excitation (dashed line) spectra of complex **2** before (blue) and after grinding (red) with a pestle. Photographs showing **2** on an agate mortar under UV irradiation ( $\lambda_{exc}=365$  nm) before (b) and after (c) grinding.

Both complexes **1** and **2** show a decrease of the excited state lifetime when the R form is mechanically converted into the MS form. However the PLQY increases when converting R into MS for complex **1**, but it decreases for complex **2** (Table 8.1).

	$\lambda_{em}(nm)$	PLQY (%)	t ( $\mu s$ )	$K_r (10^4 s^{-1})$	$K_{nr} (10^4 s^{-1})$
<b>1</b> R form	465, 494, 527	20	1.08	18.52	74.07
<b>1</b> MS form	598	51	0.514	99.22	95.33
<b>2</b> R form	542, 569(sh)	46	2	20.84	24.47
<b>2</b> MS form	602	35	1.18	29.51	54.81

Table 8.1. Photophysical properties of compounds **1** and **2** before (R form) and after grinding (MS form).

Since complex **1** displays the largest shift of the emission maximum between the R and the MS form (see Table 8.1) we have performed pressure dependent emission on complex **1** by using a diamond anvil cell (DAC) which allows pressures up to  $\sim 30$  kbar. The pressure has been calculated using a ruby microcrystal as internal reference (R-line emission at  $\sim 694$  nm). The resulting spectra are depicted in Figure 8.4.

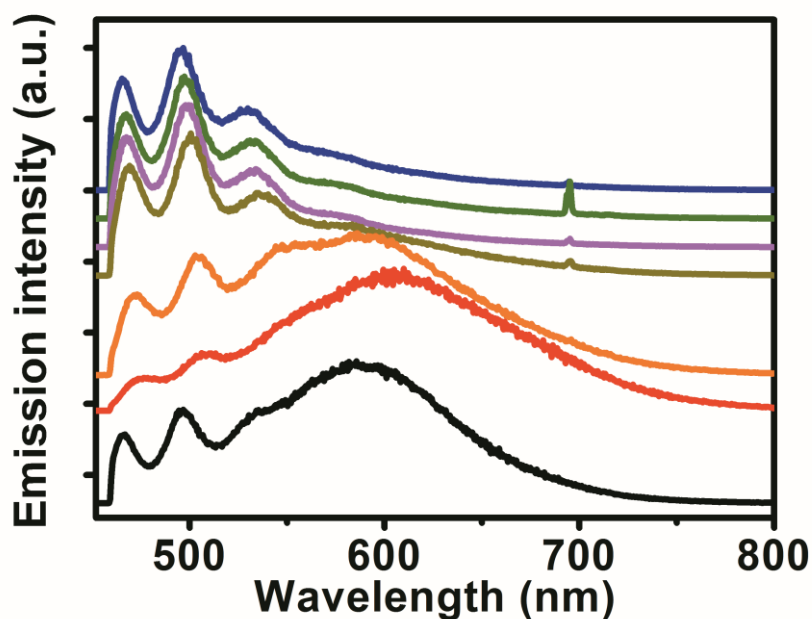


Figure 8.4. Pressure dependent emission spectra recorder for **1** at 0 kbar (blue line), 4.5 kbar (green line), 8.7 kbar (magenta line), 14.3 kbar (brown line), 24.2 kbar (orange line), 30.5 kbar (red line) and after release of the pressure (black line).

The peaks at 464 at 494 nm have been used as fingerprint of the R form while the band centered at  $\sim 600$  nm as fingerprint of the MS form. As can be observed from Figure 8.4, no significant changes in the emission spectrum occur until a pressure of  $\sim 15$  kbar is reached. When the applied pressure exceeds this threshold, the conversion of the R form into the MS form takes place. Interestingly even at a pressure of  $\sim 30$  kbar, which corresponds to the instrumental limit, the conversion of the R form into the MS form is still incomplete (Figure 8.4, red line). Moreover, upon release of the pressure, a partial conversion of the MS form back to the initial R form is observed as indicated by the relative intensity increase of the peaks at 465 and 494 (Figure 8.4, black line) respect to the band centered at  $\sim 600$  nm. Even if it's not possible to quantify the exact local pressure exerted by gentle grinding using a mortar, which has been performed by hand, these preliminary results suggest that friction exerted by grinding is more effective than simple pressure in triggering the mechanochromic response, allowing a quantitative conversion from the R form to the MS form.

## 8.2.2 Mechanochromism at the nanoscale

Complex **1**, in the R form, can be self-assembled into ultra-long ribbons in a  $\text{CH}_3\text{CN}$ , yielding structures with typical length between 250  $\mu\text{m}$  and 5 mm and rectangular section of aspect ratio about 1:10, featuring thickness in the range 2:5  $\mu\text{m}$  and width in the range 15:50  $\mu\text{m}$  (Figure 8.5).

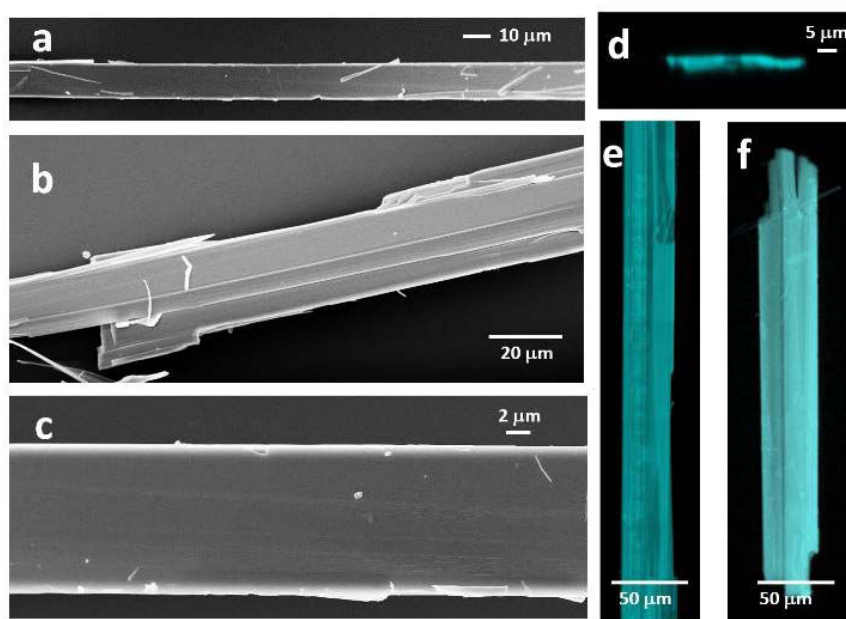


Figure 8.5. (a-c) SEM images of ultra-long ribbons formed by complex **1** at different magnifications. (d) Cross-section image of a typical ribbon reconstructed by z-stacking confocal microscopy, showing the approximately rectangular cross-section with aspect ratio about 1:10. (e,f) Confocal microscope images of typical ultra-long ribbons (color coded spectral images, wavelength range 400-700nm,  $\lambda_{\text{exc}}=375\text{nm}$ ).

The optimal morphology (flat and homogeneous in the tens of microns length scale) and photophysical properties (bright contrast upon scratching) of the ultra-long ribbons allow for the first investigation of Pt(II) complexes mechanochromism at the nanoscale, with the final aim of demonstrating the applicability of these materials in high density memory and data encryption.

We use an AFM as a nanoscopic mechanical stimulation tool, whose spatial resolution is given by the effective sharpness of the tip during typical experimental procedure. The AFM is used in contact mode, generating the mechanochromic response with fine control on the applied force, on the position and on the geometry of the system. Detection is fast and sensitive, based on fluorescence microscopy methods: wide-field microscopy coupled to AFM provides real-time monitoring of the lithography

process, and confocal spectral imaging yields high-resolution spatial and spectral information. The generated mechanochromism is persistent and stable in time for months. Mechanochromism can be triggered in two different ways (Figure 8.6a), which are here used to modulate the mechanical stress from pure pressure to high friction, and thus to extract quantitative information on the mechanism leading to the luminescence change.

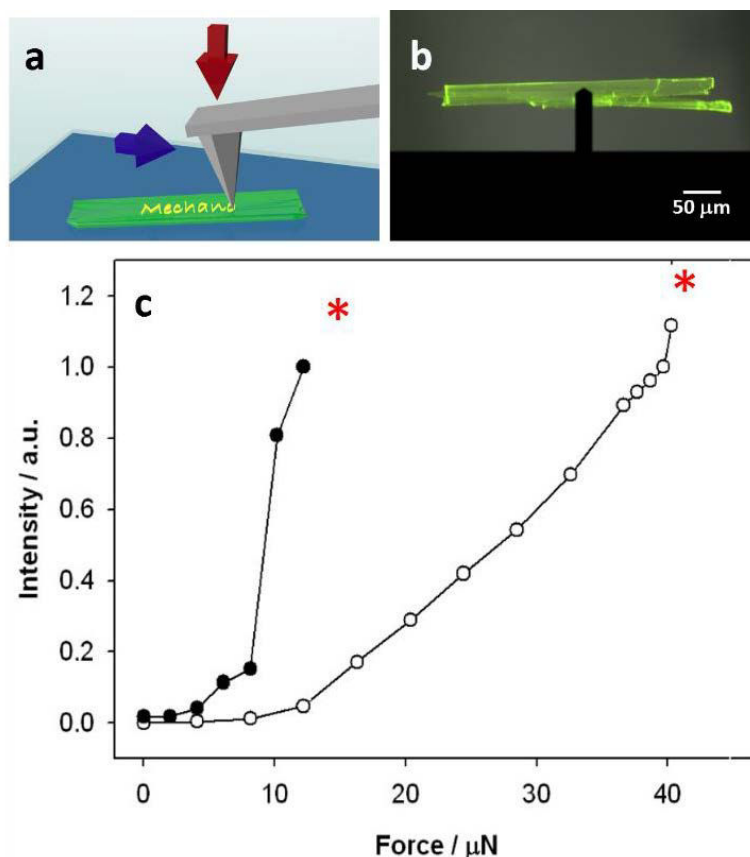


Figure 8.6. (a) Sketch of nanomechanical stresses applied with AFM. In the case of static pressure only a force perpendicular to the sample is present (red arrow) while the friction is originated by a constant perpendicular force (red arrow) and a constant force parallel to the plane of the ribbon (blue arrows). (b) Micro-graph of AFM cantilever approaching the ribbon, the fluorescence of the fiber (HC-QD filter set) is overlapped with the bright field image. (c) Plots of luminescence intensity (green channel on color CCD, FITC filter set) during application of static force (white circles) or after writing squares (20 μm side) at scan rate of 10 μm/s. Asterisks denote the breaking points, i.e. the force at which the ribbon is heavily damaged by the tip, resulting in sudden bursts of MS luminescence.

For static pressure a constant force, measured after calibration of the tip (see SI), is applied locally, through the AFM tip, on the ribbon. Since the tip does not move respect to the sample, static local pressure can be quantitatively estimated from the applied force and from the contact surface during mechanical stress. Tip geometry is

assessed by means of SEM directly after use of the tip: we observe different degrees of wear and of contamination of the tip, but we can estimate an average contact surface with diameter ranging between 80 and 150 nm. We observe first occurrence of mechanochromism at ca. 15  $\mu\text{N}$  force, which corresponds to a pressure in the range 2-7 kbar according to the actual contact surface. Fiber breaking occurs at force  $> 40 \mu\text{N}$ . At such loading, the AFM tip enters deep into the fiber and originates a sudden burst of newly scratched luminescent material.

In the case of scanning force (Figure 8.6b) the tip is scanned over the ribbon with constant applied force, the dominating mechanical stress shifts from pressure to friction. At low scan rates ( $<10 \mu\text{m/s}$ ) we observe a similar trend as for the simple pressure experiment, except that an earlier onset of mechanochromism can be detected, with *MS* emission first occurring at 4  $\mu\text{N}$  applied force, as well as an earlier damage of the fiber (15  $\mu\text{N}$ ). At high scan rates ( $>100 \mu\text{m/s}$ ) or on particularly rough surface regions, ribbons can be heavily scratched even at very low forces (ca 1  $\mu\text{N}$ , not shown), while ribbon wear and debris scattering increase due to high friction and to increased lateral forces.

Very importantly, no propagation of mechanochromism is observed. When tip approaches the surface and presses the ribbon, mechanochromism is observed only closer to the tip, within the resolution limit of fluorescence microscopy (ca 500 nm in the setup here used). Even when the tip enters deep into the material and destroys the fiber, the fracture and the consequent mechanochromism occur in a relatively small and confined region, ascribable to the size of the whole tip cone (see experimental part).

This observation led us to test the effective potential of the ultra-long mechanochromic ribbons as memory micro-devices, by using the tip of an AFM as a lithographic tool to write information on individual ribbons, following an approach similar to nanoshaving<sup>19,20</sup> or nanoscratching.<sup>21-23</sup> During the writing process, we can monitor the ribbon luminescence with UV light, or visualize what is being written by selectively exciting the *MS* form with visible light. The information stored can indeed be read with two different excitation wavelengths: UV excitation (355 nm) excites

both native and mechanically stressed forms, and provides an average vision of the emission properties of the ribbons; blue excitation (488 nm) excites selectively the mechanically stressed form (MMLCT), and is thus able to report even very small mechanochromic effects.

### **8.2.3 nanolithography**

We use software controlled nanolithography in contact mode to write information with submicron resolution. A 7-letters word (“Mechano” or “Chromic”) is written with high resolution, with each line composing the letters featuring FWHM in the range 400-700 nm, approaching the limit of resolution of confocal detection with a 63x objective (Figure 8.7). The high color contrast allows for easy detection and reading of the stored information, as apparent from the real-color coded confocal spectral images in Figure 8.7a-b. Similarly to what previously discussed for static or dynamic mechanical stresses, also in the writing process friction plays a key-role. At low writing speed ( $<10\mu\text{m/s}$ , Figure 8.7a) the ribbons are engraved with low trenches and the resulting information is detectable and clearly distinguished from the cyan background. When speed is increased to maximum  $100\mu\text{m/s}$ , with the same applied force ( $24\mu\text{N}$ ), deeper trenches are engraved, yielding more intense signal but also scattered debris which vitiates the readability of the stored information (Figure 8.7b).

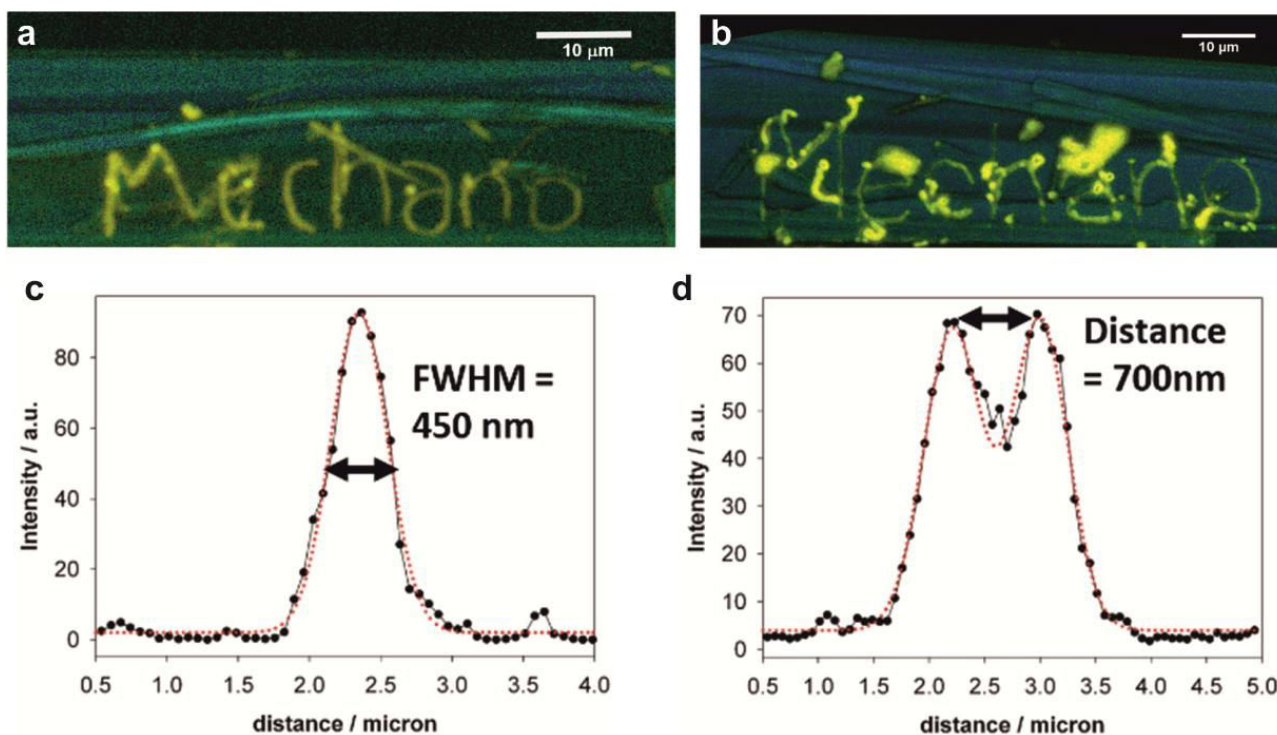
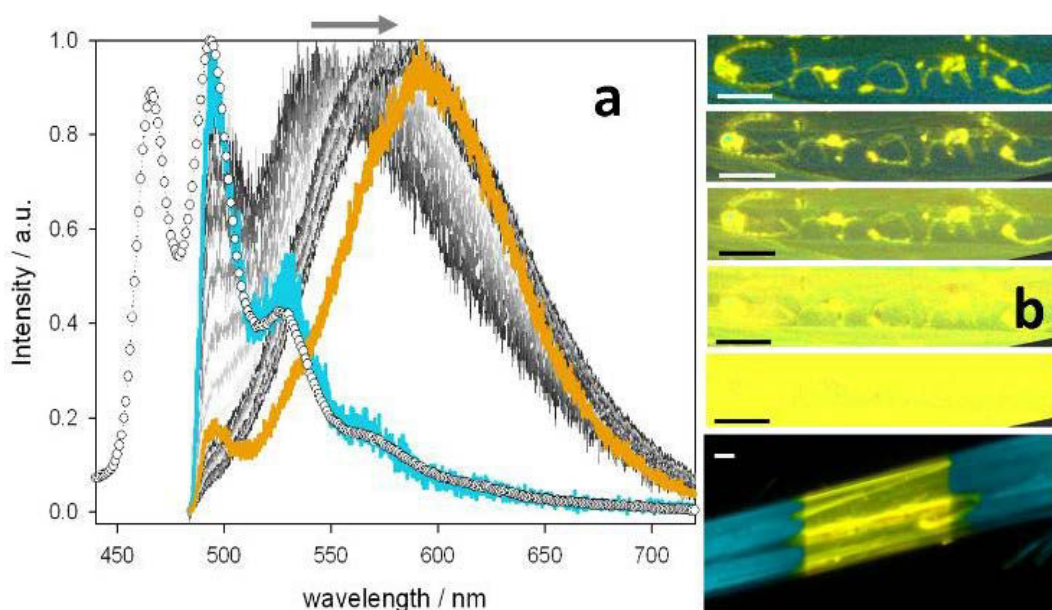


Figure 8.7. Nanolithography on ultra-long ribbons. Confocal spectral images of ribbons engraved with a 7-letters word (“Mechano”) by means of AFM nanolithography conducted at  $10 \mu\text{m/s}$  maximum scan rate (a) or  $100 \mu\text{m/s}$  maximum scan rate (b), with constant force =  $24 \mu\text{N}$ . Excitation laser used is  $488\text{nm}$  and spectral window  $490\text{-}700 \text{ nm}$  with resolution  $9\text{nm}$ , objective  $63\times$ . (c) and (d) Intensity profiles in correspondence of written letters showing the resolution of data storage through FWHM of single lines and peak-to-peak distance of adjacent resolved lines (black lines and dots denote the experimental intensity profiles, red dotted lines are Gaussian fits).

### 8.2.4 Photochromism

Finally, we find out that the ribbons are responsive not only to mechanical stresses, but also to light stimuli. Photoconversion of native R form occurs indeed upon excitation with UV or blue light: using focused laser excitation ( $405 \text{ nm}$  or  $473 \text{ nm}$ ) in a confocal microscope setup, prolonged irradiation results in photoconversion of the native blue emitting ribbons in yellow emitting ribbons (PC form), showing very similar luminescence spectrum as the mechanically stressed form. In particular, normalized spectra in Figure 8.8a reveal that photoconversion is a continuous, gradual process, which causes a progressive bathochromic shift of the emission until it reaches a state (PC) with a similar emission spectrum as MS, even though broader. Photoconversion is particularly efficient at relatively low irradiation rates, since at high excitation power leads to photodegradation of the Pt(II) complex. The prolonged exposure time needed to reach the maximum photoconversion efficiency (several

hours), together with the low irradiation power (1 microW), suggests that photoconversion relies on a purely photochemical mechanism and does not involve heat, which is instead dissipated within much a shorter time. This is also confirmed by the fact that ribbons exposed to conventional heat sources (oven or hotplates at 100 °C) do not undergo any observable photophysical or morphological transformation.



*Figure 8.8. Photoconversion of ribbons luminescence color. (a) Emission spectra of R (cyan line), MS (orange line) and during photoconversion of R into PC (gray intensity lines, shifting bathochromically), under continuous irradiation at 473 nm, at low power (10 microW, objective 60x). Spectra were taken with high resolution spectrometer in confocal setup with  $\lambda_{exc}=473$  nm and emission filter cut-off at 480nm. Emission spectrum of R obtained by a standard fluorometer (empty circles,  $\lambda_{exc}=375$ nm) is also plotted for clarity. (b) Hiding information written with AFM nanolithography (7-letters word “Chromic” was written at 100  $\mu$ m/s maximum scan rate) by local irradiation at 405 nm in a confocal setup. Confocal spectral images from top to bottom are taken with 488nm excitation at increasing irradiation time from 0 to 2h. The larger field of view of bottom image shows that photoconversion only occurred locally, within the irradiation area. Scale bars always denote 10  $\mu$ m.*

Photoconversion can be conveniently used to locally hide information written with mechanical nanolithography. We choose to test a ribbon with information written at high speed (100  $\mu$ m/s maximum scan rate) in order to have the highest possible MS signal to be disguised, ascribable both to deep trenches and to strongly luminescent debris. Figure 8.8 shows indeed a written region of a ribbon which, starting from blue-yellow contrast owing to R and MS forms, upon exposure to a focused 405nm laser

source turns completely to a yellow luminescent form within 2 hours. The information written by mechanical nanolithography is hence disguised and not any longer readable.

### **8.3 Conclusion**

We investigate the change of the photophysical properties of pegylated Pt(II) complexes in the bulk solid using mechanical grinding till the nanoscale using atomic force microscopy (AFM) on individual self-assembled ribbons. Confocal spectroscopy, used as a highly sensitive detection system, reveals that friction related mechanisms are more efficient triggering mechanochromic response than simple pressure. Data can be written with AFM nanolithography on individual self-assembled ribbons, which hence behave as micro-devices for data storage. The luminescence of written information has high contrast respect to native luminescence due to the establishment of Pt...Pt interaction (MMLCT band). Also photochromism, emission spectrum changes upon exposure to light, has been observed and conveniently used to conceal information previously written with nanolithography, since the region of the ribbon surrounding the stored information is homogeneously converted with irradiation.

### **8.4 Experimental section**

The synthesis of the compounds and their self-assembly properties are described in chapter 5. Steady-state emission and excitation spectra and time resolved emission decays were recorded on a Picoquant FT300 fluorometer with a 450 W xenon arc lamp, and a 375nm diode laser, respectively. Emission and excitation spectra were corrected for source intensity (lamp and grating) and emission spectral response (detector and grating) by standard correction curves. The absolute photoluminescence quantum yields (PLQY) were measured on a Hamamatsu Quantaurus-QY integrating sphere in air-equilibrated condition using an empty quartz tube as a reference.

#### **8.4.1 Pressure dependent emission**

High pressure emission spectra were performed at ambient temperature using a screw-driven diamond anvil cell (DAC) from Diacell designed for pressures up to ~30 kbar. Because of relatively modest pressures probed, the standard tedious procedure of preindentation and subsequent drilling of gaskets was not applied. Instead, ready-to-use laser-machined gaskets out of stainless steel were used. Low-viscosity silicon oil served as a pressure transmitting medium. Ruby microcrystals were added to a sample in the DAC as a standard pressure sensor (via detection of the shift in ruby R-line emission at ~694 nm). Photoluminescence spectra were measured with a Witec CMA200 Raman microscope at a laser excitation wavelength of 405 nm. The emission was separated from the laser line with a 450 nm longpass filter.

#### **8.4.2 Wide-field imaging**

Local fluorescence was monitored during mechanical stimulation by means of an inverted fluorescence microscope (Nikon wide-field) coupled to an Asylum AFM (MFP-3D) mounted on the stage. The microscope was equipped with a color CCD camera and with two filter sets i.e. (i) HC-QD filter set (excitation 435/400nm, emission LongPass 500nm) to monitor the average luminescence from the ribbons and (ii) FITC filter set (excitation 475/435nm, emission 530/543nm) to selectively monitor the luminescence from the mechanically stressed form.

#### **8.4.3 Confocal Imaging**

Confocal Imaging was performed on a Zeiss LSM 710 confocal microscope system equipped with built-in spectral module, 375nm, 405nm and 488nm excitation lasers, and 10x or 63x magnification objectives (Zeiss GmbH, Germany).

#### **8.4.4 Sample preparation**

Samples were prepared by depositing self-assembled ribbons onto adhesive glass slides, to obtain ribbons directly accessible (not embedded in a matrix) but also fixed on a substrate, not moving during mechanical stimulation. Glass slides were coated

with a thin layer of partially photocured optical glue (NOA 81, Norland Products Inc.), obtained by spin coating (3000 rpm, 30 s) followed by exposure to UV light (365 nm, 30 s).

#### **8.4.5 AFM studies and nanolithography**

All nanomechanical assays and lithographic patterns were performed with silicon tapping-mode cantilevers ( $k = 42 \text{ N m}^{-1}$ ) on a commercial AFM (Asylum Research, MFP-3D AFM) in contact mode. The loading force was varied in the range 0-45 microN (set-point 0-10 V) as determined through calibration of cantilever deflection and measurement of its spring constant by thermal noise method.

Static pressure was applied with an AFM tip operated in contact mode, engaged without scanning at increasing deflection voltages. A movie was recorded during loading, then intensity data was extracted with image analysis from signal integration in the green channel of the color CCD, on an area of 9 pixels centered on the tip (where the maximum luminescence intensity is recorded), and finally plotted versus applied force. Friction experiments were performed by writing squares of 20  $\mu\text{m}$  side at scan rate  $10 \mu\text{m s}^{-1}$  (0.5 Hz) or larger. Nanolithography was performed by using built-in software (Asylum Research).

## 8.5 References

- [1] Y. Sagara; T. Kato, *Nat. Chem.*, **2009**, *1*, 605-610.
- [2] X. Zhang; Z. Chi; Y. Zhang; S. Liu; J. Xu, *J. Mater. Chem. C*, **2013**, *1*, 3376-3390.
- [3] H. Sun; S. Liu; W. Lin; K. Y. Zhang; W. Lv; X. Huang; F. Huo; H. Yang; G. Jenkins; Q. Zhao; W. Huang, *Nat. Commun.*, **2014**, *5*.
- [4] S. J. Choi; J. Kuwabara; Y. Nishimura; T. Arai; T. Kanbara, *Chem. Lett.*, **2012**, *41*, 65-67.
- [5] *Chromic Phenomena: Technological Applications of Colour Chemistry*, ed. Royal Society of Chemistry, **2010**
- [6] A. Pucci; F. Di Cuia; F. Signori; G. Ruggeri, *J. Mater. Chem.*, **2007**, *17*, 783-790.
- [7] S. Hirata; T. Watanabe, *Adv. Mater.*, **2006**, *18*, 2725-2729.
- [8] A. Kishimura; T. Yamashita; K. Yamaguchi; T. Aida, *Nat. Mater.*, **2005**, *4*, 546-549.
- [9] I. Gourevich; H. Pham; J. E. N. Jonkman; E. Kumacheva, *Chem. Mater.*, **2004**, *16*, 1472-1479.
- [10] S.-J. Lim; B.-K. An; S. D. Jung; M.-A. Chung; S. Y. Park, *Angew. Chem. Int. Ed. Engl.*, **2004**, *43*, 6346-6350.
- [11] X.-P. Zhang; J.-F. Mei; J.-C. Lai; C.-H. Li; X.-Z. You, *J. Mater. Chem. C*, **2015**, *3*, 2350-2357.
- [12] T. Aotake; M. Suzuki; K. Tahara; D. Kuzuhara; N. Aratani; N. Tamai; H. Yamada *Chem. Eur. J*, **2015**, *21*, 4966-4974.
- [13] Y. Sagara; S. Yamane; T. Mutai; K. Araki; T. Kato, *Adv. Funct. Mater.*, **2009**, *19*, 1869-1875.
- [14] X. Zhu; R. Liu; Y. Li; H. Huang; Q. Wang; D. Wang; X. Zhu; S. Liu; H. Zhu, *Chem. Commun.*, **2014**, *50*, 12951-12954.
- [15] X. P. Zhang; V. Y. Chang; J. Liu; X. L. Yang; W. Huang; Y. Li; C. H. Li; G. Muller; X. Z. You, *Inorg. Chem.*, **2015**, *54*, 143-152.
- [16] J. Ni; Y. G. Wang; H. H. Wang; L. Xu; Y. Q. Zhao; Y. Z. Pan; J. J. Zhang, *Dalton Trans.*, **2014**, *43*, 352-360.
- [17] S. Kawata; Y. Kawata, *Chem. Rev.*, **2000**, *100*, 1777-1788.
- [18] M. Wuttig; N. Yamada, *Nat. Mater.*, **2007**, *6*, 824-832.
- [19] M. Liu; N. A. Amro; G.-y. Liu, *Annu. Rev. Phys. Chem.*, **2008**, *59*, 367-386.
- [20] G. R. Luis; L. Jian, *J. Phys-Condens. Mat.*, **2009**, *21*, 483001.
- [21] M. Hirtz; M. K. Brinks; S. Miele; A. Studer; H. Fuchs; L. Chi, *Small*, **2009**, *5*, 919-923.
- [22] L. Li; M. Hirtz; W. Wang; C. Du; H. Fuchs; L. Chi, *Adv. Mater.*, **2010**, *22*, 1374-1378.
- [23] T. Gan; X. Zhou; C. Ma; X. Liu; Z. Xie; G. Zhang; Z. Zheng, *Small*, **2013**, *9*, 2851-2856.

# Summary

This thesis titled “Platinum complexes and their luminescent assemblies” focuses on the synthesis and characterization of square planar Pt(II) complexes. Such complexes display large changes of their photophysical properties, upon self-assembly. The manuscript starts with a short introduction that focuses on the general photophysical and self-assembly properties of Pt(II) complexes (**Chapter 1**) and the experimental techniques employed for carrying out the work herein described (**Chapter 2**).

First, **Chapter 3** describes the synthetic protocols for the preparation of ligands and the corresponding Pt(II) compounds. In particular, the complex bearing a tridentate ligand 2,6-bis(3-(trifluoromethyl)-1*H*-1,2,4-triazol-5-yl)pyridine and 4-amyipyridine as the ancillary moiety (**Pt-CF<sub>3</sub>tz-pyC<sub>5</sub>**) has been prepared and characterized, and the photophysical properties comprehensively investigated (Figure 1). In dilute chloroform (CHCl<sub>3</sub>) solution (5x10<sup>-5</sup> M) at room temperature, the absorption spectrum displays intense bands in the UV region mainly attributed to the intraligand (<sup>1</sup>IL) and metal-perturbed interligand charge transfer (<sup>1</sup>ILCT) states (Figure 1b); whilst, upon photoexcitation the sample display a weak blue luminescence attributed to an emissive excited state with mainly <sup>3</sup>LC character.

The self-assembly properties of complex **Pt-CF<sub>3</sub>tz-pyC<sub>5</sub>** were investigated and a solvent-assisted organization into micrometer-long and highly crystalline fibers was observed (Figure 1a). Interestingly, slow evaporation of the solvent leads to the formation of yellow bright emissive microcrystalline fibers onto a substrate such as quartz, display an intense and featureless emission centered at  $\lambda_{em,max} = 559$  nm with PLQY of 0.74 (Figure 1b) and a new band at lower energy ( $\lambda = 501$  nm) in the excitation spectra due to the establishment of highly directional metallophilic

interaction (MMLCT). Also, the self-assembled fibers can be nicely grown in an aligned fashion as shown in Figure 1a so that bulk sample of the aggregates shows linearly polarized light absorption as well as highly efficient polarized yellow-orange light emission.

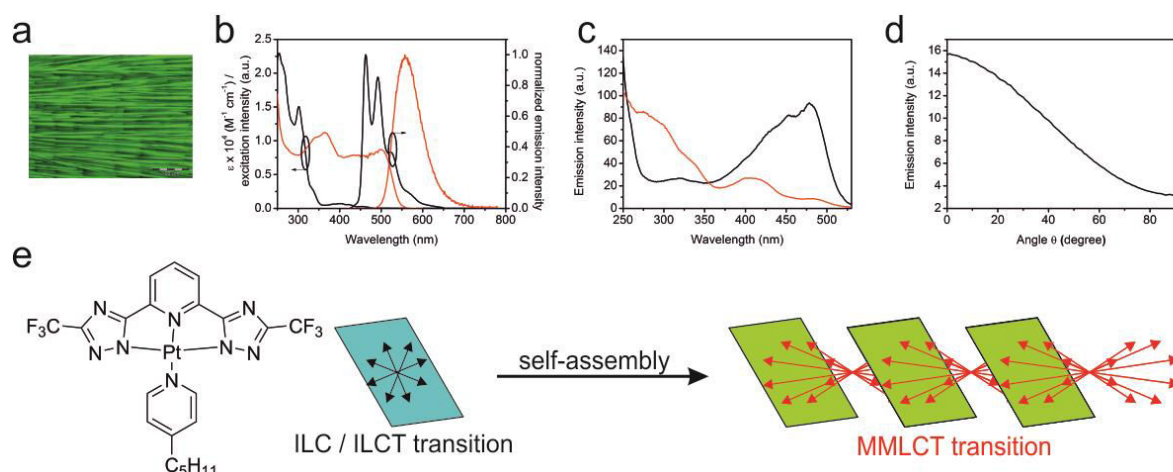


Figure 1. (a) Fluorescence microscopy image of the aligned fibers obtained from acetone under irradiation at  $\lambda = 400\text{--}440$  nm. Scale bar =  $100 \mu\text{m}$ . (b) Absorption spectra and emission spectra ( $\lambda_{\text{exc}} = 300$  nm) obtained in  $\text{CHCl}_3$  ( $5 \times 10^{-5}$  M) at room temperature (black trace) and for the fibers obtained from  $4 \text{ mg mL}^{-1}$  acetone solution at  $\lambda_{\text{em}} = 630$  nm and  $\lambda_{\text{exc}} = 300$  nm (red trace). (c) Excitation spectra ( $\lambda_{\text{em}} = 555$  nm) using linearly polarized light to excite the fibers parallel (black traces) and perpendicular (red trace) to the growth direction. (d) Emission polarization ( $\lambda_{\text{exc}} = 300$  nm,  $\lambda_{\text{em}} = 555$  nm). (e) The cartoon shows the molecular structure of the Pt(II) complex and the electronic transition before and after the self-assembly.

As far as a sample of aligned fibers is concerned, we found that the emitted light is maximized when the emission polarization is set parallel to the fiber long axis independently from wavelength and polarization angle of the excitation source (Figure 1d). Such finding, along with the fact that the emission has a  $^3\text{MMLCT}$  nature, indicates that the radiative de-excitation process arises from a transition that is aligned along the fiber long axis on which also Pt...Pt interactions are expected to lie. More interestingly, anisotropy excitation spectra suggest that the transition dipole moment of the highest energy excitation band ( $^1\text{IL}/^1\text{ILCT}$ ,  $\lambda_{\text{exc}} = 250\text{--}350$  nm) is orthogonal with respect to the low energy lying excitation band ( $^1\text{MMLCT}$ ,  $\lambda_{\text{exc}} = 350\text{--}530$  nm), as shown in Figure 1c.

On the basis of such findings and considerations, it is possible to conclude that the dipole moment of the MMLCT transition is thus oriented along the long fiber axis,

which also contains the axial  $d_z^2\pi \cdots d_z^2\pi$  intermolecular interactions. On the other hand, if one considers the transition at  $\lambda_{exc} = 300$  nm, also observed when the complex is molecularly dissolved, the associated transition dipole moment lies onto the molecular plane that is oriented orthogonally with respect to the long fiber axis. The MMLCT band is indeed perpendicular to such plane and it follows that the Pt $\cdots$ Pt metallophilic interaction provides high directionality to the fiber growth (Figure 1e).

In **Chapter 4** the effects of the introduction of a single chiral center into the molecular structure onto the photophysical properties in both solution and solid state were investigated. This is because these luminescent self-assembled structures might display very interesting chiro-optical properties<sup>1-3</sup> with possible application in chiro-optical switches<sup>4</sup> and polarized light-emitting devices such as 3D organic light-emitting diodes (3D OLEDs).<sup>5</sup> Thus, two enantiomeric Pt(II) complexes bearing a chiral ancillary moiety ((S or R)-2-hydroxy-2-phenyl-N-(pyridin-4-ylmethyl)acetamide)) were synthesized and chemically characterized (complex **4a-b**). As a result, in diluted CHCl<sub>3</sub> solution ( $5 \times 10^{-5}$  M) the two enantiomeric complexes displayed identical photophysical properties and very much similar to those above mentioned for the parental complex **Pt-CF<sub>3</sub>tz-pyC<sub>5</sub>** (Figure 2a).

When the complexes were molecularly dissolved it was not possible to detect any circular dichroic signal (CD) (concentration range  $10^{-6}$ - $10^{-4}$  M) even if the ancillary chiral pyridine presents a clear CD signal.

Upon drop-casting a  $1.03 \text{ mg mL}^{-1}$  THF solution of either the S- or the R- enantiomer onto a quartz substrate, formation of bright emissive fibers was observed. Also in this case, the formation of a low-lying absorption band and the formation of a bathochromically-shifted broad emission is due to the establishment of ground state Pt $\cdots$ Pt metallophilic interactions, and can be attributed to a <sup>1,3</sup>MMLCT band (Figure 2a).

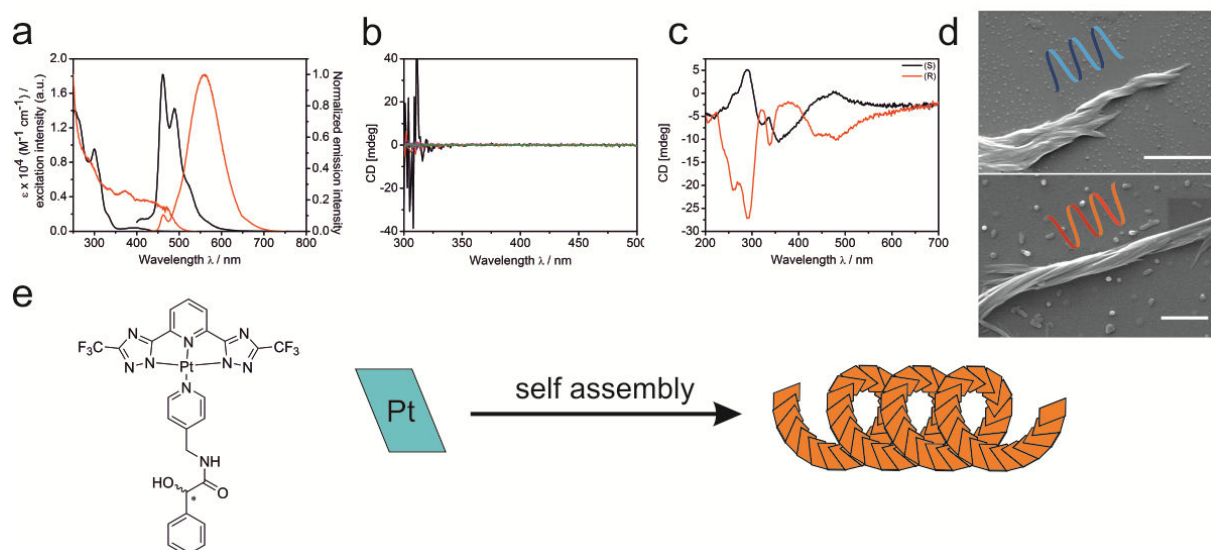


**Figure 2.** (a) Absorption spectra and emission spectra ( $\lambda_{exc} = 300$  nm) obtained in THF ( $5 \times 10^{-5}$  M) at room temperature (black trace) and for the fibers obtained from  $1.03 \text{ mg mL}^{-1}$  acetone solution at  $\lambda_{em} = 630$  nm and upon excitation at  $\lambda_{exc} = 300$  nm (red trace). (b) CD signal of the platinum complex (concentration range  $10^{-6}$ – $10^{-4}$  M). (c) CD signal of the self-assembled fibers after drop-casting a THF solution containing S- enantiomer (black trace) and R- enantiomer (red trace) onto glass. (d) SEM pictures of the chiral fibers of enantiomer R- (top) and S- (bottom) showing the different helicity. (e) Structure of the Pt(II) complex and schematic representation of the supramolecular self-assembly of the chiral Pt(II) complex **4a** (S) and **4b** (R).

Differently to what observed in solution, the self-assembled fibers display a strong CD signal (Figure 2c) and the sign of the Cotton effects is function of the enantiomeric configuration of the molecular structure of the platinum complex. Indeed, two mirroring CD spectra were obtained for complexes **4a-b**. The self-assembled structures were further characterized by means of morphological techniques such as scanning electron microscopy (SEM) and the corresponding micrographs are displayed in Figure 2d. SEM images of the enantiomerically pure samples showed the presence of interconnected fibers with a handedness as a consequence of the supramolecular chiral organization of the enantiomeric complexes in the assemblies. In particular, enantiomers R- and S- aggregate in a clockwise and counterclockwise arrangement, respectively, yielding self-assembled nanostructures with right- (*P*) and left-handed (*M*) helical configuration, respectively (Figure 2d). It is possible to hypothesize that in both cases the fibrous assemblies are composed by thinner nanostructures such as nanofibrils. Thus, formation of such chiral supramolecular

structures in the solid state samples upon establishment of metallophilic and  $\pi$ - $\pi$  interactions is indeed responsible of the amplification of the CD signal which does not occur when the complexes are molecularly dissolved.

In **Chapter 5** the self-assembly properties of an amphiphilic Pt(II) complex functionalized with a hydrophilic triethylene glycol pendant through a moiety capable to engage directional hydrogen bonding such as N–H, namely **Pt-CF<sub>3</sub>tz-pyPEG (Error! Reference source not found.a)**, were comprehensively investigated. When complex **Pt-CF<sub>3</sub>tz-pyPEG** is molecularly dissolved in air-equilibrated 1,4-dioxane ( $0.1\text{--}200 \times 10^{-5}$  M) only a weak blue emission is detected with PLQY of about 1%. Upon flash-injecting a dioxane solution of **Pt-CF<sub>3</sub>tz-pyPEG** ( $c = 2 \times 10^{-3}$  M) into water – the latter acting as the non-solvent – it was achieved to kinetically entrap this compound into a metastable state (assembly **A**). Such assembly is constituted by soft nanoparticles and displays a strong orange phosphorescence (PLQY = 84%) despite the air-equilibrated conditions due to the physical shield of the excited state located on the complex moieties. The strong bathochromically shifted emission band when compared to the emission in dilute dioxane solution is attributed to the establishment of Pt··Pt metallophilic interactions (**Error! Reference source not found.a**).<sup>6-11</sup> It was found that by playing with the solvent/non solvent ratio and using an integrating sphere setup to investigate the overall changes in the photophysical properties, it was possible to characterize and control a highly complex supramolecular landscape comprising two kinetic assemblies (namely **A** and **B**) and the thermodynamic isoform (namely, assembly **C**) as shown in figure 3.

At 95% water content, assembly **A** is stable for more than 10 hours without any detectable change in the photophysical properties. On the other hand, upon decreasing the amount of water by adding molecularly dissolved complex in pure 1,4-dioxane, which lowers the interconversion energy barrier, the system evolves to the thermodynamically favored isoform (assembly **C**). The kinetic control as well as the large spectral changes over the different assemblies allowed an unprecedented real-time visualization of the self-assembly processes which showed solvent dependent kinetics (Figure 3b-c).

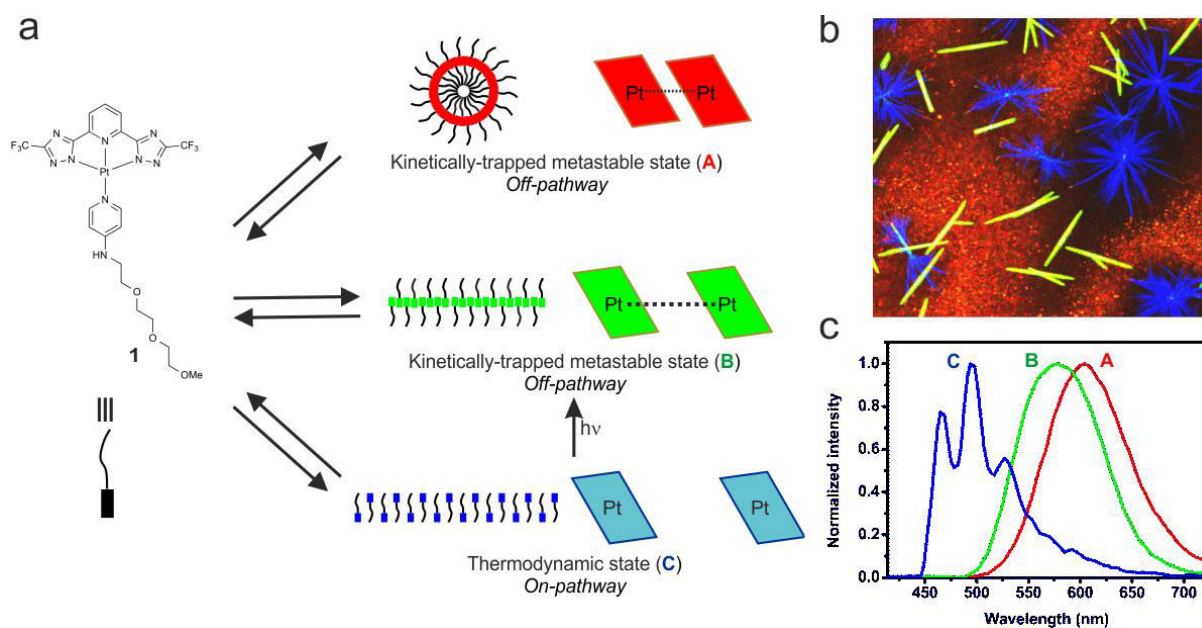


Figure 3. (a) Illustration of the landscape of the supramolecular self-assemblies of complex **1**. Left, chemical formula of the platinum(II) complex **1**. Middle, schematic illustration of the assemblies **A** (top), **B** (middle), and **C** (bottom) in dynamic equilibrium with the monomeric species. Right, the extent of the Pt...Pt interaction corresponding to each assembly are shown. The strength of the interactions decreases from **A** to **B** and is not present in **C**. (b) Confocal microscopy image of the supramolecular assemblies **A** (red), **B** (green) and **C** (blue) showing their true-color emission obtained by using lambda-mode option and (c) their respective normalized emission spectra upon  $\lambda_{exc} = 405$  nm.

Assembly **C** consists of micrometer-long ribbon-like structure, as found by SEM analysis, that possesses the same emission energy and profile as the monomeric species, but with much higher PLQY (up to 20%) suggesting the Pt...Pt interactions are indeed lost or weakened down to a negligible extent. A more accurate photophysical analysis revealed that there is an *off*-pathway that leads to the formation of a second metastable transient structure (assembly **B**), which is characterized by rod-like structure with green-yellow emission. Thermodynamic investigation has clearly demonstrated that the formation of assembly **C** ( $c = 6 \times 10^{-5}$  M in 60:40 water:dioxane) occurs *via* a cooperative nucleation-elongation mechanism characterized by a disfavored nucleation step and a subsequent favored elongation process<sup>12,13</sup>. At solvent composition of 95:5 water:dioxane, the very slow nucleation-elongation processes of **B** and **C**, while **A** is trapped, prompted investigation about the possibility to control the cooperative growth of **C** using the seeded living supramolecular

polymerization.<sup>14</sup> To this end, starting from pure assembly **A** at 95% water ( $c = 5 \times 10^{-5}$  M,  $D_h = 114.4$  nm, PDI = 0.188) we selectively obtain seeds of **C** in a rather good size distribution ( $D_h = 265.3$  nm, PDI = 0.150) upon sonication. The addition of different aliquots of such suspension of seeds **C** to an excess of pure metastable **A** (95% H<sub>2</sub>O) leads to changes in the electronic absorption spectra with respect to the reaction time with an apparent first-order kinetics with respect to [seed **C**] typical for chain growth polymerization<sup>15</sup>. Confocal microscopy investigation showed the formation of blue-emissive rods with uniform length that increases upon decreasing the amount of seeds (Figure 4 left).

Size control of assembly **C** was also achieved, however full management for obtaining *off*-pathway assembly **B** as pure isoform seems to be still precluded. This is due to the intrinsically transient nature of **B** as well as to the concomitant formation of **C**. Yet, we find out that it is possible to perform a fast **C** → **B** interconversion in 95:5% H<sub>2</sub>O:dioxane with good spatial resolution, while keeping the structural features intact, upon irradiating the former with a laser power higher than that used for imaging (Figure 4 right).

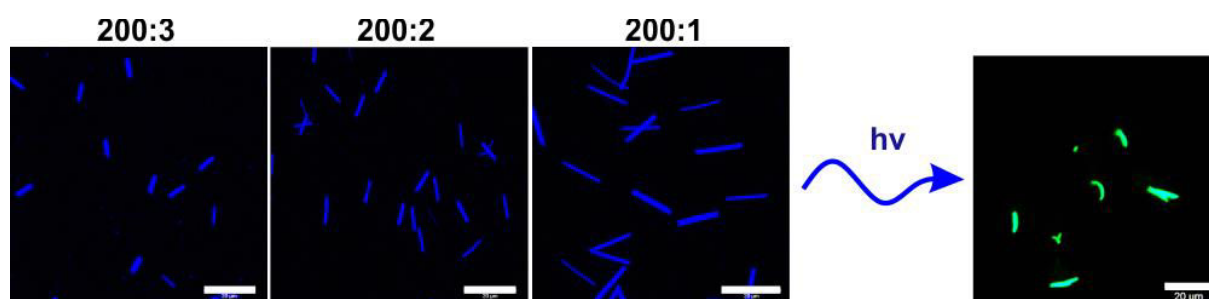


Figure 4. Confocal images of fibers obtained from seeded polymerization under different  $[A]/[C]$  condition and photoconversion.

In conclusion, in **Chapter 5** a landscape comprising two kinetic assemblies and the thermodynamic isoform was characterized in detail. The monitoring of the different emission properties, used as fingerprint for each of the assembled species, allowed an unprecedented real-time visualization of the evolving self-assemblies.

In **Chapter 6**, it is reported on how the establishment of Pt...Pt interactions between neighboring Pt(II) complexes can be advantageously used to obtain dynamic labels for imaging applications. It was found that the complexes **Tol-Pt-4OHpy** and

**CF<sub>3</sub>-Pt-4OHpy** (Figure 5) are internalized in human cervical carcinoma, HeLa, cells. The emission spectra taken from the highly emissive spots clearly demonstrated that for both complexes, the emission energy and shape correspond to those of the assembled systems in DMSO–water solution. The emission of **Tol-Pt-4OHpy** was mainly observed in the cytoplasmic region while the **CF<sub>3</sub>-Pt-4OHpy** was partially distributed in the cytoplasmic region, but bright aggregates were observed inside the nucleus, more precisely in the nucleoli. The low-lying <sup>1</sup>MMLCT absorption band makes them able to be excited also in the visible region down to  $\lambda_{exc} = 550$  nm, while the monomeric counterparts display negligible absorption in this region.

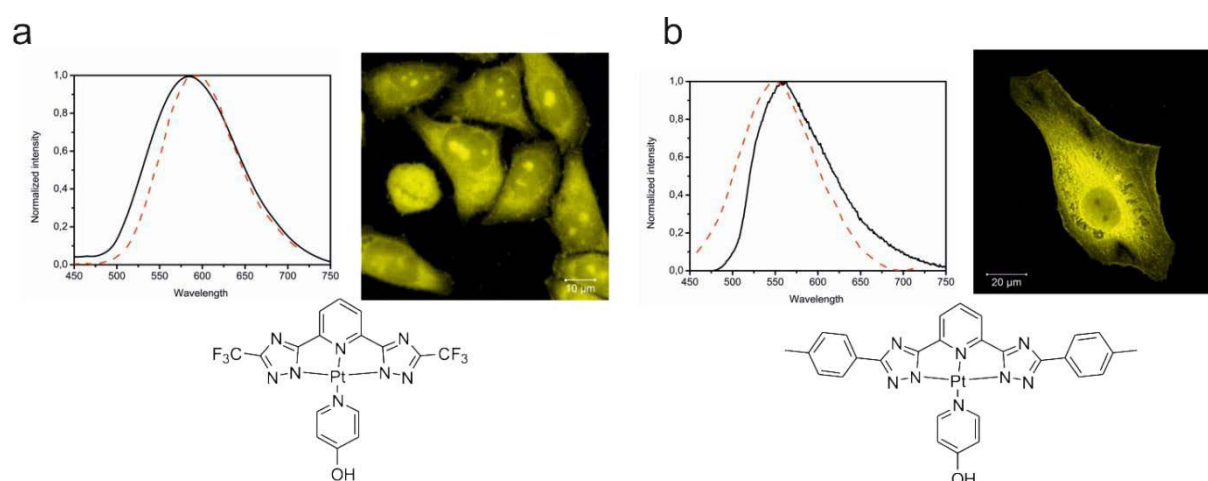


Figure 5. (a) Luminescence confocal microscopy images showing the distribution of **CF<sub>3</sub>-Pt-4OHpy** (a) and **Tol-Pt-4OHpy** (b) inside HeLa cells; emission spectra recorded in DMSO:H<sub>2</sub>O solution (black solid trace) and inside HeLa cells (dashed red trace). The samples were excited at  $\lambda_{exc} = 330$  and 405 nm for solvents and cell experiments, respectively.

It was demonstrated that the aggregation process is not only leading to the protection of the platinum complexes and prevents oxygen quenching, as already discussed above, but also to reduced photobleaching if compared to organic dyes, such as DAPI. However, cellular uptake of the platinum complexes and their internalization in HeLa cells occurred only when PBS was used as incubation media. The replacement of PBS by cell culture media prevented the complexes to be internalized by the cells.

Live cell imaging on HeLa cells incubated with **CF<sub>3</sub>-Pt-4OHpy** in cell culture while exciting at 405 nm revealed no uptake occurring before the first 30 minutes, but surprisingly the uptake of the complex starts very rapidly only when the cells were

close to apoptosis due to the long exposure to UV light.<sup>16</sup> The only area irradiated with UV light showed cellular uptake of the complex while cells in the surroundings did not exhibit any internalization since they have not been damaged.

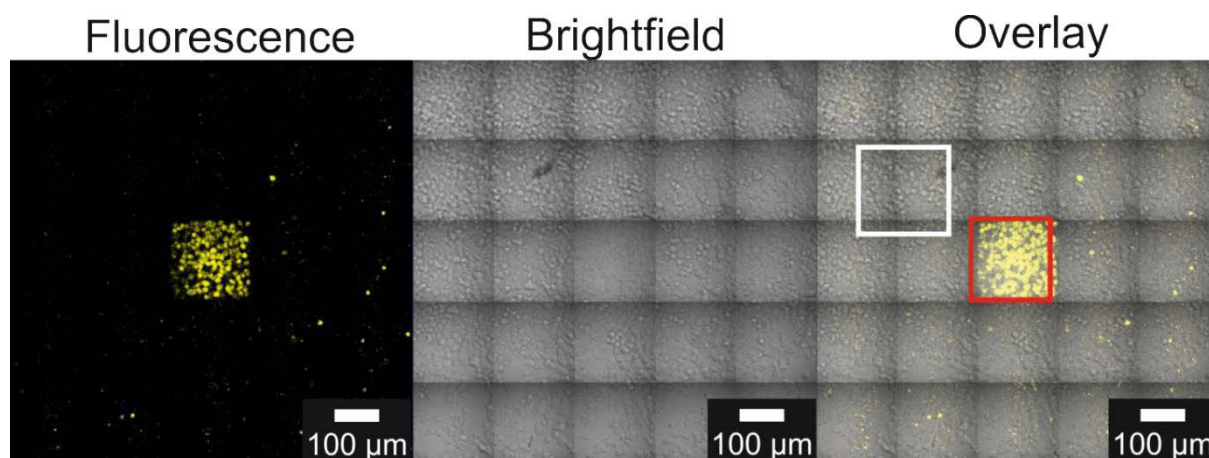


Figure 6. Light-induced internalization of **CF3-Pt-4OHpy** in culture media after 60 minutes of irradiation showing the unexcited region and the area exposed to the 405 nm laser irradiation.

As a control experiment to prove that the platinum complex is not responsible for the cell damage due to the formation of singlet oxygen or other reactive species, the system was irradiated in the same conditions at 455 and 488 nm where the platinum complexes absorb light. No cellular uptake occurred in this case. At this stage we have no evidence if the metal complexes are internalized as monomeric species and then aggregate inside the cells or they are uptaken as small aggregates. The formation of such aggregates can be considered a new class of dynamic probes, since the emission can be easily modulated and their long-lived emission easily detected. Also, by designing the coordinating ligands it is possible to internalize and localize the complexes in specific parts of the cells. The investigated complexes can be in particular used as dead cell labelling molecules.

**Chapter 7** focuses on Pt(II) complexes bearing biologically active moieties to be used as luminescent bio-imaging tags. In particular, two novel neutral Pt(II) complexes bearing a  $\beta$ -lactam unit on the ancillary pyridine ligand were synthesized and their photophysical properties investigated. The complexes showed interesting emission properties that are dominated by the formation of aggregates in the solid state due to the square-planar geometry of the Pt(II) species. Importantly, the

formation of closed-shell metal...metal interactions in such aggregates leads to novel excited states that conveniently allow excitation in the visible region. This is a fundamental achievement for the useful application of luminescent transition metal complexes for bioimaging application. The combination of the biologically active azetidinone agent and the intense and long-lived emission are of particular interest for developing efficient multifunctional biomedical systems.

As already described the photoluminescent properties of this class of compounds strongly depends not only on the ligand-field splitting, but also on the intermolecular distance between the Pt(II) ions. It has been already demonstrated that Pt...Pt separation can be modulated also in solid state upon exposure to volatile organic compounds (VOCs)<sup>17</sup> and mechanical stimuli<sup>18,19</sup> which often results in a reversible change in the color of the materials upon grinding (mechanochromism) and exposure to solvents vapors (vapochromism)<sup>20,21</sup>. Such properties have attracted increasing attention for the creation of new materials and the change in color upon aggregation has application in white light organic emitting diodes (WOLEDs)<sup>22,23</sup> as well sensing, in particular the development of "electronic noses"<sup>24</sup> that can detect harmful volatile organic (and inorganic) chemicals in the environment.

In this respect, in **Chapter 8** the mechanochromic properties of bulk materials were correlated with those at the nanoscale (single fibers) comprising a highly luminescent platinum complexes, namely **Pt-CF<sub>3</sub>tz-pyPEG** and **Pt-Toltz-pyPEG**. Different complementary techniques at bulk and nanoscopic level were employed to monitor changes in the photoluminescent properties upon mechanical grinding (tribochromism) and by pressure-dependent studies (piezochromism). In particular, an AFM tip was employed to modulate the mechanical stress from pure pressure to high friction in a single self-assembled fiber at the nanoscale. Moreover, it was found that an AFM tip can be used to write submicron features with high fidelity on individual ribbons, which are individually used as homogeneous memory substrates. The information written by AFM can also be hidden upon irradiation. The photoconversion of the fiber in the relaxed form (**R**) into a yellow emitting form (**PC**),

featuring similar luminescence as the mechanically stressed form (**MS**), reduces the luminescence contrast with the unwritten region of the ribbon.

Complex **Pt-CF<sub>3</sub>tz-pyPEG** (Figure 7a) displays bright blue emission in solid state peaking at  $\lambda_{em} = 465, 494$ , with PLQY up to 20%. Interestingly, after a gentle grinding by using a pestle, the complex becomes bright yellow with PLQY up to 51% and the emission spectrum is characterized by a broad band centered at  $\lambda_{max} = 598$  nm (Figure 7b). Upon treatment of the ground powder with a few drops of acetone, the yellow luminescence from this complex turns back to the original luminescence after drying of the solid in air for a few minutes (Figure 7e). Also, complex **Pt-Toltz-pyPEG** (Figure 7d) exhibits a similar mechanochromic response; before grinding the compound is characterized by an intense green emission with PLQY up to 46% and  $\lambda_{max} = 542$  nm; whereas, the emission spectrum becomes broader after grinding with  $\lambda_{max} = 582$  nm and PLQY up to 35% (Figure 7d). As expected, exposure to few drops of acetone restored the original emission color as shown in Figure 7g.

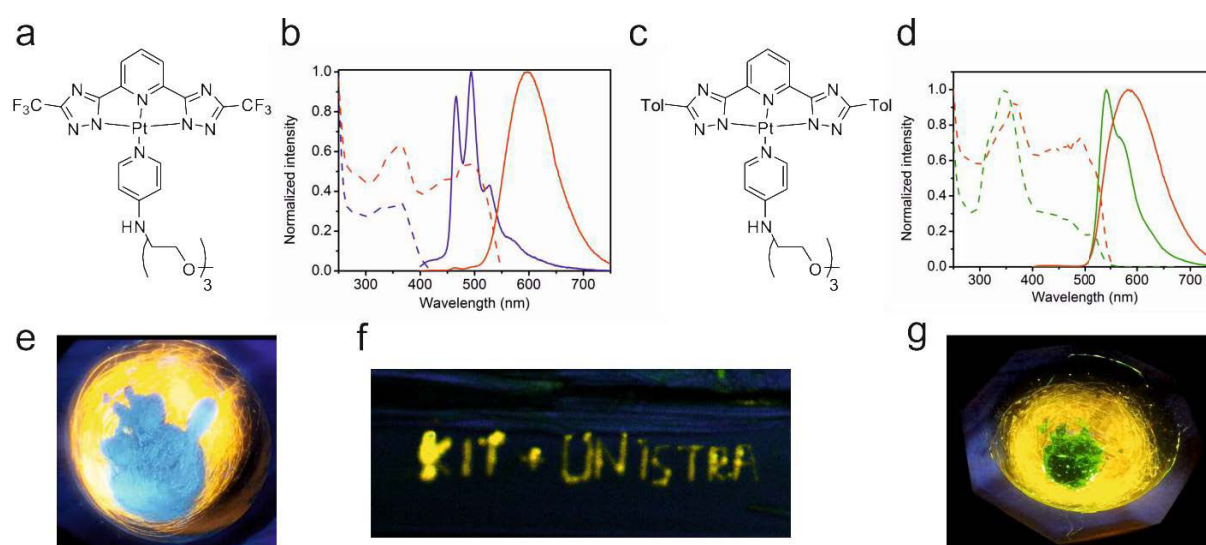


Figure 7. (a) and (c) chemical structures of **Pt-CF<sub>3</sub>tz-pyPEG** and **Pt-Toltz-pyPEG** and (b) and (d) their relative emission (solid line) and excitation spectra (dashed line) before (blue and green line) and after grinding (red line). (e) and (g) photographs of the solid after grinding showing the restoration of the original emission color upon exposure to few drops of acetone. (f) Confocal picture of a single fiber obtained from **Pt-CF<sub>3</sub>tz-pyPEG** after AFM writing.

**Pt-CF<sub>3</sub>tz-pyPEG** can be self-assembled in a CH<sub>3</sub>CN solution into ultra-long ribbons, yielding structures with typical length between 250  $\mu$ m and 5 mm and rectangular

section of aspect ratio about 1:10 and featuring thickness in the range 2:5  $\mu\text{m}$  and width in the range 15:50  $\mu\text{m}$ . It was found that is possible to use the AFM as lithographic tool (Figure 7f) to record data with sub-micrometer resolution based on the mechanochromic properties of the ribbons. Furthermore, the high control on applied force and its ability to follow surface profile guarantee the lithography of patterns with high fidelity. Also photochromism, *i.e.* emission spectrum changes upon exposure to light, has been observed on these materials. Such property can be conveniently used to conceal information previously written with nanolithography, when the region of the ribbon surrounding the stored information is homogeneously converted with irradiation.

In conclusion, in these Ph.D. thesis is reported the design, synthesis and comprehensive characterization of a set of novel luminescent platinum complexes which display fascinating self-assembly properties. It was demonstrated how such Pt(II) complexes can be self-assembled in a controlled manner managing with kinetics and thermodynamic pathways. This chemical management led to supramolecular architectures with enhanced and unique properties useful for the development of new functional materials in and out of the thermodynamic equilibrium. The prepared materials can be useful mechanochromic and data storage devices as well as to be used as novel long-lived luminescent tags in biomedical field. Finally, some of the possible applications envisaged for such compounds were also demonstrated.

## References

- [1] Y. Wang; J. Xu; Y. Wang; H. Chen, *Chem. Soc. Rev.*, **2013**, *42*, 2930-2962.
- [2] F. Garcia; L. Sanchez, *J. Am. Chem. Soc.*, **2012**, *134*, 734-742.
- [3] F. Aparicio; F. Vicente; L. Sanchez, *Chem. Commun.*, **2010**, *46*, 8356-8358.
- [4] P. Guo; L. Zhang; M. Liu, *Adv. Mater.*, **2006**, *18*, 177-180.
- [5] M. Grell; D. D. C. Bradley, *Adv. Mater.*, **1999**, *11*, 895-905.
- [6] C. A. Strassert; C. H. Chien; M. D. Galvez Lopez; D. Kourkoulos; D. Hertel; K. Meerholz; L. De Cola, *Angew. Chem. Int. Ed. Engl.*, **2011**, *50*, 946-950.
- [7] M. Mauro; A. Aliprandi; C. Cebrian; D. Wang; C. Kübel; L. De Cola, *Chem. Commun.*, **2014**, *50*, 7269-7272.
- [8] V. W.-W. Yam; K. M.-C. Wong; N. Zhu, *J. Am. Chem. Soc.*, **2002**, *124*, 6506-6507.
- [9] B. Ma; J. Li; P. I. Djurovich; M. Yousufuddin; R. Bau; M. E. Thompson, *J. Am. Chem. Soc.*, **2005**, *127*, 28-29.
- [10] C. Po; A. Y. Tam; K. M. Wong; V. W. Yam, *J. Am. Chem. Soc.*, **2011**, *133*, 12136-12143.

- [11] M. Krikorian; S. Liu; T. M. Swager, *J. Am. Chem. Soc.*, **2014**, *136*, 2952-2955.
- [12] H. M. ten Eikelder; A. J. Markvoort; T. F. de Greef; P. A. Hilbers, *J. Phys. Chem. B*, **2012**, *116*, 5291-5301.
- [13] T. F. A. De Greef; M. M. J. Smulders; M. Wolffs; A. P. H. J. Schenning; R. P. Sijbesma; E. W. Meijer, *Chem. Rev.*, **2009**, *109*, 5687-5754.
- [14] S. Ogi; K. Sugiyasu; S. Manna; S. Samitsu; M. Takeuchi, *Nat. Chem.*, **2014**, *6*, 188-195.
- [15] *Principles of Polymerization*, ed. John Wiley & Sons, Inc., **2004**
- [16] K. V. Bogdanov; A. B. Chukhlovina; A. Y. Zaritsky; O. I. Frolova; B. V. Afanasiev, *Br. J. Haematol.*, **1997**, *98*, 869-872.
- [17] M. Kato; A. Omura; A. Toshikawa; S. Kishi; Y. Sugimoto, *Angew. Chem. Int. Ed. Engl.*, **2002**, *41*, 3183-3185.
- [18] A. L. Balch, *Angew. Chem. Int. Ed. Engl.*, **2009**, *48*, 2641-2644.
- [19] T. Abe; T. Itakura; N. Ikeda; K. Shinozaki, *Dal. Trans.*, **2009**, 711-715.
- [20] A. Han; P. Du; Z. Sun; H. Wu; H. Jia; R. Zhang; Z. Liang; R. Cao; R. Eisenberg, *Inorg. Chem.*, **2014**, *53*, 3338-3344.
- [21] J. Ni; Y.-G. Wang; H.-H. Wang; L. Xu; Y.-Q. Zhao; Y.-Z. Pan; J.-J. Zhang, *Dalt Trans*, **2014**, *43*, 352-360.
- [22] L.-M. Huang; G.-M. Tu; Y. Chi; W.-Y. Hung; Y.-C. Song; M.-R. Tseng; P.-T. Chou; G.-H. Lee; K.-T. Wong; S.-H. Cheng; W.-S. Tsai, *J. Mat. Chem. C*, **2013**, *1*, 7582-7592.
- [23] B. Ma; P. I. Djurovich; S. Garon; B. Alleyne; M. E. Thompson, *Adv. Funct. Mater.*, **2006**, *16*, 2438-2446.
- [24] A. Kobayashi; M. Kato, *Eur. J. Inorg. Chem*, **2014**, *2014*, 4469-4483.



# Acknowledgements

I would like to thank my supervisor, Prof Luisa De Cola, for the great opportunity to carry on a PhD in her wonderful group. She has opened my eyes on the world of research, giving me the possibility to travel and to have discussions with the top world scientists. I really appreciate the freedom and the trust you have given me during the last 3.5 years. I have never missed anything especially in terms of materials and instruments; the only limits that I had were my skills and my imagination and I believe that a PhD student cannot dream of anything better.

I would like to thank Dr. Matteo Mauro that has always followed my research with interest and has always supported and encouraged me to continue on my way; we have always discussed the results (not always peacefully), but I am sure this has greatly contributed to the success of the work. We have published together all the content of this thesis.

I would like to thank Dr. Nadia and Dr. Chien-Wei (John Wayne), we basically started this adventure together since Münster, passing for the move here in Strasbourg (I hope I never have to move a lab of this size again). You reached the finish line before me and I hope to get there soon too. I could not wish for better friends and colleagues. Elena (Longhi Longhi Longhi) who lived our same adventure as post doc. Your joy and your passion for this job helped me not to break down in difficult times during these years. You have also taught me the profound meaning of the term entropy. I have enjoyed a lot your company, especially outside the university. For this I have to thank also Laura, Giacomo, Leana, Federica, Valentina and Ingrid who managed to drag me out of the laboratory remembering what is really important in life. I would also like to thank Amparo, always nice and kind and Veronika both of them helped me a lot in the writing of this thesis, which is when I really needed help. For this I would like to thank the whole group, in time of need, you were there to help me. Special thanks go to Federica (Fede), Claire and Ines who have always helped me to juggle within the French bureaucracy and technical problems. Without you I would probably be still trying to enroll in the first year. Thanks also to Ricardo, Youssef and Etienne, my official French translators and Loic, always dreaming Hello Kitty. Finally I would like to thank all the people that have worked with me during this PhD in particular Dedy, Roberto and Damiano.

Special thanks go to a very special person, my beautiful girl Sofia, who remained by my side all these years. We spent so many difficult times together. I could not have done it without you and I cannot imagine a future without you. I love you.

Last, but not least, thanks to my family, who made me what I am today, I think that there are no words to express the gratefulness that I have for you.

To conclude I would like to say goodbye to all the people I met during these years and good luck to the new PhDs that have started this incredible adventure as well as to all the students that I followed during my PhD.

## CURRICULUM VITAE



### Personal information

Name Surname **Alessandro Aliprandi**  
Address piazza Europa 25, 44100 Ferrara (Italy)  
Mobile +39 329 3151024; +33669756040  
E-mail(s) **[alessandro.aliprandi@gmail.com](mailto:alessandro.aliprandi@gmail.com)**  
Nationality Italian  
Date of birth 11/07/1985  
Gender Male

**Desired employment** **Researcher, R&D, group leader, problem solving**  
**Occupational field** **Applied chemistry, advanced polymers, photovoltaic, bioimaging, organic and inorganic chemistry**

### Education and training

Dates **01/09/2012 → 30/10/2015**  
Qualification PhD candidate under the supervision of Prof. Luisa De Cola  
Organization Institut de Science et d'Ingénierie Supramoléculaires I.S.I.S. (Université de Strasbourg)

Dates **01/02/2012 - 01/09/2012**  
Qualification PhD candidate under the supervision of Prof. Luisa De Cola  
Organization Center for Nanotechnology (CeNTech) (Westfälische Wilhlems-Universität Münster)  
Heisenbergstr. 11 · D –, 48149 Münster (Germany)

Dates **01/02/2011 - 01/02/2012**  
Qualification Holder of a scholarship at the Department of Chemistry (PRIN)  
Principal subject "Synthesis and characterization of sensitizers for photoelectrochemical cells"  
Organization Department of Chemistry (University of Ferrara)  
Via L. Borsari, 46, 44100 Ferrara (Italy)

Dates **12/12/2010**  
Qualification Master Degree in Chemistry grade: **110/110 cum laude**  
Principal subject Title of the thesis: "Synthesis and photoelectrochemical characterization of ruthenium complexes functionalized with catechols"(supervisor: Prof. Carlo Alberto Bignozzi, Dr. Stefano Carli)  
Organization Faculty of Mathematical, Physical and Natural Sciences (University of Ferrara)

Via L. Borsari, 46, 44100 Ferrara (Italy)

Dates	<b>12/12/2007</b>
Qualification	Bachelor Degree in Chemistry (post reform) grade: <b>110/110 cum laude</b>
Principal subject	title of thesis: "Stereoselective Synthesis of $\beta$ -C-glucosyl glycine promoted by the organocatalyst L-proline "(Supervisor Dr. Alessandro Massi)
Organisation	Faculty of Mathematical, Physical and Natural Sciences (University of Ferrara) Via L. Borsari, 46, 44100 Ferrara (Italy)
<b>Personal skills and competences</b>	Problem solving capacity, proactive behavior, passion to scientific research and informatics
<b>Languages</b>	
English	Very good Knowledge (oral and written)
Italian	Mother tongue
Social skills and competences	Friendly person with attitude for interpersonal relation and teamwork, work experience in multicultural groups. Good communication skills.
Technical skills and competences	<b>Excellent knowledge of organic chemistry</b> and supramolecular chemistry in particular synthesis of nitrogen based ligands and chiral molecules and characterization through NMR spectroscopy and mass spectrometry. Excellent knowledge of organometallic chemistry, in particular synthesis and characterization of transition metal (Fe, Co, Ru and Pt). <b>Excellent knowledge of photophysics</b> which includes UV-Vis electronic absorption, steady state and time-resolved fluorescence spectroscopy, confocal and fluorescence microscopy, circular dichroism, fluorescence anisotropy. <b>Very good knowledge of electrochemistry</b> and electrochemical analysis. Very good expertise in DSSC fabrication and characterization (I-V curves, IPCE and impedance spectroscopy).
Computer skills and competences	Good knowledge of Microsoft office, Coreldraw, SciFinder Scholar, ChemDraw, MestReNova, Origin. Good knowledge of computer assembly and problem solving.
Driving licence(s)	B
Patents	Platinum complexes, Eur. Pat. Appl. (2013) EP13306572.
Hobby and sports	I'm black belt (2 <sup>nd</sup> DAN) of Karate and I also practiced Aikido (3 <sup>rd</sup> KYU). I like martial arts and informatics.

## PUBLICATIONS

- “A multitechnique physico-chemical investigation of various factors controlling the photoaction spectra and of some aspects of the electron transfer for a series of push-pull Zn(II) porphyrins acting as dyes in DSSC” Alessio Orbelli Biroli, Francesca Tessore, Maddalena Pizzotti, Cinzia Biaggi, Renato Ugo, Stefano Caramori, Alessandro Aliprandi, Carlo Bignozzi Filippo De Angelis, Giacomo Giorgi, Emanuela Licandro, Elena Longhi. *J. Phys. Chem. C*, **2011**, 115 (46), 23170–23182
- “Sensitization of Nanocrystalline TiO<sub>2</sub> with Multibranched Organic Dyes and Co(III)/(II) Mediators: Strategies to Improve Charge Collection Efficiency” Miriam Mba, Marco D’Acunzo, Patrizio Salice, Tommaso Carofiglio, Michele Maggini, Stefano Caramori, Alessandra Campana, Alessandro Aliprandi, Roberto Argazzi Stefano Carli and Carlo A. Bignozzi *J. Phys. Chem. C*, **2013**, 117, 19885–19896.
- “Tridentate Complexes of Group 10 Bearing Bis-Aryloxy N-Heterocyclic Carbene Ligands: Synthesis, Structural, Spectroscopic, and Computational Characterization” Etienne Borré, Georges Dahm, Alessandro Aliprandi, Matteo Mauro, Samuel Dagonne, and Stéphane Bellemin-Laponnaz *Organometallics*, **2014**, 33, 4374–4384.
- “Bio-imaging with neutral luminescent Pt(II) complexes showing metal/metal interactions” Dedy Septiadi, Alessandro Aliprandi, Matteo Mauro and Luisa De Cola *RSC Adv.*, **2014**, 4, 25709–25718.
- “When self-assembly meets biology: luminescent platinum complexes for imaging applications” Matteo Mauro, Alessandro Aliprandi, Dedy Septiadi, Nermin Seda Kehra and Luisa De Cola *Chem. Soc. Rev.*, **2014**, 43, 4144–4166.
- “Self-assembly of a neutral platinum(II) complex into highly emitting microcrystalline fibers through metallophilic interactions” Matteo Mauro, Alessandro Aliprandi, Cristina Cebrián, Di Wang, Christian Kübelc and Luisa De Cola *Chem. Commun.*, **2014**, 50, 7269–7272.
- “β-Lactam Bioconjugates Bearing Luminescent Platinum(II) Tags: Synthesis and Photophysical Characterization” Roberto Soldati, Alessandro Aliprandi, Matteo Mauro, Luisa De Cola, and Daria Giacomini *Eur. J. Org. Chem.* **2014**, 7113–7121.
- “Nanopatterning of surfaces with mono- and hetero bi-metallic 1D coordination polymers: a molecular tectonics approach at the solid/liquid interface” Mohamed El Garah , Nicolas Marets , Matteo Mauro , Alessandro Aliprandi , Sara Bonacchi , Luisa De Cola , Artur Ciesielski , Veronique Bulach , Mir Wais Hosseini and Paolo Samori, *J. Am. Chem. Soc.*, **2015**, 137(26), 8450-8459.
- “Recent advances in phosphorescent Pt(II) complexes featuring metallophilic interactions: properties and applications” Alessandro Aliprandi, Damiano Genovese, Matteo Mauro and Luisa De Cola, *Chem. Lett.*, **2015**, 44, 1152–1169.
- “Controlling and imaging biomimetic self-assembly” Alessandro Aliprandi, Matteo Mauro, and Luisa De Cola *Nat. Chem.*, **2015**, in press.
- “Glyco-functionalized neutral dinuclear Rhenium complexes for optical imaging” Monica Panigati, Alessandro Palmioli, Anna Bernardi, Matteo Mauro, Alessandro Aliprandi, Dedy Septiadi and Luisa De Cola, *manuscript in preparation*.

- “Photochromism and mechanochromism at the nanoscale: data storage on individual self-assembled ribbons” Damiano Genovese, Alessandro Aliprandi, Matteo Mauro, Michael Hirtz, Harald Fuchs, Ya-suhiko Fujita, Hiroshi Uji-I, Sergei Lebedkin, Manfred Kappes and Luisa De Cola, *manuscript in preparation*.

## COMUNICACION AND POSTERS

- “20<sup>th</sup> International Symposium on the Photophysics and Photochemistry of Coordination Compounds” July 7-11 2013, Traverse City, Michigan, USA. Poster entitled: “Luminescent molecular assemblies based on Pt(II) complexes: From solution to cell imaging” A. Aliprandi, M. Mauro, L. Maggini, D. Septiadi and L. De Cola.
- “25<sup>th</sup> IUPAC Symposium on Photochemistry” July 13-18 2014, Bordeaux, France. Poster entitled: “Luminescent Pt(II) complexes: Self-assembly properties, mechanochromism and application” A. Aliprandi, M. Mauro and L. De Cola.
- “10<sup>th</sup> The International Symposium on Macrocyclic and Supramolecular Chemistry” June 28<sup>th</sup> - July 2<sup>nd</sup> 2015, Strasbourg. Oral communication entitled: “Kinetically trapped aggregates of luminescent Pt(II)-based compounds converting to thermodynamically favored fibrils” A. Aliprandi, M. Mauro and L. De Cola.
- “21<sup>st</sup> International Symposium on the Photochemistry and Photophysics of Coordination Compounds” July 5-9 2015 Kraków, Poland. Poster entitled: “Visualizing and controlling self-assembled structures based on Pt(II) complexes” A. Aliprandi, M. Mauro, L. De Cola.
- “21<sup>st</sup> International Symposium on the Photochemistry and Photophysics of Coordination Compounds” July 5-9 2015 Kraków, Poland. Poster entitled: “Glyco-functionalized neutral dinuclear Rhenium complexes for optical imaging” Monica Panigati, Alessandro Palmioli, Anna Bernardi, Matteo Mauro, Alessandro Aliprandi, Dedy Septiadi and Luisa De Cola.

## PATENTS

- “Platinum complexes as mechanochromic and piezochromic compounds” De Cola, Luisa; Mauro, Matteo; Cebrian Avila, Cristina; Aliprandi, Alessandro, 2013, Eur. Pat. Appl. (2013) EP13306572.

Alessandro ALIPRANDI

# PLATINUM COMPLEXES AND THEIR LUMINESCENT ASSEMBLIES

## Résumé

Cette thèse porte sur la synthèse et la caractérisation photophysique d'une série de composés neutres luminescents de platine (II) contenant un ligand tridentate dianionique chromophore N-donneur et un ligand auxiliaire monodentate. Les composés montrent un changement notable des propriétés de photoluminescence selon l'auto-assemblage en raison de la formation d'interactions intermoléculaires non covalentes faibles telles que metal...metal et  $\pi$ - $\pi$ . Nous avons démontré comment les complexes de Pt (II) peuvent être auto-assemblés d'une manière contrôlée et précise en jouant sur les facteurs cinétiques et thermodynamiques, ainsi que la morphologie des différents ensembles étudiés. Ces approches ont conduit à des matériaux avec des propriétés améliorées et uniques tels que le mécano-chromisme, ainsi que l'absorption et l'émission de la lumière polarisée. Les composés étudiés et leurs assemblages sont utiles non seulement pour le développement de nouveaux matériaux fonctionnels supramoléculaires en équilibre et hors- équilibre, mais aussi pour des applications en bio-imagerie.

Mots-clés: complexes de platine; luminescence; bio-imagerie; auto-assemblage; polymère supramoléculaire; émission polarisée; nano-lithographie

## Résumé en anglais

This thesis focuses on the synthesis and the photophysical characterization of a series of luminescent neutral Pt(II) compounds containing a tridentate dianionic N-donor chromophoric ligand and a monodentate ancillary moiety. The compounds exhibited notable change of the photoluminescence properties upon self-assembly due to the establishment of weak non-covalent intermolecular interactions – metal...metal and  $\pi$ - $\pi$ . We demonstrated how Pt(II) complexes can be self-assembled in a controlled and precise manner by playing with kinetic and thermodynamic factors and the morphology of the different assemblies investigated. Such approaches led to materials with enhanced and unique properties such as mechanochromism and polarized light absorption and emission. The investigated compounds and their assemblies were useful for the development of novel functional supramolecular materials in and out of the equilibrium as well as for bioimaging application.

Keywords: platinum complexes; luminescence; bioimaging; self-assembly; supramolecular polymer; polarized emission; nanolithography.